

CONTINUUM MODELING USING GRANULAR MICROMECHANICS APPROACH:  
METHOD DEVELOPMENT AND APPLICATIONS

BY

Copyright 2016

AUTHOR: PAYAM POORSOLHJOUY

Submitted to the graduate degree program in Department of Civil, Environmental, and Architectural Engineering and the Graduate Faculty of the University of Kansas in partial fulfillment of the requirements for the degree of Doctor of Philosophy.

---

Chairperson Dr. Anil Misra

---

Dr. Masoud Darabi

---

Dr. Rémy Lequesne

---

Dr. Candan Tamerler

---

Dr. Ward H. Thompson

Date Defended: July 08<sup>th</sup>, 2016

The Dissertation Committee for Payam Poorsolhjoui  
certifies that this is the approved version of the following dissertation:

CONTINUUM MODELING USING GRANULAR MICROMECHANICS APPROACH:  
METHOD DEVELOPMENT AND APPLICATIONS

---

Chairperson Dr. Anil Misra

Date approved: July 08<sup>th</sup>, 2016

## ABSTRACT

This work presents a constitutive modeling approach for the behavior of granular materials. In the granular micromechanics approach presented here, the material point is assumed to be composed of grains interacting with their neighbors through different inter-granular mechanisms that represent material's macroscopic behavior. The present work focuses on (i) developing the method for modeling more complicated material systems as well as more complicated loading scenarios and (ii) applications of the method for modeling various granular materials and granular assemblies.

A damage-plasticity model for modeling cementitious and rock-like materials is developed, calibrated, and verified in a thermo-mechanically consistent manner. Grain-pair interactions in normal tension, normal compression, and tangential directions have been defined in a manner that is consistent with the material's macroscopic behavior. The resulting model is able to predict, among other interesting issues, the effects of loading induced anisotropy. Material's response to loading will depend on the loading history of grain-pair interactions in different directions. Thus the model predicts load-path dependent failure.

Due to the inadequacies of first gradient continuum theories in predicting phenomena such as shear band width, wave dispersion, and frequency band-gap, the presented method is enhanced by incorporation of non-classical terms in the kinematic analysis. A complete micromorphic theory is presented by incorporating additional terms such as fluctuations, second gradient terms, and spin fields. Relative deformation of grain-pairs is calculated based on the enhanced kinematic analysis. The resulting theory incorporates the deformation and forces in grain-pair interactions due to different kinematic measures into the macroscopic behavior. As a result, non-classical phenomena such as wave dispersion and frequency band-gaps can be predicted. Using the grain-scale analysis,

a practical approach for calibrating model parameters corresponding to micromorphic continua is also presented that can be used for any given material system or grain assembly.



## **ACKNOWLEDGEMENTS**

First, I would like to express my gratitude to professor Anil Misra, my advisor, for giving me the opportunity to work with him and also for providing me with a huge amount of help and support. His impressive depth and breadth of knowledge has provided an ever-present source of help and support for me during the period of my PhD studies. Without his brilliant ideas and his enthusiasm for exploring different fields, this work would not have been possible. I am truly grateful for this experience.

I am also very grateful Dr. Masoud Darabi, Dr. Rémy Lequesne, Dr. Candan Tamerler, and Dr. Ward H. Thompson, for kindly accepting to serve as my PhD committee members, and for their insightful comments and ideas. I am also indebted to my previous lab-mates, especially Dr. Ranganathan Parthasarathy and Dr. Viraj Singh, for spending invaluable time in our discussions about the research. I would also like to thank the research grant CMMI-1068528 from the National Science Foundation (NSF) for supporting this work.

Finally but most importantly, I would like to express my deepest gratitude to my parents, Mr. Behrouz Poorsolhjoui and Mrs. Fariba Roudneshin, and my brother, Aidin Poorsolhjoui, for their unconditional love and support. This work would have not been possible without them, and is hence, dedicated to them.

## **Table of Contents**

ABSTRACT.....	iii
ACKNOWLEDGEMENTS.....	v
LIST OF FIGURES.....	xi
LIST OF TABLES.....	xviii
1 INTRODUCTION.....	1
1.1 Motivation.....	1
1.2 Objectives and scope.....	3
1.3 Dissertation outline.....	4
2 GRANULAR MICROMECHANICS MODEL.....	8
2.1 Granular Micromechanics model with kinematic constraint.....	9
2.2 Granular Micromechanics model with static constraint.....	16
2.3 Two-dimensional model used for modeling 2D grain assemblies.....	19
2.4 Summary.....	22
3 NONLINEAR GRANULAR MICROMECHANICS: MODELING DAMAGE AND PLASTICITY.....	25
3.1 Thermomechanical framework for granular micromechanics with damage and plasticity	
26	
3.2 Thermomechanical formulation for granular systems.....	29
3.2.1 Kinematics of granular meso-structure.....	29
3.2.2 Thermomechanics equations for granular system.....	30
3.3 Inter-granular coupled damage-plasticity relationships.....	33
3.4 Inter-granular loading-unloading-reloading relationships.....	36
3.5 Constitutive relationship for granular cementitious materials.....	40
3.6 Results and Discussions.....	42

3.6.1	Calibration and identification of model parameters.....	43
3.6.2	Model prediction under confined compression and extension .....	44
3.6.3	Failure prediction under multi-axial loading .....	52
3.6.4	Behavior under strain control loading.....	61
3.7	Summary and Conclusions.....	65
4	FAILURE, AS A FUNCTION OF LOADING PATH AND EFFECT OF INTERMEDIATE PRINCIPAL STRESS.....	68
4.1	Introduction .....	68
4.2	Loading procedures .....	72
4.3	Results and Discussion.....	74
4.3.1	Failure in loadings of Type 1 and Type 2.....	74
4.3.2	Macro-scale failure analysis .....	77
4.3.3	Micro-scale behavior; load-bearing and failure mechanisms .....	80
4.3.4	Localized failure and fault angle.....	91
4.3.5	Fault angle with Matsouka-Nakai criterion .....	96
4.4	Summary and Conclusions.....	98
5	GRAIN SIZE EFFECT USING GRANULAR MICROMECHANICS.....	101
5.1	Introduction .....	101
5.2	Scaling laws for grain-size effect.....	102
5.3	Model calibration .....	104
5.4	Results and Discussions .....	105
5.4.1	Triaxial compression results .....	105
5.4.2	Volume control test results .....	115

5.5	Summary and Conclusions.....	122
6	MODELING INHERENT ANISOTROPY USING GRANULAR MICROMECHANICS .....	124
6.1	Introduction .....	124
6.2	Discussion on materials with different levels of anisotropy .....	127
6.3	Modeling anisotropy using granular micromechanics with kinematic constraint.....	129
6.3.1	Derivation of stiffness tensor .....	130
6.3.2	Density distribution function .....	132
6.4	Modeling anisotropy using granular micromechanics with static constraint.....	140
6.4.1	Derivation of compliance and stiffness tensors .....	140
6.4.2	Density distribution function .....	144
6.5	Elastic wave propagation and effects of model parameters .....	149
6.6	Summary and conclusions.....	156
7	Micromorphic granular micromechanics .....	158
7.1	Kinematics of Granular Media.....	159
7.2	Macro-scale and Micro-scale Dynamics .....	164
7.3	Micro-scale and Macro-scale Constitutive Equations.....	166
7.4	Summary .....	176
8	IDENTIFICATION OF HIGHER ORDER MICRO- AND MACRO-SCALE STIFFNESS COMPONENTS USING GRANULAR MICROMECHANICS.....	178
8.1	Introduction .....	178
8.2	Micromorphic Granular Micromechanics, without grain spins .....	179
8.2.1	Kinematics of Granular Media.....	179
8.2.2	Macro-scale Stress and Micro-scale Force Conjugates .....	182

8.2.3	Micro-scale and Macro-scale Constitutive Equations .....	183
8.2.4	Constitutive coefficients for 2D Granular System.....	185
8.3	Variational principle and balance equations .....	189
8.4	Identification of macro and micro-scale constitutive coefficients .....	190
8.4.1	Numerical simulation methodology for discrete 2D granular system .....	191
8.4.2	Methodology for identification of constitutive coefficients .....	193
8.5	Results and Discussions .....	197
8.6	Summary and conclusion .....	202
9	BALANCE EQUATIONS AND WAVE PROPAGATION .....	205
9.1	Introduction .....	205
9.2	Variational principle and balance equations .....	206
9.3	Displacement equations of motion.....	211
9.4	Plane wave propagation within isotropic micromorphic media.....	213
9.4.1	Displacement waves in isotropic media.....	215
9.4.2	Spin waves in isotropic media .....	219
9.5	Plane wave propagation within transversely isotropic micromorphic media .....	222
9.5.1	Propagation of displacement waves in x direction .....	224
9.5.2	Propagation of displacement waves in y direction .....	226
9.6	Results and Discussions .....	231
9.6.1	Dispersion behavior of isotropic materials .....	231
9.6.2	Dispersion behavior of transversely isotropic materials.....	238
9.7	Summary and conclusions.....	244
10	CONCLUDING REMARKS AND FUTURE WORKS .....	246

10.1	Concluding remarks.....	246
10.2	Future works.....	248
	Appendix A.....	250
	LIST OF REFERENCES .....	252

## **LIST OF FIGURES**

Figure 1.1. Schematic representation of modeling length scales and the corresponding computational demand.....	2
Figure 2.1 Local inter-granular Cartesian coordinates shown at an intergranular contact location .....	10
Figure 2.2 (a) Schematic view of the biaxial shear experiment, (b) undeformed and deformed shape of the granular assembly under applied biaxial shear loading.....	20
Figure 2.3 Two grains in contact, showing local and global coordinate axes and geometry of the contact in 2D Granular Micromechanics .....	20
Figure 2.4 Schematic description of the granular micromechanics approach with both kinematic and static assumptions and comparing with traditional continuum mechanics approach .....	23
Figure 3.1 Normal force-displacement relationship in compression and tension (a) and the shear direction damage parameter as a function of normal displacement (b). The local Cartesian coordinate system is shown in the inset.....	40
Figure 3.2 Compressive stress-strain behavior (a), and tensile stress-strain behavior (b) under different confinement levels. The inset in part (a) represents experimental measurements from Bazant et al [54].....	45
Figure 3.3 Stress-strain behavior for confined compression (a) and tension (b) in terms of the deviatoric to mean stress ( $q/p$ ) ratio and applied axial strain.....	45
Figure 3.4 -Evolution of volumetric strain with loading for both confined compression (a) and tension (b) at different confinement levels. Initial compression followed by dilation can be seen for confined compression tests at low confinement.....	46
Figure 3.5 Stress paths plotted in the deviatoric stress–mean stress ( $q-p$ ) space for both confined compression (a) and tension (b). The failure envelope is shown by joining the end-points of the stress paths .....	47
Figure 3.6 Results from unconfined compressive cyclic loading: stress-strain curves for axial (a) and lateral (b) directions, and example inter-granular force-displacement curves for the normal (c) and tangential (d) directions.....	48
Figure 3.7 Results from unconfined tensile cyclic loading: stress-strain curves for (a) axial and (b) lateral directions, and example inter-granular force-displacement curves for the (c) normal and (d) tangential directions .....	49

Figure 3.8 Inter-granular forces and displacements in different  $\theta$ -directions for confined compressive loading: normal force (a), tangential force (b), normal displacement (c), and tangential displacement (d). Unloading and subsequent loading in the tensile regime can be clearly seen from (a) and (c). The grain-scale mechanism of volume-change behavior can be seen from (c) as the inter-granular displacements become increasingly tensile with loading..... 50

Figure 3.9 Inter-granular forces and displacements in different  $\theta$ -directions for confined tensile loading: normal force (a), tangential force (b), normal displacement (c), and tangential displacement (d). Unloading and subsequent loading in the tensile regime can be clearly seen from (a) and (c)..... 51

Figure 3.10 (a) Failure envelope in biaxial loading condition material loaded from initially unloaded state shown by the dashed line. Also loading-paths for two-stage loading used to illustrate the effect of induced anisotropy. (b) Failure envelopes for material that has been loaded in stage 1 along the solid line in part (a) up to one of the depicted points and then loaded in stage 2 in different directions till failure..... 53

Figure 3.11 Triaxial failure envelopes for material from the unloaded stage (a1-a4), material initially loaded in compression hydrostatically up to 20 MPa (b1-b4), material initially loaded in compression biaxially up to 20 MPa (c1-c4). Different views presented are the isometric 3D view (a1-c1), top view (a2-c2), front view (a3-c3), and side view (a4-d4). Solid lines inside the isometric 3D graphs represent the normal to  $\pi$ -plane ..... 55

Figure 3.12 Eigenvalues of the tangent stiffness tensor for the material under hydrostatic compression (a), biaxial compression (b), uniaxial compression (c), and biaxial compression-tension (d). Eigenvalues are normalized with three times the bulk modulus. Horizontal axis is normalized with the uniaxial compressive strength showing that the failure stress under hydrostatic compression is  $\sim 14.5$  times, biaxial compression  $\sim 2.5$  times, and biaxial compression-tension  $\sim 0.2$  times of uniaxial strength, respectively ..... 58

Figure 3.13 Stress-strain curves (a and c) and eigenvalues of the tangent stiffness tensor (b and d) for the uniaxial tensile loading and hydrostatic tensile loading cases, respectively..... 60

Figure 3.14 Inter-granular forces and displacements in different  $\theta$ -directions for a uniaxial tensile test: existence of tangential force (b) and displacement (c) and mixed-mode nature of deformation and failure can be discerned..... 61

Figure 3.15 Results from simulations of constant displacement ratio tests showing the calculated stress-paths for different strain ratios,  $\gamma = d\varepsilon_{11}/d\varepsilon_{22}$ , and  $\sigma_{33} = 0.1 \sigma_{11}$ . The bottom right inset presents the evolution of volumetric strain versus the axial strain. The top left inset presents experimental data from the literature..... 62



Figure 3.16 Stress paths plotted in the deviatoric stress–mean stress (q-p) space for volume control tests with different ratios, $\alpha$ , between lateral strain and axial strain. Simulations are done for different initial confining pressures of 10, 20, 30, and 40 MPa, respectively. The thick dashed line with filled squares represents the envelope derived from Figure 6 and shows the consistency of the results of two different simulations. Change of lateral stress vs axial strain is presented in the insets for two initial confining values .....	64
Figure 4.1 Failure criteria on normal-tangential stress plane .....	70
Figure 4.2 Schematic of the applied principal stress components for (a) Type 1 and (b) Type 2 loading paths. Schematic representations of: (c) the two types of loading paths in the octahedral plane, and (d) the evolution of Lode angle during the loading paths .....	73
Figure 4.3 Maximum principal stress, $\sigma_{11}$ , at failure versus intermediate principal stress, $\sigma_{22}$ , for different values of minimum principal stress, $\sigma_{33}$ , in loadings of (a) Type 1 and (b) Type 2 .....	75
Figure 4.4 Failure stress state in octahedral plane for different values of minimum principal stress, $\sigma_{33}$ , for the two loading types (a) Type 1 and (b) Type 2 .....	77
Figure 4.5 Evolution of normalized eigenvalues of the tangent stiffness tensor during the application of the 9 loading cases (a1-c3) in Type 1 loading until failure .....	78
Figure 4.6 Evolution of normalized eigenvalues of the stiffness tensor during the application of the 9 loading cases (a1-c3) in Type 2 loading until failure.....	79
Figure 4.7 Normal and tangential components of forces for different polar angles in loadings of Type 1 (first and third columns) and Type 2 (second and fourth columns) for cases where the minimum principal stresses are 0 (case a1, first row), 4 MPa (case b1, second row), and 20 MPa (case c1, third row) .....	81
Figure 4.8 Normal and tangential components of forces for different polar angles in loadings of Type 1 and Type 2 in azimuth angles of 0, 45, and 90 degrees (first, second and third rows respectively) for $\sigma_3=0.0$ MPa and $\sigma_2=30$ MPa.....	84
Figure 4.9 Normal and tangential components of forces for different polar angles in loadings of Type 1 and Type 2 in azimuth angles of 0, 45, and 90 degrees (first, second and third rows respectively) for $\sigma_3=0.0$ MPa and $\sigma_2=60$ MPa.....	85
Figure 4.10 Normal and tangential components of forces for different polar angles in loadings of Type 1 and Type 2 in azimuth angles of 0, 45, and 90 degrees (first, second and third rows respectively) for $\sigma_3=4.0$ MPa and $\sigma_2=44$ MPa.....	86

Figure 4.11 Normal and tangential components of forces for different polar angles in loadings of Type 1 and Type 2 in azimuth angles of 0, 45, and 90 degrees (first, second and third rows respectively) for $\sigma_3=4.0$ MPa and $\sigma_2=84$ MPa.....	88
Figure 4.12 Normal and tangential components of forces for different polar angles in loadings of Type 1 and Type 2 in azimuth angles of 0, 45, and 90 degrees (first, second and third rows respectively) for $\sigma_3=20$ MPa and $\sigma_2=85$ MPa.....	89
Figure 4.13 Normal and tangential components of forces for different polar angles in loadings of Type 1 and Type 2 in azimuth angles of 0, 45, and 90 degrees (first, second and third rows respectively) for $\sigma_3=20$ MPa and $\sigma_2=160$ MPa.....	90
Figure 4.14 Directions of principal Stress components and the fault angle .....	92
Figure 4.15 The variation of fault angle versus the intermediate principle stress for different values of confining stress in loadings of Type 1. (b) The determinant of the acoustic tensor versus directions for Type 1 loading with different values of $\sigma_{22} = \sigma_{33} = \sigma_{conf}$ .....	93
Figure 4.16 Variation of eigenvalues of the acoustic tensors for Type 1 loading where $\sigma_{22} = \sigma_{33} = \sigma_{conf} = 0, 4, 18,$ and $20$ MPa in (a), (b), (c), and (d) respectively .....	95
Figure 4.17 Fault angle versus intermediate principal stress for different values of minimum principal stress for loadings of Type 1 (a) and Type 2 (b), derived using Matsouka-Nakai criterion .....	97
Figure 5.1- Evolution of the deviatoric stress, $q=\sigma_{11}-\sigma_{22}$ , during triaxial loading (application of $\epsilon_{11}$ ) for initial confining pressures of 0.0, 5.0, and 20.0 MPa for all grain sizes .....	107
Figure 5.2 Evolution of the deviatoric stress, $q=\sigma_{11}-\sigma_{22}$ , during triaxial loading (application of $\epsilon_{11}$ ) for initial confining pressures of 50, 100, 200, and 400 MPa for all grain sizes .....	108
Figure 5.3 Change of failure stress for lowly confined cases, $\sigma_{conf} \leq 20$ MPa, and yield stress for highly confined cases, $\sigma_{conf} > 20$ MPa by change of grain size .....	110
Figure 5.4 Evolution of volumetric strain during loading for all sizes and different initial confinement values .....	111
Figure 5.5 Eigenvalues of the acoustic tensor at failure state for different directions in triaxial experiments with 0.0, 5.0, and 20 MPa initial confinement, on specimens with grains with size of 0.02, 0.002, 0.0002, and 0.00002. The orientation of the failure plane (fault angle) is also shown for each case.....	113
Figure 5.6 The effect of grain size on the direction of failure plane (Fault angle vs. $1/\sqrt{d}$ ).....	114

Figure 5.7 Evolution of deviatoric stress against the volumetric stress for constant volume tests after initial confinements of 0.0, 5.0, and 20 MPa, on grain sizes of 0.02, 0.01, 0.002, and 0.001 ..... 116

Figure 5.8 Evolution of  $\sigma_{11}$  and  $\sigma_{22}$  against  $\epsilon_{11}$  for constant volume tests after initial confinements of 0.0, 5.0, and 20 MPa, on grain sizes of 0.02, 0.01, 0.002, and 0.001 ..... 117

Figure 5.9 Evolution of the normal and tangential components of intergranular force vectors in different directions for simulations made on material with grain sizes of 0.01 and with confinements of 0.0 and 20 MPa ..... 118

Figure 5.10 Evolution of the eigenvalues of the stiffness tensor against  $\epsilon_{11}$  for constant volume tests after initial confinements of 0.0, 5.0, and 20 MPa, on grain sizes of 0.02, 0.01, 0.002, and 0.001..... 121

Figure 6.1 Density distribution function for materials with different levels of elastic symmetry and the parameters that need to be included in the harmonics expansion in order to show the required anisotropies ..... 139

Figure 6.2 Variation of the two Poisson ratios of transversely isotropic materials with changing (sections a1 and b1)  $\beta_s$  while  $\beta_t=a_{20}=a_{40}=0.5$ ; (sections a2 and b2)  $\beta_t$  while  $\beta_s=a_{20}=a_{40}=0.5$ ; (sections a3 and b3)  $a_{20}$  while  $\beta_s= \beta_t =a_{40}=0.5$ ; (sections a4 and b4)  $a_{40}$  while  $\beta_s= \beta_t=a_{40}=0.5$ ..... 147

Figure 6.3 Sections of the quasi-longitudinal, pure shear and quasi-shear components of wave velocity surface with 12 plane (graphs a-c respectively) and with 23 plane (graphs d-f respectively) while changing ratio of  $\beta_s =0.1\sim 0.9$  with  $a_{20}=a_{40}=2.0$ ,  $\beta_t =0.5$ . Arrows represent the direction of variation of the surface while increasing  $\beta_s$ . For visualization purposes the values of wave velocities are reduced by 0.025. Calculations are done with kinematic approach (a-f) and static approach ( $a'-f'$ ). ..... 152

Figure 6.4 Sections of the quasi-longitudinal, pure shear and quasi-shear components of wave velocity surface with 12 plane (graphs a-c respectively) and with 23 plane (graphs d-f respectively) while changing ratio of  $\beta_t =0.1\sim 0.9$  with  $a_{20}=a_{40}=2.0$ ,  $\beta_s =0.5$ . Arrows represent the direction of variation of the surface while increasing  $\beta_t$ . For visualization purposes the values of wave velocities are reduced by 0.025. Calculations are done with kinematic approach (a-f) and static approach ( $a'-f'$ )..... 153

Figure 6.5 Sections of the quasi-longitudinal, pure shear and quasi-shear components of wave velocity surface with 12 plane (graphs a-c respectively) and with 23 plane (graphs d-f respectively) while changing ratio of  $a_{20}=-0.5\sim 2.0$  with  $a_{40}=2.0$ ,  $\beta_s = \beta_t =0.5$ . Arrows represent the direction of variation of the surface while increasing  $a_{20}$ . For visualization purposes the values of wave

velocities are reduced by 0.025. Calculations are done with kinematic approach (a-f) and static approach (a'-f')	154
Figure 6.6 Sections of the quasi-longitudinal, pure shear and quasi-shear components of wave velocity surface with 12 plane (graphs a-c respectively) and with 23 plane (graphs d-f respectively) while changing ratio of $a_{40}=-0.5\sim 2.0$ with $a_{20}=2.0$ , $\beta_s = \beta_t =0.5$ . Arrows represent the direction of variation of the surface while increasing $a_{40}$ . For visualization purposes the values of wave velocities are reduced by 0.025. Calculations are done with kinematic approach (a-f) and static approach (a'-f')	155
Figure 7.1 Schematic representation of the two coordinate systems, $x$ and $x'$ and the neighbor grains in the material point	160
Figure 8.1- Representation of material point and the global coordinate system, $x$ , and the local coordinate system, $x'$ , located at the material point's center of mass	180
Figure 8.2 The granular assembly used in this study	191
Figure 8.3 Schematics of the boundary grains' displacement applying average strain, fluctuation strain, and second gradient strain (a.1, a.2, and a.3 respectively), grains displacement in the three loading schemes (b.1, b.2, and b.3), histogram of normal component of inter-granular displacement (c.1, c.2, and c.3), histogram of tangential component of inter-granular displacement (d.1, d.2, and d.3), and histogram of grain interactions' energies (e.1, e.2, and e.3)	195
Figure 9.1 Dispersion graphs for different components of displacement waves	233
Figure 9.2 Dispersion graphs for different components of spin waves	234
Figure 9.3 Phase velocity of different components of displacement waves vs their frequency	235
Figure 9.4 Group velocity of different components of displacement waves vs their frequency	236
Figure 9.5 Phase velocity of different components of spin waves vs their frequency	237
Figure 9.6 Group velocity of different components of spin waves vs their frequency	238
Figure 9.7 Dispersion, phase velocity vs. frequency, and group velocity vs. frequency for displacement waves propagating in $x$ direction in transversely isotropic materials	239
Figure 9.8 Dispersion, phase velocity vs. frequency, and group velocity vs. frequency for displacement waves propagating in $y$ direction in transversely isotropic materials	241

Figure 9.9 Evolution of ratios of phase velocities of different components of longitudinal and transverse components of displacement waves propagating in x and y directions by changing  $a_{20}$  ..... 242

## **LIST OF TABLES**

Table 3.1 Model parameters used in this study.....	44
Table 5.1 Size effect parameters used in this study .....	105
Table 6.1 Closed form equations of all components of stiffness matrix of a completely anisotropic material, derived based on the present method.....	134
Table 6.2 Directional density distribution function, used for materials with different levels of anisotropy.....	137
Table 6.3 List of parameters defined for showing components of stiffness matrix of anisotropic materials.....	146
Table 8.1 Components of two fourth rank stiffness tensors ( $C^M$ and $C^m$ ) for the two sets of grain properties, derived for the unit cell, the RVE, and using the present model .....	199
Table 8.2 Components of the sixth rank stiffness tensor for the two sets of grain properties, derived for the unit cell, the RVE, and using the present model .....	200
Table 8.3 Table of micro-scale constitutive coefficients derived for the assembly (units: K in kN/mm and G in N.mm).....	201
Table 9.1 Shape factors for spherical and cubic unit cells.....	212
Table 9.2 Micro-scale parameters (left) and the corresponding macro-scale constitutive parameters (right) .....	232

# 1 INTRODUCTION

## 1.1 Motivation

Macroscopic mechanical behavior of materials is highly dependent on their microstructure. The significance of micro-scale mechanisms influencing macro-scale behavior has been recognized in the context of continuum mechanics in the pioneering works of Cosserat [1], Mindlin [2], Toupin [3], Eringen [4], Green and Rivlin [5] and Germain [6]. Indeed, the early developments of continuum mechanics are known to proceed from some micromechanical conception of deformable materials (see Navier [7], Cauchy [8], and Piola [9, 10]). In particular, in materials with granular structure, the microstructure plays a clear role in defining the macroscopic properties of the material.

In some granular materials, grains can be identified due to their distinct grain boundaries, such as in the cases of grain packings and clean sands. However, for a preponderance of granular materials, grain structure identification is not straightforward although they exhibit a strongly granular texture. Hydraulic cements, clays, concrete, rocks and certain polymers are examples of such materials. In any case, the microstructure and the corresponding micromechanical properties have significant effect on the macroscopic behavior of the material. Thus material modeling without microstructural consideration, as it is done in traditional continuum mechanics, invariably leads to neglect of certain characteristic features. In order to incorporate the microstructure of

different granular materials into models of their macroscopic behavior many approaches applicable at different scales can be used as depicted in Figure 1.1.

At the smallest scale, one can conceive of atomistic models which investigate the material behavior by modeling atomic interactions. The building block scales for atomistic models are of the order  $1 \text{ \AA} = 10^{-10} \text{ m}$ . Using this approach, the material can be modeled in the finest scale possible and can lead to highly accurate results [11-13]. It should be noted, however, that atomistic models and multi-scale models are prohibitively expensive for computations at large scales.

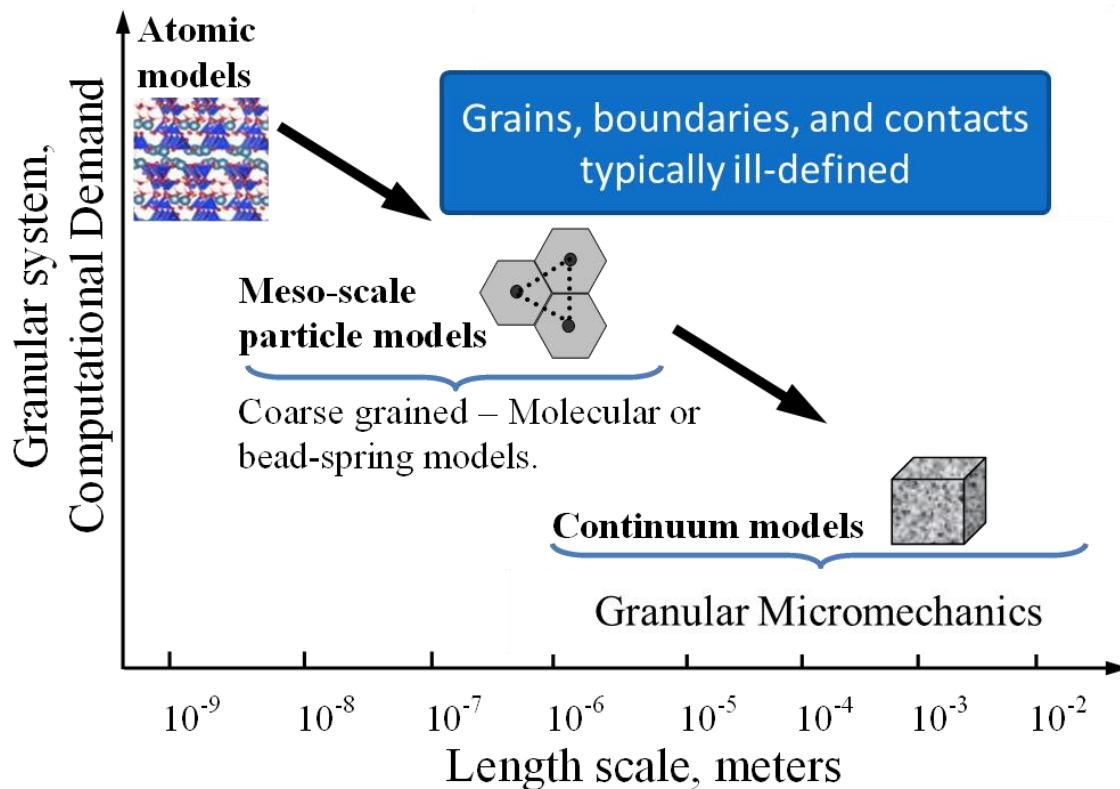


Figure 1.1. Schematic representation of modeling length scales and the corresponding computational demand

At the scales ranging from atomistic ( $\sim 10^{-9} \text{ m}$ ) to continuum ( $> 10^{-3} \text{ m}$ ), a number of coarse grained methods of incorporating micro-scale effects can be conceived, such as molecular models, bead-spring models or discrete element models [14-17]. These models also pose significant challenges,



including, among others, the specification of local interaction laws between coarse grained particles, the generation of highly idealized microstructure, defining particles, their shapes and sizes, their contacts and interaction relationships, the evolution of their contacts during loading, surface properties and their change during loading, and the sheer computational expense associated with performing parametric studies. Finally in a larger scale, the method of granular micromechanics incorporates data from the material microstructure into the continuum model [18-22]. In this approach, it is neither needed, nor intended to study the exact behavior of all grains within the material point. The macroscopic behavior of the material is derived by averaging the behavior of grain-pair interactions in different direction.

The granular micromechanics method offers an attractive paradigm for developing continuum models of granular material systems by incorporating micro-scale effects [21, 22]. In the method of granular micromechanics the material is envisioned as a collection of meso-scale grains mutually interacting with each other. The interactions of all grains contribute in defining the macroscopic behavior of material. This approach traces its genesis to the continuum models of grain assemblies developed in the second-half of the last century (see for example [18, 23-27]). This approach has been applied to model a range of issues germane to granular material behavior, including among others elasto-plasticity [28], rate-dependent damage and plasticity [22], instability analysis [29, 30] and second gradient and micro-polar effects [31-33], to give a small subset of contributions along these lines.

## **1.2 Objectives and scope**

Although there have been lots of improvements on this modeling methodology, there are multiple challenges in the method of granular micromechanics to be faced and the method can be developed

for more and more sophisticated material systems and complex loading scenarios. The wide range of potentials of the method for predicting different phenomena happening in different complex materials and the possibility of further developments on the model and its applications on different material systems serve as the main motivation for this PhD work.

The accomplishments in this PhD work can be decomposed into the following two distinct parts:

1. Theoretical developments on the model methodology in order to enable it to model more complicated material systems as well as more complex loading scenarios
2. Application of the method for modeling infrastructure materials (e.g. cementitious materials and certain rocks) and prediction of their behavior under different loading conditions

A more detailed description of the content of the dissertation is given in the following section.

### **1.3 Dissertation outline**

In Chapter 1 an introduction on different approaches for material modeling and a motivation for using the method of Granular Micromechanics is presented. Then an outline of the current work is presented.

Chapter 2 is devoted to the introduction of the method of granular micromechanics. Two general types of the method (method with *kinematic* constraint and method with *static* constraint) are then presented. In both methods, macroscopic constitutive equations relating macro-scale stress and strain tensors are derived based on microscopic intergranular force-displacement relationships.

Global stiffness and compliance tensors are then derived using the methods with kinematic and static constraint respectively. All these derivations are done within the linear-elastic region in which the intergranular force-displacement relationships are assumed to be linear resulting in a linear constitutive relationship in the macro-scale.

Chapter 3 focuses on the derivation of the nonlinear damage-plasticity model and its application for modeling cementitious materials. First the method of granular micromechanics with damage and plasticity is derived from a completely thermo-mechanical viewpoint. The internal energy density and dissipation potential functions are defined as functions of their corresponding kinematic measures and damage and plasticity parameters in both macro and micro scales. Setting the macroscopic internal energy density and dissipation potential functions equal to the volume average of their corresponding microscopic functions and substituting the results in the macro-scale Clausius-Duhem inequality, a Clausius-Duhem type inequality is derived for grain-pair interactions. The resulting force-displacement relationships show the effects of damage and plasticity in macro-scale. Force-displacement relationships for loading, unloading, and reloading steps are then presented after the criteria for defining whether the contact is undergoing loading, unloading, or reloading. In order to derive the behavior of cementitious materials, the free energy and dissipation potential functions in micro-scale are defined in a way that the resultant macroscopic behavior replicates the experimentally observed behavior of these materials. The derived model is then calibrated with conventional triaxial test results and then verified by simulating multiple loading scenarios.

In Chapter 4, a study of failure of materials, in particular cementitious and rock-like materials, has been studied. First, the concept of material failure has been investigated and then, the presented

material model is used for checking different failure criteria and also predicting failure behavior under different loading paths.

In Chapter 5, a framework for incorporating the effects of grain-size into the macroscopic behavior of the material is formulated. Using this approach, multiple experiments on materials with different grain sizes have been simulated and it is seen that by incorporating the size-effect from micro-scale into the material behavior, the macroscopic effect can be predicted.

In Chapter 6, the method of granular micromechanics with both static and kinematic constraints has been developed for modeling materials with all different levels of inherent anisotropy. Properties of grain-pair interactions in different directions have been formulated in a systematic manner that is consistent with the elastic symmetries resulting in different levels of isotropy in the material. Macroscopic stiffness tensor for anisotropic materials as a function of microstructural and micromechanical properties are then derived. It is shown that the derived macroscopic stiffness tensors comply completely with the symmetry requirements of materials with all different levels of anisotropy.

In Chapter 7, a complete micromorphic theory which takes into account, among other measures, the spins of grains is presented. The kinematic analysis is enhanced by incorporating terms that represent 1) average displacement and spins of grain, 2) fluctuations in the gradient of grain displacements and spins, and 3) second gradient of the fluctuations in grain displacements and spins. Corresponding to each one of these kinematic measures a work-conjugate stress measure is introduced in the model. Stiffness tensors correlating the macroscopic stress and strain tensors are then formulated based on intergranular stiffness coefficients and geometry of the grain assembly (or the granular material).

Chapter 8 is focused on the identification of a material or grain assembly as a micromorphic media. A practical approach has been formulated for calibrating the inter-granular stiffness coefficients corresponding to all different kinematic measures of the micromorphic material and using those grain-scale stiffness coefficients, the macroscopic stiffness tensors for the given granular assembly is derived.

In Chapter 9, the micromorphic model derived in Chapter 7 has been used for studying wave propagation through materials. First, applying the balance of internal potential energy, external work, and the kinetic energy in the micromorphic material, equilibrium equations and boundary conditions pertinent to the micromorphic materials with grain spins have been formulated. Implementing the constitutive theory of micromorphic media, formulated in Chapter 7, into the balance equations, equations of motion are derived. These equations of motion are then used to solve the problem of elastic wave propagation through isotropic and transversely isotropic materials. For modeling the properties of transversely isotropic materials, the method presented in Chapter 6 has been used.

Finally in Section 10, a summary of the findings of the present work, conclusions, and a discussion on possible future works are presented.

## 2 GRANULAR MICROMECHANICS MODEL

It is known that material microstructure and its corresponding micromechanical features play a significant role in defining its macroscopic behavior [34, 35]. In the method of granular micromechanics, the material microstructure is taken into account in direct manner when modeling the macroscopic response of the material to loading. In this method, the material point is modeled as a collection of grains, each one interacting with its neighbor grains through different inter-granular mechanisms.

Equating the internal energy created by all the grain-pair interactions with the macro-scale energy created by the macroscopic stress and strain tensors result in a microscopically sound model of the macro-scale behavior of the material. Thus in this model response of all grain-pair interactions to loading contribute in deriving the overall macroscopic response of the material. By implementing the behavior of grain-pair interactions in all generic orientations, the method automatically incorporates the effect of material's microstructure, micromechanical properties, and the micro-scale phenomena that take place at the interacting grains. The approach is consistent with the idea of coarse graining for modeling polymeric or complex multi-atomic systems [12, 36, 37] and follows a similar paradigm as that of peridynamics [38] and quasi-continuum mechanics [39]. The method also bears similarity to the microplane model [40] and the virtual internal bond (VIB) model [41] where the material behavior is derived considering the behavior of planes or bonds of every generic orientation.

The method generally can be categorized in two distinct categories which are called a) Granular micromechanics method with *kinematic* constraint and b) Granular micromechanics method with *static* constraint. In this chapter, the two types of the first gradient method will be developed and for both of them, global constitutive equations are derived. Macroscopic stiffness tensors from the two methods are presented based on inter-granular stiffness coefficients and micro-structural parameters of the model.

## 2.1 Granular Micromechanics model with kinematic constraint

As it is already mentioned, in the method of granular micromechanics, the material point is envisioned as a collection of grains, each one interacting with its neighbors through different grain scale mechanisms [42]. The first step in the micro-macro identification in this method is to identify the kinematics of grains inside the material point. Let us consider two neighbor grains inside the material point, say grains n and p, with position vectors  $x_i^p$  and  $x_i^n$ , respectively. The displacement of grain p can be written using Taylor series expansion of the displacement of grain n, thus resulting in the relative displacement of the two grains to be formulated as

$$u_i^p = u_i^n + u_{i,j}^{n\alpha} (x_j^p - x_j^n) \Rightarrow \delta_i^\alpha = u_i^p - u_i^n = u_{i,j}^{n\alpha} (x_j^p - x_j^n) = \varepsilon_{ij}^{n\alpha} (x_j^p - x_j^n) = \varepsilon_{ij}^{n\alpha} l_j \quad (2.1)$$

where  $u_i$  represents the grain displacement field and the vector  $l_j$  represents the vector joining the centroids of the two neighbor grains. Superscripts n and p corresponds to grains n and p, and the superscripts  $\alpha$  corresponds to the  $\alpha^{\text{th}}$  contact of the grain. Subscripts follow the conventions of index notation and summation over repeated indices is implied here and throughout this work

unless explicitly noted otherwise. It should also be noted that in this derivation terms of order 2 and higher and also grains rotation have been neglected in order to derive the first gradient model. From Eq. 2.1 it can be seen that the inter-granular displacement vector is derived as the projection of the strain tensor in the direction of the grain-pair interaction line and then scaled with the length of the interaction line. This assumption is generally known as the *kinematic* constraint.

In order to facilitate defining intergranular force-displacement relationships, a local coordinate system has been defined for each inter-granular contact. This coordinate system is composed of three mutually orthogonal axes, namely axes  $n_i$ ,  $s_i$ , and  $t_i$ . In this local coordinate system,  $\mathbf{n}$  is the unit vector in the direction of the line connecting the centers of the two particles and  $\mathbf{s}$  and  $\mathbf{t}$  are two orthogonal unit vectors in the plane whose normal vector is  $\mathbf{n}$ . Generally, the two vectors  $\mathbf{s}$  and  $\mathbf{t}$  can be chosen arbitrarily in the tangential plane (the plane with normal vector of  $\mathbf{n}$ ) but for future derivations and without loss of generality, the following three unit vectors are used in the derivations.

$$\begin{aligned} n_i &= \langle \cos \theta, \sin \theta \cos \phi, \sin \theta \sin \phi \rangle \\ s_i &= \langle -\sin \theta, \cos \theta \cos \phi, \cos \theta \sin \phi \rangle \\ t_i &= \langle 0, -\sin \phi, \cos \phi \rangle \end{aligned} \tag{2.2}$$

where  $\theta$  and  $\phi$  are the polar and azimuth angle in the spherical coordinate system as depicted in Figure 2.1.

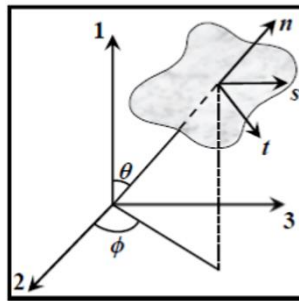


Figure 2.1 Local inter-granular Cartesian coordinates shown at an intergranular contact location



The relative displacement vector is then decomposed into three components along these three coordinate axes. The component in the direction of the vector joining particle centroids, denoted by  $\delta_n$ , represents the relative normal displacement between the two grains while two others,  $\delta_s$  and  $\delta_t$ , represent the two components of tangential displacement between them. These components can be found simply by dot product of the displacement vector and the unit vectors in the three directions as  $\delta_n = \delta_i n_i$ ,  $\delta_s = \delta_i s_i$ , and  $\delta_t = \delta_i t_i$ .

For elastic granular systems, the Helmholtz free energy may be defined in terms of the micro-scale kinematic quantities belonging to grain-pair interactions. Thus, the internal energy density,  $W$ , can be written as the volume average of the energies of all grain-pair interactions as

$$W = \frac{1}{V} \sum_{\alpha}^N W^{\alpha}(\delta_j^{\alpha}) \quad (2.3)$$

where  $W^{\alpha}(\delta_j^{\alpha})$  is the energy belonging to the  $\alpha^{\text{th}}$  grain-pair interaction written in terms of that particular grain-pair's relative displacement and  $N$  is the total number of grain-pair interactions. Each grain-pair interaction is counted just once. Now since the Cauchy stress is defined as the work conjugate of the symmetric part of displacement gradient tensor (i.e. strain tensor), applying chain rule of differentiation and Eq. 2.3, macroscopic Cauchy stress of the Volume Element (VE) is derived as

$$\sigma_{ij} = \frac{\partial W}{\partial \varepsilon_{ij}} = \frac{1}{V} \sum_{\alpha=1}^N \frac{\partial W^{\alpha}}{\partial \delta_k^{\alpha}} \frac{\partial \delta_k^{\alpha}}{\partial \varepsilon_{ij}} \quad (2.4)$$

In micro-scale, the work conjugate of inter-granular displacement vector, represented by intergranular force vector and denoted by  $f_i$ , can be defined as

$$f_k^{\alpha} = \frac{\partial W^{\alpha}}{\partial \delta_k^{\alpha}} \quad (2.5)$$

By substituting Eq. 2.5 into Eq. 2.4 and using Eq. 2.1 the Cauchy stress of the granular system can now be obtained as a function of grain interactions as follows

$$\sigma_{ij} = \frac{1}{V} \sum_{\alpha=1}^N f_k^\alpha l_l^\alpha \frac{\partial \varepsilon_{kl}^{n\alpha}}{\partial \varepsilon_{ij}} \quad (2.6)$$

Note that  $l_i$  can be replaced by  $ln_i$  where the scalar value  $l$  denotes the length of the vector joining the two centroids.

For further simplification a relationship between grain-scale strain and the overall Representative Volume Element (RVE) strain is necessary. However it should be noted that for being able to derive such a relationship, exact knowledge of the material's microstructural properties such as grain shapes and sizes, their boundaries, surface properties, inter-granular bond mechanisms, and also problem's initial and boundary conditions, etc. are needed. Such detailed information is generally unattainable for most, if not all, materials [43].

However, this unfortunate missing information is compensated by the fortunate fact that generally in solving the problem we are not interested in the precise and detailed solution and the exact motion of each and every grain in the RVE. The difference between the approximate average solution and the exact solution belonging to each particle can be explained in statistical mechanics sense in terms of grain displacement *fluctuations*. So the huge amounts of complexities in the problem dictate the use of statistical approximations which are not affected by the aforementioned missing information while in fact those average solutions are what we are looking for. Furthermore, it can be proved that the amount of fluctuations of the response has an inverse relationship with the size of the RVE. So using RVE with sufficiently large number of grains will imply less and less relative fluctuations from the average values that are determined from the statistical approximations of the average values [44].

In the light of this argument, the mean field assumption, albeit approximate, provides a feasible approach for the derivation of the RVE constitutive law and has been shown to describe a number of phenomena exhibited by granular materials [18, 20, 42]. Thus the grain scale strain is set equal to the overall RVE strain tensor. Eq. 2.6 is therefore simplified as

$$\sigma_{ij} = \frac{1}{V} \sum_{\alpha=1}^N f_k^\alpha l_l^\alpha \frac{\partial \varepsilon_{kl}^{n\alpha}}{\partial \varepsilon_{ij}} = \frac{1}{V} \sum_{\alpha=1}^N f_k^\alpha l_l^\alpha \delta_{ik} \delta_{jl} = \frac{1}{V} \sum_{\alpha=1}^N f_i^\alpha l_j^\alpha \quad (2.7)$$

Inter-granular force vector is now decomposed into one normal component,  $f_n$ , in the direction of the contact line and two tangential components,  $f_s$  and  $f_t$ , in the plane whose normal vector is the contact line. This will be useful for writing the inter-particle constitutive equations in a more convenient and physically meaningful manner. Inter-granular governing equations can now be written as

$$\begin{Bmatrix} f_n \\ f_s \\ f_t \end{Bmatrix} = \begin{pmatrix} k_n & 0 & 0 \\ 0 & k_s & 0 \\ 0 & 0 & k_t \end{pmatrix} \begin{Bmatrix} \delta_n \\ \delta_s \\ \delta_t \end{Bmatrix} \quad (2.8)$$

It is seen, in Eq. 2.8 that the microscopic stiffness components in directions  $n$ ,  $s$ , and  $t$  are taken as  $k_n$ ,  $k_s$ , and  $k_t$  respectively. However, for modeling isotropic materials, the stiffness coefficients in the two tangential directions,  $k_s$  and  $k_t$ , should be equal. For further derivation, it is useful to write the intergranular force-displacement relationships in the RVE coordinate system. This may be done using the rotation tensor that should be defined as follows for each inter-granular contact

$$T = \begin{pmatrix} n_1 & s_1 & t_1 \\ n_2 & s_2 & t_2 \\ n_3 & s_3 & t_3 \end{pmatrix} \quad (2.9)$$

Thus, the inter-granular force-displacement relationship can be written as

$$f_i = K_{ij} \delta_j; \quad K_{ij} = T_{ip} k_{pq} T_{jq} \quad (2.10)$$

Where  $\mathbf{k}$  is the stiffness tensor in grain's local coordinates (See Eq. 2.8) and  $\mathbf{K}$  is the stiffness tensor in RVE coordinates. At this point the kinematic assumption that defines microscopic displacements as a function of RVE strain tensor is utilized.

$$\delta_i^\alpha = \varepsilon_{ij} l_j^\alpha = l^\alpha \varepsilon_{ij} n_j^\alpha \quad (2.11)$$

Now substituting Eq. 2.11 into Eq. 2.10 and the result into Eq. 2.7 will lead to

$$\sigma_{ij} = \frac{1}{V} \sum_{\alpha=1}^N f_i^\alpha l_j^\alpha = \frac{1}{V} \sum_{\alpha=1}^N K_{ik} \delta_k^\alpha l_j^\alpha = \frac{1}{V} \sum_{\alpha=1}^N K_{ik} l_l^\alpha l_j^\alpha \varepsilon_{kl} \quad (2.12)$$

Since the strain tensor,  $\varepsilon_{kl}$ , is constant for the RVE it can be taken out of the summation resulting in

$$\sigma_{ij} = \left( \frac{1}{V} \sum_{\alpha} \left( (l^\alpha)^2 n_l^\alpha n_j^\alpha K_{ik}^\alpha \right) \right) \varepsilon_{kl} \quad (2.13a)$$

$$C_{ijkl} = \frac{1}{V} \sum_{\alpha} \left( (l^\alpha)^2 n_l^\alpha n_j^\alpha K_{ik}^\alpha \right) \quad (2.13b)$$

The relationship provided in Eq. 2.13b can be used to calculate the material point's stiffness tensor for a discrete system where the location of all grains and their inter-granular contacts and stiffness coefficients are known. However, since we are interested in an approximate solution, it is intended here to change this summation to integration over the whole domain. For this purpose,  $N_p$  is defined as the number density of grain-pair interactions within the assembly and  $\xi$  as an inter-granular contact directional density distribution function [18]. Using these parameters and assuming that the assembly is sufficiently large and contains sufficiently large number of grains and inter-granular contacts in different direction, the summation in Eq. 2.13b can be changed into integration as

$$C_{ijkl} = l^2 N_p \int_{\theta=0}^{\pi} \int_{\phi=0}^{2\pi} \left( K_{ik} n_j n_l \right) \xi \sin \theta d\phi d\theta \quad (2.14)$$

Similarly Eq. 2.7 can be rewritten in integral form as

$$\sigma_{ij} = lN_p \int_0^{2\pi} \int_0^{\pi} f_i(\theta, \phi) n_j(\theta, \phi) \xi(\theta, \phi) \sin \theta d\theta d\phi \quad (2.15)$$

The directional density distribution function serves as a statistical tool that defines the probability distribution of the properties of contacts (namely bond length and stiffness) in different directions. It should be noted that this density distribution function should be normalized in a way that its integral around the surface of a sphere is guaranteed to be equal to unity.

It is clear that the introduction of the density distribution function facilitates modeling inherently anisotropic materials (See Chapter 6 of the present work). However, for modeling isotropic materials, it is evident that there should be no directional preference for the grain-pair interactions and their properties. So the number density of grain-pair interactions and their stiffness and lengths in different directions should be independent of the direction. Having this in mind, in addition to the requirement of having a normalized distribution, for modeling inherently isotropic materials in 3D domain, the directional density distribution function should be  $\xi = 1/4\pi$ . In this case, the integrals presented in Eq. 2.14 can be calculated analytically. After calculating all components of the stiffness tensor,  $C_{ijkl}$ , material's young modulus (E) and Poison's ration ( $\nu$ ) are derived as

$$E = l^2 N_p k_n \frac{2k_n + 3k_s}{4k_n + k_s} \quad (2.16)$$

$$\nu = \frac{k_n - k_s}{4k_n + k_s}$$

Note that in Eq. 2.16, the subscripts n and s represent normal and tangential components of stiffness which are scalar parameters. Throughout this work, subscripts n, s, and t have been used for referring to the components of force, displacement, and stiffness in the three directions, n, s, and t. Index notation conventions do *not* apply to them.

The above results are consistent with the stiffness tensors for isotropic materials that need only two constants to show their linear elastic behavior. However, for modeling inherently anisotropic materials, different functions of the orientation within the space need to be defined and used as  $\xi(\theta, \phi)$ . A comprehensive discussion on modeling materials with all different levels of inherent anisotropy using this approach is presented in Chapter 6.

## 2.2 Granular Micromechanics model with static constraint

In order to formulate the method of granular micromechanics with static constraint, the Gibbs free energy may be defined in terms of the micro-scale force measures belonging to grain-pair interactions.

Thus, the Gibbs energy volume density,  $G$ , is written as

$$G = \frac{1}{V} \sum_{\alpha}^N G^{\alpha}(f_j^{\alpha}) \quad (2.17)$$

where  $G^{\alpha}(f_j^{\alpha})$  is the energy belonging to the  $\alpha^{\text{th}}$  grain-pair interaction written in terms of that particular grain-pair's force measures. The average displacement gradient tensor (strain tensor) is defined as the work conjugate of the Cauchy stress tensor and is derived, using chain rule, as

$$\varepsilon_{ij} = \frac{\partial G}{\partial \sigma_{ij}} = \frac{1}{V} \sum_{\alpha=1}^N \frac{\partial G^{\alpha}}{\partial f_k^{\alpha}} \frac{\partial f_k^{\alpha}}{\partial \sigma_{ij}} \quad (2.18)$$

In the statically constrained approach, grain displacements are defined as work conjugates of the inter-granular force vector and can thus be derived as

$$\delta_i^{\alpha} = \frac{\partial G^{\alpha}}{\partial f_i^{\alpha}} \quad (2.19)$$

Traditionally, statically constrained methods contend that the inter-granular force vector is equal to the projection of the stress tensor in the direction of grain-pair interaction line and then scaled by the distance between the two centroids. In the present method, however, using a least squares approximation, this static constraint has been enhanced and can be written as

$$f_i = l\sigma_{ij}N_{jk}^{-1}n_k \quad (2.20)$$

where the second rank fabric tensor  $N_{ij}$  is defined as [45, 46]

$$N_{ij} = \frac{1}{V} \sum_{\alpha=1}^N l_i^\alpha l_j^\alpha \quad (2.21)$$

For a more detailed description of the derivation of Eq. 2.20 based on least squares approximation see [29]. Now substituting Eq. 2.19 and 2.20 into Eq. 2.18, the strain tensor can be rewritten as

$$\varepsilon_{ij} = \frac{\partial G}{\partial \sigma_{ij}} = \frac{1}{V} \sum_{\alpha=1}^N \delta_i^\alpha l N_{jr}^{-1} n_r = \frac{l N_{jr}^{-1}}{V} \sum_{\alpha=1}^N \delta_i^\alpha n_r \quad (2.22)$$

Constitutive equation in the grain-scale needs to be introduced in the formulation at this point. That is a set of equations relating inter-granular force vectors to the inter-granular displacement measures. For this purpose, as it was done in the method with kinematic constraint, displacement vector is decomposed into components in the normal and tangential directions.

$$\delta_n^\alpha = \delta_i^\alpha n_i; \quad \delta_s^\alpha = \delta_i^\alpha s_i; \quad \delta_t^\alpha = \delta_i^\alpha t_i \quad (2.23)$$

Having defined the normal and tangential components of displacement vector, constitutive equation in the grain-scale can be written as

$$\{\delta\}_{3 \times 1} = [s]_{3 \times 3} \{f\}_{3 \times 1}; \quad \begin{Bmatrix} \delta_n \\ \delta_s \\ \delta_t \end{Bmatrix} = \begin{bmatrix} 1/k_n & 0 & 0 \\ 0 & 1/k_s & 0 \\ 0 & 0 & 1/k_t \end{bmatrix} \begin{Bmatrix} f_n \\ f_s \\ f_t \end{Bmatrix} \quad (2.24)$$

Note that the each compliance coefficient is defined simply as inverse of its corresponding stiffness coefficient. Now in order to write the constitutive equations in the RVE coordinate system, the rotation tensor defined in Eq. 2.9 should be used

$$\delta_i = S_{ij} f_j; \quad S_{ij} = T_{ip} s_{pq} T_{jq} \quad (2.25)$$

where  $S$  and  $s$  are the compliance tensors in RVE coordinate system and in the local grain-pair  $nst$  coordinate system. Now substituting Eq. 2.25 along with the static constraint given in Eq. 2.20 into the equation derived for macroscopic strain, Eq. 2.22, we get

$$\varepsilon_{ij} = \left( \frac{l^2 N_{jr}^{-1} N_{ls}^{-1}}{V} \sum_{\alpha=1}^N S_{ik}^{\alpha} n_r^{\alpha} n_s^{\alpha} \right) \sigma_{kl} \quad (2.26a)$$

$$S_{ijkl} = \frac{l^2 N_{jr}^{-1} N_{ls}^{-1}}{V} \sum_{\alpha=1}^N S_{ik}^{\alpha} n_r^{\alpha} n_s^{\alpha} \quad (2.26b)$$

Now using the same number density of grain-pair interactions and the directional density distribution function,  $N_p$  and  $\xi$ , as what was used in the method with kinematic constraint, the summation in Eq. 2.26b can be changed into integration as

$$S_{ijkl} = \frac{l^2 N_{jr}^{-1} N_{ls}^{-1}}{V} \int_{\theta=0}^{\pi} \int_{\phi=0}^{2\pi} (S_{ik}^{\alpha} n_r^{\alpha} n_s^{\alpha}) \xi \sin \theta d\phi d\theta \quad (2.27)$$

For the case of isotropic materials, the contacts density should be independent of the orientation and the density distribution function should be always equal to  $1/4\pi$  regardless of direction. In this case the integrals presented in Eq. 2.27 can be done analytically and closed-form solutions can be found. After computing all components of the compliance tensor,  $S_{ijkl}$ , materials constitutive parameters, Young's modulus and Poison's ration, can be derived. For an isotropic material (or granular assembly) where grain sizes are all equal, Poison's ratio and Young's modulus are derived as follows



$$E = \frac{5L^2 N_p}{3} \frac{K_n K_s}{2K_n + 3K_s} \quad (2.28)$$

$$\nu = \frac{K_n - K_s}{2K_n + 3K_s}$$

Since the grain-scale constitutive equations in both kinematic and static methods, Eq. 2.8 and 2.24 respectively, are defined linearly, the macroscopic stiffness and compliant tensors derived in Eq. 14 and Eq. 26 respectively will also be applicable for problems in linear elastic region. In order to model material's non-linear behavior in macro-scale, constitutive equations in micro-scale should be defined in non-linear fashion.

### 2.3 Two-dimensional model used for modeling 2D grain assemblies

The same approach that was discussed in the previous sections can be used for modeling two-dimensional problems. Two-dimensional modeling approach is justifiable when the problem size in one direction is significantly smaller than that in the other two directions. This is the case for the biaxial loading experiment presented in Figure 2.2. In this experiment grain assemblies formed of equal-sized circular rods (of 9.5 mm diameter and 25 mm height) were used. The undeformed dimensions of the typical rod assembly are 400mm x 250 mm. The loading and the data acquisition procedures have been described in detail in the paper by Misra and Jiang [47]. Briefly, the loading was applied in an incremental manner and sufficient time was allowed for equilibration for each load increment. Figure 2.2(b) shows a schematic of the undeformed and deformed rod assembly. At the end of each loading step, the assembly was imaged and analyzed to determine particle locations and orientations.

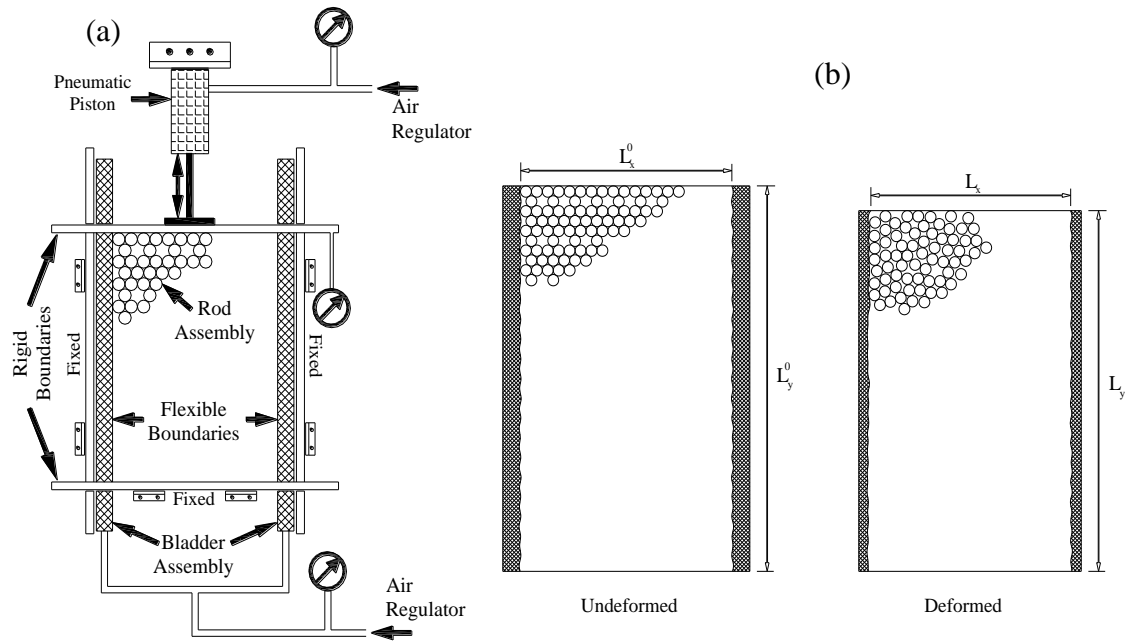


Figure 2.2 (a) Schematic view of the biaxial shear experiment, (b) undeformed and deformed shape of the granular assembly under applied biaxial shear loading

The method discussed in the previous sections should be reformulated in two-dimensional space in order to model this kind of experiments. In the two-dimensional framework, for each contact, the local coordinate axes are defined separately. The unit vector joining the two centroids of two particles is called  $\mathbf{n}$  and the tangential unit vector is called  $\mathbf{s}$  (see Figure 2.3).

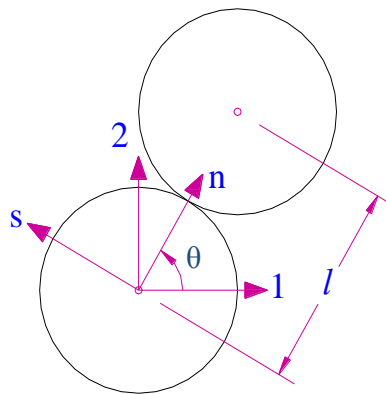


Figure 2.3 Two grains in contact, showing local and global coordinate axes and geometry of the contact in 2D Granular Micromechanics

The Cartesian components of the unit vectors in two-dimensional analysis can be written as

$$\begin{aligned} n_i &= \langle \cos \theta, \sin \theta \rangle \\ s_i &= \langle -\sin \theta, \cos \theta \rangle \end{aligned} \quad (2.29)$$

where  $\theta$  is the polar angle measured from the positive  $\mathbf{x}$  axis. Note that in the 2D formulation, the indices can take values of only 1 or 2 and the summation over repeated indices holds. Normal and tangential components of displacement vector are computed as  $\delta_n = \delta_i n_i$  and  $\delta_s = \delta_i s_i$ , and the microscopic (contact) force laws can be written in the following general form

$$\begin{aligned} f_n &= f_n(\delta_n, \delta_s) \\ f_s &= f_s(\delta_n, \delta_s) \end{aligned} \quad (2.30)$$

The tangential stiffness tensor for the RVE can now be derived as the derivative of the stress tensor with respect to the strain tensor and using Eq. 2.13a

$$\begin{aligned} C_{ijkl}^k &= \frac{\partial \sigma_{ij}}{\partial \varepsilon_{kl}} = \frac{1}{V} \sum_{\alpha} \frac{\partial (f_j l_i)}{\partial \varepsilon_{kl}} = \frac{1}{V} \sum_{\alpha} l_i \left( n_j \frac{\partial f_n}{\partial \varepsilon_{kl}} + s_j \frac{\partial f_s}{\partial \varepsilon_{kl}} \right) \\ &= \frac{1}{V} \sum_{\alpha} l_i \left\{ n_j \left( \frac{\partial f_n}{\partial \delta_n} \frac{\partial \delta_n}{\partial \varepsilon_{kl}} + \frac{\partial f_n}{\partial \delta_s} \frac{\partial \delta_s}{\partial \varepsilon_{kl}} \right) + s_j \left( \frac{\partial f_s}{\partial \delta_n} \frac{\partial \delta_n}{\partial \varepsilon_{kl}} + \frac{\partial f_s}{\partial \delta_s} \frac{\partial \delta_s}{\partial \varepsilon_{kl}} \right) \right\} \\ &= \frac{1}{V} \sum_{\alpha} l_i \left\{ n_j \left( k_{nn} \frac{\partial \delta_n}{\partial \varepsilon_{kl}} + k_{ns} \frac{\partial \delta_s}{\partial \varepsilon_{kl}} \right) + s_j \left( k_{sn} \frac{\partial \delta_n}{\partial \varepsilon_{kl}} + k_{ss} \frac{\partial \delta_s}{\partial \varepsilon_{kl}} \right) \right\} \end{aligned} \quad (2.31)$$

where superscript  $k$  stands for the kinematic method. Note that it is assumed that under small deformations, the terms associated with the change of volume,  $V$ , and vector,  $l_i$ , are negligible

$$\begin{aligned} \frac{\partial \delta_n}{\partial \varepsilon_{kl}} &= \frac{\partial}{\partial \varepsilon_{kl}} (\varepsilon_{ij} l_j n_i) = \delta_{ik} \delta_{jl} l_j n_i = n_k l_l \\ \frac{\partial \delta_s}{\partial \varepsilon_{kl}} &= \frac{\partial}{\partial \varepsilon_{kl}} (\varepsilon_{ij} l_j s_i) = \delta_{ik} \delta_{jl} l_j s_i = s_k l_l \end{aligned} \quad (2.32)$$

It should be noted that for contact of grains of different shapes and materials, many solutions have been presented which can be used as intergranular force-displacement relationships. For instance,

for contact of spherical particles, Hertz-Mindlin contact theory of elastic spheres can be used for interaction in normal direction [48]

$$f_n = -\lambda k |\delta_n|^{\eta+1} \quad (2.33)$$

while the shear (tangential) force-displacement relationship is obtained as follows [49].

$$f_s = \mu |f_n| \left( 1 - \left( 1 - \left| \frac{\beta_\delta}{\mu} \right| \right)^{\frac{3}{2}} \right) \text{sign}(\delta_s); \quad \text{where } \beta_\delta = \frac{\delta_s}{\lambda \delta_n} \quad (2.34)$$

In Eqs. 2.29 and 2.30,  $\mu$  is the friction coefficient, parameters  $k$ ,  $\lambda$ , and  $\eta$  are material properties given as

$$\lambda = \frac{2-\nu}{2(1-\nu)}; \quad k = \frac{8G\sqrt{R}}{3(2-\nu)}; \quad \eta = 0.5 \quad (2.35)$$

where  $\nu$  is Poisson's ratio,  $R$  is the radius of particles, and Eq. 2.34 is valid for  $\beta_\delta \leq \mu$ . When  $\beta_\delta$  exceeds  $\mu$ , the shear force becomes  $f_s = \mu |f_n| \text{sign}(\delta_s)$  [29].

It is important to note that the force-displacement relationships can be defined in a general manner and the inter-granular stiffness matrix shown in Eq. 2.8 need not be diagonal and the stiffness matrix shown in Eq. 2.8 is used only for linear elastic isotropy.

## 2.4 Summary

In this section the basic frameworks of the method of granular micromechanics in two categories: 1) with kinematic constraint and 2) with static constraint are introduced and developed. A schematic representation of the two approaches and the usual continuum approach are shown in Figure 2.4.

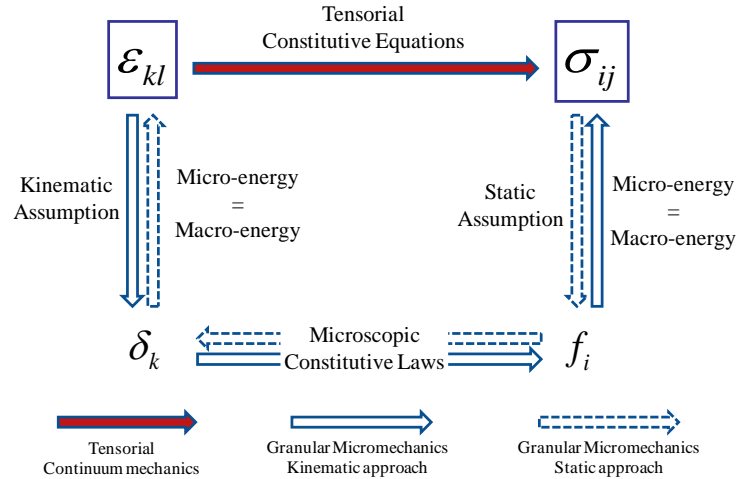


Figure 2.4 Schematic description of the granular micromechanics approach with both kinematic and static assumptions and comparing with traditional continuum mechanics approach

In the traditional continuum mechanics approach, the macroscopic Cauchy stress tensor is calculated as the product of the fourth rank stiffness tensor and the strain tensor. In the granular micromechanics method with kinematic constraint, knowing the macroscopic strain tensor, inter-granular displacement vectors are defined as projections of the strain tensor in the direction of grain-pair interaction line and then scaled by the length of the contact line (kinematic constraint). Then by defining inter-granular force vectors as work conjugates to the inter-granular displacement vectors, internal energy of each inter-granular contact is calculated. Setting the macroscopic strain energy density equal to the volume average of grain-pair internal energies, macroscopic stress and stiffness tensor are derived.

The method with static constraint will be used for cases where initially the stress tensor is known, typical case for load control experiments. In this method inter-granular force vector is defined as the projection of the macroscopic stress tensor in the direction of grain-pair interaction line, scaled with contact length and then modified using a fabric tensor defining the geometry of the assembly (static constraint enhanced by least squares). Having defined inter-granular displacement vectors as

conjugates of the force vectors, internal energy of the contact is calculated. Finally equating macroscopic and microscopic energies, the macroscopic strain and compliance tensors are derived.

The critical step in both of these two approaches is defining the inter-granular force vectors as a function of the intergranular displacement vectors. In the most general case, the three components of force vector can be defined as

$$\begin{aligned} f_n &= f_n(\delta_n, \delta_s, \delta_t) \\ f_s &= f_s(\delta_n, \delta_s, \delta_t) \\ f_t &= f_t(\delta_n, \delta_s, \delta_t) \end{aligned} \tag{2.36}$$

where each component of the inter-granular force vector is defined as a function of all the three components of inter-granular displacement vector.

Using linear functions for the force components and avoiding coupling between normal and tangential components of force and displacement vectors, results in a linear elastic theory for isotropic materials. On the other hand, defining the functions in a general manner, as shown in Eq. 2.36, results in a nonlinear model for nonlinear anisotropic materials.

### **3 NONLINEAR GRANULAR MICROMECHANICS: MODELING DAMAGE AND PLASTICITY**

Modeling damage and plasticity using traditional tensorial continuum mechanics becomes very complicated when it comes to complex materials and granular assemblies. Defining 3D yield surfaces, their evolution during loading, material hardening or softening, flow rule, etc., all make modeling damage and plasticity within continuum framework a very complicated task [50, 51].

In the method of granular micromechanics, the behavior of grain-pair interactions is used as building blocks of the macroscopic behavior of the material. Part of the problem of dealing with stress and strain tensors, as it should be done in traditional continuum mechanics, stems from the fact that these parameters are tensorial entities and imagining the evolution of their different components will be difficult, especially when dealing with damaged and plastic material. In the method of granular micromechanics, instead, the terms that are dealt with are normal and tangential *components* of the intergranular displacement and force *vectors*. These are *scalar* variables. So defining the relationship between them and their evolution becomes significantly easier and more straightforward. Defining the force-displacement relationships as scalar function, even multi-variable functions, results in a theory that will be able to predict the macroscopic phenomena happening in the material automatically. Without dealing with the complexity of defining yield functions, hardening or softening, flow rules, etc., in the three-dimensional stress or strain spaces, material's macroscopic behavior will be predicted.

In this chapter, a granular micromechanics model suitable for cementitious materials has been derived in a thermos-mechanically consistent framework [52, 53]. In the subsequent discussion,

the thermodynamically consistent derivation of the model is first presented. By including a properly defined energy density and dissipation potential function in both macroscopic and microscopic (grain-scale) level, a Clausius-Duhem type inequality is derived for inter-granular interactions. The inequality is then applied to derive constitutive equations for the grain interactions that incorporate damage and plasticity at the grain-scale. The inter-granular constitutive equations are devised in a way that is compatible with the macroscopic behavior of cementitious materials as observed by experimental data available in the literature [54, 55]. In order to ensure that the model can correctly predict the material behavior in complex loading scenarios, specifically in cyclic loading, a loading-unloading-reloading criterion is proposed in the grain-scale which decides whether each grain-pair interaction is undergoing loading, unloading, or reloading at any given instant during its loading history.

Model parameters are calibrated by simulating certain experimental observations. Using the calibrated parameters, the developed model is then applied to simulate the behavior of cementitious materials under various multi-axial loading conditions. The model results are verified by comparison with experimental observations and the advantages of the current approach are discussed. Specifically, the relationships of the grain-scale behavior and the macro-scale behavior are investigated with the aim to understand the mechanisms that control behavior under different loading conditions. This work has been published in 2015 [56].

### **3.1 Thermomechanical framework for granular micromechanics with damage and plasticity**

We consider a Volume Element (VE) of cementitious material of mass density  $\rho$ . From first law of thermodynamics, the variation of internal energy density of the VE is written as follows



$$\rho \dot{e} = p^i - q_{k,k} + \rho h \quad (3.1)$$

where,  $e$  is the internal energy per unit mass,  $p^i$  is the power density of internal forces,  $q_k$  is the heat flux vector, and  $h$  is the heat source per unit mass. The superimposed dot ( $\dot{\phantom{x}}$ ) denotes the time derivative. Further, the second law of thermodynamics, stating that the change of entropy of the system is greater than or equal to supply of entropy through heat, provides the following inequality

$$\rho \theta \dot{s} - \rho h + q_{k,k} - \frac{q_k \theta_{,k}}{\theta} \geq 0 \quad (3.2)$$

where,  $s$  is the entropy per unit mass, and  $\theta$  is the thermodynamic temperature. Making use of Helmholtz free energy per unit mass,  $w$ , expressed as

$$w = e - s\theta \quad (3.3)$$

Eq. 3.1 can be written as

$$\rho \theta \dot{s} = p^i - q_{k,k} + \rho h - \rho \dot{\theta} s - \rho \dot{w} \quad (3.4)$$

Eq. 3.2 and 3.4 are combined to yield the well-known Clausius-Duhem inequality which neglecting heat flux can be written as

$$p^i - \rho \dot{w} - \rho \dot{\theta} s = d \geq 0 \quad (3.5)$$

where  $d$  denotes the dissipation per unit volume [57]. For small deformations, Helmholtz free energy and entropy per unit volume may be defined as:  $W = \rho w$  and  $S = \rho s$  leading to the following useful form of Clausius-Duhem inequality

$$p^i - \dot{W} - S\dot{\theta} = d \geq 0 \quad (3.6)$$

For further discussion, we assume that the power density of internal forces,  $p^i$ , is a function of the symmetric part of first gradient of displacement, that is  $p^i = \sigma_{ij} \dot{u}_{(i,j)} = \sigma_{ij} \dot{\epsilon}_{ij}$ , where  $\sigma_{ij}$  is the Cauchy stress. In general, the power density of internal forces could be a function of higher gradients

of displacements as well as rotations which would lead to higher gradient models or micromorphic material models (see [6, 58-60]). However, the discussion on this chapter deals with the traditional first gradient model (See Chapter 7 for a complete micromorphic theory). The Helmholtz free energy density of rate-dependent materials with damage and plasticity is taken to be a function of the independent kinematic variable,  $\varepsilon_{ij}$ ; an internal variable associated with plastic strain,  $\varepsilon_{ij}^p$ ; a second internal variable associated with damage,  $D_{ij}$ ; and the temperature,  $\theta$ , expressed in the following general form:  $W = W(\varepsilon_{ij}, \varepsilon_{ij}^p, D_{ij}, \theta)$ . In addition, the dissipation density,  $d$ , is defined as

$$d = \frac{\partial \psi}{\partial \dot{D}_{ij}} \dot{D}_{ij} + \frac{\partial \psi}{\partial \dot{\varepsilon}_{ij}^p} \dot{\varepsilon}_{ij}^p \geq 0 \quad (3.7)$$

where  $\psi = \psi(\varepsilon_{ij}, \theta, D_{ij}, \dot{D}_{ij}, \varepsilon_{ij}^p, \dot{\varepsilon}_{ij}^p)$  is a dissipation potential function. Differentiating the Helmholtz free energy,  $W$ , with time we obtain

$$\dot{W} = \frac{\partial W}{\partial \varepsilon_{ij}} \dot{\varepsilon}_{ij} + \frac{\partial W}{\partial \varepsilon_{ij}^p} \dot{\varepsilon}_{ij}^p + \frac{\partial W}{\partial D_{ij}} \dot{D}_{ij} + \frac{\partial W}{\partial \theta} \dot{\theta} \quad (3.8)$$

and combining Eq 3.6, 3.7 and 3.8, the following equation is found

$$\left( \sigma_{ij} - \frac{\partial W}{\partial \varepsilon_{ij}} \right) \dot{\varepsilon}_{ij} - \left( \frac{\partial W}{\partial D_{ij}} + \frac{\partial \psi}{\partial \dot{D}_{ij}} \right) \dot{D}_{ij} - \left( \frac{\partial W}{\partial \varepsilon_{ij}^p} + \frac{\partial \psi}{\partial \dot{\varepsilon}_{ij}^p} \right) \dot{\varepsilon}_{ij}^p - \left( \frac{\partial W}{\partial \theta} + S \right) \dot{\theta} = 0 \quad (3.9)$$

Since Eq. 3.9 should hold for any arbitrary values of  $\dot{\varepsilon}_{ij}$ ,  $\dot{D}_{ij}$ ,  $\dot{\varepsilon}_{ij}^p$ , and  $\dot{\theta}$  it would appear that their coefficients should be simultaneously equal to zero. However, it is notable that the coefficients in second term and third term of Eq. 3.9 can, in general, be functions of  $\dot{D}_{ij}$  and  $\dot{\varepsilon}_{ij}^p$ , respectively, such that these coefficients cannot be completely arbitrary. In this case, a weaker conclusion stating orthogonality of  $\partial W / \partial D_{ij} + \partial \psi / \partial \dot{D}_{ij}$  and  $\dot{D}_{ij}$ , and similarly of  $\partial W / \partial \varepsilon_{ij}^p + \partial \psi / \partial \dot{\varepsilon}_{ij}^p$  and  $\dot{\varepsilon}_{ij}^p$ , must be made [61]. According to Ziegler [52], the stronger statements of the terms inside the parentheses being

equal to zero can be made for idealized materials. Here, we proceed with our derivation using the weaker, more conservative conclusion of orthogonality. Thus

$$\sigma_{ij} - \frac{\partial W}{\partial \varepsilon_{ij}} = 0 \quad (3.10a)$$

$$\left( \frac{\partial W}{\partial D_{ij}} + \frac{\partial \psi}{\partial \dot{D}_{ij}} \right) \dot{D}_{ij} = 0 \quad (3.10b)$$

$$\left( \frac{\partial W}{\partial \varepsilon_{ij}^p} + \frac{\partial \psi}{\partial \dot{\varepsilon}_{ij}^p} \right) \dot{\varepsilon}_{ij}^p = 0 \quad (3.10c)$$

$$\frac{\partial W}{\partial \theta} + S = 0 \quad (3.10d)$$

In a purely phenomenological continuum approach, appropriate forms of free energy and dissipation would be formulated and further derivation performed to determine the constitutive relationship, the yield function, and damage and plastic potentials. Here we depart from this conventional approach and consider the granular system from its micro-scale (grain-scale).

## 3.2 Thermomechanical formulation for granular systems

### 3.2.1 Kinematics of granular meso-structure

When the external load is applied, the grains translate and rotate resulting in a relative displacement between them [18, 19]. Relative displacement  $\delta_i$  between two nearest neighbor grains  $n$  and  $p$  ignoring the grain rotations is written as

$$\delta_i = u_i^p - u_i^n \quad (3.11)$$

Where,  $u_i$  is the particle displacement; superscripts refer to the interacting particles. To obtain the continuum description of this discrete model, we utilize the Taylor series expansion of the displacement such that the displacement of grain  $p$  may be written as:

$$u_i^p = u_i^n + u_{i,j}^n (x_j^p - x_j^n) \quad (3.12)$$

where, the point of expansion is chosen as the centroid of grain  $n$ . In Eq. 12,  $u_{ij}$  is the displacement gradient, and  $x_j^n$  and  $x_j^p$  are the position vectors of the centroids of grains  $n$  and  $p$ , respectively. Thus, the relative displacement,  $\delta_i$ , between two nearest neighbor grains  $n$  and  $p$  representing the  $\alpha$ -th inter-granular interaction is given by

$$\delta_i^\alpha = u_{i,j}^n (x_j^p - x_j^n) = u_{i,j}^n l_j^\alpha \quad (3.13)$$

where  $l_j$  is the inter-granular branch vector joining the centroids of grains  $n$  and  $p$ .

### 3.2.2 Thermomechanics equations for granular system

We observe that for a granular system, the VE free energy, dissipation potential and temperature may be defined in terms of the micro-scale quantities arising from the inter-granular interactions. For that purpose, the Helmholtz free energy volume density,  $W$ , and the dissipation potential,  $\psi$ , are written as follows:

$$W = \frac{1}{V} \sum_{\alpha}^N W^\alpha (\delta_j^\alpha, \delta_j^p, D_j^\alpha, \theta^\alpha) \quad (3.14a)$$

$$\psi = \frac{1}{V} \sum_{\alpha=1}^N \psi^\alpha (\delta_j^\alpha, D_j^\alpha, \dot{D}_j^\alpha, \delta_j^{p\alpha}, \dot{\delta}_j^{p\alpha}, \theta^\alpha) \quad (3.14b)$$

where each inter-granular interaction, denoted by superscript  $\alpha$ , has been counted once and  $N$  is the total number of inter-granular interactions.  $W^\alpha$  and  $\psi^\alpha$  denote the contributions of the  $\alpha^{\text{th}}$  grain

interaction to free energy and dissipation potential, respectively and are functions of the following variables: the inter-granular displacement vector defined in Eq. 3.13,  $\delta_j^\alpha$ ; the internal variables associated with damage and plasticity of the inter-granular interactions,  $D_j^\alpha$  and  $\delta_j^{p\alpha}$ , respectively; and the temperature,  $\theta$ .

Now, substituting Eq. 3.14a into Eq. 10a, the following expression for the macroscopic Cauchy stress of the RVE can be obtained

$$\sigma_{ij} = \frac{\partial W}{\partial \varepsilon_{ij}} = \frac{1}{V} \sum_{\alpha=1}^N \frac{\partial W^\alpha}{\partial \delta_k^\alpha} \frac{\partial \delta_k^\alpha}{\partial \varepsilon_{ij}} \quad (3.15)$$

Further, by substituting Eq. 3.14a and 3.14b into the orthogonality conditions given in Eq. 3.10b and 3.10c, the following equations are derived using chain rule:

$$\sum_{\alpha=1}^N \left( \left( \frac{\partial W^\alpha}{\partial D_k^\alpha} + \frac{\partial \psi^\alpha}{\partial \dot{D}_k^\alpha} \right) \frac{\partial \dot{D}_k^\alpha}{\partial \dot{D}_{ij}} \dot{D}_{ij} \right) = 0 \quad (3.16a)$$

$$\sum_{\alpha=1}^N \left( \left( \frac{\partial W^\alpha}{\partial \delta_k^{p\alpha}} + \frac{\partial \psi^\alpha}{\partial \dot{\delta}_k^{p\alpha}} \right) \frac{\partial \dot{\delta}_k^{p\alpha}}{\partial \dot{\varepsilon}_{ij}^p} \dot{\varepsilon}_{ij}^p \right) = 0 \quad (3.16b)$$

where we have considered that the time dependence of the micro- and macro-scale quantities are same such that  $\partial D_k^\alpha / \partial D_{ij} = \partial \dot{D}_k^\alpha / \partial \dot{D}_{ij}$  and  $\partial \dot{\delta}_k^{p\alpha} / \partial \dot{\varepsilon}_{ij}^p = \partial \delta_k^{p\alpha} / \partial \varepsilon_{ij}^p$ . Using Eq. 3.14a and Eq. 3.10d leads to

$$\sum_{\alpha=1}^N \frac{1}{\varphi^\alpha} \frac{\partial W^\alpha}{\partial \theta^\alpha} + \sum_{\alpha=1}^N S^\alpha = 0 \quad (3.16c)$$

In Eq. 3.16c the VE temperature is defined as  $\theta = \sum_{\alpha=1}^N \varphi^\alpha \theta^\alpha$ , where  $\varphi^\alpha$  is the volume fraction

associated with the  $\alpha^{th}$  grain-interaction, and the entropy per unit volume is defined as

$$S = \frac{1}{V} \sum_{\alpha=1}^N S^\alpha.$$

We note that the microscopic inter-granular force vector conjugate to the displacement vector can be defined as

$$f_k^\alpha = \frac{\partial W^\alpha}{\partial \delta_k^\alpha} \quad (3.17a)$$

Further, the summations in Eq. 3.16 should hold for any value of  $N$ , and thus, the equality should be satisfied in a term-by-term manner. So the following set of equations which resemble the ones in Eq. 3.10 are obtained

$$\left( \frac{\partial W^\alpha}{\partial D_k^\alpha} + \frac{\partial \Psi^\alpha}{\partial \dot{D}_k^\alpha} \right) \frac{\partial \dot{D}_k^\alpha}{\partial \dot{D}_{ij}} \dot{D}_{ij} = 0 \quad (3.17b)$$

$$\left( \frac{\partial W^\alpha}{\partial \delta_k^{p\alpha}} + \frac{\partial \Psi^\alpha}{\partial \dot{\delta}_k^{p\alpha}} \right) \frac{\partial \dot{\delta}_k^{p\alpha}}{\partial \dot{\epsilon}_{ij}^p} \dot{\epsilon}_{ij}^p = 0 \quad (3.17c)$$

$$S^\alpha + \frac{1}{\varphi^\alpha} \frac{\partial W^\alpha}{\partial \theta^\alpha} = 0 \quad (3.17d)$$

Under the assumption that the inter-granular damage parameter may be obtained as the projection of the VE damage tensor in the direction of inter-granular branch vector,  $n_j$ , the terms outside the parentheses in Eq. 3.17b can be simplified as follows:

$$\frac{\partial \dot{D}_k^\alpha}{\partial \dot{D}_{ij}} \dot{D}_{ij} = \frac{\partial (\dot{D}_{kr} n_r)}{\partial \dot{D}_{ij}} \dot{D}_{ij} = n_r \delta_{ik} \delta_{jr} \dot{D}_{ij} = \dot{D}_{kj} n_j = \dot{D}_k^\alpha \quad (3.18a)$$

Similarly, assuming that the inter-granular plastic displacement is the projection of the VE plastic strain to the inter-granular branch vector, Eq. 3.17c leads to

$$\frac{\partial \dot{\delta}_k^{p\alpha}}{\partial \dot{\epsilon}_{ij}^p} \dot{\epsilon}_{ij}^p = \frac{\partial (\dot{\epsilon}_{kr}^p l_r)}{\partial \dot{\epsilon}_{ij}^p} \dot{\epsilon}_{ij}^p = l_r \delta_{ik} \delta_{jr} \dot{\epsilon}_{ij}^p = \dot{\epsilon}_{kj}^p l_j = \dot{\delta}_k^{p\alpha} \quad (3.18b)$$

Eqs. 3.17 and 3.18 can now be combined to obtain

$$\left( f_j^\alpha - \frac{\partial W^\alpha}{\partial \delta_j^\alpha} \right) \dot{\delta}_j^\alpha - \left( \frac{\partial W^\alpha}{\partial D_j^\alpha} + \frac{\partial \psi^\alpha}{\partial \dot{D}_j^\alpha} \right) \dot{D}_j^\alpha - \left( \frac{\partial W^\alpha}{\partial \delta_j^\alpha} + \frac{\partial \psi^\alpha}{\partial \dot{\delta}_j^{p\alpha}} \right) \dot{\delta}_j^{p\alpha} - \left( \frac{1}{\varphi^\alpha} \frac{\partial W^\alpha}{\partial \theta^\alpha} + S^\alpha \right) \dot{\theta}^\alpha = 0 \quad (3.19)$$

which leads to the following micro-scale Clausius-Duhem type inequality for the  $\alpha^{\text{th}}$  inter-granular interaction:

$$f_j^\alpha \dot{\delta}_j^\alpha - \dot{W}^\alpha - S^\alpha \dot{\theta}^\alpha = d^\alpha \geq 0 \quad (3.20)$$

In Eq. 20, the microscopic dissipation,  $d^\alpha$ , is defined as

$$d^\alpha = \frac{\partial \psi^\alpha}{\partial \dot{D}_j^\alpha} \dot{D}_j^\alpha + \frac{\partial \psi^\alpha}{\partial \dot{\delta}_j^{p\alpha}} \dot{\delta}_j^{p\alpha} \geq 0 \quad (3.21)$$

and the time derivative of micro-scale free energy,  $W^\alpha$ , is

$$\dot{W}^\alpha = \frac{\partial W^\alpha}{\partial \delta_j^\alpha} \dot{\delta}_j^\alpha + \frac{\partial W^\alpha}{\partial D_j^\alpha} \dot{D}_j^\alpha + \frac{\partial W^\alpha}{\partial \delta_j^{p\alpha}} \dot{\delta}_j^{p\alpha} + \frac{\partial W^\alpha}{\partial \theta^\alpha} \dot{\theta}^\alpha \quad (3.22)$$

### 3.3 Inter-granular coupled damage-plasticity relationships

For convenience a local Cartesian coordinate system,  $\mathbf{nst}$ , is now defined separately for each contact composed of three unit vectors: normal vector  $n_i$  in the direction of inter-granular branch vector,  $l_i$ , and two orthogonal vectors lying in the tangential plane denoted as  $s_i$  and  $t_i$ , whose direction cosines are repeated here for convenience

$$\begin{aligned}
n_i &= \langle \cos \theta, \sin \theta \cos \phi, \sin \theta \sin \phi \rangle \\
s_i &= \langle -\sin \theta, \cos \theta \cos \phi, \cos \theta \sin \phi \rangle \\
t_i &= \langle 0, -\sin \phi, \cos \phi \rangle
\end{aligned} \tag{3.23}$$

with  $\theta$  and  $\phi$  the polar and azimuth angle in the spherical coordinate system as depicted in Figure 2.1. Now displacement vector between the two particles,  $\delta_i$ , can be decomposed into two parts: one along the normal vector given as  $\delta_n = \delta_i n_i$ , and the other in the tangential plane given as

$$\delta_w = \sqrt{(\delta_i s_i)^2 + (\delta_i t_i)^2}.$$

The inter-granular free energy and dissipation potential considering grain-scale damage and plasticity can be conveniently written as follows in terms of the normal and shear components following the above decomposition

$$\begin{aligned}
W^\alpha &= W_n^\alpha + W_w^\alpha \\
\psi^\alpha &= \psi_n^\alpha + \psi_w^\alpha
\end{aligned} \tag{3.24}$$

For the coupled damage-plasticity phenomena addressed in this work, the inter-granular free energy is assumed to take the following form

$$\begin{aligned}
W_n^\alpha &= \frac{1}{2} E_n^\alpha (1 - D_n^\alpha) (\delta_n^\alpha)^2 - h_n^\alpha \delta_n^{p\alpha} \\
W_w^\alpha &= \frac{1}{2} G_w^\alpha (1 - D_w^\alpha) (\delta_w^\alpha)^2 - h_w^\alpha \delta_w^{p\alpha}
\end{aligned} \tag{3.25}$$

Where  $E_n^\alpha$  and  $G_w^\alpha$  are the inter-granular elastic stiffness,  $h_n^\alpha$  and  $h_w^\alpha$  are the inter-granular generalized forces, and  $\delta_n^{p\alpha}$  and  $\delta_w^{p\alpha}$  are the inter-granular plastic displacements in normal and shear directions, respectively. The inter-granular dissipation potential components are taken to be represented by the sum of damage and plastic dissipations in the following classical form [61]

$$\begin{aligned}
\psi_n^\alpha &= Y_n^\alpha |\dot{D}_n^\alpha| + Z_n^\alpha |\dot{\delta}_n^{p\alpha}| \geq 0 \\
\psi_w^\alpha &= Y_w^\alpha |\dot{D}_w^\alpha| + Z_w^\alpha |\dot{\delta}_w^{p\alpha}| \geq 0
\end{aligned} \tag{3.26}$$



where dissipation coefficients  $Y$  and  $Z$  denote generalized forces that are conjugates of the inter-granular damage and plastic dissipation, respectively. Using Eqs. 3.17b and 18a, it follows that

$$\left( \frac{\partial W^\alpha}{\partial D_n^\alpha} + \frac{\partial \Psi^\alpha}{\partial \dot{D}_n^\alpha} \right) \dot{D}_n^\alpha = 0; \quad \left( \frac{\partial W^\alpha}{\partial D_w^\alpha} + \frac{\partial \Psi^\alpha}{\partial \dot{D}_w^\alpha} \right) \dot{D}_w^\alpha = 0 \quad (3.27)$$

Thus, the dissipation coefficient,  $Y$ , defined as the dual of inter-granular damage  $D$  is found as follows

$$Y_n^\alpha = \frac{1}{2} E_n^\alpha (\delta_n^\alpha)^2 \text{sign}(\dot{D}_n^\alpha); \quad Y_w^\alpha = \frac{1}{2} G_w^\alpha (\delta_w^\alpha)^2 \text{sign}(\dot{D}_w^\alpha) \quad (3.28)$$

In view of positive semi-definiteness of the dissipation potential in Eq. 3.26, it is clear from Eq. 3.28 that damage is irreversible, that is the rate of damage must satisfy  $\dot{D}_n^\alpha \geq 0$  and  $\dot{D}_w^\alpha \geq 0$ . It is also notable that the dissipation coefficient,  $Y$ , is the undamaged elastic energy of the inter-granular interaction. Similarly, using Eqs. 3.17c and 3.18b, we find

$$\left( \frac{\partial W^\alpha}{\partial \delta_n^{p\alpha}} + \frac{\partial \Psi^\alpha}{\partial \dot{\delta}_n^{p\alpha}} \right) \dot{\delta}_n^{p\alpha} = 0; \quad \left( \frac{\partial W^\alpha}{\partial \delta_w^{p\alpha}} + \frac{\partial \Psi^\alpha}{\partial \dot{\delta}_w^{p\alpha}} \right) \dot{\delta}_w^{p\alpha} = 0 \quad (3.29)$$

Thus, the dissipation coefficient,  $Z$ , defined as dual to the inter-granular plastic displacements is given as

$$Z_n^\alpha = h_n^\alpha \text{sign}(\dot{\delta}_n^{p\alpha}); \quad Z_w^\alpha = h_w^\alpha \text{sign}(\dot{\delta}_w^{p\alpha}) \quad (3.33)$$

Again, in view of Eq. 3.26 it is clear that plastic displacements are only admissible when the inter-granular generalized forces take the same sign as the rate of plastic displacements. The grain-scale free energy and dissipation defined in the manner of Eq. 3.24-29 represent coupled damage and plasticity wherein the dissipation due to damage is partly independent and partly coupled with plasticity. Similar coupling has been proposed in the context of purely continuum modeling (see among others [62-65]). Note that for modeling materials that are isotropic in the initial unloaded state, the terms that cross-link normal and shear components have been neglected and the response

on the shear plane ( $s$ - $t$  plane) is taken to be isotropic. It is noteworthy that in the granular systems composed of many components possibilities of sinks that trap the macroscopic energy in microscopic (grain-scale) motions may be present as shown by [66-68]. Further in lattice models, dissipation due to rupture of elastic links are used for describing material damage [69-71]. Such losses are modeled in the approach presented here in a phenomenological sense using inter-granular dissipation mechanism given by Eq. 3.26. Now, using Eq. 3.17a and 3.26, the inter-granular forces are obtained as follows

$$\begin{aligned}
 f_n^\alpha &= \frac{\partial W^\alpha}{\partial \delta_n^\alpha} = k_n^\alpha \delta_n^\alpha = E_n^\alpha (1 - D_n^\alpha) \delta_n^\alpha \\
 f_w^\alpha &= \frac{\partial W^\alpha}{\partial \delta_w^\alpha} = k_w^\alpha \delta_w^\alpha = G_w^\alpha (1 - D_w^\alpha) \delta_w^\alpha
 \end{aligned} \tag{3.31}$$

### 3.4 Inter-granular loading-unloading-reloading relationships

To complete the inter-granular constitutive relationships for coupled damage-plasticity, we introduce the following criterion for loading, unloading, and reloading conditions at the inter-granular scale utilizing “yield” function,  $F$ :

- (1) Loading –  $F_n^\alpha = 0$ , and  $\dot{\delta}_n^\alpha > 0$ , and  $F_w^\alpha = 0$ , and  $\dot{\delta}_w^\alpha > 0$ .
- (2) Unloading –  $F_n^\alpha < 0$ , and  $\dot{\delta}_n^\alpha < 0$ , and  $F_w^\alpha < 0$ , and  $\dot{\delta}_w^\alpha < 0$ .
- (3) Reloading –  $F_n^\alpha < 0$ , and  $\dot{\delta}_n^\alpha > 0$ , and  $F_w^\alpha < 0$ , and  $\dot{\delta}_w^\alpha > 0$ .

The “yield” function is defined as

$$\begin{aligned}
 F_n^\alpha &= |\delta_n^\alpha| - \max |\delta_n^\alpha| \leq 0; \\
 F_w^\alpha &= \delta_w^\alpha - \max \delta_w^\alpha \leq 0
 \end{aligned} \tag{3.32}$$

where the left superscript refers to the instantaneous maximum normal and tangential displacement components belonging to the  $\alpha^{th}$  contact. It should be noted that the instantaneous maximum normal displacement takes different values for tension and compression. Thus, the “yield” function is evaluated separately for tensile and compressive interactions. The grain-scale constitutive relationships during unloading are defined as:

$$\begin{aligned} f_n^\alpha &= k_n^{u\alpha} \left| \delta_n^\alpha - \beta_n \left( \max \delta_n^\alpha \right) \right| \\ f_w^\alpha &= k_w^{u\alpha} \left( \delta_w^\alpha - \beta_w \left( \max \delta_w^\alpha \right) \right) \end{aligned} \quad (3.33)$$

where the parameters  $0 \leq \beta_n \leq 1$  and  $0 \leq \beta_w \leq 1$  are constants defined as the ratio of maximum plastic displacement to the instantaneous maximum displacement as follows

$$\beta_n = \frac{\max \delta_n^{p\alpha}}{\max \delta_n^\alpha}; \quad \beta_w = \frac{\max \delta_w^{p\alpha}}{\max \delta_w^\alpha} \quad (3.34)$$

and  $K^u$  is the inter-granular unloading stiffness given as

$$\begin{aligned} k_n^{u\alpha} &= \frac{E_n^\alpha \left( 1 - \max D_n^\alpha \right)}{\left( 1 - \beta_n \right)} \\ k_w^{u\alpha} &= \frac{G_w^\alpha \left( 1 - \max D_w^\alpha \right)}{\left( 1 - \beta_w \right)} \end{aligned} \quad (3.35)$$

To model nonlinearity during reloading, the force-displacement relationship is assumed to be similar as that given by Eq. 3.30, where the reloading initial stiffness is a constant times the unloading stiffness and the resultant curve passes through the point at which unloading initiates.

It is notable, that different sub-granular mechanisms govern the deformation behavior under tension and compression leading to asymmetric inter-granular interactions [20]. As the grains are pulled apart under tension, the behavior is governed by accumulation of sub-granular scale (micro- and nano-scale) de-cohesion, void growth, and strain localization, which contribute to both damage, plasticity and eventual separation . In contrast, when the grains are compressed against

each other, the behavior is governed by a combination of stiffening due to increasing confinement and the loss of stiffness due to sub-granular scale pore compaction and shear localization. Consequently, the inter-granular stiffness increases with increasing confinement even as there is accumulation of damage and plastic displacement. Within the genre of modeling approach considered in this work, these diverse mechanisms are not modeled explicitly but rather they are represented in practical manner by utilizing appropriate functions for evolution of damage, plastic displacements and elastic constants. The normal component of inter-granular damage coefficient is modeled as follows

$$D_n = \begin{cases} 1 - e^{-\frac{|\delta_n|}{B_n}} & ; \delta_n \geq 0 \text{ (tension)} \\ \tan^{-1}\left(\frac{\delta_n}{B_{nc}}\right) & ; \delta_n < 0 \text{ (compression)} \\ 1 - \frac{\delta_n}{B_{nc}} & \end{cases} \quad (3.36)$$

where constants  $B_n$  and  $B_{nc}$  are the model parameters. The resultant inter-granular force-displacement curve has a peak and subsequent softening under tension and an asymptotic behavior under compression as shown in Figure 3.1a. Parameter  $B_n$  corresponds to the peak in the tensile inter-granular force-displacement curve, while the parameter  $B_{nc}$  corresponds to the point of departure from linearity in the compressive inter-granular force-displacement curve. The tangential component of inter-granular damage coefficient is modeled as

$$D_w = 1 - e^{-\frac{|\delta_w|}{B_w}} \quad (3.37)$$

where the effect of compression on the tangential behavior is modeled by defining  $B_w$  as a bi-linear function of the normal displacement governed by model parameters  $\alpha_1$ ,  $\alpha_2$ , and  $\alpha_3$  as depicted in Figure 3.1b and expressed as

$$B_w = \begin{cases} B_{wo} & ; \quad \delta_n \geq 0 & \text{(tension)} \\ B_{wo} - \alpha_2 \delta_n & ; \quad \frac{1-\alpha_1}{\alpha_2} B_{wo} \leq \delta_n < 0 & \text{(compression)} \\ \alpha_2 B_{wo} - \alpha_3 p \left( \delta_n - \frac{1-\alpha_1}{\alpha_2} B_{wo} \right) & ; \quad \delta_n < \frac{(1-\alpha_1)}{\alpha_2} B_{wo} & \text{(compression)} \end{cases} \quad (3.38)$$

Since the parameter  $B_w$  is the displacement at the peak in the tangential inter-granular force-displacement curve, the maximum tangential force becomes larger as the grains are compressed together. Further, to model the effect of stiffening under compression, the inter-granular normal stiffness coefficient,  $E_n$ , is taken to be a function of the mean stress,  $p$ , as follows:

$$E_n = \begin{cases} E_{no} & ; \quad \delta_n \geq 0 & \text{(tension)} \\ E_{no}(1 + \alpha_4 p) & ; \quad \delta_n < 0 & \text{(compression)} \end{cases} \quad (3.39a)$$

where the constant  $\alpha_4$  defines the growth of normal stiffness with increasing confinements and the stiffness coefficient in compression (with zero mean pressure) is given as

$$E_{no}^C = \frac{2}{\pi e} \frac{B_n}{\delta_n} E_{no}^T R \approx 0.234 \frac{B_n}{\delta_n} E_{no}^T R \quad (3.39b)$$

Defining  $E_{no}^C$  using Eq. 3.39b guarantees two important properties of the material. First, it guarantees equal stiffness coefficients at the unloaded state in tension and compression. Further, it also guarantees the maximum normal force in compression to be equal to  $R$  times the maximum normal force in tension, making  $R$  a parameter with clear physical significance that needs to be calibrated for the material.

Using these force functions, the normal and tangential behavior of the grain-pair contacts are derived and shown in Figure 3.1. Figure 3.1(a) shows the force-displacement relationship in normal direction while Figure 3.1(b) shows the dependence of the tangential damage parameter on the normal component of displacement.

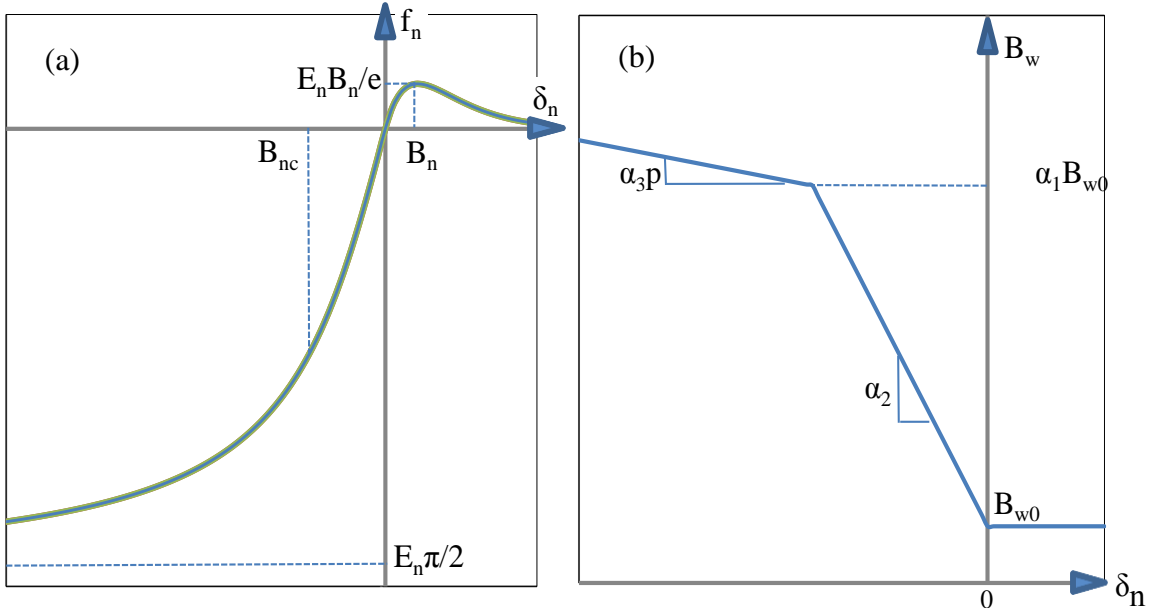


Figure 3.1 Normal force-displacement relationship in compression and tension (a) and the shear direction damage parameter as a function of normal displacement (b). The local Cartesian coordinate system is shown in the inset

The inter-granular generalized forces,  $h_n^\alpha$  and  $h_w^\alpha$ , conjugate to the plastic displacement are taken as

$$h_n^\alpha = \frac{E_n (1 - \max D_n)}{\beta_n} \delta_n^{p\alpha}; \quad h_w^\alpha = \frac{G_w (1 - \max D_w)}{\beta_w} \delta_w^{p\alpha} \quad (3.40)$$

so that the dissipation is equal to the plastic work.

### 3.5 Constitutive relationship for granular cementitious materials

The constitutive relationship for an RVE of a granular system can now be obtained by introducing Eq. 3.17a into Eq. 3.15 and using Eq. 3.13 as follows

$$\sigma_{ij} = \frac{1}{V} \sum_{\alpha=1}^N f_k^\alpha l_l^\alpha \frac{\partial \varepsilon_{kl}^n}{\partial \varepsilon_{ij}} \quad \text{where } \varepsilon_{kl}^n = u_{(k,l)}^n \quad (3.41)$$

in which strain  $\varepsilon_{kl}$  is the symmetric part of the displacement gradient. It is clear that relationships between grain-scale strains and the overall RVE strain are needed for further development. However, such relationships are unique for each grain neighborhood and can only be obtained for well-defined granular micro-structures and inter-granular interactions (see for example [19, 72]). For most cementitious materials, the granular-structure and inter-granular interactions are ill-defined, since these materials are formed by conglomerations of grains of atomic sizes and larger with many different shapes, sizes, aspect ratios, and compositions. Computational approaches based upon simulated discrete coarse-grained granular structures can be conceived. However, these discrete models suffer from the need to simulate a coarse-grained structure at an appropriate scale as depicted in Figure 1.1, define appropriate grain-scale constitutive laws, implement effective computational schemes, and be coupled to higher scales. Such discrete models not only add to the computational expense, but fail to offer the versatility of systematically investigating the influence of the macro-scale parameters, such as material density and inherent anisotropy, as well as the grain-scale parameters, such as effect of inter-granular degradation, presence of boundary layers, different shapes and sizes. In light of this difficulty, the mean field assumption, albeit approximate, provides a feasible approach for the derivation of the VE constitutive law and has been shown to successfully describe different phenomena exhibited by granular materials [18, 20, 42]. In this case, the average stress tensor of an RVE given by Eq. 3.41 is simplified to:

$$\sigma_{ij} = \frac{1}{V} \sum_{\alpha=1}^N f_i^\alpha l_j^\alpha \quad (3.42)$$

which is a widely used expression for Cauchy stress tensor in granular mechanics (see for example [23, 73]). The stress defined in this way is also traced to the virial of Clausius [74, 75], has counterparts in the statistical mechanics of fluids [76, 77], and has been a subject of recent discussion in the context of molecular and atomistic modeling [78, 79]. For sufficiently large RVE

containing variously oriented grain interactions, the summation in Eq. 3.42 can be approximated by the following integral under certain simplifying assumptions [23, 42, 73]

$$\sigma_{ij} = N \int_0^{2\pi} \int_0^{\pi} f_i(\theta, \phi) l_j(\theta, \phi) \xi(\theta, \phi) \sin \theta d\theta d\phi \quad (3.43)$$

where  $N$  is the number density of pair interactions, and  $\xi(\theta, \phi)$  is a directional probability density function defined such that the product  $N\xi(\theta, \phi)\sin\theta d\theta d\phi$  gives the number density of pair interactions in the solid angle  $\sin\theta d\theta d\phi$ . Using Eq. 31, the inter-granular force vector,  $f_i$ , can be written as

$$f_i = K_{ij} \delta_j \quad (3.44)$$

where  $K_{ij} = k_n n_i n_j + k_w (s_i s_j + t_i t_j)$ . Thus the macroscopic constitutive relationship can be obtained as

$$\sigma_{ij} = \left( l^2 N \int_{\theta=0}^{\pi} \int_{\phi=0}^{2\pi} K_{ik} n_j n_l \xi(\theta, \phi) \sin \theta d\theta d\phi \right) \varepsilon_{kl} = C_{ijkl} \varepsilon_{kl} \quad (3.45)$$

### 3.6 Results and Discussions

The derived damage-plasticity granular micromechanics model is applied for simulating the behavior of cementitious materials under various loading conditions. The simulation results are compared to typical experimental data available in the literature [54, 55]. Since the inter-granular forces are nonlinear functions, a numerical approach is required for evaluating the overall stress-strain behavior. Simple forward Euler method utilizing adequately small increments appears sufficient for the simulations presented in this work. Numerical approaches based upon Newton's methods or other incremental approaches may be used when the model is implemented for solution of boundary value problems [21, 80].



### 3.6.1 Calibration and identification of model parameters

Model parameters were calibrated using conventional triaxial test results. In particular, under elastic conditions Eq. 3.45 can be integrated to obtain closed-form expressions, such that for isotropic materials the model parameters can be obtained in terms of measured Young's modulus,  $E$ , and Poisson's ratio,  $\nu$ , as follows

$$E_{no} = \frac{3E}{Nl^2(1-2\nu)}; \quad G_w = \frac{3E(1-4\nu)}{Nl^2(1-2\nu)(1+\nu)} \quad (3.46)$$

The mean inter-granular distance,  $l$ , is assumed to be 10  $\mu\text{m}$  and the number density of pair interactions,  $N_p$ , is taken to be  $10^{18}\text{m}^{-3}$ . These assumptions are reasonable estimates for cementitious materials formed from powder precursor whose particle sizes are in the order of  $\sim 10$   $\mu\text{m}$ . Parameters  $B_n$ ,  $B_{nc}$ , and  $B_{wo}$  govern the strain at which the peak-stress or failure occurs in uniaxial compression, thus they are obtained by minimizing the error between the calculated and predicted peak or failure stress-strain state. Table 3.1 lists the above parameters used in the calculation based upon a cohesive material with Young's modulus = 78 GPa, the Poisson's ratio = 0.167, the peak stress under uniaxial compression = 40 MPa and corresponding strain = 0.15%, and a ten times smaller peak stress under uniaxial tension = 4 MPa and corresponding strain = 0.015%. Parameters  $\alpha_2$ ,  $\alpha_3$ , and  $\alpha_4$  represent the stiffening effect due to confinement and can be calibrated using results of confined axisymmetric triaxial test results. For simulations reported here, typical values that lead to results similar to those available in the literature have been used.

Table 3.1 Model parameters used in this study

Model Parameters	value
$E_{no}^T$	3.5 kN/m
R	17.5
$G_w$	1 kN/m
$B_n$	$7 \times 10^{-10}$ m
$B_{nc}$	$3 \times 10^{-9}$ m
$B_{wo}$	$1.5 \times 10^{-9}$ m
$\alpha_1$	10.5
$\alpha_2$	7
$\alpha_3$	0.01
$\alpha_4$	$0.05 \text{ MPa}^{-1}$

### 3.6.2 Model prediction under confined compression and extension

Predicted stress-strain behavior under confined compression and tension are presented in Figures 3.2 through 3.7. In Figure 3.2, the overall stress-strain curves are plotted in terms of the deviatoric stress,  $q = \sigma_{11} - \sigma_{22}$  (vertical axis), versus  $\epsilon_{11}$  and  $\epsilon_{22}$  (positive and negative horizontal axis respectively) for different confinements,  $\sigma_{22} = \sigma_{33} = \sigma_c$ . These curves are calculated by first applying a hydrostatic confinement,  $\sigma_{11} = \sigma_{22} = \sigma_{33} = \sigma_c$ , and subsequently, increasing axial strain  $\epsilon_{11}$  incrementally while keeping constant  $\sigma_{22} = \sigma_{33} = \sigma_c$ .

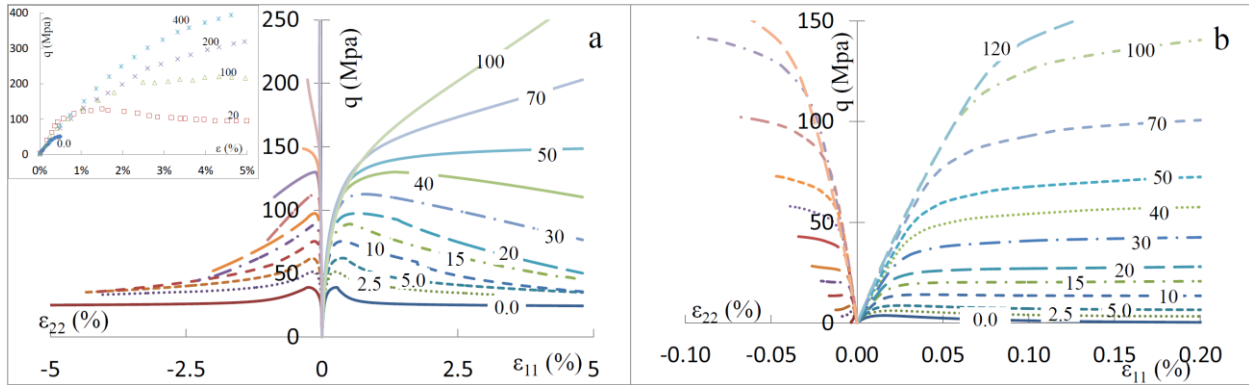


Figure 3.2 Compressive stress-strain behavior (a), and tensile stress-strain behavior (b) under different confinement levels. The inset in part (a) represents experimental measurements from Bazant et al [54]

From Figure 3.2 it can be observed that by increasing the confinement, the stress-strain behavior under both compression and tension transitions from brittle to ductile. At low confinement, the stress-strain curves are characterized by peak stress followed by strain-softening. With increasing confinement, softening is suppressed and at very high confinement, the stress-strain curves show gradual ‘yield’ followed by hardening. Furthermore, the strain corresponding to the peak stress and the nominal ‘yield’ point increases with increasing confinement. The effect of confinement on the behavior can be further seen from the plot of deviatoric stress,  $q$ , normalized by the initial mean stress,  $p = \sigma_c$  given in Figure 3.3. These observations are in agreement with experimental results as seen from the measured stress-strain curves from [54] given in the inset of Figure 3.2.

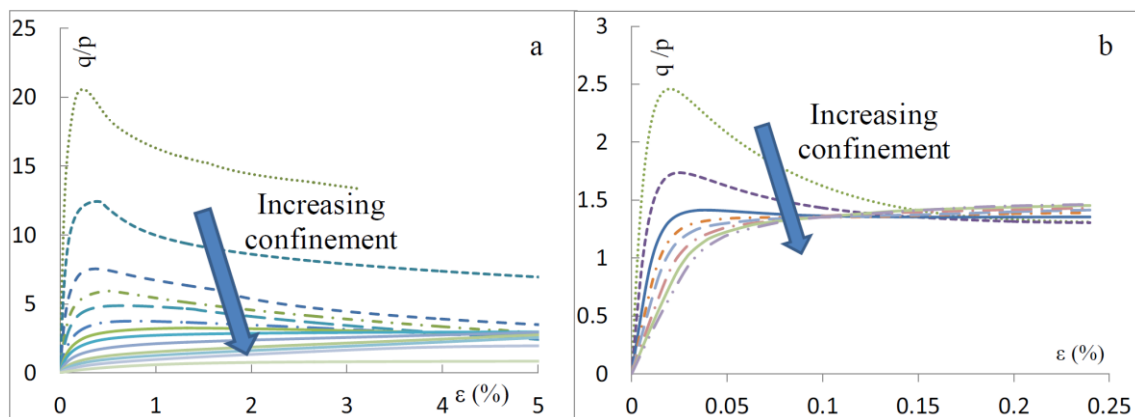


Figure 3.3 Stress-strain behavior for confined compression (a) and tension (b) in terms of the deviatoric to mean stress ( $q/p$ ) ratio and applied axial strain

It is also noteworthy that with increasing confinement, the lateral strains become smaller. Under small confining pressures, the lateral strains tend to be particularly large in the post-peak regime. The lateral strains influence the volume change behavior of these materials. Figure 3.4 plots the volumetric strain versus the applied vertical strain for both compressive and tensile tests under different confinement levels. It can be seen that under low confinement for compressive loading, the volumetric strain is compressive (negative) in the pre-peak regime, but as loading proceeds, becomes dilative (positive) in the post-peak regime. Under high confining pressures the volumetric strain always remains compressive. For tensile loading, the volumetric strain is always dilative; however, with increasing confinement, the volumetric strain becomes increasingly smaller.

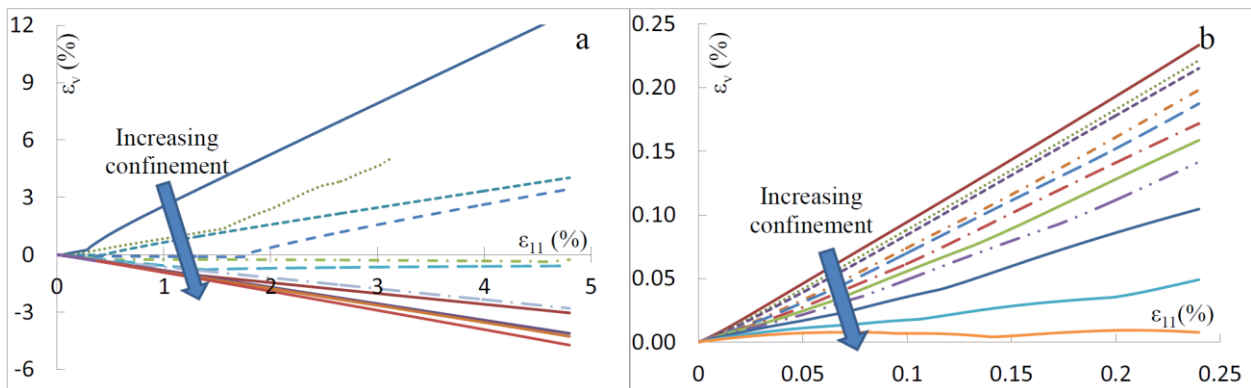


Figure 3.4 -Evolution of volumetric strain with loading for both confined compression (a) and tension (b) at different confinement levels. Initial compression followed by dilation can be seen for confined compression tests at low confinement

To illustrate the model capability of replicating the observed behavior, the failure behavior of the simulations is plotted in deviatoric stress,  $q = \sigma_{11} - \sigma_{22}$ , and mean stress,  $p = \sigma_{ii} / 3$ , space. Figure 3.5 shows the loading stress-path which begin from the initial confinement and end at failure. The failure envelope is formed by connecting the end points of the stress-paths. Under compression, the failure envelope is predicted to be nonlinear with increasing confinement which agrees with

experimental observations. Further, the failure envelope has a cap signifying that the material fails by collapse under hydrostatic loading at  $p=260$  MPa.

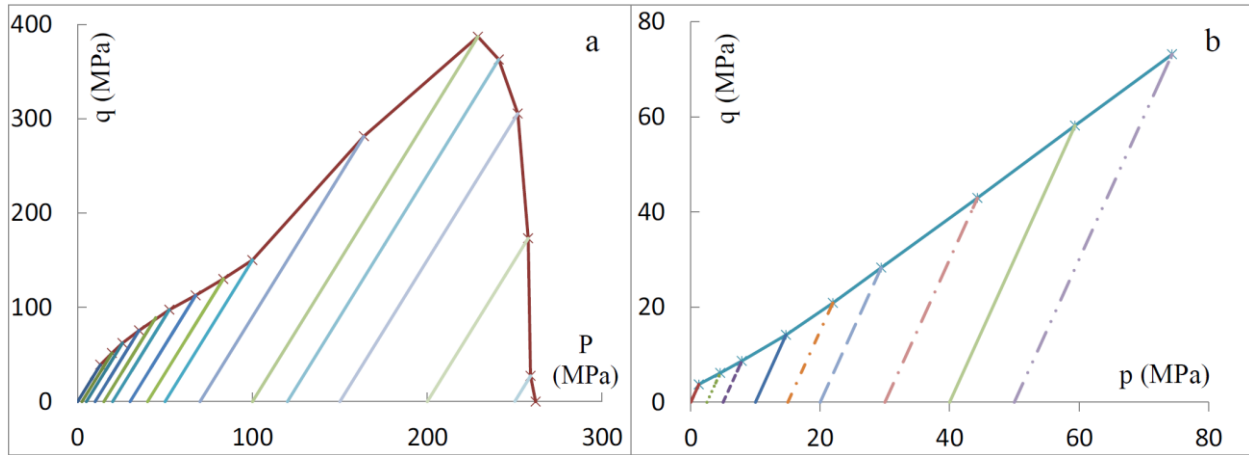


Figure 3.5 Stress paths plotted in the deviatoric stress–mean stress ( $q$ - $p$ ) space for both confined compression (a) and tension (b). The failure envelope is shown by joining the end-points of the stress paths

In Figure 3.6 and 3.7, model’s capability to describe the behavior under cyclic loading is demonstrated. The overall stress-strain curves for the cases of unconfined compressive and tensile loading are shown in panels (a) and (b) of Figures 3.6 and 3.7. Typical inter-granular normal and tangential force-displacement curves under compressive and tensile loading are shown in panels (c) and (d) of Figures 3.6 and 3.7.

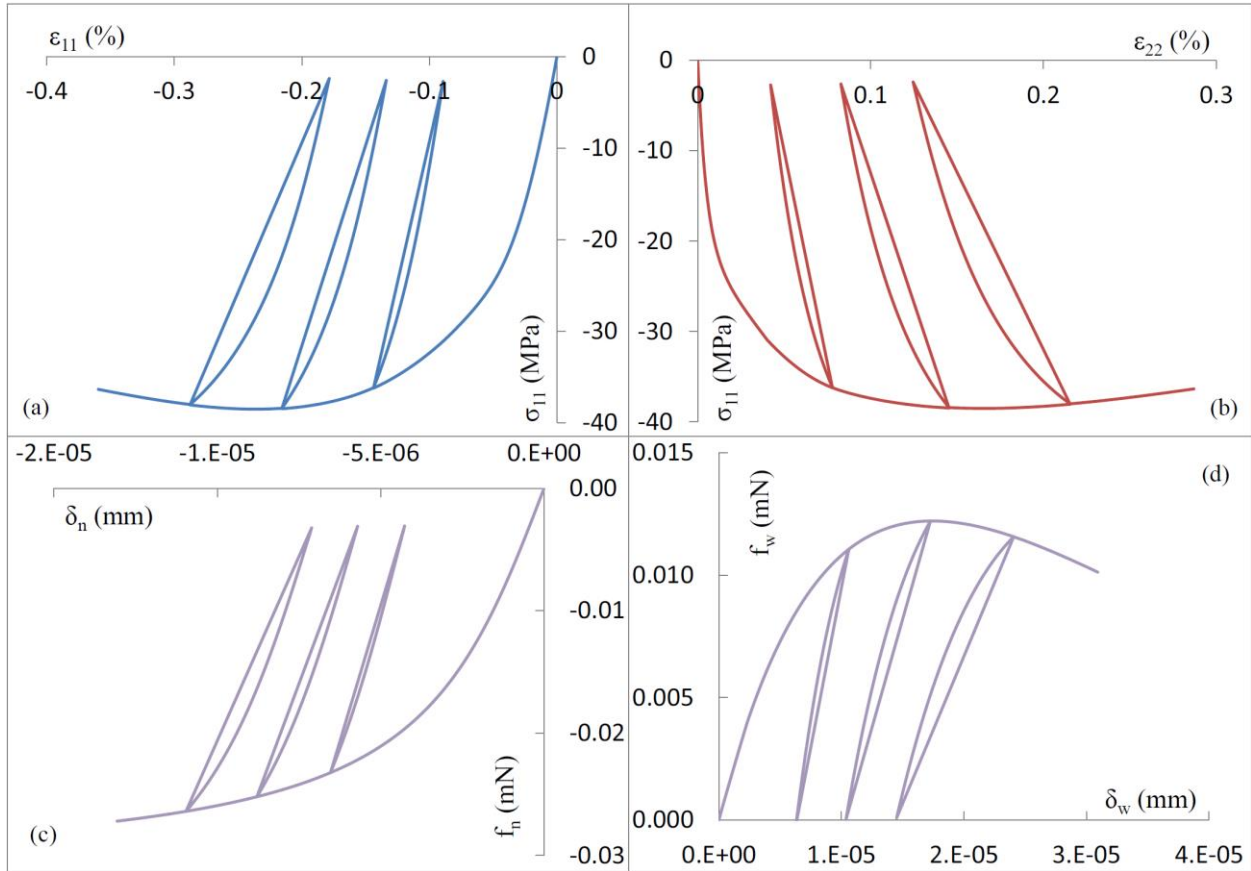


Figure 3.6 Results from unconfined compressive cyclic loading: stress-strain curves for axial (a) and lateral (b) directions, and example inter-granular force-displacement curves for the normal (c) and tangential (d) directions

In these figures, compression is shown as negative following usual convention. These results illustrate the unloading-reloading scheme for inter-granular normal and tangential force-displacement described in section 3.4 of the current chapter. It is notable that the unloading stiffness decreases as the displacement of unloading point goes higher which is a manifestation of inter-granular damage. The effect of damage is particularly significant for the cases of softening that is modeled in the inter-granular tensile and shear behavior seen from the curves of Figures 3.6d, 3.7c and 3.7d.

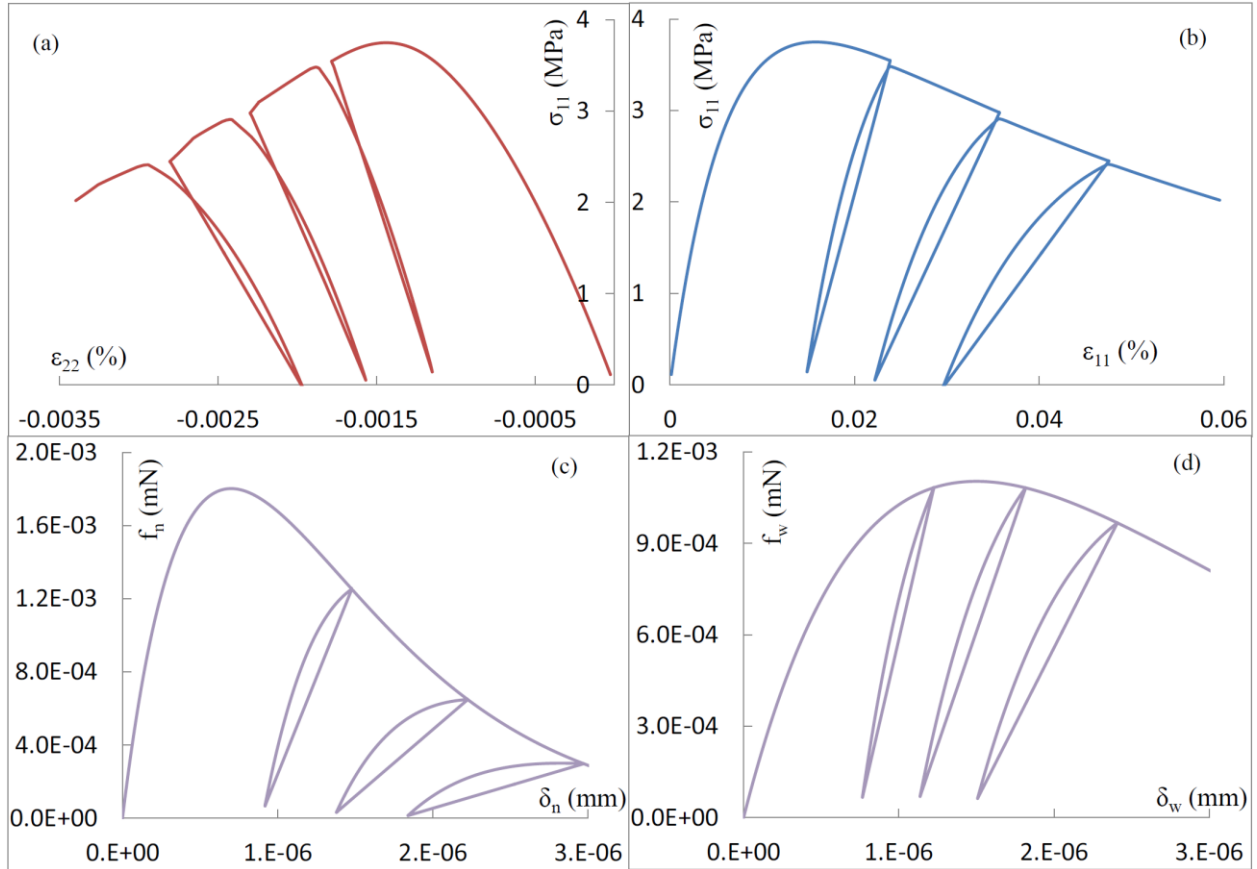


Figure 3.7 Results from unconfined tensile cyclic loading: stress-strain curves for (a) axial and (b) lateral directions, and example inter-granular force-displacement curves for the (c) normal and (d) tangential directions

It is evident from the developed constitutive relationship that the overall stress-strain behavior is determined by cooperating and competing mechanisms described by the inter-granular force-displacement relationships under the applied loading. When the applied loading is specified as a mix of stress and strain components, as in the case of confined triaxial loadings discussed above, both the inter-granular forces and displacements evolve in a complex manner. In Figures 3.8 and 3.9 the evolution of forces and displacements in different inter-granular directions is shown for the case of (1) a confined compressive loading, and (2) a confined tensile loading.

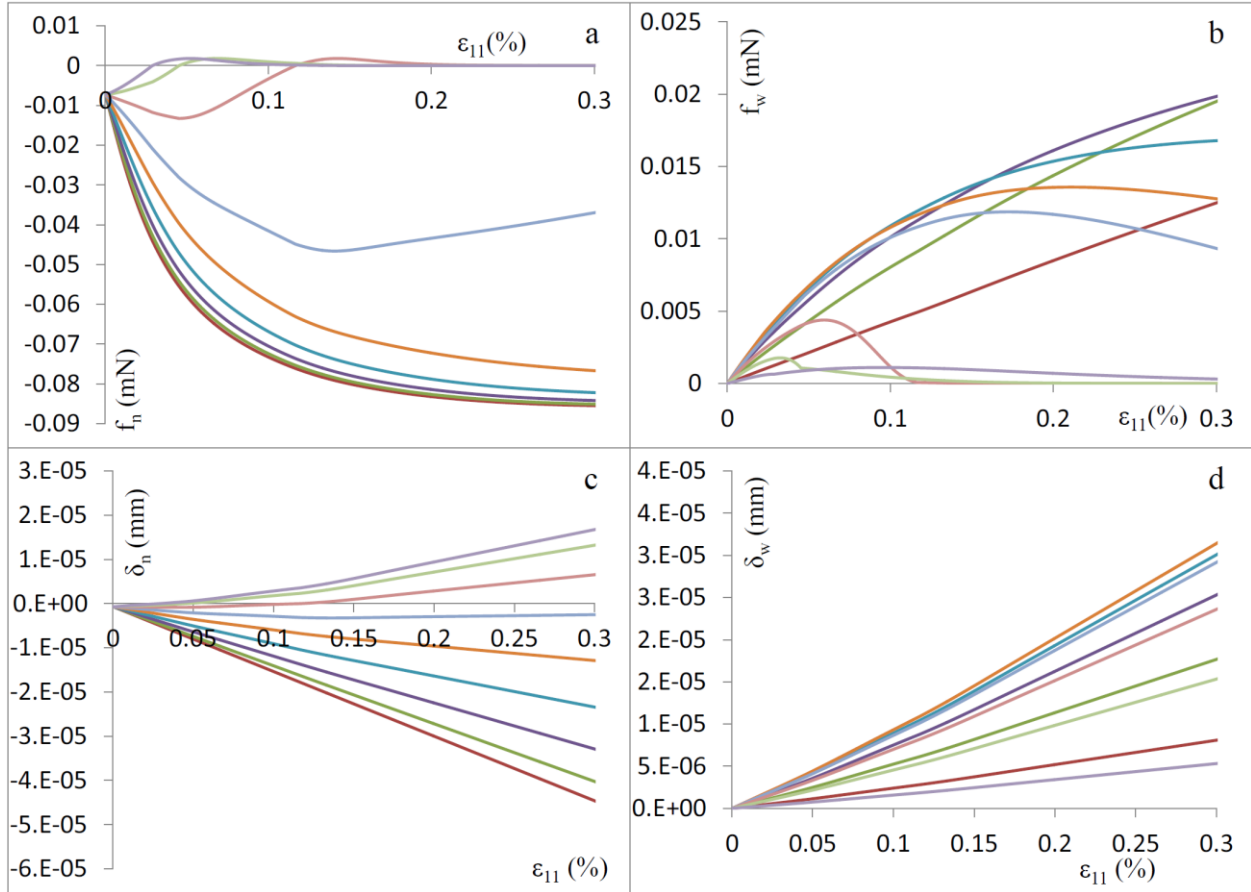


Figure 3.8 Inter-granular forces and displacements in different  $\theta$ -directions for confined compressive loading: normal force (a), tangential force (b), normal displacement (c), and tangential displacement (d). Unloading and subsequent loading in the tensile regime can be clearly seen from (a) and (c). The grain-scale mechanism of volume-change behavior can be seen from (c) as the inter-granular displacements become increasingly tensile with loading

Since the loading is axisymmetric, the inter-granular forces-displacements are independent of azimuthal angle,  $\phi$ . Thus, the curves in Figures 3.8 and 3.9 represents the force-displacement relationship for grain-pair interactions with different values of  $\theta$  and arbitrary  $\phi$ . Under hydrostatic confinement, all inter-granular interactions have equal initial compressive normal force and displacements, while the tangential forces and displacements are zero. For confined compressive loading, as the axial strain is increased, the inter-granular interactions that are oriented closer to the loading direction experience compressive loading. On the other hand, those closer to



lateral direction experience unloading and enter tensile regime, while intermediate orientations may undergo compressive loading followed by unloading and loading in tensile regime.

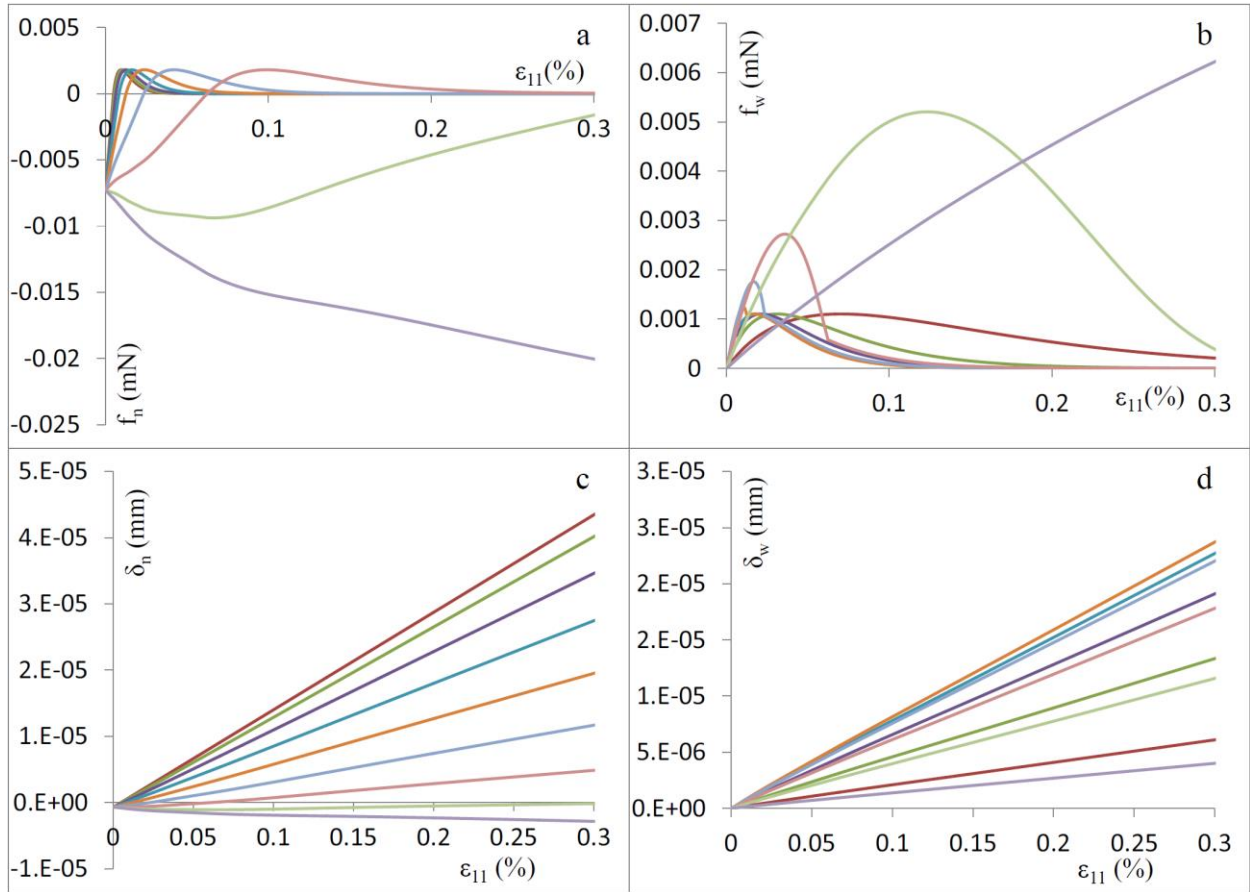


Figure 3.9 Inter-granular forces and displacements in different  $\theta$ -directions for confined tensile loading: normal force (a), tangential force (b), normal displacement (c), and tangential displacement (d). Unloading and subsequent loading in the tensile regime can be clearly seen from (a) and (c)

For confined tensile loading, the inter-granular interactions that are oriented closer to the loading direction undergo compressive unloading, then enter tensile regime and fail in tension. Orientations closer to lateral direction experience further compression and hardening. Further for both the cases of overall compressive and tensile loading, the inter-granular shear forces are higher for  $\theta = \pi/4$  orientation at the early stage of loading. However, as loading progresses, the inter-granular interactions that bear higher shear forces undergo damage and softening, resulting in a progressive crossover of orientations that are required to sustain larger forces. Moreover, the

tangential behavior is influenced by the inter-granular normal displacement. Thus, those orientations that undergo increasing compression exhibit stiffening in tangential response, while those unloading or in tensile state exhibit smaller stiffness. It is clear that as the loading proceeds, different grain-scale mechanisms contribute differently to the overall behavior of VE at various loading stages. The advantage of the developed approach is that the evolution of these mechanisms is not specified *a priori*; instead this evolution develops in response to the overall loading and the loading state of each inter-granular interaction.

### 3.6.3 Failure prediction under multi-axial loading

Failure at macro scale is usually characterized by a number of phenomena which progressively make the transition in the system from a stable continuum state into an unstable discontinuous state [81-84]. Based upon stability analyses, three general failure criteria have come to be widely accepted in continuum mechanics, 1) material instability, 2) diffuse failure, and 3) localized failure (see for example [29]). The loss of material stability or strain uncontrollability is characterized by singularity of the symmetric part of tangent stiffness matrix.

In Figure 3.10, the results of failure analysis under biaxial loading paths in which the loading is within the biaxial stress plane  $\sigma_{11}$ - $\sigma_{22}$  and  $\sigma_{33}=0$  are presented. Figure 3.10a shows the failure envelope (plotted as dashed line) for loading stress paths starting from an initially unloaded condition. The stress-strain behavior for each loading path is simulated by applying stress as follows:  $\sigma_{11}=A\cos(\gamma)$ ,  $\sigma_{22}=A\sin(\gamma)$  and  $\sigma_{33}=0$ , where  $A$  is the loading stress-level, and  $\gamma$  is the angle between the loading line in  $\sigma_{11}$ - $\sigma_{22}$  plane and the positive  $\sigma_{11}$  axis. The failure envelope is then generated by joining stress conditions for which the tangent stiffness matrix becomes singular. For

the numerical results in this work, the calculations are terminated when the determinant of the tangent stiffness matrix becomes 0.001 times the determinant of the initial tangent stiffness matrix.

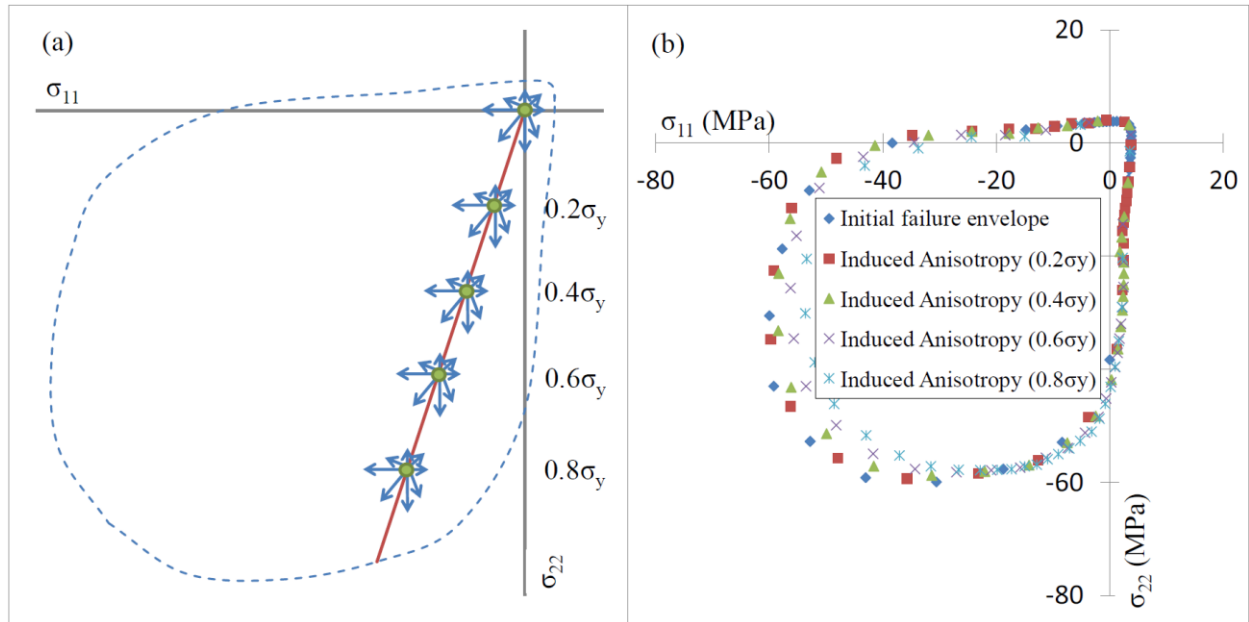


Figure 3.10 (a) Failure envelope in biaxial loading condition material loaded from initially unloaded state shown by the dashed line. Also loading-paths for two-stage loading used to illustrate the effect of induced anisotropy. (b) Failure envelopes for material that has been loaded in stage 1 along the solid line in part (a) up to one of the depicted points and then loaded in stage 2 in different directions till failure

Clearly, the simulated envelope replicates very well the experimentally observed behavior of cementitious materials. It is particularly remarkable that the model predicts the compression-tension asymmetry of the failure envelope. The asymmetry results from the force laws which are defined independently for compressive and tensile interactions, leading to fundamentally different macroscopic behavior of the material in compression and tension. A comparison with experimental data has also been presented with an earlier version of the present model derived from purely mechanistic arguments [20]. It is noteworthy, that the present work utilizes significantly revised inter-granular force-displacement relationships derived in thermomechanical framework that permit modeling of phenomena not addressed in the previous versions.

Cementitious materials modeled here are assumed to be initially isotropic, but since inter-granular interactions oriented in different directions experience different damage and plasticity at different

loading levels, as discussed in the case of axisymmetric loading, the material will exhibit anisotropic behavior (called induced anisotropy) once it has been loaded in one particular direction.

The effect of induced anisotropy is illustrated by a set of two-stage simulations. The loading process is shown in Figure 3.10a by the solid line passing through the origin. In stage 1, a proportional loading originating from unloaded state is first applied up to a prescribed load-level given as a fraction of the uniaxial compressive strength,  $\sigma_y$ . In stage 2, several different proportional loading paths that originate from the end of stage 1 are applied until failure is achieved. Figure 3.10b shows calculated failure envelopes. It is seen that the failure surface derived in this manner is different from the one derived for the material which has not experienced the initial loading. The effect of induced anisotropy can be clearly seen as the envelope no longer retains its symmetry about  $\sigma_{11}=\sigma_{22}$  line. Moreover, the effect of induced anisotropy becomes larger with the stage 1 loading-level, such that the failure stress magnitude along some stress-paths could be ~20% smaller than that of the virgin material.

In Figure 3.11, the failure behavior under triaxial loading is shown. For computing the triaxial behavior, the stress components are varied such that,  $\sigma_{11}=A\cos(\gamma)\sin(\varphi)$ ,  $\sigma_{22}=A\sin(\gamma)\sin(\varphi)$  and  $\sigma_{33}=A\cos(\varphi)$ , where  $A$  is the loading stress-level,  $\gamma$  and  $\varphi$  are constants between  $[0-2\pi]$  and  $[0-\pi]$ , respectively such that  $\sqrt{\sigma_{11}^2 + \sigma_{22}^2 + \sigma_{33}^2} = A$ . If  $\varphi=\pi/2$ , then the biaxial stress-path is recovered.

Again the failure was identified by singularity of the symmetric part of tangent stiffness matrix using the numerical criterion used for biaxial loading case. The stress state corresponding to failure is plotted as a point cloud on the stress space  $\sigma_{11}-\sigma_{22}-\sigma_{33}$  as shown in Figure 3.11, which gives 4 different views: row 1 gives the isometric view and the subsequent rows present views along z-, y- and x-axes.

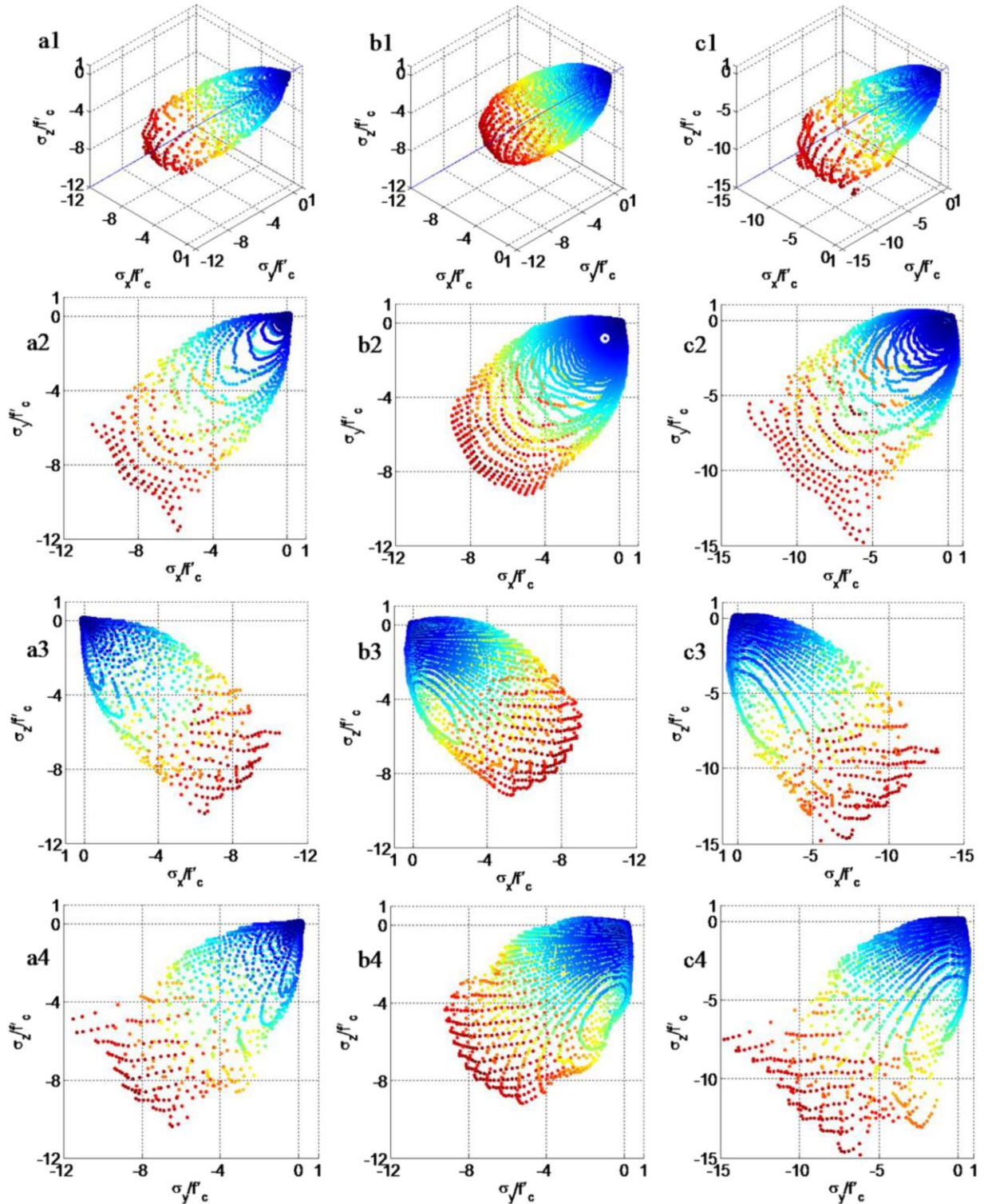


Figure 3.11 Triaxial failure envelopes for material from the unloaded stage (a1-a4), material initially loaded in compression hydrostatically up to 20 MPa (b1-b4), material initially loaded in compression biaxially up to 20 MPa (c1-c4). Different views presented are the isometric 3D view (a1-c1), top view (a2-c2), front view (a3-c3), and side view (a4-d4). Solid lines inside the isometric 3D graphs represent the normal to  $\pi$ -plane

The failure surfaces in Figure 3.11a are for material loaded from an initial unloaded state. It should also be noted that the hydrostatic compression direction reaches failure in a stress level which is significantly greater than the uniaxial compressive strength. In hydrostatic compressive loading, all inter-granular interactions are compressive in normal direction and in tangential direction there is no force or displacement. Compressive force-displacement relationship has a horizontal asymptote as it can be seen in Figure 3.1a and the asymptote happens later as the mean pressure increases.

In Figure 3.11b and 3.11c the effects of induced anisotropy caused by an initial loading is shown, by performing the loading in two stages. In the simulations leading to Figure 3.11b, the material has been initially loaded in hydrostatic compression up to  $\sigma_{11}=\sigma_{22}=\sigma_{33}=20$  MPa and then in stage 2, loaded in different directions until failure state defined previously is reached. In Figure 3.11c, the initial compressive loading is performed in biaxial plane ( $\sigma_{33}=0$ ) up to  $\sigma_{11}=\sigma_{22}=20$  MPa and then the material is loaded up to failure in different directions. The failure stress states are plotted as point clouds to represent the failure envelope. In the 3D views of the failure surfaces (Figures 3.11a1, 3.11b1, 3.11c1), the vector normal to the “ $\pi$ -plane” is also included (solid line) to facilitate visualization of the failure surface. The views of the 3D failure surface are presented in Figure 3.11 which show the effects of the anisotropy induced in the material by stage 1 loading. It is seen that the failure surface derived for the material initially loaded in hydrostatic compression (Figure 3.11b) has significantly changed in size compared to that of the virgin failure envelope (Figure 3.11a). The surface belonging to the material initially loaded in biaxial direction (Figure 3.11c) also appears to have rotated. Since the initial loading was in  $xy$  plane, the rotation is visible in Figures 3.11c3 and 3.11c4. In addition, the size of the failure envelope has increased significantly compared to the virgin failure envelope.

When the material is loaded hydrostatically in all its inter-granular contacts, regardless of their direction, only normal forces and displacement components of the same magnitude will develop and no contact will have tangential force or displacement components. It is clear that since all grain interactions are experiencing the same loading history, no anisotropy will be introduced in the material in the sense of implying different behavior in different directions. At the end of stage 1 in this type of loading, parameters defining the constitutive equations for all grain interactions have the same values and they all behave in the same manner. So the failure envelope does not rotate and only changes size because the constitutive parameters have changed compared to those of the virgin material. However, in the case of material being previously loaded biaxially, it is clear that grain interactions in different directions will undergo different force-displacement history in both normal and tangential directions. Thus at the end of loading stage 1, interactions in different directions will react differently to the next loading phase due to their different constitutive parameters. This then implies that the macroscopic behaviors in different directions will be different leading to rotation of the failure envelop seen in Figure 3.11c.

It is noteworthy, that different mechanisms lead to failure under different loading paths. The failure mechanism at the macro-scale can be investigated by considering the evolution of eigenvalues of the symmetric part of tangent stiffness matrix. The eigenvalues represent the six Kelvin deformation modes [85]. In Figure 3.12, we show the evolution of eigenvalues with loading for 4 loading paths – hydrostatic compression (Figure 3.12a), biaxial compression (Figure 3.12b), uniaxial compression (Figure 3.12c), and biaxial compression-tension (Figure 3.12d).

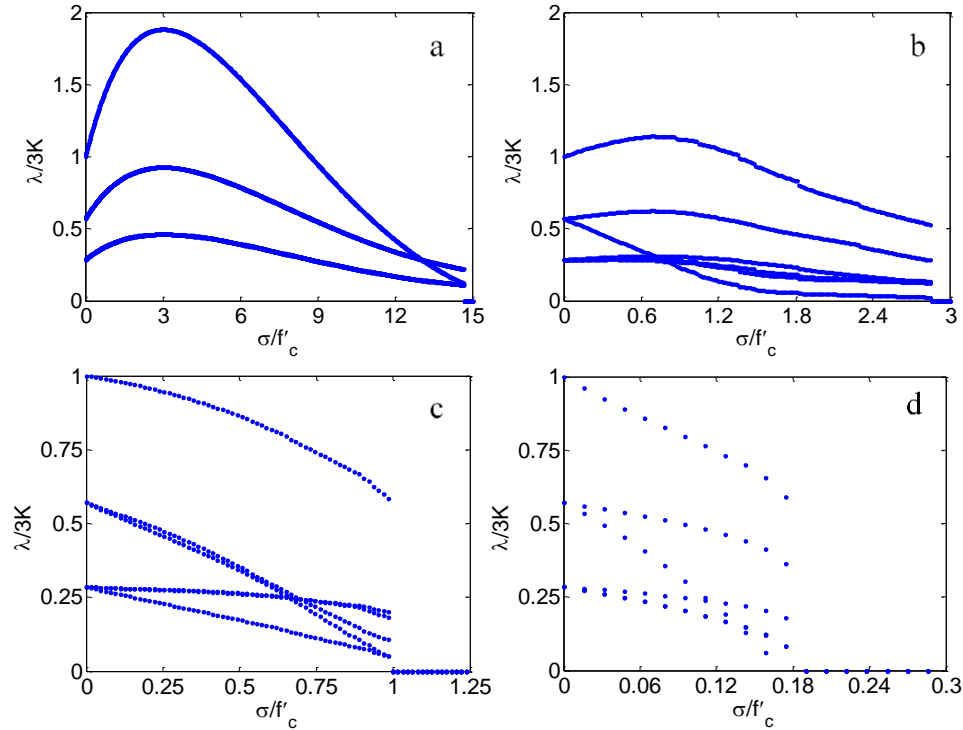


Figure 3.12 Eigenvalues of the tangent stiffness tensor for the material under hydrostatic compression (a), biaxial compression (b), uniaxial compression (c), and biaxial compression-tension (d). Eigenvalues are normalized with three times the bulk modulus. Horizontal axis is normalized with the uniaxial compressive strength showing that the failure stress under hydrostatic compression is  $\sim 14.5$  times, biaxial compression  $\sim 2.5$  times, and biaxial compression-tension  $\sim 0.2$  times of uniaxial strength, respectively

The eigenvalues have been normalized by three times the initial bulk modulus of the material (39 GPa), which is equal to the highest eigenvalue in the unloaded state. The three eigenvalues in the unloaded isotropic state represent the dilatational and shear modes in a descending order. The two shear modes are related by factor 2. In the case of hydrostatic loading (Figure 3.12a), as the loading progresses, the material isotropy is maintained such that only 3 eigenvalues are obtained and the two shear modes are related by factor 2. In this loading case, the eigenvalues first increase as the material experiences stiffening, reach a peak and then decrease till material failure which is clearly governed by the dilatational mode. In the remaining three cases of biaxial compression, uniaxial compression, and biaxial compression-tension, loading results in anisotropy, such that there are 5 distinct eigenvalues and their associated deformation modes which are combination of extension,



compaction, and shear. In these three loading cases, the failure is governed by the mode that combines extension and compaction.

It is observed from Figure 3.11 that the tensile failure strength, represented by the root mean square of failure stress, is significantly higher under isotropic loading ( $\sigma_{11}=\sigma_{22}=\sigma_{33}$ ) in comparison to that under uniaxial loading ( $\sigma_{11}\neq 0, \sigma_{22}=\sigma_{33}=0$ ). This observation as well as the predicted characteristic shape of the failure envelope in the tensile octant in Figure 3.11 and tensile quadrant of Figure 3.10 agrees with those widely reported for cementitious materials under triaxial and biaxial loading (see for example [86]).

In Figure 3.13, the stress-strain curves as well as the eigenvalues of the symmetric part of tangent stiffness matrix under hydrostatic and uniaxial tensile loading are presented. The peak stress under isotropic loading is  $\sigma_{11}=\sigma_{22}=\sigma_{33}=3\text{MPa}$ , such that the tensile strength is 5.2 MPa. In contrast, under uniaxial loading the strength is 3.4 MPa. The failure in the two cases is governed by different mechanisms as seen from the evolution of eigenvalues in Figure 3.12b and 3.12d. In the hydrostatic loading case, the behavior is exclusively governed by the inter-granular behavior in the normal direction. The grain-scale mechanism is reflected in the behavior of the eigenvalue corresponding to the dilatational mode which reaches zero and hence governs the material failure as seen from Figure 3.13d.

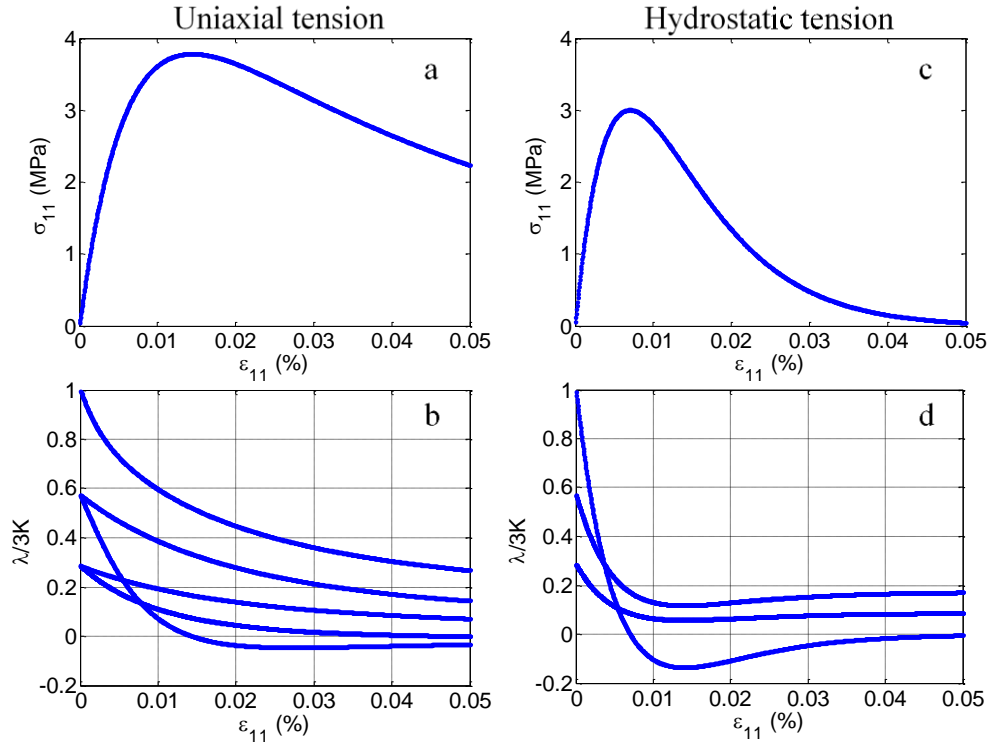


Figure 3.13 Stress-strain curves (a and c) and eigenvalues of the tangent stiffness tensor (b and d) for the uniaxial tensile loading and hydrostatic tensile loading cases, respectively

However under uniaxial tension, loading develops in both normal and tangential inter-granular directions as shown in Figure 3.14, resulting in dissipation of energy through multiple mechanisms. Thus in uniaxial loading, the material reaches failure sooner than what is indicated by Von-Mises type failure criteria. Again, the grain-scale mechanism is reflected in the behavior of the eigenvalue corresponding to the combined mode which reaches zero and hence governs the material failure as seen from Figure 3.13c.

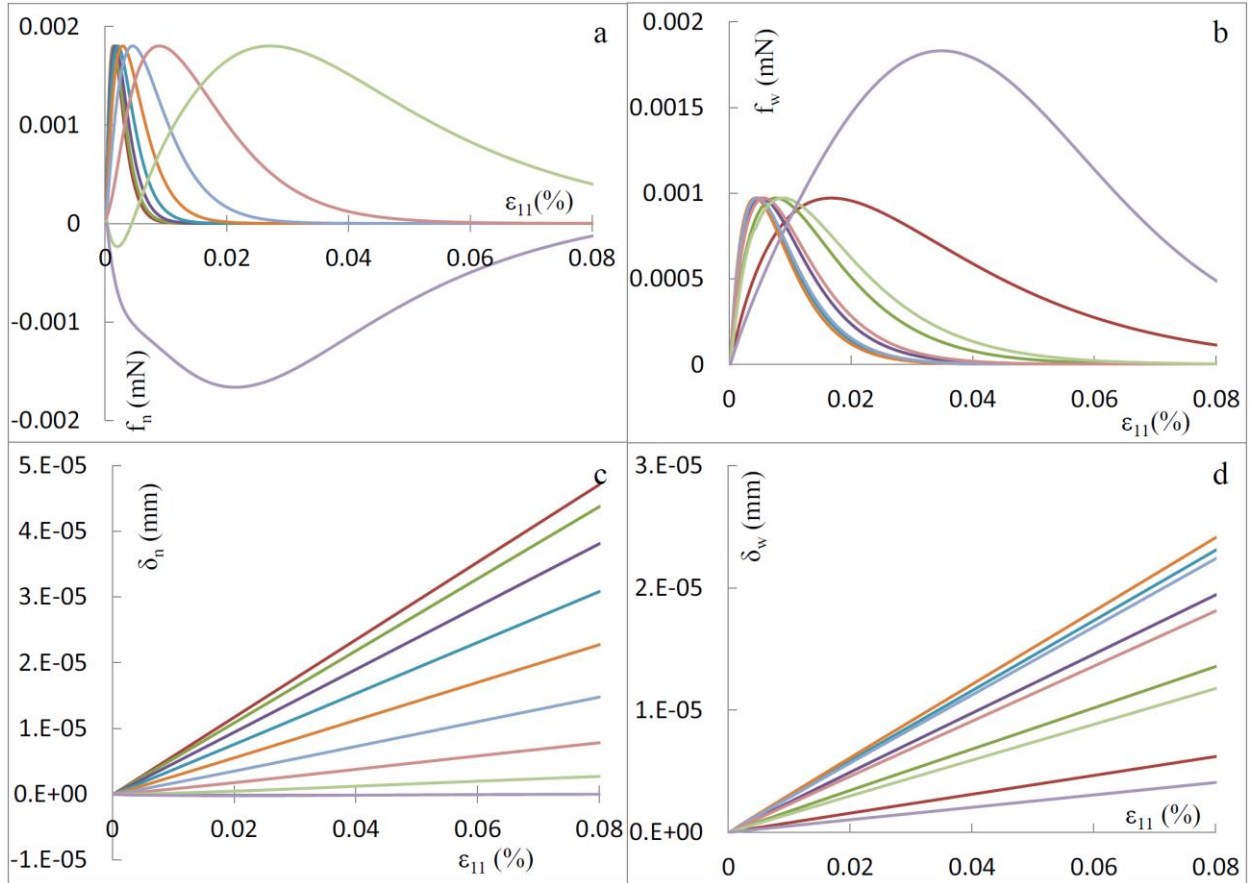


Figure 3.14 Inter-granular forces and displacements in different  $\square$ -directions for a uniaxial tensile test: existence of tangential force (b) and displacement (c) and mixed-mode nature of deformation and failure can be discerned

### 3.6.4 Behavior under strain control loading

Many laboratory tests on cementitious materials are performed by controlling the boundary displacements. The results of these tests can be simulated by assessing the stress-strain behavior under strain controlled loading. In Figure 3.15, the results from simulations of a ‘so called’ constant displacement ratio test are presented. In this simulation, two principal strains are specified with a negative constant ratio, such that  $d\epsilon_{11}/d\epsilon_{22}=\gamma$  (constant), where the axial strain,  $\epsilon_{11}$ , is compressive while the lateral strain,  $\epsilon_{22}$ , is tensile. In addition, a confining stress is maintained in the third direction, such that  $\sigma_{33}/\sigma_{11}=\text{constant}$ . Figure 3.15 plots the axial stress,  $\sigma_{11}$ ,

versus the lateral stress,  $\sigma_{22}$ , for different values of  $\gamma$  and  $\sigma_{33}/\sigma_{11}=0.1$  (note that compression is shown as positive in this plot).

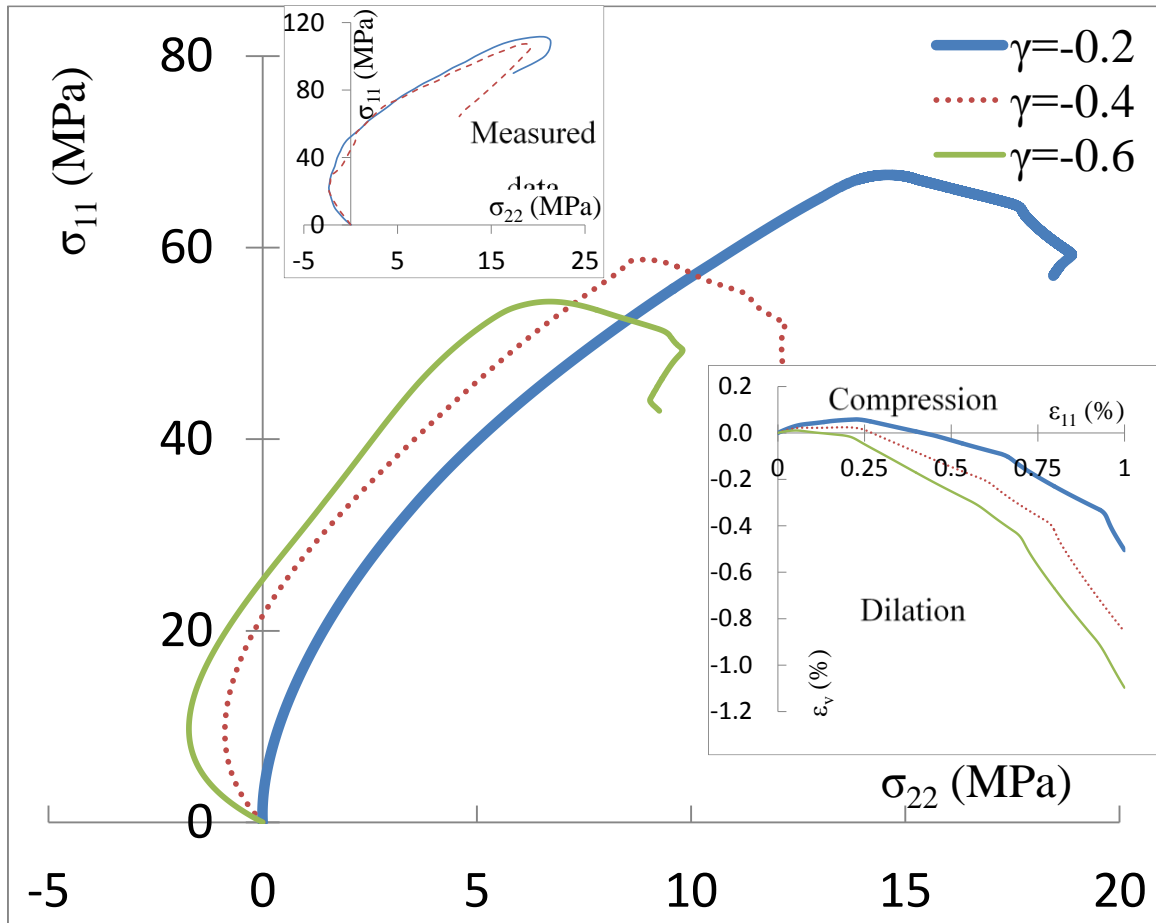


Figure 3.15 Results from simulations of constant displacement ratio tests showing the calculated stress-paths for different strain ratios,  $\gamma=d\epsilon_{11}/d\epsilon_{22}$ , and  $\sigma_{33}=0.1 \sigma_{11}$ . The bottom right inset presents the evolution of volumetric strain versus the axial strain. The top left inset presents experimental data from the literature

The simulated curves replicate the experimental observations reported by [55] and shown as top left inset in Figure 3.15. At low loading levels, the resultant stress components,  $\sigma_{11}$  and  $\sigma_{22}$ , are in the pre-peak phase. As the loading progresses, the stress component in lateral direction,  $\sigma_{22}$ , reaches a peak tensile stress, and eventually becomes compressive. At this state, all the three principal stress components are compressive. Upon further loading, the stress component in the compression direction,  $\sigma_{11}$ , reaches failure and can undergo softening leading to overall material failure. The magnitude of peak tensile stress as well as the stress state where overall failure occurs

is determined by the ratio,  $\gamma$ . This result is a clear manifestation of directionally dependent nonlinearity that evolves with loading. For  $\gamma=-0.6$ , the grain interactions whose orientations are closer to 2-direction experience larger tensile loading, such that they achieve peak forces and softening. The tensile softening in the 2-direction leads to an induced anisotropy and contributes to the overall weakening of the material.

In contrast, for  $\gamma=-0.2$ , the grain interactions whose orientations are closer to 2-direction experience low or even no (for  $\gamma=0$ ) tensile loading. In this case, the material behavior is governed primarily by compressive inter-granular behavior and the overall failure occurs at a higher loading level caused by a combination of shear and normal inter-granular failure. For some intermediate values of  $\gamma$ , the grain interactions whose orientations are closer to 2-direction may first experience tensile loading followed by unloading and subsequent compressive loading. Clearly, for these experiments, the tensile peak observed in the lateral stress,  $\sigma_{22}$ , is not always related to tensile failure in the 2-direction which is in contrast to conventional interpretation of these experimental results. Volume strain curves for different values of  $\gamma$  are presented also as an inset in the graph. It is seen that in all  $\gamma$  values, the overall behavior of the material is first compressive as expected. However, as the loading progresses the material experiences positive (tensile) strain in the 3-direction leading to an overall dilative response.

Figure 3.16 gives the simulated results for the volume control tests. In this simulation, an isotropic confining pressure is applied first. Subsequently, a completely strain control loading regime is applied on the material. Compressive strain increment is applied in the axial direction while in the two lateral directions, tensile strain increments equal to  $d\varepsilon_{22}=d\varepsilon_{33}=\alpha d\varepsilon_{11}$  are applied, where  $\alpha$  is a constant. The volumetric strain can be calculated as  $d\varepsilon_v = d\varepsilon_{ii} = d\varepsilon_{11}(1+2\alpha)$  implying constant volume in the case where  $\alpha = -0.5$ . For  $\alpha > -0.5$ , the volume change is compressive, and for  $\alpha < -$

0.5, the volume change is dilative. Figure 3.16 shows the resultant stress paths plotted in the deviatoric stress,  $q = \sigma_{11} - \sigma_{22}$ , and mean stress,  $p = \sigma_{ii}/3$ , space (compression is shown as positive).

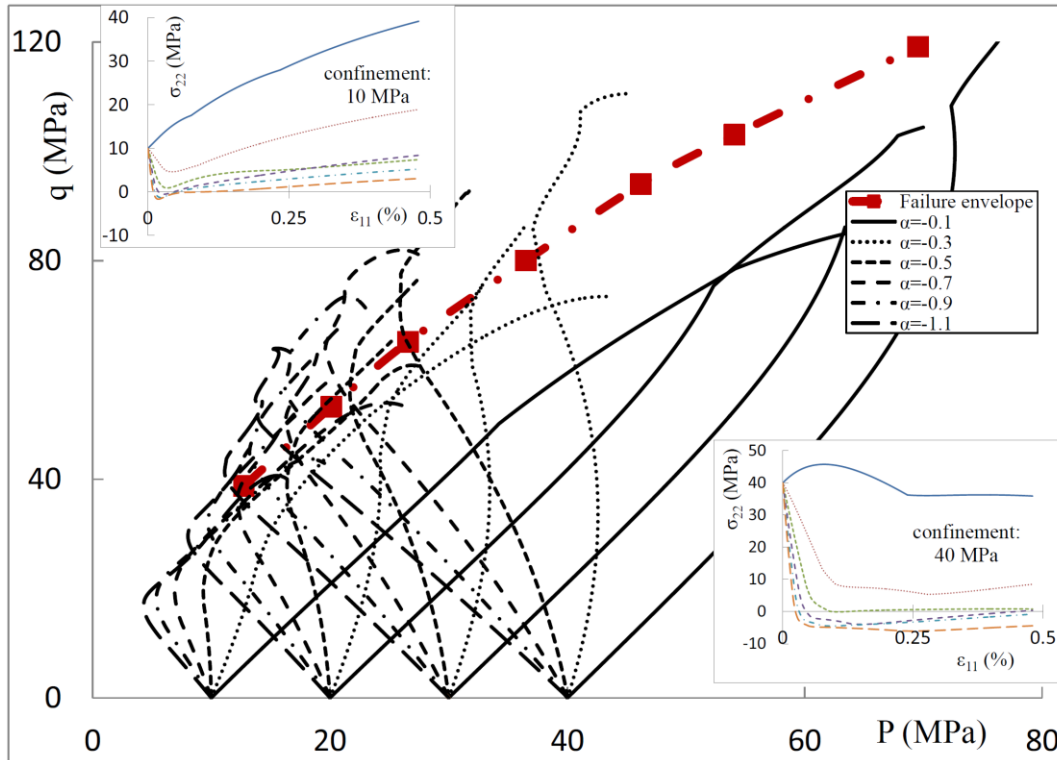


Figure 3.16 Stress paths plotted in the deviatoric stress–mean stress ( $q$ - $p$ ) space for volume control tests with different ratios,  $\alpha$ , between lateral strain and axial strain. Simulations are done for different initial confining pressures of 10, 20, 30, and 40 MPa, respectively. The thick dashed line with filled squares represents the envelope derived from Figure 6 and shows the consistency of the results of two different simulations. Change of lateral stress vs axial strain is presented in the insets for two initial confining values

The failure envelope obtained under confined loading shown in Figure 3.5 is also plotted in Figure 3.16 as dark dashed line with square dots. It is observed that the stress paths under volume controlled loading reach failure that agrees with that under confined axial loading, which is also in agreement with experimental observations of weakly cemented materials [87, 88]. It is seen that for simulation under compressive volume change ( $\alpha > -0.5$ ), the mean and the deviatoric stresses generally tend to increase up to the failure point. However for the case of large initial confinement,  $p > 30$  MPa, some softening is observed especially for the case of  $\alpha = -0.3$ .

In contrast, for simulation under dilative volume change ( $\alpha < -0.5$ ), the mean stress first decreases and then increases until failure. The stress path behavior under compressive and dilative loading is governed partly by the stress evolution in the lateral direction as the loading progresses. In the insets, we plot the lateral stress,  $\sigma_{22}$ , against the applied axial strain,  $\epsilon_{11}$ , for two initial confinements,  $p=10$  MPa and 40 MPa and different  $\alpha$  values. Except for the highly compressive case of  $\alpha=-0.1$ , the lateral stress first undergoes unloading, in some cases into tensile regime, followed by varying rates of reloading. The inter-granular orientations close to the lateral direction first unload and reach failure under tensile conditions. Thus the material is unable to sustain further lateral loads, except in the case of large initial confinement.

### 3.7 Summary and Conclusions

In this chapter a granular micromechanics model applicable to damage and plasticity of cementitious material is formulated and derived in thermomechanics framework. The resultant model is found to capture many features of the macroscopic and microscopic behavior exhibited by these materials. We observe that continuum models for materials that show damage and plasticity abound in the literature (see reviews in [89, 90] as well as some recent models that include more refined description of damage and plasticity including nonlocal effects [64, 65, 91-95]). These citations, that represent only a small subset of a vast literature base, proceed from purely continuum concepts and require *a priori* assignment of a complex set of evolution laws regarding yield criteria, plastic potentials, damage and hardening functions, that have to be phenomenologically motivated. In the absence of adequate experimental results the formulation of such evolution laws becomes rather daunting. The advantage of the presented approach is that

it uses simple scalar functions defined for interactions of two neighboring grains. Thus, the macroscopic response is obtained as integration of the responses of inter-granular pair interactions in all different directions, whereby the material's microstructure and the corresponding micromechanical characteristics are inherently included in the macroscopic behavior. Furthermore, the derived model can be used to describe behavior of different material systems that possess granular characteristics by specifying two scalar functions at the grain-pair interaction, namely the free energy function and the dissipation potential function.

Using the dissipation potential and free energy functions along with the macroscopic thermodynamic constraints, a Clausius-Duhem type inequality applicable to grain-pair interaction was found. The inequality was applied to find inter-granular constitutive equations that incorporate damage and plasticity, and include unified loading-unloading-reloading criteria at the grain-scale. The derived model was then particularized to simulate cementitious materials' behavior. Microscopic constitutive equations and their corresponding parameters were defined such that the resulting overall macroscopic response is compatible with the known behavior of the material under consideration. For this purpose, following the previous efforts on modeling these materials using granular micromechanics, modifications to inter-granular constitutive equations were made. By using appropriate choices of the grain-scale damage functions and the parameters of the microscopic constitutive equations, compressive-tensile asymmetry in macroscopic behavior was ensured. In the normal direction the stiffness coefficient was taken to be dependent on mean stress to model the effect of stiffening under compression. In the tangential direction, the damage functions were formulated to be dependent upon both tangential and normal displacements, and the mean pressures thus incorporating the effects of friction and confinement on shear behavior.



The model parameters were calibrated by fitting the experimental data corresponding to conventional triaxial test results. The simulations were performed for axisymmetric triaxial loadings with different confining pressures, biaxial loading, confined cyclic loading, confined volume control loading, and constant displacement ratio tests. The results were seen to agree very well with the available experimental data in the literature. Notably, the model provides insight to the grain-scale behavior within a continuum material point responsible for different macroscopic features of the material. By observing the evolution of inter-granular forces and displacements the mechanisms that govern the experimentally observed phenomena are explained. Detailed analyses are performed to understand the relationship between grain-scale mechanisms and macro-scale behavior of volume change, softening, and failure behavior under different multi-axial loading conditions. These reveal interesting correspondence between microscopic inter-granular mechanisms and what is observed in macro-scale behavior of the material.

## 4 FAILURE, AS A FUNCTION OF LOADING PATH AND EFFECT OF INTERMEDIATE PRINCIPAL STRESS

In this chapter, the nonlinear damage-plasticity model derived in Chapter 3, in the context of granular micromechanics approach, has been applied for studying failure of cementitious and rock-like materials. Inspired by the results of simple loading scenarios in both two- and three-dimensions, (see Figures 3.10 and 3.11), the author decided to study the complex phenomenon of failure more in depth.

The work in this chapter is focused upon different failure criteria that are in use as well as study of the different mechanisms involved in load-bearing and failure. This work is currently under review in International Journal of Solids and Structures [96].

### 4.1 Introduction

Failure and instability are key interrelated phenomena that govern the mechanical behavior of material and structural systems [81, 97, 98]. Failure is most appropriately described as a sequence of events which progressively take the material from the initial stable state into an unstable and discontinuous state [99, 100]. The essential feature of a material system at failure stage is that it cannot continue bearing further external load which is often characterized by its inability to sustain higher stress (i.e.  $\dot{\sigma}_{ij} = 0$ ). Consequently, the failure criterion may be defined as  $\lambda_{\min}(C_{ijkl}) = 0$  where  $\lambda$  is the eigenvalue and  $C_{ijkl}$  is the tangent stiffness tensor. However, in practice, material

failure criteria are seldom specified in this form. In some case, material failure criteria are defined in terms of displacement, displacement gradient, strain or invariants of strain tensor [101]. Such criteria, which in the most general case can be written as  $F(\varepsilon_{ij})=0$ , have the practical advantage that strains can be conveniently measured during loading. Strain/elongation based failure criteria was stated as early as the 17<sup>th</sup> century by Mariotto [102] and similar criteria was advanced by Saint Venant [103]. In this type of model, it is assumed that the material fails when the maximum strain reaches the value of strain and yield point in simple shear test. Failure criteria are also written in terms of energy, that is  $F(\sigma_{ij}\varepsilon_{ij})=0$ , such as those of maximum strain energy or maximum distortional energy [104]. But most commonly, failure criteria are described as a general function of the stress tensor acting on the material, which in its most general case can be written as  $F(\sigma_{ij})=0$ .

The general form of failure criteria as a function of the stress tensor can be visualized as a surface in the 3-dimensional (3D) stress space where the coordinate axes represent the three components of principal stress. For many geomaterials, failure has been observed to often occur along planes. Thus, some classical failure criteria have been written as functions of the normal and tangential components of the stress acting on that specific plane. In these cases, the failure criteria, which were initially written in 3D stress space, are usually transformed into a function in the 2D plane of normal-tangential stress. Naturally, the failure state is defined as a critical combination of normal and tangential components of stress ( $\sigma$  and  $\tau$ ) on a plane of a critical direction (such as the Mohr-Coulomb failure criteria). Defining failure in this manner, typically, results in the neglect of the intermediate component of principal stress since the maximum shear stress is a function of the maximum and minimum components of principal stress alone and is independent of the intermediate principal stress as shown in Figure 4.1 for illustration.

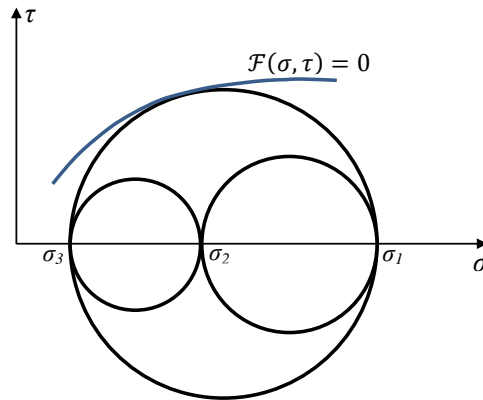


Figure 4.1 Failure criteria on normal-tangential stress plane

Conventional axisymmetric triaxial tests are ideal experiment settings for evaluating such a failure criteria and are widely used for measuring failure behavior of geomaterials [105, 106]. In these tests, which are usually performed on cylindrical samples, the specimen is first loaded hydrostatically until a desired level of confinement is reached. Subsequently, while keeping the two components of lateral stress constant, the vertical stress is increased incrementally until the desired level or the failure state. It is evident that in these experiments, during the whole loading process, the two lateral components of stress tensor are equal. Thus the minimum and intermediate components of stress tensor ( $\sigma_3$  and  $\sigma_2$  respectively) are equal during the loading process and at failure, and hence, there is no effect of intermediate principal stress. True triaxial tests for rocks and other geomaterials were developed in late 1960s and early 1970 (see for example Mogi [107-109] and [110] for a comprehensive historical account) in order specifically to illustrate the effects of intermediate principal stress. In these experiments, rectangular prismatic specimens are loaded in three orthogonal directions such that throughout the experiment the three principal stresses can vary independently and it is possible to reach failure at a state in which none of the two principal stresses are equal. The true triaxial tests show that failure stress does depend on the intermediate principal stress in contrast to the results of failure criteria in terms of stress components on the

shear failure plane [110]. In the past decade or so, Haimson and coworkers [111-113] have conducted comprehensive true triaxial tests on different rock samples demonstrating the effects of intermediate principal stress on both the failure stress state and failure direction.

Further, as it is clear from the expression  $F(\sigma_{ij})=0$ , even the most general form of failure criteria presented in terms of stress tensor neglects the effect of loading path. Using such criteria, failure is defined as a function of the stress state. But it is well known that failure is the cumulative effect of the loading process through which the material transforms from a continuous state to an unstable state. Since the response of a material to loading depends upon the loading-path, as noticed experimentally for different materials [114-116], failure stress should also be a function of the loading-path rather than stress state itself.

In this chapter, the nonlinear damage-plasticity method of granular micromechanics presented in Chapter 3 has been used to study failure of cementitious and rock-like materials. Since the grain-pairs oriented in various directions experience their own unique loading history, the failure stress state depends upon all components of stress tensor. Similarly, the orientation of the failure plane also depends on the collective responses of grain-pair interactions. In addition, since the micro-scale contact force laws are nonlinear, the material's overall response is highly loading path dependent as the grain-pair interactions in various directions experience unique loading histories. During a loading path, grain-pairs oriented in various directions can be in different loading stages including initial loading, hardening, softening, and unloading, or reloading stages. As a consequence, the response of the material at any loading stage is not only a function of the stress state at that point, but is a function also of the loading path reaching to that stress state.

## 4.2 Loading procedures

The derived granular micromechanics model (See Chapter 3) is used to demonstrate the effect of (1) intermediate principal stress, and (2) loading path on the failure stress state and failure plane orientation in cementitious materials. Two different types of triaxial loading paths (denoted here as Type 1 and Type 2) have been simulated in order to illustrate the aforementioned effects (shown in Figure 4.2). Loading of Type 1 has been previously used in rock mechanics [110, 112] to illustrate the effect of intermediate principal stress on failure state. In this loading process, as seen in Figure 4.2a, the material is initially loaded hydrostatically in compression until a prescribed confinement level is reached. One of the stress components,  $\sigma_3$ , is then kept constant and the other two increased further to a prescribed level. The intermediate principal stress,  $\sigma_2$ , is then kept constant at this prescribed level while the major principal stress,  $\sigma_1$ , is increased until failure is reached. Note that all these loadings are performed in linear fashion and with identical loading increments for all components of stress. It is clear that in this type of loading, stress components at failure point are ordered as  $\sigma_3 = \sigma_{conf} \leq \sigma_2 \leq \sigma_1$ . In this study, the material response have been simulated for different levels of confining stress ( $\sigma_3 = \sigma_{conf}$ ) as in the physical experiments. Further, for every confining stress ( $\sigma_3 = \sigma_{conf}$ ) value, the simulations have been performed for different levels of intermediate principal stress,  $\sigma_2$ .

To evaluate the loading-path dependency of material response, an alternative loading sequence, denoted as Type 2, was simulated. In this alternative loading sequence, depicted in Figure 4.2b, all the three principal stress components are monotonically increased but with different values of stress increments for the three principal stresses. The increment sizes are defined by dividing the failure stress states computed for each simulation in Type 1 loading by the desired number of

increments. The expectation is that in this way the three stress components will increase monotonically towards the Type 1 loading failure stress state. The intention is to investigate whether the material will fail at a different stress state than that of Type 1 loading path. As seen in Figure 4.2, a key aspect of Type 2 loading is the absence the initial hydrostatic confinement which is applied in Type 1 loading.

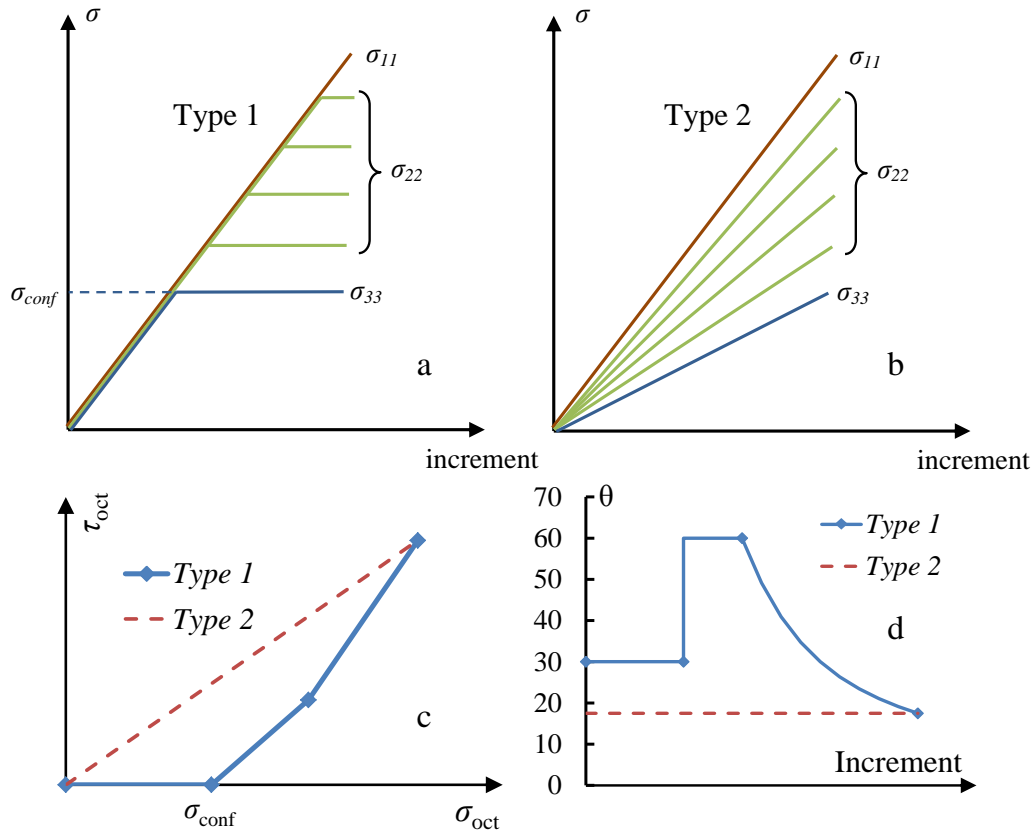


Figure 4.2 Schematic of the applied principal stress components for (a) Type 1 and (b) Type 2 loading paths. Schematic representations of: (c) the two types of loading paths in the octahedral plane, and (d) the evolution of Lode angle during the loading paths

The difference between the two types of loading is best seen in the octahedral stress space shown in Figure 4.2c. In loading of Type 1, during the hydrostatic phase of loading, octahedral shear stress remains zero and only the octahedral normal stress is increasing. Subsequently, the octahedral shear stress increases as the minor principal stress is held constant, and once the intermediate principal stress is also held constant, the rate of octahedral shear stress increase

becomes larger. In contrast, for Type 2 loading, both shear and normal components of octahedral stress increase monotonically with a constant slope during the entire loading procedure. In Figure 4.2d the evolution of Lode angle [117] during the loading process for the two loading Types is presented. Lode angle is shown, experimentally to be an important parameter in defining failure [118-121] and failure models for incorporating its effect on failure stress state have been proposed (see for example [122, 123]). It is seen in Figure 4.2d that in loading of Type 1, Lode angle is equal to  $(30^\circ)$  during the whole hydrostatic confinement process. Immediately after confinement, it reaches the value of  $60^\circ$  and remains constant during the loading phase in which the intermediate principal stress is increased. During the final part of the loading in which both the minor and the intermediate principal stresses are constant, the Lode angle decreases to a final value determined by the failure stress state. On the other hand, in loading of Type 2, the value of Lode angle is constant during the whole loading procedure and is equal to the final value of Lode angle from Type 1.

## 4.3 Results and Discussion

### 4.3.1 Failure in loadings of Type 1 and Type 2

For the stress-controlled loading paths, it is expedient to consider the *diffuse* failure defined as the stress state at which the rate of stress increase vanishes. This failure state corresponds to singular tangent stiffness matrix. In Figures 4.3a and 4.3b, the maximum principal stress,  $\sigma_1$ , at failure is shown (vertical axis) versus the intermediate principal stress,  $\sigma_2$  (horizontal axis), for the two loading types, respectively. Different curves in the graphs belong to tests with different values of minimum principal stress,  $\sigma_3$ . The furthest left point of each curve in both Figures 4.3a and 4.3b belong to the conventional triaxial tests in which the intermediate and the minor principal stresses



are equal ( $\sigma_2 = \sigma_3$ ). Thus by joining the aforementioned points, the failure surfaces for the conventional triaxial compression tests are obtained and is shown in thick solid line indicated by  $\sigma_{22} = \sigma_{33}$ . The furthest right point of each curve belong to cases in which the intermediate principal stress,  $\sigma_2$ , is equal to the maximum principal stress,  $\sigma_1$ . These points are joined by the dashed lines and indicated by  $\sigma_{11} = \sigma_{22}$  in Figure 4.3. It is clear that the two thick solid lines (representing failure in  $\sigma_{22} = \sigma_{33}$ ) and also the dashed lines (representing failure in  $\sigma_{11} = \sigma_{22}$ ) are very different for the two different loading types.

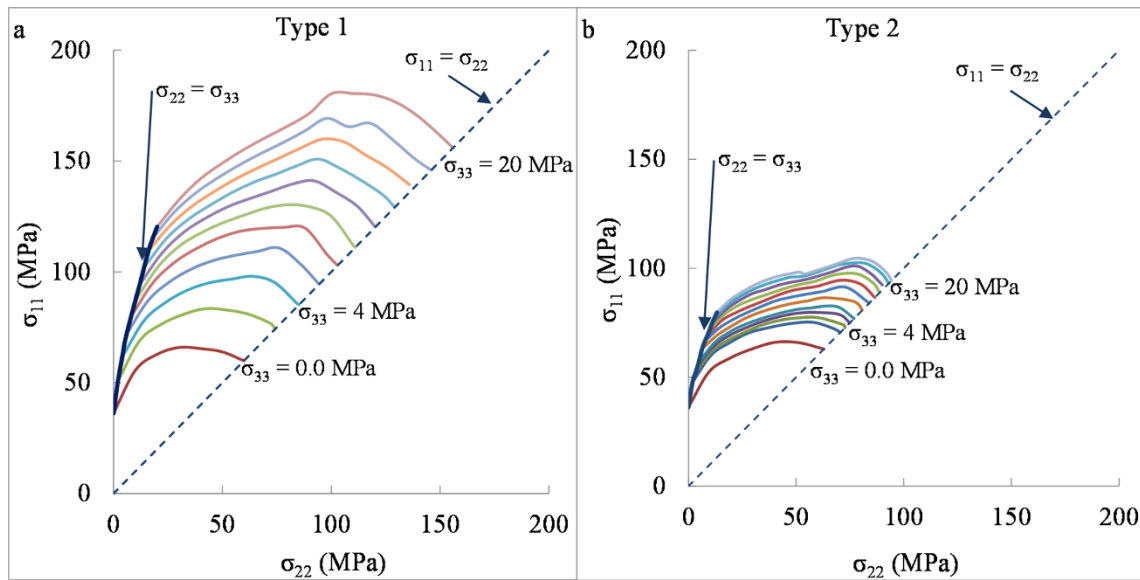


Figure 4.3 Maximum principal stress,  $\sigma_{11}$ , at failure versus intermediate principal stress,  $\sigma_{22}$ , for different values of minimum principal stress,  $\sigma_{33}$ , in loadings of (a) Type 1 and (b) Type 2

As expected, increasing level of minimum principal stress leads to a higher failure stress for both loading types. However more importantly, for a given minimum principal stress it is seen that the failure stress depends upon the intermediate principal stress as seen from the behavior of each curve separately. For both loading types, the maximum principal stress at failure ( $\sigma_1$ , shown in vertical axis) initially increases by increasing the intermediate principal stress ( $\sigma_2$ , shown in horizontal axis) up to a peak value and then decreases. It is also noteworthy that the results in

Figure 4.3a are consistent with those given in [107, 112] and summarized in [110] from other investigations. The predicted behavior is, needless to say, at stark variance with many traditional failure criteria, such as traditional Mohr-Coulomb, for which all these loading paths would lead to failure at the same value of  $\sigma_I$  since the intermediate principal stress does not affect the normal and tangential stress components on the failure plane.

The effect of initial confining stress on the failure state and path dependent nature of material behavior is clearly demonstrated by comparing the results from the simulations for Type 1 and Type 2 loadings. The failure stresses derived in Type 1 loading path are significantly higher than those in Type 2. The clear difference in the ability of the material to sustain loads is attributed to the difference in the loading-paths. While it is apparent that failure criteria that ignore the effect of intermediate principal stress cannot adequately predict the failure behavior, it is also evident, from these results, that even the most general form of failure criteria defined in terms of stress tensor  $F(\sigma_{ij})=0$  will not be able to sufficiently describe failure behavior of the material. A successful failure criterion needs to consider the stress-path rather than only the stress state and failure criteria that need to evolve with loading path need to be conceived. The predicted effect of loading path is significant as the relative difference between failure-stresses derived from the two paths can reach up to 50%. Failure states for both the loading types in octahedral stress space are also presented in Figure 4.4. As it was clearly seen from Figure 4.2c, in both loading paths the normal component of octahedral stress increases during the loading process. But the evolution of tangential octahedral stress is qualitatively different in the two loading types. In Type 2 loading, immediately with the start of loading process tangential component of octahedral stress begins to increase. In contrast, in loading of Type 1 during the hydrostatic confinement, octahedral tangential stress is absent. From Figure 4.4 it is clear that at failure both components of octahedral

stress are significantly higher (up to 30%) in Type 1 loading compared to Type 2 loading. This shows that the failure criteria defined in octahedral stress space are also inadequate for predicting failure state (see for example [124]). Clearly, the application of initial confinement has the effect of shifting and enlarging the failure surface as briefly introduced in Chapter 3.

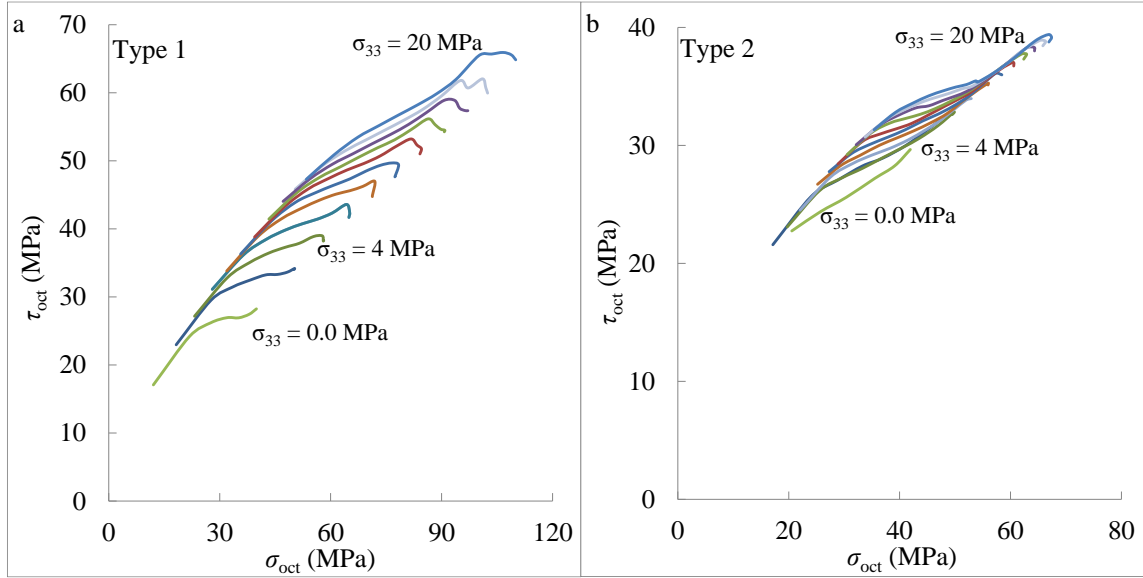


Figure 4.4 Failure stress state in octahedral plane for different values of minimum principal stress,  $\sigma_{33}$ , for the two loading types (a) Type 1 and (b) Type 2

### 4.3.2 Macro-scale failure analysis

To understand the failure behavior under different loading paths, it is useful to examine the macro-scale failure mechanisms. To illustrate the failure mechanism three loading paths corresponding to three confining stress conditions are selected for each loading type. For the Type 1 loading, three values of confining stress are considered a) unconfined case:  $\sigma_{\text{conf}} = 0.0$  MPa, b) moderately confined case:  $\sigma_{\text{conf}} = 4.0$  MPa, and c) highly confined case:  $\sigma_{\text{conf}} = 20.0$  MPa. For each of these three confining stresses, three cases of intermediate principal stress are considered as follows: 1)  $\sigma_3 = \sigma_2 < \sigma_1$ , 2)  $\sigma_3 < \sigma_2 < \sigma_1$ , and 3)  $\sigma_3 < \sigma_2 = \sigma_1$ . The resulting 9 cases are labeled a1 to a3, b1 to

b3 and c1 to c3. For comparison, the Type 2 loading paths that correspond to the failure stress conditions for these 9 cases are also studied.

The failure mechanism at the macro-scale can be investigated by considering the evolution of eigenvalues of the symmetric part of the  $6 \times 6$  tangent stiffness matrix. The eigenvalues represent the six Kelvin deformation modes [85, 125, 126]. Since the macro-scale failure is defined by singular tangent stiffness matrix, it is characterized by the vanishing of one of the eigenvalues. Figures 4.5 and 4.6 present the evolution of all the eigenvalues of the tangent stiffness matrix during loading for all the aforementioned cases until failure point is reached.

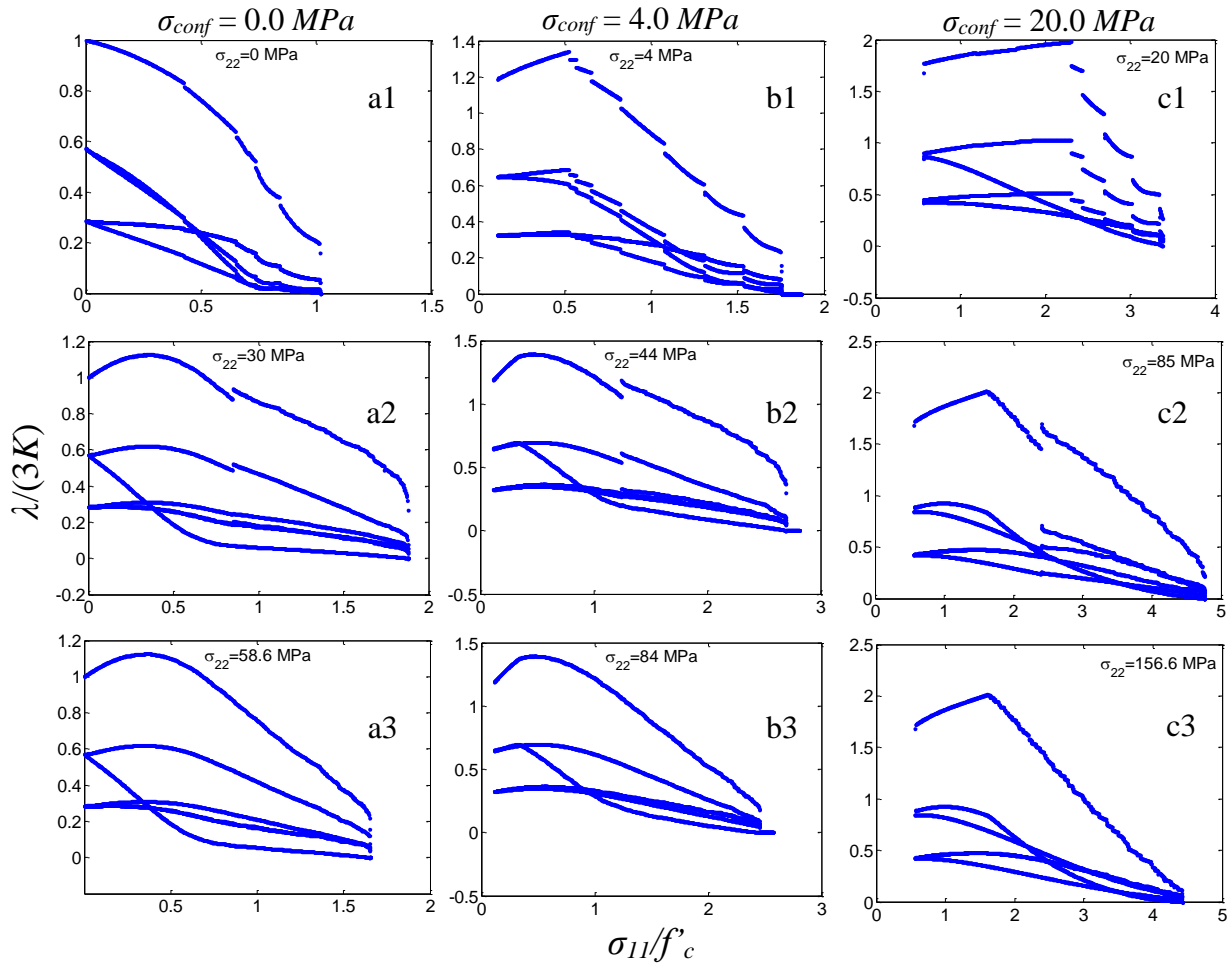


Figure 4.5 Evolution of normalized eigenvalues of the tangent stiffness tensor during the application of the 9 loading cases (a1-c3) in Type 1 loading until failure

For the numerical calculations performed here, the failure point is defined as the point at which one of the eigenvalues is equal or less than 0.001 times the corresponding eigenvalue of the initial tangent stiffness matrix.

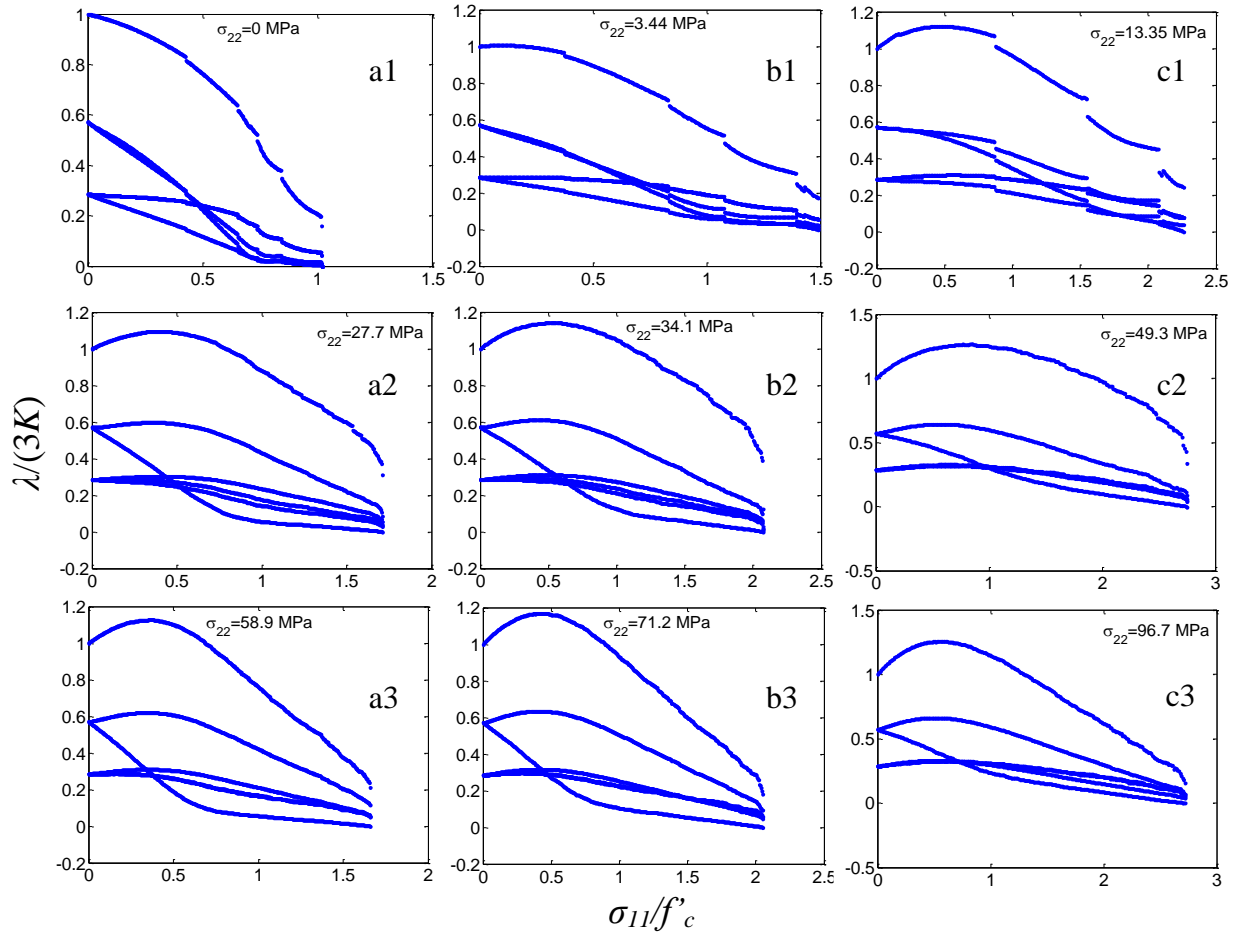


Figure 4.6 Evolution of normalized eigenvalues of the stiffness tensor during the application of the 9 loading cases (a1-c3) in Type 2 loading until failure

In Figures 4.5 and 4.6, the eigenvalues have been normalized by three times the initial bulk modulus of the material, which is same as the highest eigenvalue in the unloaded state. To further facilitate the comparisons, the maximum principal stress (shown in horizontal axis) is also normalized by the uniaxial compressive strength ( $f'_c$ ). The three eigenvalues in the unloaded isotropic state for all the cases represent the dilatational and shear modes in a descending order. The two shear modes are related by a factor of 2. For Type 1 loading, the initial maximum

normalized eigenvalues for cases b and c (Figure 4.5) are larger than 1 as the material in these two cases have been subjected initial hydrostatic loading and as a result the stiffness has increased. For Type 2 loading, in all cases, the initial maximum normalized eigenvalue of the stiffness tensor start from 1 since no initial confinement is applied on the material. As the loading progresses, the number of independent eigenvalues increase in all the cases as the material suffers loading induced anisotropy.

An examination of the graphs shows that the number of independent eigenvalues clearly depends upon the loading path. It is noteworthy that the largest eigenvalue representing the dilatational model shows an increase (except in cases a1 of Figure 4.5, and a1 and b1 of Figure 4.6) which indicates hardening due to increasing mean or octahedral normal stress and may represent an initial material volume contraction followed by volume dilation. In most cases for low confinement and small intermediate principal stress, the failure is controlled by a shear mode (see Figures 4.5a1-a3 and 4.5b1-b2, Figures 4.6a1-a3, b1-b2 and c1-c2) which tends to agree with the shear plane failure observed in laboratory tests. However, for simulations with higher confinement and intermediate principal stress, the modes tend to be mixed as almost all eigenvalues tend towards failure criterion at the same step.

### **4.3.3 Micro-scale behavior; load-bearing and failure mechanisms**

The difference in results from two loading paths is captured automatically in the method of granular micromechanics. Grain-pair interactions in different directions go through different loading histories based upon their directions and the macroscopic loading path. This accompanied by the nonlinear nature of the grain-pair interaction force laws and the possibility of loading-unloading-reloading switch, results in path dependent macroscopic response from the material. At

any point during the loading process, the state of grain-pair interaction in any direction directly depends upon its loading history. In Figure 4.7, the evolutions of normal and tangential forces (vertical axes) are presented versus the normalized value of maximum principal stress. Columns 1 and 2 present normal component of force, and columns 3 and 4 show the tangential component of force for different polar angles ( $\theta$ ) for the cases where  $\sigma_{22} = \sigma_{33}$  (cases a1, b1 and c1 for Type 1 and 2 loading paths). Since the loading is axis-symmetric in this case, the behaviors of grain-pairs oriented in different azimuthal directions ( $\phi$ ) are same. Thus only curves giving the evolution of forces in the polar angles (different  $\theta$ ) are presented.

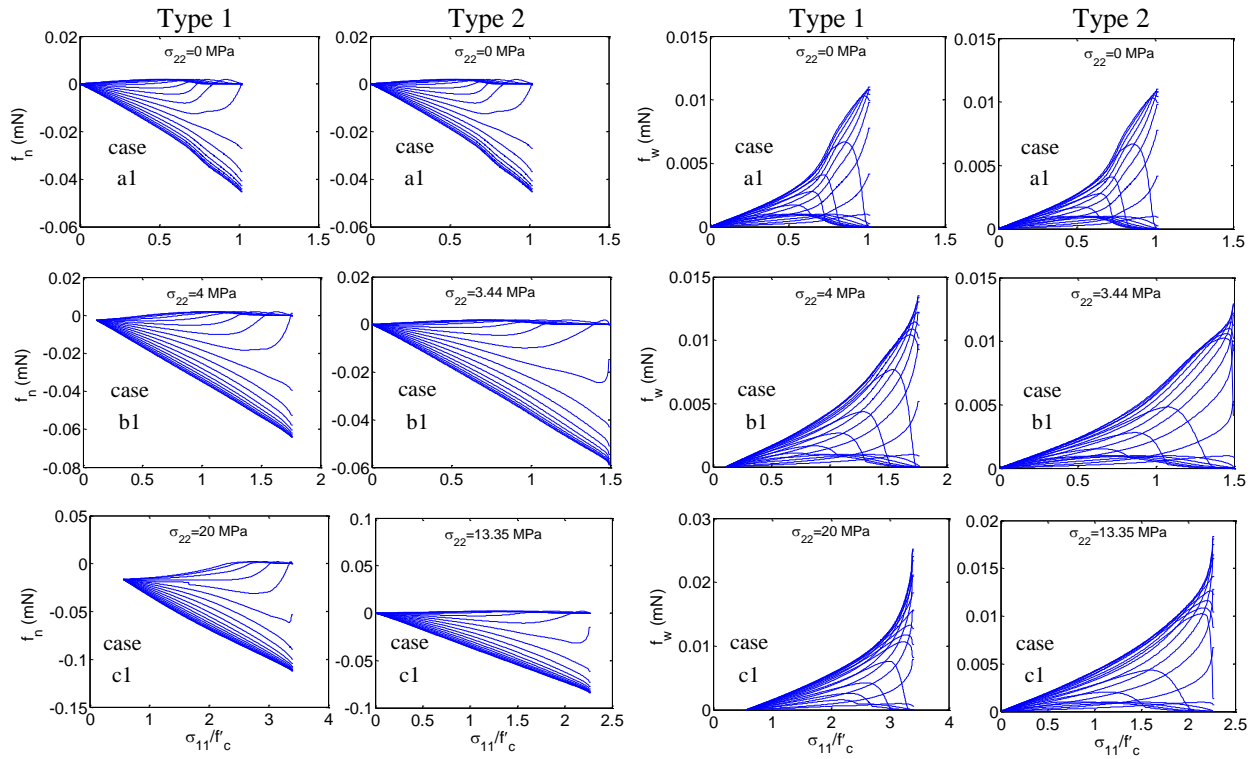


Figure 4.7 Normal and tangential components of forces for different polar angles in loadings of Type 1 (first and third columns) and Type 2 (second and fourth columns) for cases where the minimum principal stresses are 0 (case a1, first row), 4 MPa (case b1, second row), and 20 MPa (case c1, third row)

From Figure 4.7, it can be observed that for the case of zero minor principal stress (set of curves in top row) both Type 1 and 2 behaviors are identical since the initial conditions are the same. In contrast, for cases with non-zero minor principal stress, all the directions are initially under

compression for Type 1 loading, while for Type 2 loading the initial normal forces are zero. As loading progresses, the grain-pairs oriented in the direction of loading experience compression and those inclined in the direction perpendicular to loading experience unloading for Type 1 loading and tension for Type 2 loading. In addition, grain-pairs oriented in the intermediate directions which are under compression in early part of the loading, at some point, due to the macroscopic dilation, go through unloading and eventually experience tension. The effect of normal component on the tangential component of force vector can be readily seen by examining the tangential force curves. It is seen that the tangential force components for directions which are under compression are significantly higher than those of the tensile directions.

Also, the grain-pairs which are initially under compression and go through compressive unloading and finally become tensile, exhibit change of stiffness in tangential direction. For loading with non-zero minor principal stress, since all directions are initially under compression for Type 1 loading, their unloading and tensile failure in the normal direction as well as shear failure are delayed in comparison to the Type 2 loading. This difference in the micro-scale distribution and evolution of grain-pair behavior eventually results in considerably stiffer behavior with higher failure strength for Type 1 loading compared to Type 2 loading. In addition to the macroscopic strength behavior, the discontinuities observed in the eigenvalues of stiffness matrices shown in Figures 4.5 and 4.6 correspond to the tensile grain-pair failures. When the grain-pair interactions that are undergoing tension fail, they cause minor instabilities in the macroscopic response of the material which manifest as discontinuities in eigenvalues of the stiffness tensor.

Similar micro-scale analysis is performed for other loading cases (with different relative values of minimum, intermediate, and maximum principal stress components) to understand the load bearing and failure mechanisms of the material and their load path dependence. Here the evolution of



normal and tangential components of inter-granular force vectors for other cases that were simulated, which include cases a2, a3, b2, b3, c2, and c3 for both loading types 1 and 2 are described. Analysis of the evolution of force vectors for these cases is different from those for the axisymmetric cases (a1, b1, and c1). In these loading cases, the lateral components of stress tensor ( $\sigma_{22}$  and  $\sigma_{33}$ ) are not equal and thus loading is not axis-symmetric. So the behavior of grain-pair interactions in different directions inside the 2-3 plane will not be identical. For this reason, study of the behavior of grain-pair interactions in different azimuth directions is also required.

In loading of Type 1, case a2, the material is first loaded, in biaxial direction until  $\sigma_{11} = \sigma_{22} = 30$  MPa and is then loaded uniaxially in 11 direction until failure (loading path for which the eigenvalue behavior is shown in Figure 4.5.a2). Loading of Type 2, case a2, also corresponds to a loading path in which  $\sigma_{33}$  is always kept at zero while  $\sigma_{22}$  and  $\sigma_{11}$  are increasing linearly but with different increments (The evolution of eigenvalues of the stiffness tensor for this simulation is shown in Figure 4.6.a2). In Figure 4.8, the evolution of normal and tangential components of inter-granular force vectors in different directions are presented for loading of case a2, in both Type 1 and 2. Note that the grain-pair interactions for which the azimuth angle ( $\phi$ ) is  $0^\circ$ ,  $45^\circ$ , and  $90^\circ$  are chosen and shown in, the first row (Figure 4.8.a-d), the second row (Figure 4.8.e-h), and the third row (Figure 4.8.i-l) respectively. Note that the same numbering scheme is used for all figures in this section (Figure 4.8 through 4.13).

For Type 1 loading, it is seen that for the grain interactions where  $\phi = 0$  (grain-pair interactions lying on the 1-2 plane), during the loading sequence where  $\sigma_{11} = \sigma_{22}$  normal components of force are all equal and tangential components are zero. Also, these directions always remain compressive through loading and never experience any unloading or tension and thus their tangential force components are also monotonically increasing because the amount of compressive

force on them is always increasing (See Eq. 3.38 for the dependence of the tangential damage parameter on normal displacement component).

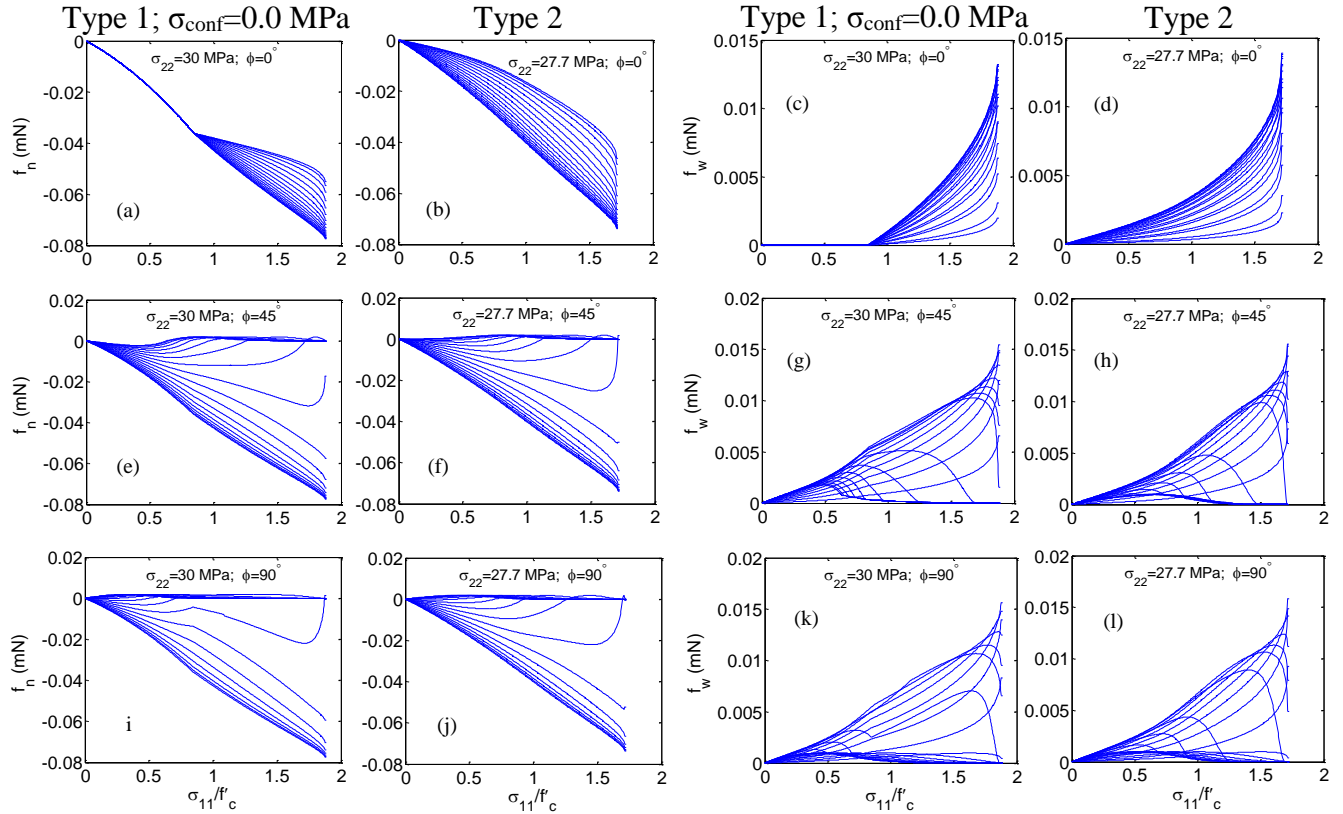


Figure 4.8 Normal and tangential components of forces for different polar angles in loadings of Type 1 and Type 2 in azimuth angles of 0, 45, and 90 degrees (first, second and third rows respectively) for  $\sigma_3=0.0$  MPa and  $\sigma_2=30$  MPa

In other azimuth directions however ( $45^\circ$  and  $90^\circ$ ), some polar angles are experiencing compressive loading and consequently high tangential forces, while other directions experience compressive unloading and even tensile loading and consequently smaller tangential force and tangential strength. In this case also, it is seen that the discontinuities present in the eigenvalues of the stiffness tensor (seen in Figure 4.5.a2 and Figure 4.6.a2) correspond to failures of the tangential contacts. It is interesting to note that the results for the two types of loading (Type 1 and 2) are just marginally different (1% difference in the failure stress is seen). This similarity in

the in the microscopic scale is reflected in the macroscopic stress conditions. For this case, neither of the two loading paths have an initial confining stage.

In loading of Type 1 and 2, case a3, the specimen is loaded biaxially ( $\sigma_1 = \sigma_2$ ) until failure is reached without any initial confinement. Note that this loading scheme is identical for both types 1 and 2. The normal and tangential components of force vector for different directions are presented in Figure 4.9.

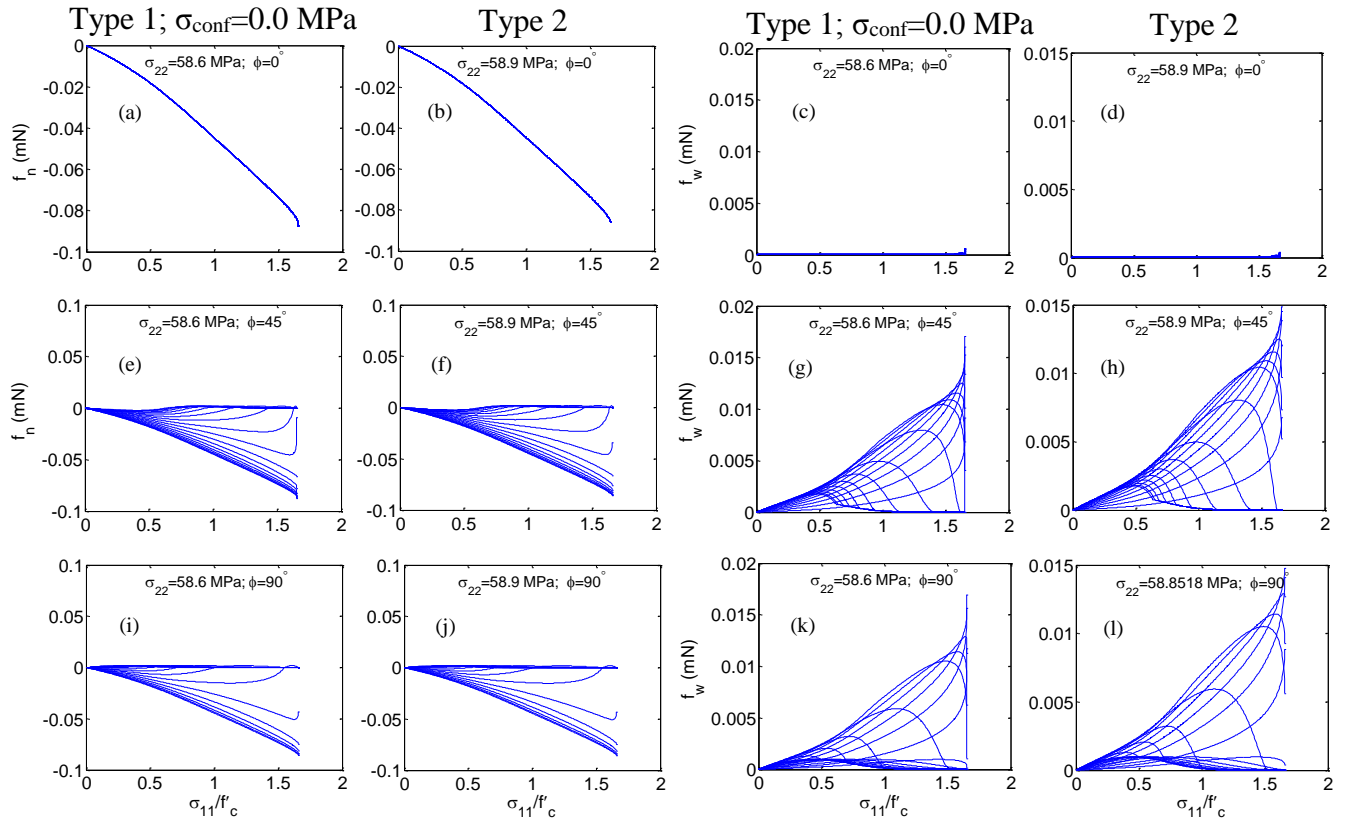


Figure 4.9 Normal and tangential components of forces for different polar angles in loadings of Type 1 and Type 2 in azimuth angles of 0, 45, and 90 degrees (first, second and third rows respectively) for  $\sigma_3=0.0$  MPa and  $\sigma_2=60$  MPa

Considering the macroscopic stress tensor in this condition, it is evident that all grain-pair interactions that lie in the  $\phi = 0$  plane will have the same amount of normal force and thus no tangential force will develop in that direction. In other azimuth directions, some polar directions are always under compression while others experience unloading and eventually tension. The

effect of this change of normal force is seen in the tangential force as well. Again, note that the discontinuities in the eigenvalues of the stiffness matrix (Figure 4.5a3 and Figure 4.6a3) coincide with the failure of tensile contacts.

Same comparison has been made for cases b and c ( $\sigma_{\text{conf}} = 4 \text{ MPa}$  and  $\sigma_{\text{conf}} = 20 \text{ MPa}$ ). Normal and tangential components of force vectors for case b2 are shown in Figure 4.10.(a), (e), (i) and Figure 4.10.(c), (j), and (k), respectively for Type 1 loading. And for the corresponding Type 2 loading the force evolution is given in Figure 4.10. (b), (f), (j) and Figure 4.10. (d), (h), and (l) respectively.

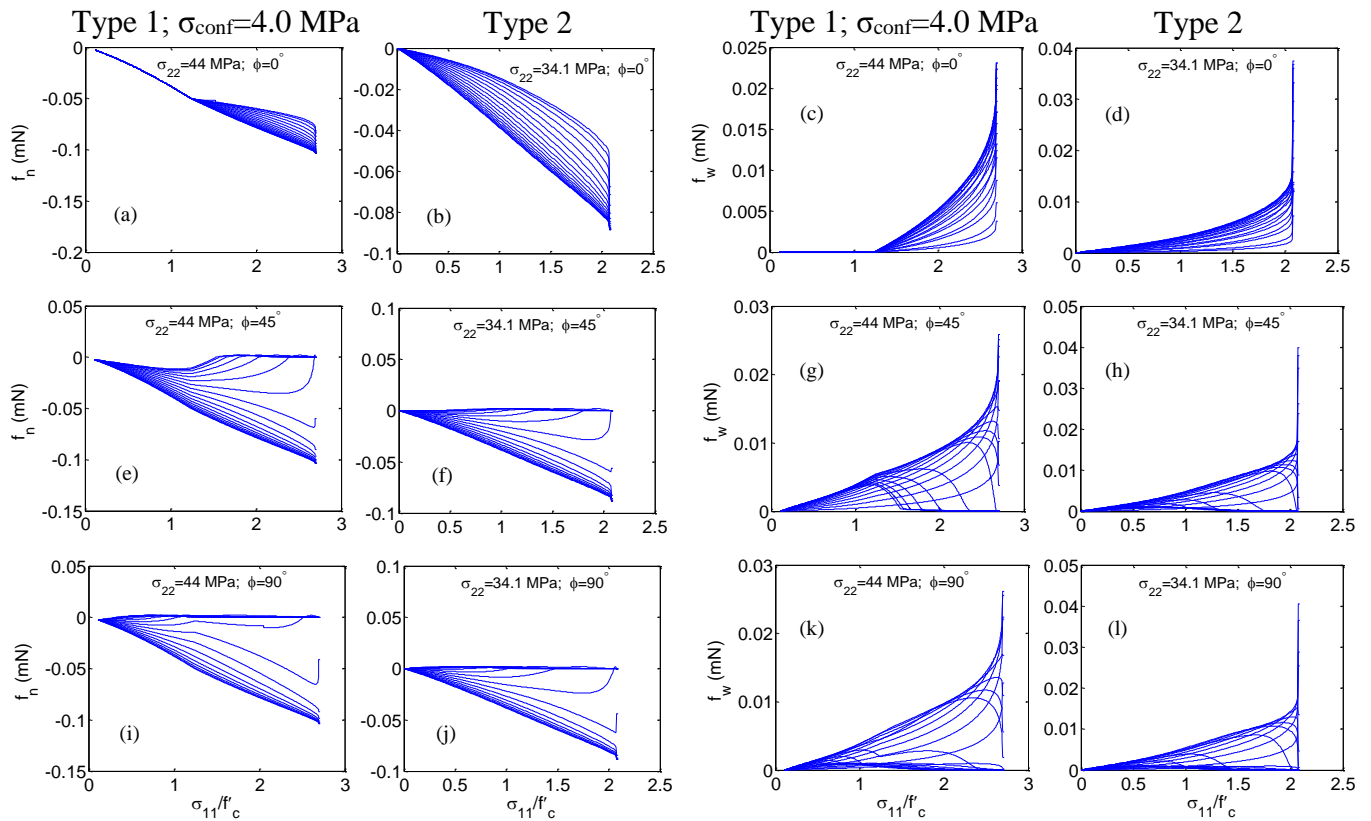


Figure 4.10 Normal and tangential components of forces for different polar angles in loadings of Type 1 and Type 2 in azimuth angles of 0, 45, and 90 degrees (first, second and third rows respectively) for  $\sigma_3=4.0 \text{ MPa}$  and  $\sigma_2=44 \text{ MPa}$

In this case, it is seen that, the results from the two loading types are significantly different. The Type 1 is characterized by an initial confinement, while for Type 2 loading there is a monotonic increase of all components of principal stress simultaneously but with different increments in different directions. This difference results in significant qualitative and quantitative differences between the microscopic responses of the material to the two loading types.

In loading of Type 1, after the initial hydrostatic pressure and during the biaxial loading, normal contacts in the directions where  $\phi = 0$  experience the same amount of normal force (biaxial loading  $\sigma_{11} = \sigma_{22}$ ) and zero tangential force. In the subsequent loading sequence, these directions always experience compressive loading and the tangential forces are always increasing. In other azimuth directions ( $\phi = 45^\circ$  and  $90^\circ$ ) however, some polar directions experience further compression and some undergo compressive unloading and eventually tensile loading and failure. In loadings of Type 2, however, no hydrostatic confinement or biaxial loading is applied. The three components of stress are always increasing and with different increments. Thus normal components of force vector in all directions evolve differently. Some only experience compressive loading (such as those in the azimuth direction of  $\phi = 0$ ) while others experience compressive unloading and tensile loading as well. In the planes for which  $\phi = 45^\circ$  and  $90^\circ$  all these different cases can be found. The effects of these different loading stages exhibit themselves in the tangential components of force vectors too. So it is seen that in this case, loading of Type 2 results in failure significantly earlier than Type 1. The underlying reason is the change in the behavior of grain-pair interactions due to the presence or lack of hydrostatic and biaxial loading stages.

In simulation for case b3, the normal and tangential components of inter-granular forces for Type 1 loading have been presented in Figure 4.11.(a), (e), (i) and Figure 4.11.(c), (g), and (k)

respectively. And for the corresponding Type 2 loading, the forces are given in Figure 4.11.(b), (f), (j) and Figure 4.11.(d), (h), and (l) respectively.

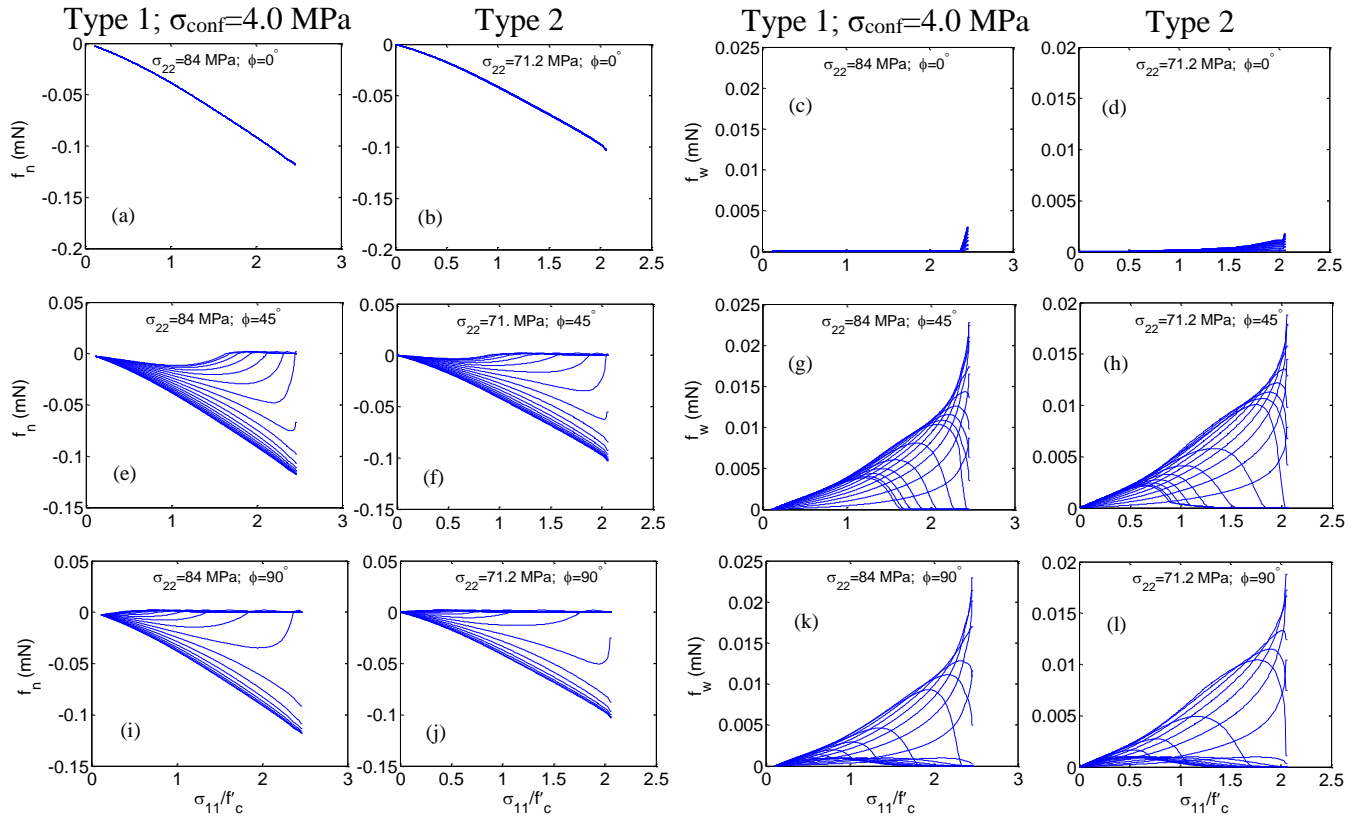


Figure 4.11 Normal and tangential components of forces for different polar angles in loadings of Type 1 and Type 2 in azimuth angles of 0, 45, and 90 degrees (first, second and third rows respectively) for  $\sigma_3=4.0$  MPa and  $\sigma_2=84$  MPa

In this case in both loading types (Type 1 and Type 2) and during the whole loading stage, the two horizontal components of stress are equal,  $\sigma_2 = \sigma_3$ . So in the directions where  $\phi = 0$  the normal force components are all equal and compressive and no tangential components in the inter-granular force vector develops. However in other two azimuth directions ( $\phi = 45^\circ$  and  $90^\circ$ ), the grain-pair that are more inclined to the vertical direction are compressive while those inclined towards the horizontal direction experience unloading and eventually tension. The effect of the qualitative and

quantitative change of normal response on the tangential response can also be seen in the evolution of tangential components of force.

Same analyses have been done for the cases where minimum principal stress is 20 MPa and the results for both loading types are presented in the following graphs. Figure 4.12 presents the forces for the case where at failure  $\sigma_3 < \sigma_2 < \sigma_1$  (Case c2) while Figure 4.13 shows the results for the case where  $\sigma_3 < \sigma_2 = \sigma_1$  (Case c3).

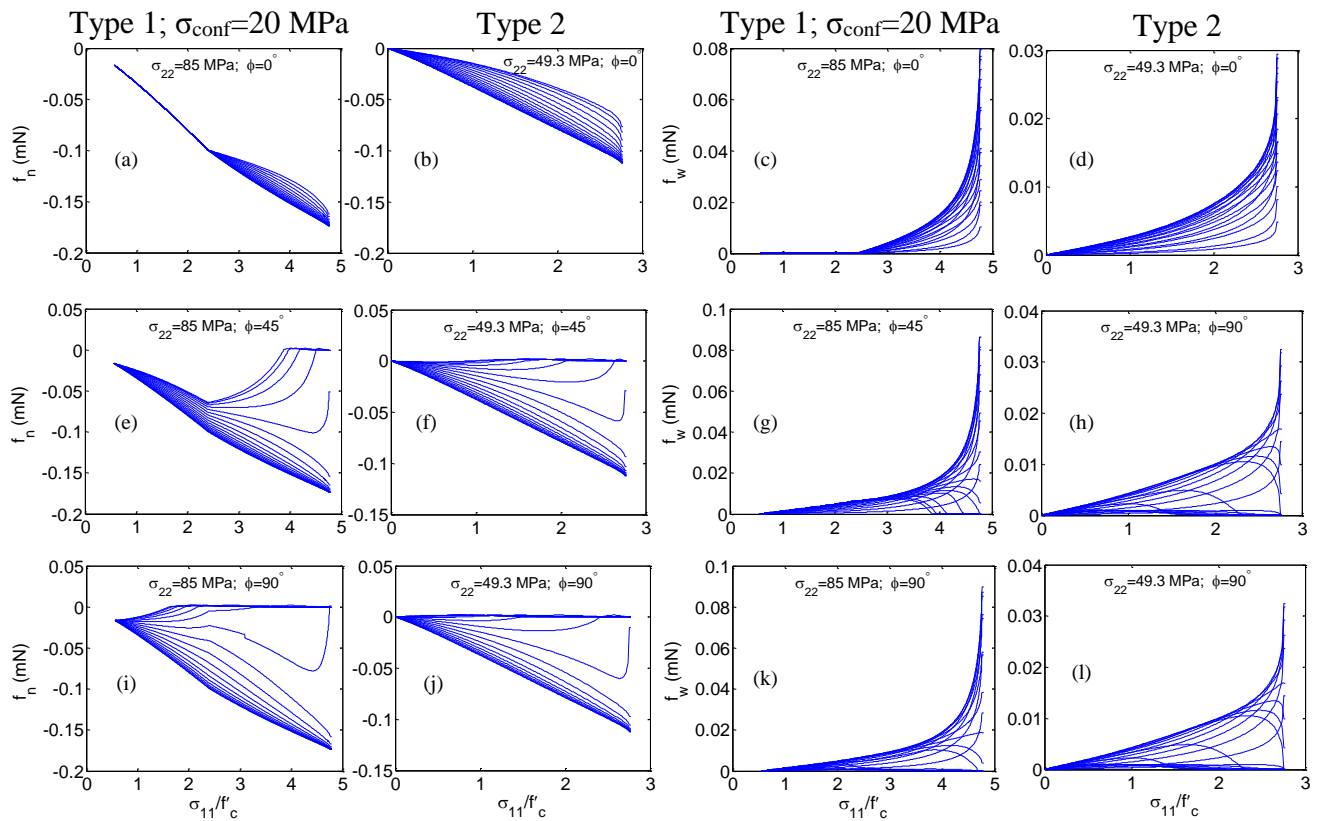


Figure 4.12 Normal and tangential components of forces for different polar angles in loadings of Type 1 and Type 2 in azimuth angles of 0, 45, and 90 degrees (first, second and third rows respectively) for  $\sigma_3=20$  MPa and  $\sigma_2=85$  MPa

The results in Figures 4.12 and 4.13 are similar to Figures 4.10 and 4.11 respectively. The only difference is that in Figures 4.12 and 4.13 the confinement is equal to 20 MPa (for Type 1) while in Figures 4.10 and 4.11 it is 4 MPa. This in turn plays an important role in the large difference

between the failure stresses for the two loading types. Since in loadings of Type 1 the material has experienced a relatively large amount of confinement (20 MPa) and this is missing in Type 2, loading of Type 1 results in a much higher failure stress compared to Type 2 (See Figure 4.12 and 4.13, and also Figure 4.3 for the stark difference between the failure stress state in the two loading paths)

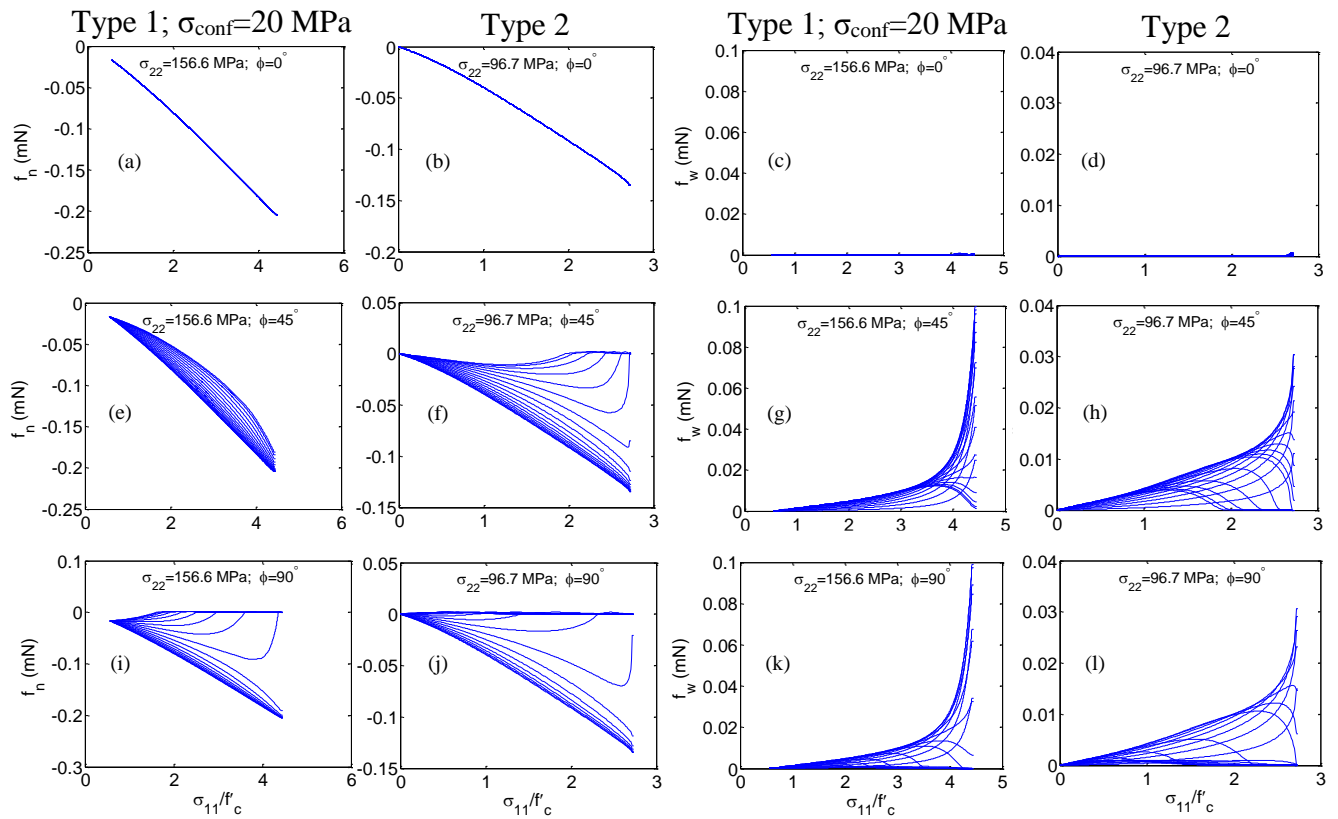


Figure 4.13 Normal and tangential components of forces for different polar angles in loadings of Type 1 and Type 2 in azimuth angles of 0, 45, and 90 degrees (first, second and third rows respectively) for  $\sigma_3=20$  MPa and  $\sigma_2=160$  MPa

Note that in these two cases, there is a significant part of the loading process for which in loading of Type 1, no tangential force is developed in any direction, while in Type 2 the tangential forces develop from the very beginning of the loading procedure. This contributes to a higher strength for Type 1, because tangential force components will fail later. Further, in loadings of Type 1,



most of grain-pair interactions remain compressive or go through unloading very late in the loading process. While in Type 2, from the beginning, there are many grain-pair interactions that go through tensile loading and will natural fail very early. The additive effect of these two mechanisms (normal and tangential) contribute to a much higher failure strength in Type 1 compared to Type 2 (72% increase in failure strength in case c2 and 62% increase in case c3).

#### 4.3.4 Localized failure and fault angle

The orientation of macro-scale failure plane, known as fault angle, can be investigated by considering the *localized failure* that manifest as discontinuities in the displacement gradient field leading to localization of weakened discontinuities within the material [29]. To evaluate the localized failure it is necessary to calculate the localization matrix (also known as the acoustic tensor) for all generic directions within the material. Localization matrix,  $\Gamma_{ij}$ , is the matrix derived from contracting the tangent stiffness tensor with the normal vector.

$$\Gamma_{jl} = C_{ijkl} n_i n_k \quad (4.1)$$

It is clear that the acoustic tensor is calculated for a given direction, characterized by its unit normal vector,  $n_i$ . The material is said to have reached the state of localized failure when the minimum eigenvalue of its localization tensor for a given direction vanishes. The key benefit of evaluating localization failure is that the localization tensor is a function of the direction, unlike the stiffness tensor which is a property of the material point. Singularity of localization matrix of a given direction implies that failure has localized on that particular plane. For consistency with experimental measurements of failure planes, we call the polar angle between the failure plane's normal vector and the  $\sigma_I$ -direction the fault angle and denote it by  $\alpha$ , as depicted in Figure 10.

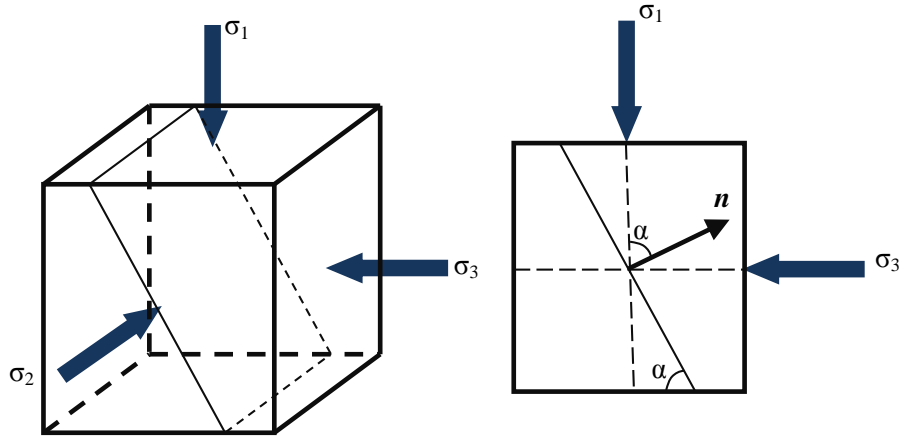


Figure 4.14 Directions of principal Stress components and the fault angle

It is known that for traditional Mohr-Coulomb criterion the failure direction is given as  $45^\circ + \phi/2$ , where  $\phi$  is the friction angle of the material. However, experimental studies show that for different stress states at failure, failure plane directions vary significantly and are not a constant material property [97, 112, 127, 128]. Moreover, even in the general case of failure envelopes defined in the tangential-normal stress plane ( $F(\sigma, \tau) = 0$ ), although the fault angle is not prescribed by the friction angle of the material, it is still only a function of the maximum and minimum principal stress components (as it can be inferred from Figure 4.1).

In the method of granular micromechanics presented here, the macro-scale localized failure is determined by the overall cooperative and competitive grain-scale mechanisms which depend on all components of the macroscopic stress tensor. For this reason, failure plane depends on both the stress conditions and the loading path. Variation of fault angle versus the intermediate principal stress for all the simulations with Type 1 loading is given in Figure 4.15a. Different sets of data points in figure 4.15a belong to different values of minimum principal stress,  $\sigma_3$ .

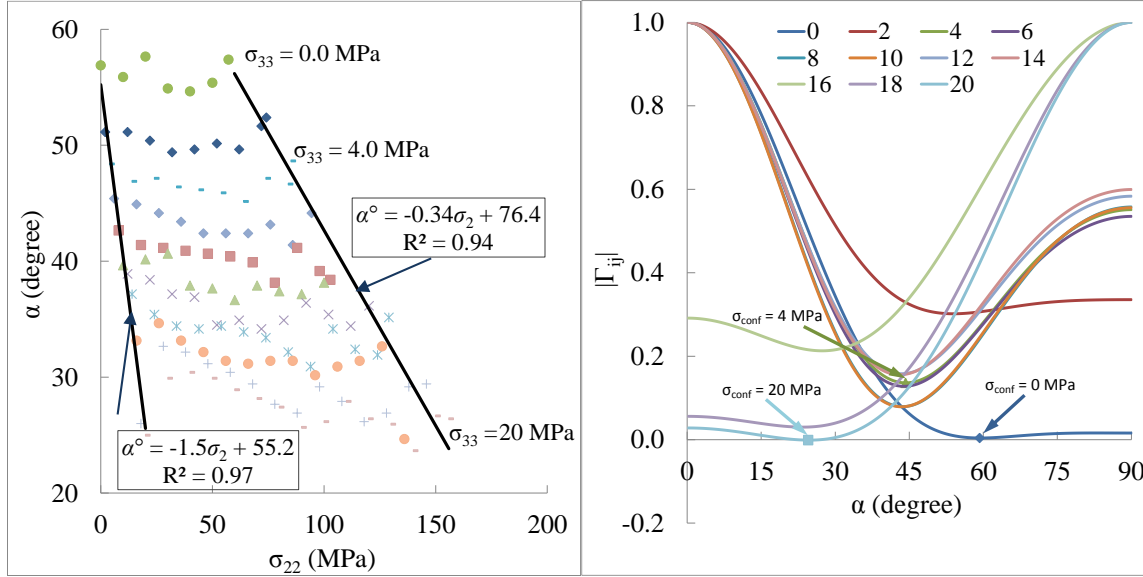


Figure 4.15 The variation of fault angle versus the intermediate principal stress for different values of confining stress in loadings of Type 1. (b) The determinant of the acoustic tensor versus directions for Type 1 loading with different values of  $\sigma_{22} = \sigma_{33} = \sigma_{conf}$

It is seen that the fault angle,  $\alpha$ , changes within a large interval of  $24^\circ$  to  $58^\circ$  by changing the loading conditions in Type 1. By increasing the amount of minimum principal stress,  $\sigma_3$ , the fault angle decreases significantly. For the two limiting cases where the intermediate principal stress,  $\sigma_2$ , is equal to the minimum principal stress (cases a1, b1 and c1), and also, where it is equal to the maximum principal stress (cases a3, b3 and c3) the following two linear relationships are found relating the fault angle to the intermediate principal stress

$$\begin{aligned} \alpha &= -1.5\sigma_2 + 55.2; & \text{where } \sigma_2 &= \sigma_3 \\ \alpha &= -0.34\sigma_2 + 76.4; & \text{where } \sigma_2 &= \sigma_1 \end{aligned} \quad (4.2)$$

Further, fault angle is seen to depend not only on the minimum principal stress,  $\sigma_3$ , but also on the intermediate principal stress  $\sigma_2$ . For a constant confining pressure, the value of the fault angle generally decreases by increasing the amount of intermediate principal stress, however, a completely uniform trend is not seen here. In simulations with zero or small confining pressure, fault angle does not change much by changing  $\sigma_2$  while in higher confinements it decreases by

increasing  $\sigma_2$ . Results from experiments on siltstone by Haimson and Rudnicki [112] show also decreasing fault angle by increasing  $\sigma_3$ . However they report increasing fault angle by increasing the intermediate principal stress  $\sigma_2$  which is in contradiction with the present results.

It should be noted that minimum principal stress,  $\sigma_3$ , and the intermediate principal stress,  $\sigma_2$ , both lie in the lateral direction and increasing them will result in higher mean stress. Now the fault angle,  $\alpha$ , is defined as the angle between normal to the failure plane and the vertical direction. So it is not measured with respect to any of the two horizontal directions, 2 or 3. Thus it seems reasonable that the effects of the two lateral components of stress on fault angle,  $\alpha$ , are qualitatively similar. Increasing both of the lateral components of stress leads to decrease in the fault angle (as seen in Figure 4.15a).

Figure 4.15b shows the determinant of acoustic tensor (normalized with its maximum value for each particular simulation), in the vertical axis versus direction in the horizontal axis. The cases that are reported here include results from loadings of Type 1, with all different values of confining pressure,  $\sigma_{conf}$ , and  $\sigma_2 = \sigma_3 = \sigma_{conf}$ . Different curves correspond to different values of minimum and intermediate principal stress. It is observed that the polar angle corresponding to the direction at which the determinant of the acoustic tensor becomes zero shifts from larger values ( $\sim 60$ ) to smaller values ( $\sim 25$ ). For the cases with small confinement, the determinants of the acoustic tensor are largest in the horizontal directions. While for the cases where confinement is high, determinant of the acoustic tensor in vertical directions are highest. The localized failure is given by the lowest point of the curve, which represent the numerical value that was associated with failure as discussed in section 4.3.2. It is noteworthy that failure at low confinement is characterized by large fault angle which will manifest itself as shear bands. On the other hand, failure at high confinement is characterized by shallow fault angle and will manifest a combination of compaction

and shear bands. The distinction between these two different mechanisms is a macroscopic one [129, 130]. However, the shift from failure due to the formation of shear band to mixed compaction or shallow shear bands can be understood from micro-scale mechanisms using the study of grain-pair force distributions. The hardening mechanism implemented in the tangential behavior of grain-pair interactions at high confinement (through the definition of  $B_w$  in Eq. 3.38) ensures that the failure is only partly determined by shearing mechanism.

The eigenvalues of the acoustic tensor at the failure point for loadings of Type 1 with  $\sigma_2 = \sigma_3 = \sigma_{conf}$  have been shown in Figure 4.16 for confinement stress of 0, 4, 18, and 20 MPa. The three eigenvalues correspond to one dilatational mode (labeled as P in Figure 4.16) and two shear mode (labeled as S in Figure 4.16).

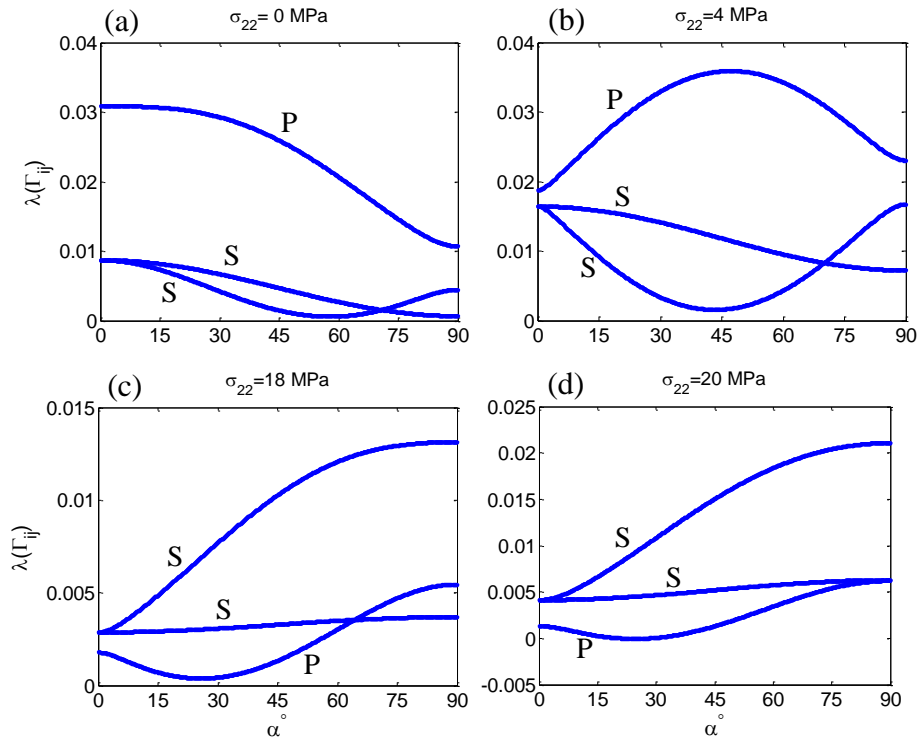


Figure 4.16 Variation of eigenvalues of the acoustic tensors for Type 1 loading where  $\sigma_{22} = \sigma_{33} = \sigma_{conf} = 0, 4, 18,$  and  $20$  MPa in (a), (b), (c), and (d) respectively

It is seen that in cases where confinement is low (Figure 4.16a and b), the eigenvalues corresponding to the shear mode are lower and responsible for failure and determination of the localized failure direction. However, in cases with high confinement (Figure 4.16c and d), the smaller eigenvalue corresponds to dilatational mode which controls the localized failure.

### 4.3.5 Fault angle with Matsouka-Nakai criterion

An alternative approach for determining the fault angle as a function of the principal stress components is through the Matsouka-Nakai failure criterion [131] defined as

$$F(\sigma_{ij}) = \frac{I_1 I_2}{I_3} - K_{M-N} = 0; \quad \text{where } K_{M-N} = 9 + 8 \tan^2 \phi \quad (4.3)$$

where  $I_1$ ,  $I_2$ , and  $I_3$  are the first, second, and third invariants of stress tensor respectively and  $\phi$  is the internal friction angle. Using this criterion along with the well-known equation for fault angle,  $\alpha = 45^\circ + \phi/2$ , it is possible to derive the direction of failure plane. It is noteworthy that in Matsouka-Nakai method also since the failure criterion is a function of all the invariants of stress tensor, failure state and the failure direction are functions of all the three principal stresses, which is in contrast with other traditional criteria which neglect the effect of intermediate principal stress. The internal friction angle,  $\phi$ , relevant to the Matsouka-Nakai failure criterion was calculated using Eq. 4.3 and the failure stress states obtained from all our simulations. Figure 4.17 shows the resultant fault angle as a function of the intermediate principal stress derived from Matsouka-Nakai criterion.

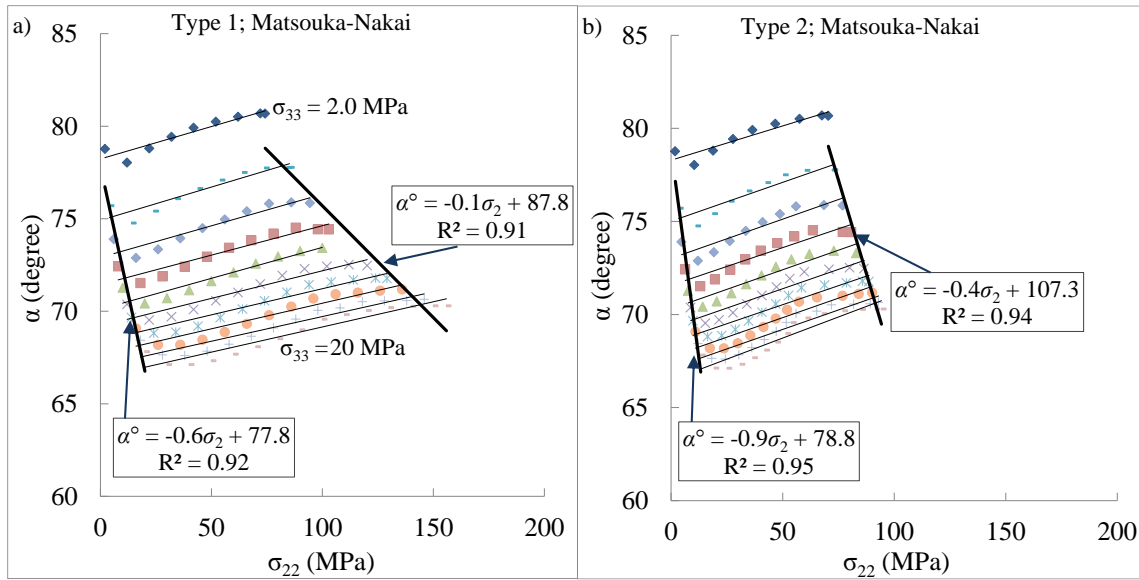


Figure 4.17 Fault angle versus intermediate principal stress for different values of minimum principal stress for loadings of Type 1 (a) and Type 2 (b), derived using Matsouka-Nakai criterion

From Figure 4.17 it is observed that the failure directions for both loading scenarios are similar although the stress values at failure for the two loading types, Type 1 and Type 2, are significantly different. Again it is seen that linear relationships between the fault angle and the intermediate principal stress can be found for the limiting cases. The equations provided in Figure 4.17 for these limiting cases are not identical solely due to differences in the failure stress components, but the values of the fault angles in two loading types derived with Matsouka-Nakai method are identical. Results from application of Matsouka-Nakai criterion show that the fault angle decreases significantly by increasing the minimum principal stress. Contrary to the results from the present method, fault angle is increasing by increasing the intermediate principal stress for the constant minor principal stress. Furthermore, this criterion predicts far larger fault angles than those determined by the present method in Figure 4.15a.

#### 4.4 Summary and Conclusions

Thermo-mechanics based granular micromechanics formulation for the constitutive relationships of cementitious materials is applied to study the failure behavior of rock-like cemented granular materials under true triaxial loading condition. A wide range of simulations are performed under the true triaxial loading conditions designed such that they represent the model's ability to capture the effect of intermediate principal stress and the loading path on the failure behavior.

For a given loading path, maximum principal stress at failure is clearly seen to depend upon, in addition to the minimum principal stress, the intermediate principal stress component. As expected, maximum principal stress increases with increasing the minimum principal stress component. Moreover, it is shown that by increasing the intermediate principal stress, the maximum principal stress will also change, which is in contrast with traditional failure criteria defining failure as a function of the normal and tangential components of stress on a failure plane. It is observed, in the results of the present model, that by increasing the intermediate component of principal stress the maximum principal stress at failure increases, reaches a peak value, and then decreases. This result is seen to conform very well to the recent experimental results.

Path dependent nature of the material response to loading is also demonstrated in the failure behavior through simulations performed for two types of loading paths. Loadings of Type 1, in which an initial hydrostatic confinement is applied on the material, lead to higher strength from the material and higher maximum principal stress at failure compared to loadings of Type 2 where all principal stress components are increased simultaneously but with different increments. The macro-scale failure mechanism is investigated by considering the evolution of eigenvalues of the symmetric part of the  $6 \times 6$  tangent stiffness matrix which indicate the Kelvin deformation mode(s) at failure. For low confinement and small intermediate principal stress, the failure is controlled by



a shear mode. In comparison, for simulations at higher confinement and larger intermediate principal stress, the modes tend to be mixed as almost all eigenvalues tend towards failure criterion at the same step.

Evolution of normal and tangential components of inter-granular force vectors is presented and it is seen that the two loading types result in different behavior in grain interactions in different directions. Grain-pair interactions in different directions go through different loading history due to their orientation and also the stress state applied on the material. Most notably, the presence and lack of initial hydrostatic confinement (as seen in loadings of Type 1 and 2 respectively) plays a significant role in defining the failure stress state. The effect of confinement, in the micro-scale, is characterized by compressive hardening in normal direction and zero force in the tangential direction. Cumulative effect of these two factors ultimately results in a much higher failure stress compared to the cases that lack initial confinement. To a smaller degree, the presence of biaxial loading phase (with equal increments in the two directions), has similar effect. Overall, it is seen that the interactions between grains in different directions provides a useful insight to the failure from a microscopic view.

Direction of failure plane is also studied and it is seen that the fault angle also depends on all component of the principal stress. By changing the stress state at failure, fault angle varies in the interval of  $24^\circ$  to  $58^\circ$  for loading of Type 1. In particular, it is seen that the fault angle decreases significantly by increasing the minimum principal stress in both loading types. It is also seen in loading of Type 1 that the fault angle decreases with increasing the intermediate principal stress. The reason is that both the minimum and intermediate principal stress components are in the horizontal direction and lie in the plane perpendicular to the direction of application of axial loading. Thus increasing both horizontal components of principal stress (which leads to increasing

the lateral confinement) leads eventually to smaller fault angle. The eigenvalue analysis of the localization tensor shows change in the macro-scale failure mechanism from shear dominated at low confinement to a mixture of shear and compaction at higher confinement, which agrees with the decreasing fault angle. Similar transitions from shear to compaction bands have been observed experimentally in true triaxial tests on rock samples.

In general, based on the results presented here, it is concluded that failure criteria in the traditional form, defining failure as a function of the stress state, are not sufficient for reliably evaluating failure state of the material. A given stress state might be a failure stress state in a given loading path leading to that state, while another loading path reaching that same stress state might not result in failure. Failure is a gradual process that happens through the loading process. Stress-state at any time during the loading cannot be used to evaluate whether the material has failed at that point. Rather, it is the *path* of loading leading to that particular stress-state which may or may not cause failure.

## **5 GRAIN SIZE EFFECT USING GRANULAR MICROMECHANICS**

### **5.1 Introduction**

The motivation to develop the method of granular micromechanics is to have a material model for modeling the behavior of a continuum while incorporating effects from micro- (grain-) scale. In this approach, the main advantage stems from the fact that the macroscopic response of the material is derived based on the behavior of the grain-pair interactions in all different directions within the material point [43, 96]. This results in implementing the differences in the behavior of grain-pair interactions in different directions, in both the initial state and also during the loading procedure and affected by the loading history, into the macroscopic behavior in an automatic manner.

But in addition to this, the fact that the macroscopic behavior is derived from interactions between grains, makes the method particularly powerful in representing the effects of material's microstructure into the continuum model. One of the most important microstructural properties of the materials is grain size [132]. The effects of grain size on the macroscopic behavior of materials, especially cementitious and rock-like materials, has been studied extensively [133-138]. Recently, Yin et al devised an approach for implementing grain size effect into the macroscopic behavior of the material by incorporating its effect into the micromechanical properties of grains [139].

In this chapter, the nonlinear damage-plasticity granular micromechanics model has been enhanced by implementing the effects of grain size into the material model from a grain-scale

viewpoint. The effects of grain size has been implemented on the grain-scale properties, including intergranular contact length, inter-granular stiffness coefficients in both normal and tangential directions, inter-granular strengths in both normal and tangential directions, and also the volume density of grain-pair interactions. Implementing these effects into the material model, macroscopic behavior of the material has been derived as a function of grain size.

## 5.2 Scaling laws for grain-size effect

The objective of this section is to incorporate the effect of size of grains within the material point in the modeling procedure. The granular micromechanics approach used for this study, is the one that was formulated and calibrated in Chapter 3. In order to include the effects of grains sizes in the formulation, let us consider two grain assemblies with average grain sizes of  $d_1$  and  $d_2$ . The two assemblies are assumed to be similar otherwise; meaning that properties of contacts and grains are the same for the two assemblies. In this case, it is reasonable to assume that

$$l_2 = l_1 \left( \frac{d_2}{d_1} \right) \quad (5.1)$$

It should be noted that the volume density of grain-pair interactions in the RVE will also be changed by changing grain size in the following manner

$$\rho_2^c = \rho_1^c \left( \frac{d_2}{d_1} \right)^\alpha \quad (5.2)$$

where  $\alpha$  is a numerical parameter that can be different for different problems and will also depend on the number of dimensions of the problem (whether the problem is in 1, 2, or 3 dimensions) and also geometry of the grains [136]. In any case, it is evident that the value of the parameter should

be negative. Further in order to incorporate the effects of grain-size on the material behavior, the initial inter-granular stiffness coefficients are assumed to depend on the grain-size as

$$(E_n)_2 = (E_n)_1 \left( \frac{d_2}{d_1} \right)^\beta \quad \text{and} \quad (G_w)_2 = (G_w)_1 \left( \frac{d_2}{d_1} \right)^\beta \quad (5.3)$$

where  $\beta$  is a numerical parameter that shows how the inter-granular stiffness coefficients depend on grain-size. Considering size-effect law [136], it is evident that value  $\beta$  should also be negative. It should be noted that in this equation the subscripts 1 and 2 refer to the number of grain assembly only.

We should also note that by changing the grain size, the relative displacement between neighbor grains will also change due to the change in the magnitude of branch vector,  $l_i$ , as seen from Eq. 5.1. So the model parameters that represent the position, in displacement axis, where the force reaches its peak (See the definition of damage parameters given in Chapter 3) should also change. Thus the following size-effect relationships are proposed.

$$(B_n)_2 = (B_n)_1 \left( \frac{d_2}{d_1} \right)^\gamma; \quad (B_{nc})_2 = (B_{nc})_1 \left( \frac{d_2}{d_1} \right)^\gamma; \quad (B_{w0})_2 = (B_{w0})_1 \left( \frac{d_2}{d_1} \right)^\gamma; \quad (5.4)$$

Now considering the relationship between different components of inter-granular force and displacement vectors (Eq. 3.31) and the micro-scale size-effect relationships provided in Eq. 5.1 and 5.3, the normal and tangential components of inter-granular force vectors can be shown to follow this relationship

$$(f_n)_2 = (f_n)_1 \left( \frac{d_2}{d_1} \right)^{\beta+1} \quad \text{and} \quad (f_w)_2 = (f_w)_1 \left( \frac{d_2}{d_1} \right)^{\beta+1} \quad (5.5)$$

In this manner, the microscopic measures of displacement, stiffness, and force have been modified according to the grain size. Thus the resulting macroscopic measures of stiffness,  $C_{ijkl}$ , and stress,  $\sigma_{ij}$ , will be changed automatically. Substituting Eq. 5.1, 5.2, 5.3, and 5.5 into the relationships for

stress and stiffness tensors (Eq. 3.43 and 3.45) the size-effect relationships for stiffness tensor and stress tensor will be derived as

$$\left(C_{ijkl}\right)_2 = \left(C_{ijkl}\right)_1 \left(\frac{d_2}{d_1}\right)^{2+\alpha+\beta} ; \quad \left(\sigma_{ij}\right)_2 = \left(\sigma_{ij}\right)_1 \left(\frac{d_2}{d_1}\right)^{2+\alpha+\beta} \quad (5.6)$$

It should, however, be noted that the relationships in Eq. 5.6 are only valid for the undamaged state of the material. In addition, if the linear material model discussed in Chapter 2 is implemented, the proportional relationships given in Eq. 5.6 would be applicable. But in the case of the nonlinear damage-plasticity model that is used here for modeling cementitious and rock-like materials, the change of damage parameter as a function of grain size (given in Eq. 5.4) will create more complicated changes in the macroscopic behavior of the material. In fact this effect will be enhanced by the change that is applied on the damage parameters in normal tension and compression, as well as tangential direction. Nevertheless, in the initial stage, it is seen that, as expected, the scaling effect of grain size on stress tensor is similar to that on stiffness tensor components

### 5.3 Model calibration

Inspired by the experimental results presented in [132], multiple simulations of conventional triaxial tests on cementitious materials have been performed. Samples with grains of different sizes (ranging from 0.02 mm to 0.00001 mm) have been used in simulating triaxial compressive tests with different initial confining pressures (0.0 MPa to 400.0 MPa). Note that the model properties that were presented in Chapter 3, Table 3.1, belong to the specimen with grain size of  $10 \mu\text{m} = 0.01 \text{ mm}$ . Size-effect parameters used in this study are shown in Table 5.1.

Table 5.1 Size effect parameters used in this study

Size effect Parameters	$\alpha$	$\beta$	$\gamma$
value	-1.2	-1.0	1.0

## 5.4 Results and Discussions

Using the constitutive model derived in Chapter 3 and model parameters presented in Tables 3.1 as well as the size effect parameters presented in Table 5.1, two well-known types of experiment have been simulated on cementitious materials with different grain sizes. Triaxial compression tests with different amounts of initial hydrostatic confinement have been first simulated for grain sizes ranging from 0.02 mm to 0.00001 mm. Constant volume tests have also been performed on the material with the given model parameters and with grain sizes ranging from 0.02 mm to 0.001 mm.

### 5.4.1 Triaxial compression results

A number of triaxial compressive tests on samples with different grain sizes have been simulated. These experiments are performed in two steps, an initial hydrostatic confinement followed by a deviatoric loading in the vertical direction. In the confinement step, a hydrostatic stress of desired value is applied incrementally to the specimen ( $\sigma_{11} = \sigma_{22} = \sigma_{33} = \sigma_{conf}$ ). Afterwards in the deviatoric loading step, keeping the values of the two horizontal components of stress ( $\sigma_{22}$  and  $\sigma_{33}$ ) constant, loading proceeds in the vertical (1-1) direction.

It is well-known that by increasing the initial confinement, tangential stiffness and the failure stress increase. In this study, it is intended to show, not only the effect of increase on initial confinement,

but also that of grain-size change. In order to show the results more clearly, the results of the triaxial compression simulations have been divided into two parts, small confinement and large confinement. Figure 5.1 shows the evolution of the deviatoric stress,  $q = \sigma_{11} - \sigma_{conf}$ , versus  $\varepsilon_{11}$  during the deviatoric loading process for triaxial experiments with 0.0, 5.0, and 20 MPa of initial confinement, on grains of different sizes.



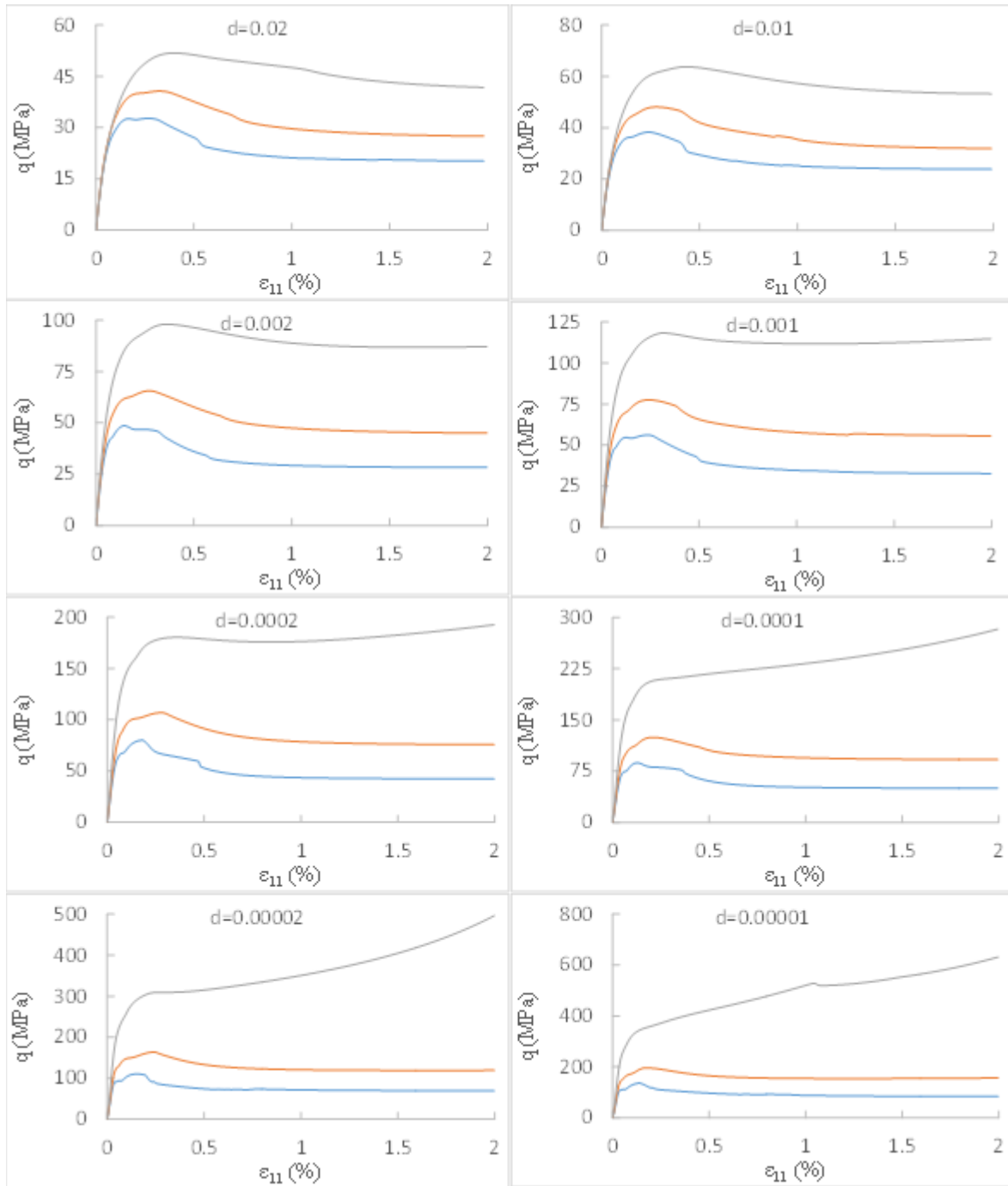


Figure 5.1- Evolution of the deviatoric stress,  $q=\sigma_{11}-\sigma_{22}$ , during triaxial loading (application of  $\epsilon_{11}$ ) for initial confining pressures of 0.0, 5.0, and 20.0 MPa for all grain sizes

The same set of results for triaxial compression tests with large amount, 50, 100, 200, and 400 MPa, of initial confinement are also presented in Figure 5.2.

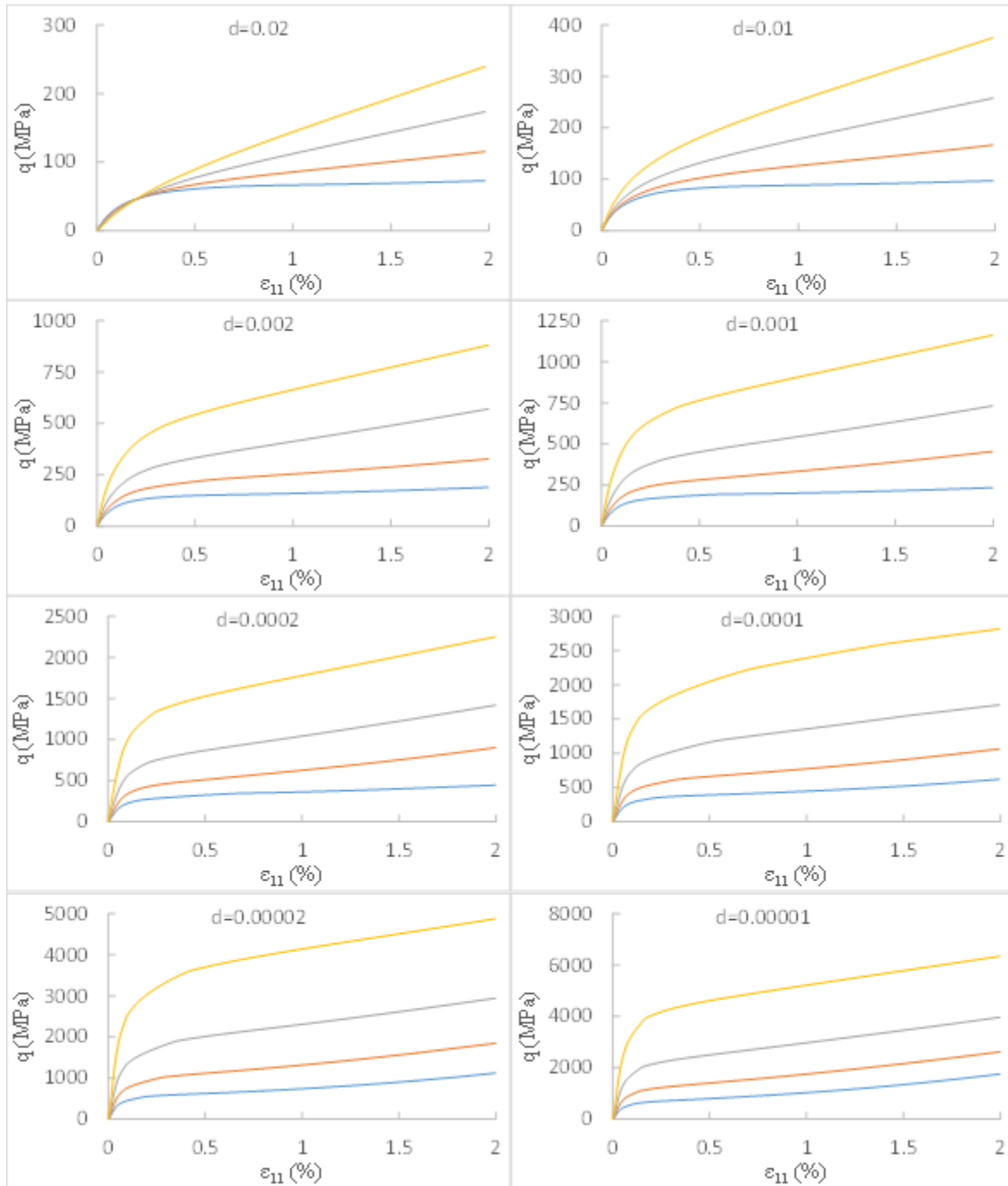


Figure 5.2 Evolution of the deviatoric stress,  $q=\sigma_{11}-\sigma_{22}$ , during triaxial loading (application of  $\epsilon_{11}$ ) for initial confining pressures of 50, 100, 200, and 400 MPa for all grain sizes

In Figures 5.1 and 5.2, each graph presents the  $q-\epsilon_{11}$  curves for different values of initial confinement. There are multiple points that can be inferred from the results. It is seen that

simulations for all grain sizes show an increase of stiffness and also strength by increasing the amount of initial hydrostatic confinement. This effect is seen for both large and small amounts of confinement, though it is more obvious in higher confinements (Figure 5.2).

It is also interesting to note the shift that happens from “brittle” failure to “ductile” failure. It is well-known that without changing grain sizes, by increasing the initial confinement, failure transforms from brittle to ductile. In this context, brittle failure is characterized by an obvious peak point in the stress-strain curve, i.e. failure point where the stiffness (slope of the stress-strain curve) reaches zero. Whereas ductile failure is used to describe the nonlinear behavior for cases in which the material has a yield point (i.e. a point of sudden significant reduction in stiffness), followed by hardening behavior, with no apparent peak in the stress-strain curve. This transition from brittle to ductile failure by increasing confinement has been observed previously for multiple granular materials by different sets of experimental data [54] and also using the method of Granular Micromechanics for grains of size 0.01 mm [56].

The results in this study, while confirming the above observation, show that this transition can take place by reduction in the size of grains as well. It is seen, from both Figures 5.1 and 5.2, that reduction of grains’ size results in transition of failure from a more brittle type to a more ductile type. This effect is most obvious, by comparing the behavior after 20 MPa of confinement for different grain sizes, in Figure 5.1. It is seen that for larger grain sizes ( $d > 0.0001\text{mm}$ ) an obvious peak point exists in the stress-strain curves, representing a brittle behavior. While for smaller grain sizes, the stress-strain curve shows only a yield point followed by strain-hardening.

It is also interesting to observe the evolution of failure points and yield points by changing the grain-sizes. In Figure 5.3a, the evolution of the deviatoric stress component at *failure* for different sizes in simulations with confinement values of smaller than or equal to 20 MPa have been

presented. However, as it was stated before, for higher confinement values no obvious failure point is observed. For these cases, Figure 5.3b presents the evolution of the deviatoric component of stress at *yield* point for different sizes.

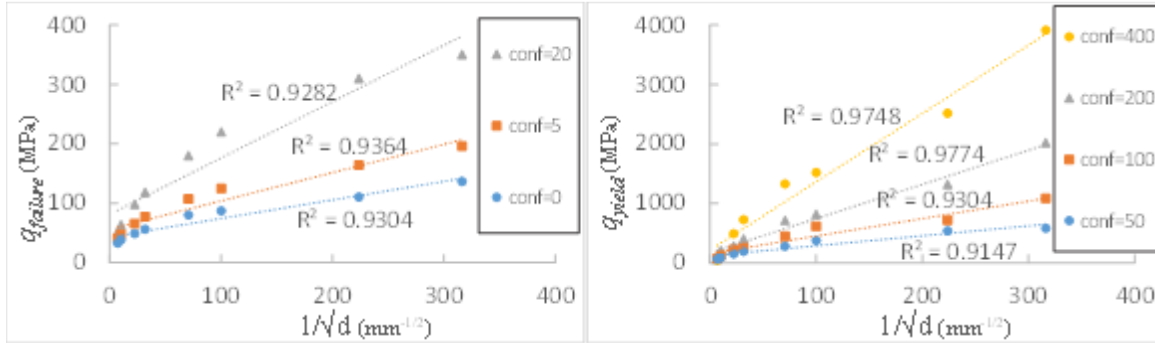


Figure 5.3 Change of failure stress for lowly confined cases,  $\sigma_{conf} \leq 20$  MPa, and yield stress for highly confined cases,  $\sigma_{conf} > 20$  MPa by change of grain size

Note that the horizontal axis in these graphs present  $1/\sqrt{d}$ . It is interesting to note that both failure points and yield points grow significantly with decreasing the grain size. Failure/yield points are seen to be changing in a proportional manner, with a very good approximation with increasing  $1/\sqrt{d}$ . This is in agreement with the experimental observations such as [132].

In order to study the behavior of the material in the lateral directions (2 and 3), Figure 5.4 presents the evolution of volumetric stress ( $\varepsilon_v = \varepsilon_{ii} = \varepsilon_{11} + \varepsilon_{22} + \varepsilon_{33}$ ) during the deviatoric loading process.

It is seen here that triaxial tests with small amount of confinement result in a small period of compaction (compressive volume strain) followed by dilation (tensile volume strain). As the initial confinement increases the volumetric strain tends more and more toward compressive region. This happens to the degree that for very large amounts of initial confinement, no dilation is measured and the volume is always decreasing. However, here again the effect of grain size can be observed readily. By decreasing the grain size, the volume strain tends significantly toward tensile region. The effect is such that for the smallest grain size ( $d=0.00001$  mm) the volume strain is always tensile, regardless of the amount of initial confinement and no amount of initial

confinement can force the material to experience dilation. So a specimen made from very small grains, will always go through dilation in a triaxial compressive test, regardless of how large the value of the initial hydrostatic confining pressure is.

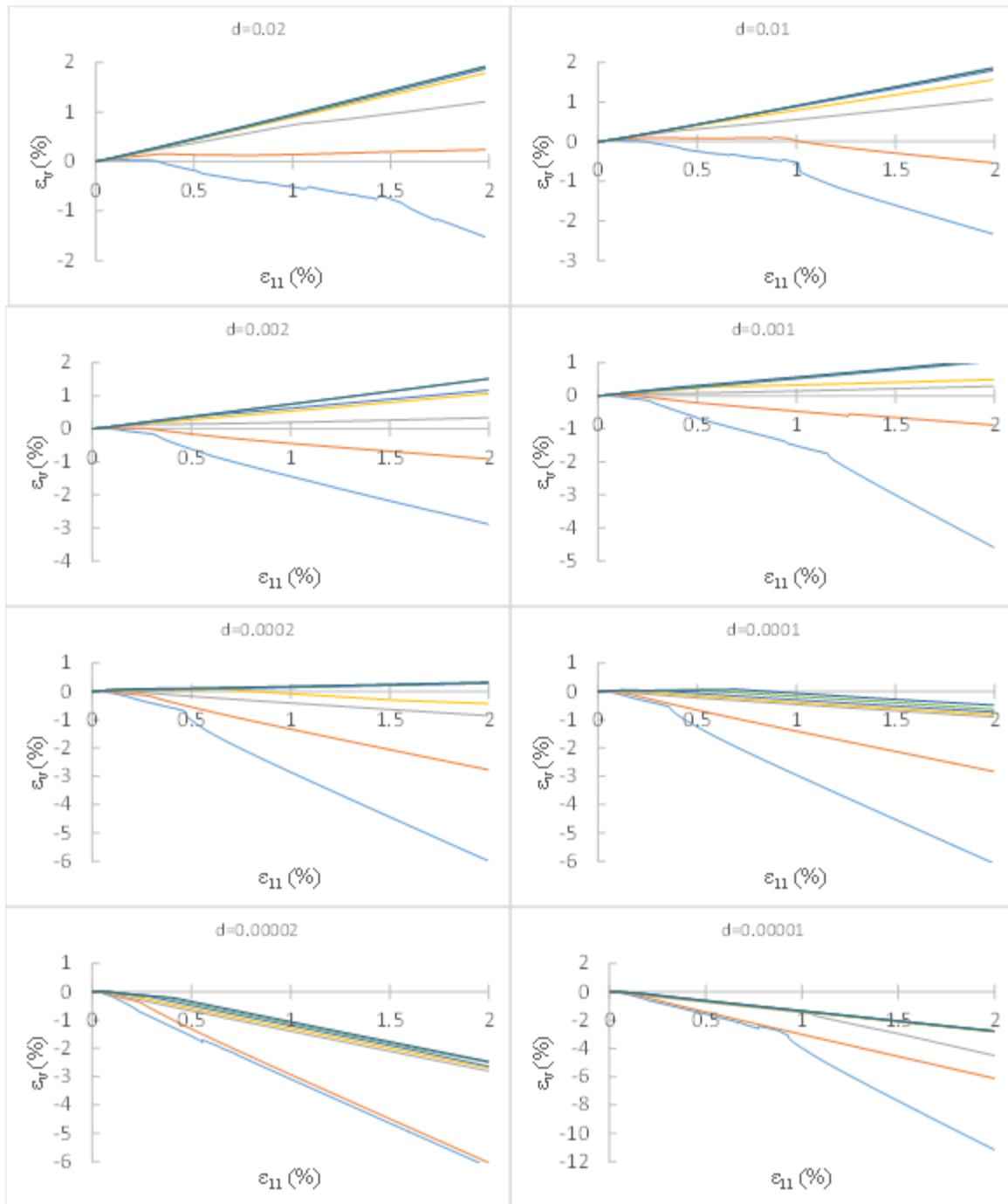


Figure 5.4 Evolution of volumetric strain during loading for all sizes and different initial confinement values

In order to calculate the direction of failure *localized failure* is studied. At this stage the displacement field still remains continuous, while the displacement gradient has become discontinuous and stress concentration bands (compression band, dilation band, shear band, or a combination of these) emerge within the material [29]. The nature and direction of these strain localization bands depends on the properties of the material as well as the loading procedure. This step of failure corresponds to singularity of the tangential localization tensor (See Chapter 4, section 4.3.4 for a more detailed description on calculation of failure direction). As it was mentioned before, the obvious advantage of the study of localized failure (i.e. loss of positive-definiteness of the localization tensor) is that it deals with the localization tensor, which is uniquely calculated for each direction within the material and it will thus predict the direction of the failure plane (i.e. the so-called *fault angle*). For this purpose, the eigenvalues of the localization tensor at failure state are calculated for every generic orientation. The orientation for which the eigenvalues reaches zero earlier, is the direction of failure plane.

In Figure 5.5, the eigenvalues of the acoustic tensor belonging to different directions are shown at failure state. The results belonging to grain sizes of 0.02 mm, 0.002 mm, 0.0002 mm, and 0.00002 mm are presented in first, second, third, and fourth rows of Figure 5.5, respectively. It is important to note that only for triaxial tests with confinements of 0.0, 5.0 and 20 MPa a clear failure point (peak in the stress-strain curve) was observed. For this reason, the results presented here also include triaxial compression tests with 0.0, 5.0, and 20 MPa of confinement (First, third, and second columns in Figure 5.5, respectively).

The eigenvalues of the localization tensor (acoustic tensor) correspond to one longitudinal wave (P wave) and two shear waves (S waves) [140]. It is seen, from Figure 5.5, that in all these experiments, the eigenvalue that reaches zero earlier belongs to the shear component of the

acoustic tensor. This implies that for conventional triaxial tests, failure will consist of formation of shear bands.

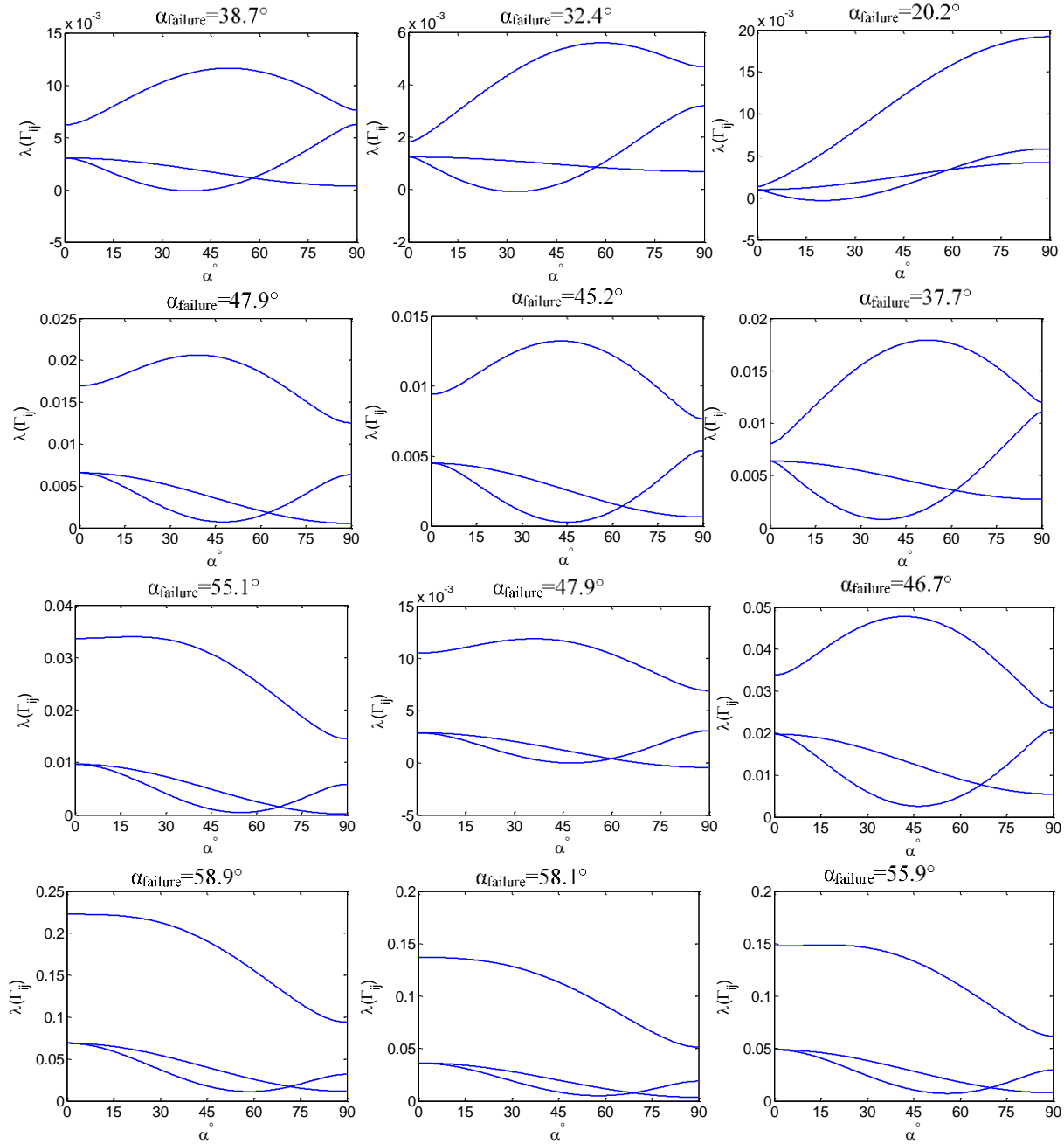


Figure 5.5 Eigenvalues of the acoustic tensor at failure state for different directions in triaxial experiments with 0.0, 5.0, and 20 MPa initial confinement, on specimens with grains with size of 0.02, 0.002, 0.0002, and 0.00002. The orientation of the failure plane (fault angle) is also shown for each case

In addition, it is seen that increasing the confinement leads to decrease in the fault angle. This result is also consistent with the observation made by an extensive set of experiments on rocks where the fault angle is reported to decrease by increase of confinement in conventional triaxial tests [112]. On the other hand, by decreasing the grains' sizes, while keeping the amount of initial hydrostatic confinement constant, it is seen that the fault angle increases significantly. So the grain size is seen, not only to affect the strength of the material, but to control the direction of the failure plane as well. In Figure 5.6 the change of direction of failure plane with change of grain size and initial confinement is presented.

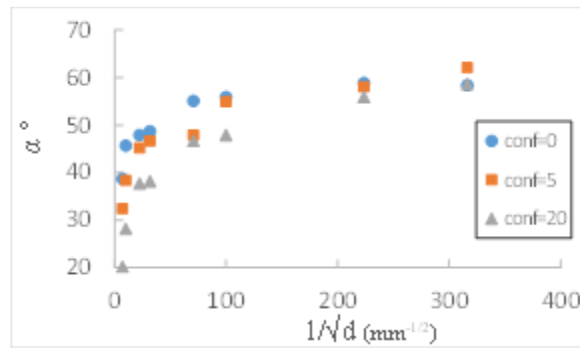


Figure 5.6 The effect of grain size on the direction of failure plane (Fault angle vs.  $1/\sqrt{d}$ )

Figure 5.6 presents the change of fault angle vs.  $1/\sqrt{d}$ . The three sets of data presented in this figure present the fault angle for simulations with 0.0, 5.0, and 20 MPa of confinement. It is seen clearly in this figure that for the case with no initial confinement, the fault angle for large grain sizes is very close to  $45^\circ$ , implying pure shear band. However by reducing the grain size, the fault angle increases up to  $\sim 60^\circ$ , implying a failure plane that is more inclined toward the vertical direction. This shows that by reducing the grain size failure mechanism shifts from complete shear band to a combination of shear and dilation bands. Further, for the cases with some amount of initial confinement, 5.0 and 20 MPa, fault angle for the largest grain size is much smaller than  $45^\circ$ , implying a failure plane that is more inclined toward the horizontal direction. The fault angle is



then increased up to about  $60^\circ$  by decreasing the grain sizes. It is thus seen that for cases with some initial confinement the failure mechanism shifts from compression-shear band to dilation-shear band by decreasing grain size.

#### 5.4.2 Volume control test results

In order to further demonstrate the ability of the method to incorporate the effect of grain size on the material behavior, volume control experiments are also simulated. This experiment is also composed of two parts. First, a desired amount of hydrostatic confining stress is applied on the specimen. This step is then followed by a completely strain control loading in the three principal directions. Compressive strain increments,  $d\varepsilon_{11}$ , are applied in the vertical direction, while tensile increments,  $d\varepsilon_{22} = d\varepsilon_{33} = \alpha(d\varepsilon_{11})$ , are applied on the two horizontal directions. Note that  $\alpha$  is negative constant.

In this step, the volumetric strain increment can be calculated as  $d\varepsilon_v = d\varepsilon_{ii} = d\varepsilon_{11}(1+2\alpha)$ . So the parameter  $\alpha$  will directly control the value of volume change. A very common subset of volume control tests is the *constant volume test* where  $\alpha$  is kept equal to -0.5 resulting in no volume change ( $d\varepsilon_v = 0$ ) during the whole loading process. The results of these experiments are commonly shown in the p-q (mean stress-deviatoric stress) plane. Figure 5.7 presents the q-p graphs for the constant volume tests with initial hydrostatic confinements of 0.0, 5.0, and 20 MPa and for grain sizes of 0.02 mm, 0.01 mm, 0.002 mm, and 0.001 mm. In all these cases it is seen that during the first increments of loading, mean stress remains constant and then decreases (the amount of reduction in mean stress increases with increase of initial confinement). The mean stress then reaches a minimum and starts increasing. However the deviatoric stress, q, is increasing

monotonically until failure. After failure in the vertical direction, the deviatoric stress will also start decreasing.

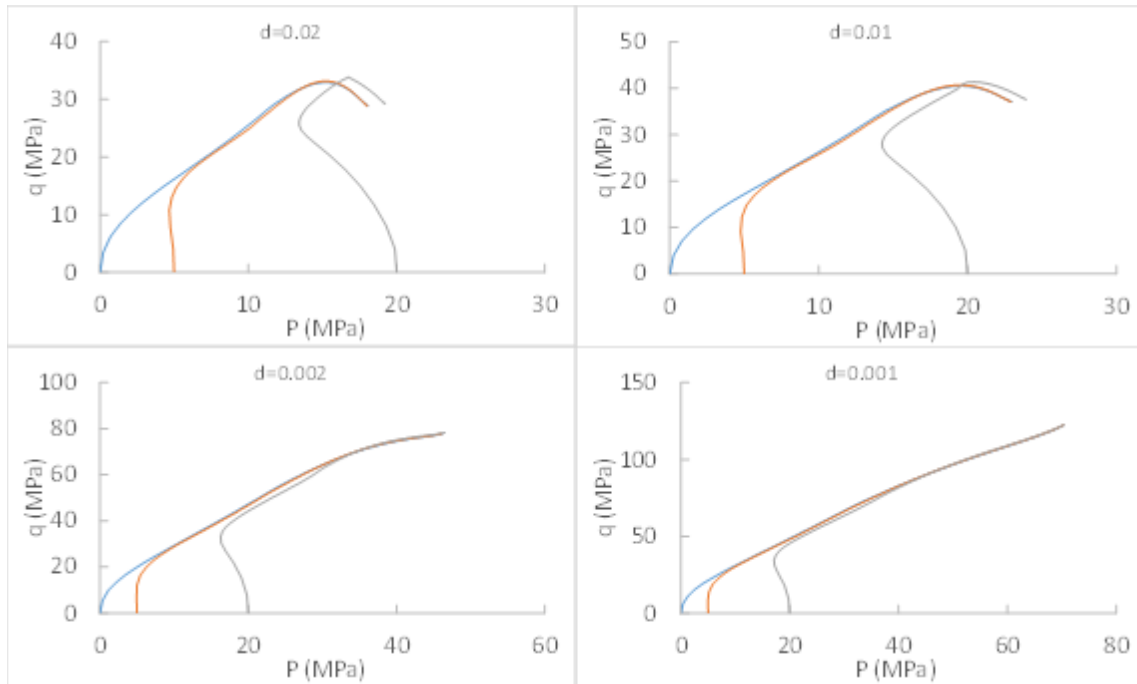


Figure 5.7 Evolution of deviatoric stress against the volumetric stress for constant volume tests after initial confinements of 0.0, 5.0, and 20 MPa, on grain sizes of 0.02, 0.01, 0.002, and 0.001

The trend of change in the deviatoric and mean stress components are governed by the evolution of vertical and lateral components. In Figure 5.8 the evolution of vertical and horizontal components of stress for the above cases has been reported. It is interesting to note that the vertical component of stress is always monotonically increasing from its initial value (the confining pressure) until failure state is reached. The reason is that in this direction, the loading is always compressive. However, the lateral directions which are loaded in tension, as expected, initially undergo compressive unloading and even occasionally reach tensile region (note that the strain controlled loading in the lateral direction is tensile). However, since the tensile strength is much smaller than compressive strength, soon the grain-pair interactions in tensile direction fail and they

also become compressive. Consequently the overall behavior of the material becomes more and more compressive as well.

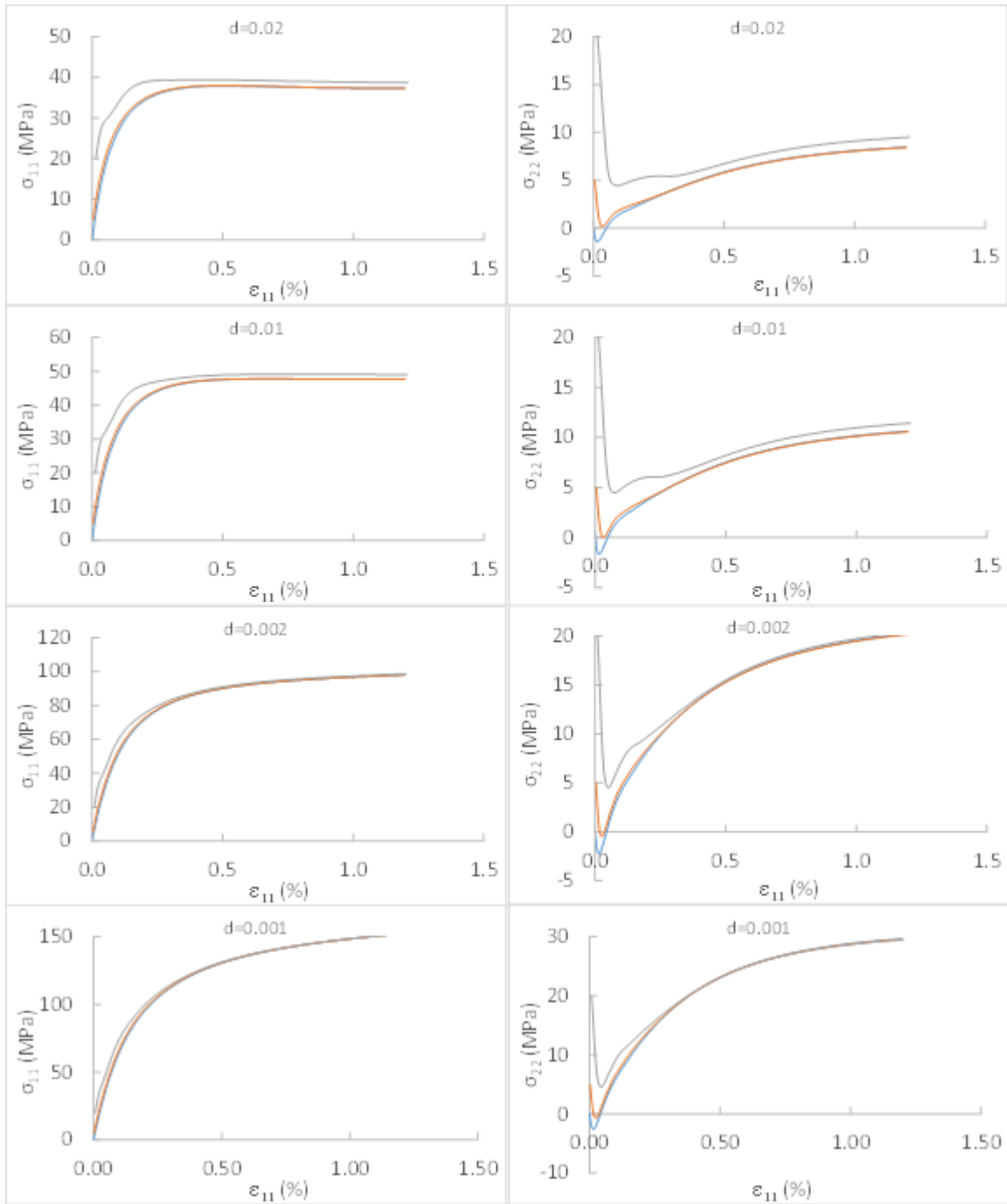


Figure 5.8 Evolution of  $\sigma_{11}$  and  $\sigma_{22}$  against  $\epsilon_{11}$  for constant volume tests after initial confinements of 0.0, 5.0, and 20 MPa, on grain sizes of 0.02, 0.01, 0.002, and 0.001

An important advantage of the present method is the fact that the macroscopic response is derived by studying grain-pair interactions in all different directions separately. For this loading procedure, in Figure 5.9, the evolution of normal and tangential components of intergranular force vector for experiments with 0.0 and 20 MPa of confinement on grain size of 0.01mm has been presented.

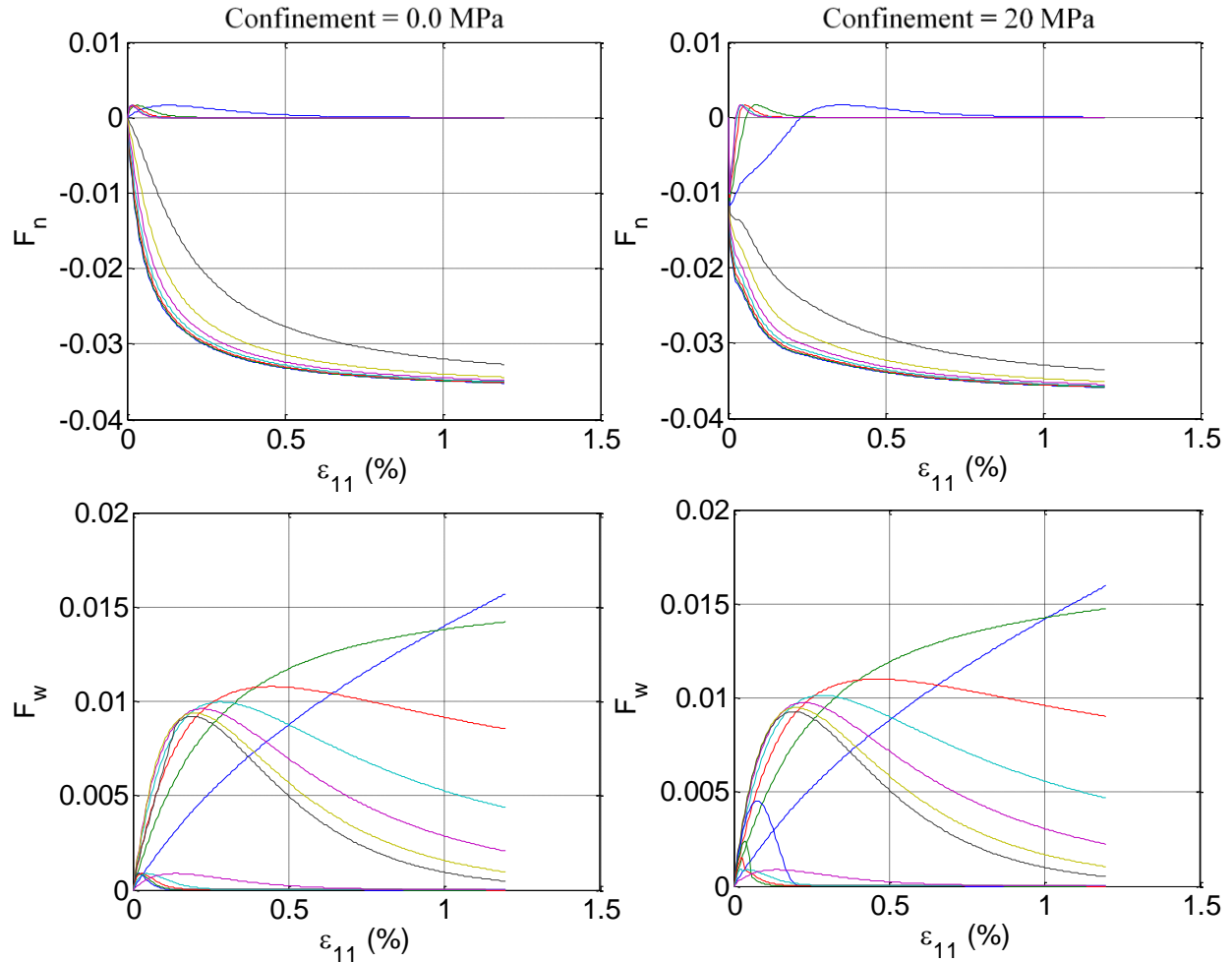


Figure 5.9 Evolution of the normal and tangential components of intergranular force vectors in different directions for simulations made on material with grain sizes of 0.01 and with confinements of 0.0 and 20 MPa

Note that these graphs present the evolution of the forces since the end of the initial confinement and the beginning of the strain controlled deviatoric loading. For the case of non-confined

experiment, normal components of intergranular force in all directions start at zero. In the directions that are more inclined toward the lateral direction (2-2 and 3-3 directions) the grain-pair interactions experience tension (since  $\varepsilon_{22}$  and  $\varepsilon_{33}$  have been applied in tension). These directions, however, fail very early since the tensile strength is much smaller than the compressive strength. On the other hand, the grain-pair interactions that are more inclined toward the vertical direction are under strain controlled compressive loading and will continue carrying the displacement without failing. The effect of the normal interaction on the tangential component of the force is also seen by comparing the tangential components of force corresponding to compressive and tensile grain-pair interactions (See Eq. 3.38 defining the damage parameter in the tangential direction as a function of normal component of displacement).

For the case where some initial confinement has been applied on the material, as it is seen in Figure 5.9, the material remains isotropic in the confinement step. Grain-pair interactions in all directions undergo same amount of normal force and displacement and zero tangential force and displacement. By starting the strain controlled deviatoric loading process, grain-pair interactions that are more inclined to the lateral directions (that are loaded in tension) will undergo compressive unloading and finally lose all their compression. They will continue being loaded in tension and finally fail in tension. However, the grain-pair interactions that are more inclined to the vertical direction experience more compression and carry the compressive displacement without failing.

So it is seen that eventually and in both cases (confined and unconfined), after some point, tensile interactions are failed and the behavior is governed fully by compressive grain-pair interactions. The result of this micro-scale phenomenon can be seen in the evolution of macroscopic stress components (shown in Figure 5.8). It is seen in Figure 5.8 that even the lateral components of stress,  $\sigma_{22} = \sigma_{33}$ , after a relatively small period of compressive unloading and occasionally a tensile

loading, will become more and more compressive. The reason is that, as it was discussed before, the tensile grain-pair interactions fail very quickly and they will not have any more contribution to the macroscopic stress tensor.

In order to understand the failure mechanism, a study on the evolution of the eigenvalues of the stiffness tensor for all these experiments is also performed. Figure 5.10 presents the evolution of eigenvalues of the volume control tests with the three values of initial confinement of 0.0, 5.0, and 20 MPa and for grain sizes of 0.02 mm, 0.01 mm, 0.002 mm, and 0.001 mm vs. the axial compressive strain. In the figure, the graphs in the first, second, third, and fourth row represent results for grains sizes of 0.02, 0.01, 0.002, and 0.001 mm respectively. As expected, the initial eigenvalues of the stiffness tensor increase by both, increasing the initial confinement and also reduction of grain size. By the end of the hydrostatic confinement step and at the beginning of the deviatoric loading, the material is still isotropic (because grain-pair interactions in all different directions experience the same amount of normal force and displacement and no tangential force or displacement). In this stage the stiffness tensor has only three distinct eigenvalues. One of these eigenvalues (the largest one) belongs to the dilatational mode. The intermediate component belongs to the deviatoric component in the normal direction and the smallest value (which is equal to half of the deviatoric component) belongs to the shear (isochoric) component.

However, during the deviatoric loading process, it is clear that the loading is axisymmetric. Because of the nonlinear force-displacement relationships used in this study, the normal and tangential stiffness coefficients will change due to the displacement they experience. So the loading will *induce* anisotropy into the material and the material will change into a transversely isotropic material. For a description of the elastic properties and eigenvalues and eigenvectors of the stiffness matrix of transversely isotropic materials see Appendix A.

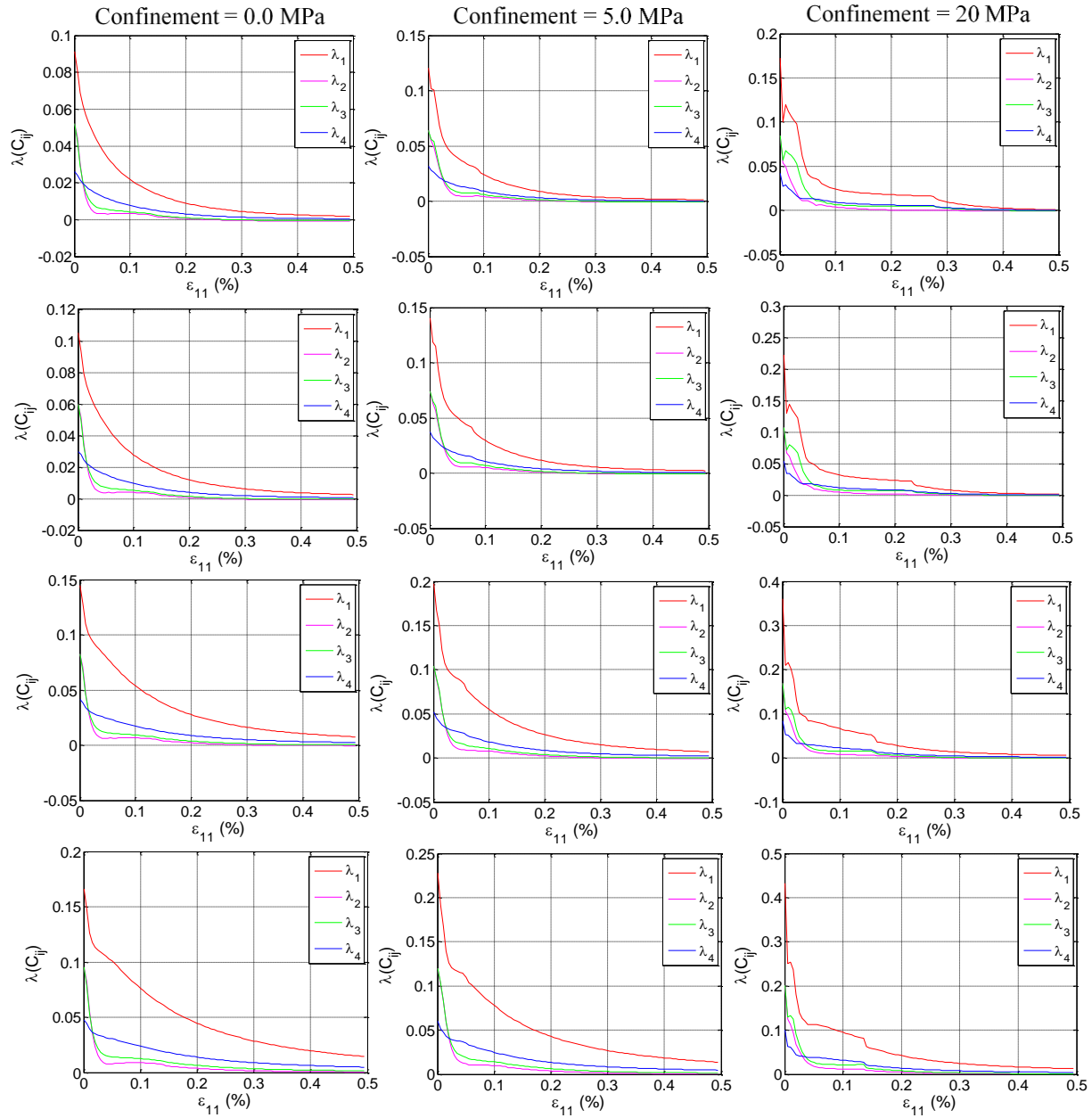


Figure 5.10 Evolution of the eigenvalues of the stiffness tensor against  $\varepsilon_{11}$  for constant volume tests after initial confinements of 0.0, 5.0, and 20 MPa, on grain sizes of 0.02, 0.01, 0.002, and 0.001

It is seen, from Figure 5.10, that at the beginning of the deviatoric loading process, the largest eigenvalue is  $\lambda_1$ , which belongs to the dilatational model. While  $\lambda_4$ , which belongs to the shear mode, is the smallest eigenvalue. However, during the loading process and due to the induced anisotropy, the intermediate eigenvalue,  $\lambda_2$ , is decomposed into two distinct values,  $\lambda_2$  and  $\lambda_3$ .

After very few steps of the loading, these two branches decrease very rapidly and are the ones that will reach zero first. It is inferred that failure will be due to the combined action of dilatational and deviatoric (shear) modes. This implies that failure consists of formation of shear-dilation or shear-compression bands, rather than only shear bands in the  $45^\circ$  direction

It is seen, by close study of Figure 5.10, that all the eigenvalues decrease during the loading process. Initially, the smallest eigenvalue belongs to the shear mode in the plane of rotational symmetry ( $23$  plane). However, as the loading proceeds, the eigenvalues corresponding to the other shear term (in  $12$  plane) and deviatoric component also decrease very rapidly and tend toward zero. So, it is concluded that in constant volume experiments, the failure is a combination of shear-compression or shear-dilation bands.

## **5.5 Summary and Conclusions**

The method of Granular Micromechanics for the damage-plasticity behavior of cementitious materials, that was previously derived and validated in Chapter 3, has been expanded in the present Chapter to incorporate the effects of grain size. Grain size effect has been implemented into the modeling process from a micromechanical viewpoint.

The effects of grain size on the volume density of grain-pair interactions, relative displacement between two neighbor grains, initial stiffness of the intergranular contact in normal and tangential directions, and finally the damage parameters in normal and tangential directions have been incorporated in the model by introduction of simple size-effect proportional laws. These proportional laws are then incorporated into the macroscopic behavior through the developed modeling procedure.



The proposed model is then applied to simulate two different types of experiments. Triaxial compressive tests and also volume control tests have been simulated for materials with different grain sizes. It is seen that ultimately in all these cases, reduction of grain size, just like increasing the initial confining pressure, results in an increase in the initial stiffness, increase in the failure stress, increase in strain at failure, and a transition of failure from *brittle* to *ductile* type of failure. Also the change of grain size is seen to change the direction of failure plane significantly.

It is seen that incorporating the effect of grain size on the macroscopic behavior of the material from a microscopic viewpoint results in significant change in the behavior of grain-pair interactions. This will in turn affect the macroscopic behavior of the material. It is seen that not only the materials' macroscopic stiffness and strength are affected by change of grain size, but the failure plane direction and consequently the failure mechanism are also affected by change of grain size. In the triaxial test with no initial confinement, failure in a material with large grain size is mainly due to the formation of shear bands. Whereas decreasing the grain size results in a significantly higher fault angle (failure plane more inclined to the vertical direction), implying the formation of shear-dilation band. On the other hand, increasing the lateral confinement (by increasing the amount of initial hydrostatic confinement) results in a smaller value of fault angle. This implies that failure due to formation of shear-bands (for unconfined test) will be changed into formation of shear-compression bands (for highly confined tests). In the volume control test, however, failure is always in a combination of shear and dilatational modes.

## 6 MODELING INHERENT ANISOTROPY USING GRANULAR MICROMECHANICS

### 6.1 Introduction

Many materials show direction dependent response to loading or anisotropic behavior at macro-scale. In the broadest scheme, the directional dependency of material behavior is categorized into two major categories; namely *inherent* anisotropy and *induced* anisotropy. If the material shows direction dependent response to loading from the initial unloaded state, it is said to have inherent anisotropy. These include granular materials in which inter-granular mechanisms in different directions are not same, multiphase materials and materials with micro-cracks and fissures [140-145]. Directional dependent nature of materials response to loading is enhanced further by effect of loading, even for initially (*inherently*) isotropic materials. As loading progresses and the material is no longer in its initial unloaded state, different micro-scale mechanisms in different directions lead to the evolution of material directional dependent behavior. These phenomena include, but are not limited to, change of the inter-particle interactions, change in the shapes and sizes of particles, change of surface properties, change of contacts, damage and fracture, pore collapse, bond breakage, hardening or softening of the generally non-linear inter-particle behavior. Accumulation of effects of these phenomena results in enhanced direction dependent behavior which is usually referred to as *induced* anisotropy [47, 146-150].

For analyzing structures that are made of anisotropic granular materials, it is beneficial to use material constitutive models that are derived by considering the microscopic properties. One of

the most promising approaches for predicting the behavior of this class of materials is using micromechanical models where micro and macro scales are related to each other using a proper set of assumptions with constitutive laws defined in microscopic scale. This allows for the constitutive laws to represent more conveniently the directional properties of the material.

Other researchers have previously attempted to model anisotropic materials with similar methods, particularly microplane model. Traditionally, efforts for modeling anisotropic materials were through defining microscopic stiffness coefficients as functions of the direction of the contact [151, 152]. This approach was shown to be helpful for materials with less severe anisotropy and also not general anisotropy. More recently, the spectral decomposition approach was presented [153] which uses a spectral decomposition of stiffness tensor. Using this approach, it is possible to model transversely isotropic and orthotropic materials, however the method has been unable to model materials with higher level of anisotropy (namely materials with only one plane of elastic symmetry and completely anisotropic materials with no elastic symmetry). The granular micromechanics approach provides a feasible method for incorporating the influence of micro-scale mechanisms into continuum models [18, 56, 154].

For modeling isotropic materials, the method uses two micro-scale stiffness coefficients, one for the normal and one for the tangential direction. This is consistent with the number of independent components in the stiffness tensor of isotropic materials (Lamé constants). In the extended granular micromechanics model presented here, a directional density distribution function with maximum 18 parameters has been introduced which accounts for the directional distribution of number, length, and stiffness of grain-pair interactions. Further, in the most general case, 3 independent inter-granular stiffness coefficients (one for normal and two for the two tangential directions) govern the inter-granular behavior of the material. Thus, in its most general case the

model uses a total of  $3+18=21$  parameters (equal to the number of independent components in the stiffness matrix of a completely anisotropic (*triclinic*) material).

In this chapter, both methods of granular micromechanics (that with kinematic constraint and that with static constraint) have been enhanced to incorporate the effects of inherent anisotropy. For modeling isotropic materials, the method uses two micro-scale stiffness coefficients, one for the normal and one for the tangential direction. This is consistent with the number of independent components in the stiffness tensor of isotropic materials (Lamé constants). In the extended granular micromechanics model presented here, a directional density distribution function with maximum of 18 parameters has been introduced which accounts for the directional distribution of number, length, and stiffness of grain-pair interactions in a systematic manner that is consistent with the elastic symmetries resulting in different levels of isotropy. Further, in the most general case, 3 independent inter-granular stiffness coefficients (one for normal and two for the two tangential directions) govern the inter-granular behavior of the material. Thus, in its most general case the model uses a total of  $3+18=21$  parameters. This is equal to the number of independent components of a fully populated symmetric  $6\times 6$  matrix where are components are independent from each other.

Further, by appropriately modifying the distribution function according to the elastic symmetries of materials with different intermediate levels of isotropy, the method is shown to be able to recover the symmetries in the resulting macroscopic stiffness components. The distribution function is modified for one plane of elastic symmetry to obtain *monoclinic* materials, three mutually orthogonal planes of elastic symmetry to obtain *orthotropic* materials, and for an additional axis of rotational symmetry to obtain *transversely isotropic* materials. Closed-form solutions for stiffness components of completely anisotropic materials using both kinematic and

static approaches are presented. Finally, as a measure to show the effects of the micromechanical parameters of the model on the macroscopic behavior, elastic wave velocity [155] is discussed and its variation by changing micromechanical parameters is shown. Parts of this work have been published in 2016 [43].

## 6.2 Discussion on materials with different levels of anisotropy

In this section, a review of the stiffness matrix of materials with different levels of anisotropy is presented and the effect of planes of elastic symmetry on the number of nonzero independent coefficients in the stiffness matrix has been studied.

For a completely anisotropic material with no elastic symmetry the stiffness tensor,  $C_{ijkl}$ , can be written as a fully populated, symmetric,  $6 \times 6$  matrix with  $6 \times (6+1)/2 = 21$  independent components. If the material has only one plane of elastic symmetry, the number of independent components of the stiffness matrix will be reduced to 13. Provided that the plane of elastic symmetry is a coordinate plane, stiffness tensor will have 13 nonzero, mutually independent components and all the other components will be equal to zero. Otherwise, there will be more non-zero components in the stiffness tensor, but there will still be only 13 *independent* parameters [156, 157]. The stiffness tensor for materials whose only plane of elastic symmetry are 23, 13, and 12 planes respectively can be written as

$$\begin{pmatrix} c_{11} & c_{12} & c_{13} & c_{14} & 0 & 0 \\ c_{12} & c_{22} & c_{23} & c_{24} & 0 & 0 \\ c_{13} & c_{23} & c_{33} & c_{34} & 0 & 0 \\ c_{14} & c_{24} & c_{34} & c_{44} & 0 & 0 \\ 0 & 0 & 0 & 0 & c_{55} & c_{56} \\ 0 & 0 & 0 & 0 & c_{56} & c_{66} \end{pmatrix} \quad (6.1a)$$

$$\begin{pmatrix} c_{11} & c_{12} & c_{13} & 0 & c_{15} & 0 \\ c_{12} & c_{22} & c_{23} & 0 & c_{25} & 0 \\ c_{13} & c_{23} & c_{33} & 0 & c_{35} & 0 \\ 0 & 0 & 0 & c_{44} & 0 & c_{46} \\ c_{15} & c_{25} & c_{35} & 0 & c_{55} & 0 \\ 0 & 0 & 0 & c_{46} & 0 & c_{66} \end{pmatrix} \quad (6.1b)$$

$$\begin{pmatrix} c_{11} & c_{12} & c_{13} & 0 & 0 & c_{16} \\ c_{12} & c_{22} & c_{23} & 0 & 0 & c_{26} \\ c_{13} & c_{23} & c_{33} & 0 & 0 & c_{36} \\ 0 & 0 & 0 & c_{44} & c_{45} & 0 \\ 0 & 0 & 0 & c_{45} & c_{55} & 0 \\ c_{16} & c_{26} & c_{36} & 0 & 0 & c_{66} \end{pmatrix} \quad (6.1c)$$

If the material has two orthogonal planes of elastic symmetry, then the plane perpendicular to those two planes will also be a plane of elastic symmetry and the material is called an *orthotropic* material. Stiffness matrix of orthotropic materials has 9 independent constants and in material's principal directions, there will not be any interaction between normal and tangential components of stress and strain tensor. Stiffness tensor for an orthotropic material in its principal coordinate system will be of the following form

$$\begin{pmatrix} c_{11} & c_{12} & c_{13} & 0 & 0 & 0 \\ c_{12} & c_{22} & c_{23} & 0 & 0 & 0 \\ c_{13} & c_{23} & c_{33} & 0 & 0 & 0 \\ 0 & 0 & 0 & c_{44} & 0 & 0 \\ 0 & 0 & 0 & 0 & c_{55} & 0 \\ 0 & 0 & 0 & 0 & 0 & c_{66} \end{pmatrix} \quad (6.2)$$

Note that it can be easily shown that if the stiffness tensor is written in a coordinate system different from the material's principal coordinate system, the stiffness tensor will have more non-zero terms than that shown in Eq. 6.2. Nevertheless, the number of *independent* components of the stiffness tensor of an orthotropic material will always have 9 independent components, regardless of the coordinate system in which it is written.

If, furthermore, the material has a single axis of rotational symmetry and every plane containing that axis is a plane of rotational symmetry, the material is called *transversely isotropic*. In this

case, number of independent components of elastic stiffness matrix will be reduced to 5. Assuming, without loss of generality, that axis  $I$  is the axis of axisymmetry, the stiffness matrix will have the following form

$$\begin{pmatrix} c_{11} & c_{12} & c_{12} & 0 & 0 & 0 \\ c_{12} & c_{22} & c_{23} & 0 & 0 & 0 \\ c_{13} & c_{23} & c_{22} & 0 & 0 & 0 \\ 0 & 0 & 0 & \frac{c_{22}-c_{23}}{2} & 0 & 0 \\ 0 & 0 & 0 & 0 & c_{55} & 0 \\ 0 & 0 & 0 & 0 & 0 & c_{55} \end{pmatrix} \quad (6.3)$$

And finally if the material behaves identically in all different directions, it is said to be isotropic. For a completely isotropic material, all components of elastic stiffness tensor can be formulated using the two well know Lamé's constants ( $\lambda$  and  $\mu$ ) or alternatively modulus of elasticity (E) and Poisson's ratio ( $\nu$ ).

$$\begin{pmatrix} \lambda+2\mu & \lambda & \lambda & 0 & 0 & 0 \\ \lambda & \lambda+2\mu & \lambda & 0 & 0 & 0 \\ \lambda & \lambda & \lambda+2\mu & 0 & 0 & 0 \\ 0 & 0 & 0 & \mu & 0 & 0 \\ 0 & 0 & 0 & 0 & \mu & 0 \\ 0 & 0 & 0 & 0 & 0 & \mu \end{pmatrix} \quad (6.4)$$

It is seen that the number of independent components of the stiffness tensor depends on the elastic symmetries of the material. By taking into account the elastic symmetries present in materials with each level of anisotropy, the distribution of inter-granular contacts and their stiffness coefficients can be modified to represent their macroscopic behavior.

### 6.3 Modeling anisotropy using granular micromechanics with kinematic constraint

### 6.3.1 Derivation of stiffness tensor

In chapter 2, the general derivation of the model and calculation of the different components of stiffness tensor were presented. In particular, the summation formula for calculating the stiffness tensor was presented in Eq. 2.13 which is repeated here for convenience.

$$C_{ijkl} = \frac{I}{V} \sum_{\alpha} (l^{\alpha})^2 n_j^{\alpha} n_l^{\alpha} K_{ik}^{\alpha} \quad (6.5)$$

Writing the grain-pair stiffness tensor in the RVE coordinates,  $[K]$ , in terms of its normal and tangential components using Eq. 2.10, the stiffness tensor given in Eq. 6.5 can be written in expanded form as

$$C_{ijkl} = \frac{1}{V} \sum_{\alpha=1}^N n_j^{\alpha} n_l^{\alpha} \left( (l^{\alpha})^2 K_n^{\alpha} n_i^{\alpha} n_k^{\alpha} + (l^{\alpha})^2 K_s^{\alpha} s_i^{\alpha} s_k^{\alpha} + (l^{\alpha})^2 K_t^{\alpha} t_i^{\alpha} t_k^{\alpha} \right) \quad (6.6)$$

Not that the subscripts n, s, and t represent the normal and tangential stiffness coefficients and do not follow the index notation conventions. It is clear from Eq. 6.6 that the terms in the summation are products of the direction cosines, the branch length and stiffness coefficients associated with grain-pairs. For statistical modeling, these product terms can be binned into discrete solid angles. Thus, the summation in Eq. 6.6, over the total number of contacts within the system, can be rewritten as a summation over  $\theta$  and  $\phi$  as

$$C_{ijkl} = \frac{I}{V} \sum_{\theta} \sum_{\phi} \left[ \left( \sum_{\rho}^{N^{\rho}} (l^{\rho})^2 K_n^{\rho} \right) n_j n_l n_i n_k + \left( \sum_{\rho}^{N^{\rho}} (l^{\rho})^2 K_s^{\rho} \right) n_j n_l s_i s_k + \left( \sum_{\rho}^{N^{\rho}} (l^{\rho})^2 K_t^{\rho} \right) n_j n_l t_i t_k \right] \quad (6.7)$$

where  $N^{\rho}(\theta, \phi)$  is the total number of grain-pair contacts for a given solid angle defined by  $\theta$  and  $\phi$ , such that

$$N = \sum_{\theta} \sum_{\phi} N^{\rho}(\theta, \phi) \quad (6.8)$$



and the summation over  $\rho$  is the sum of the product of branch length square and the grain-pair stiffness for all grain-pairs in that solid angle. We now introduce a directional density distribution function,  $\xi(\theta, \phi)$ , defined as

$$\xi(\theta, \phi) = \frac{\sum (l^\rho)^2 K_n^\rho}{\sum_{\alpha=1}^N (l^\alpha)^2 K_n^\alpha} \quad (6.9)$$

which represents the relative measure of material stiffness in a given direction resulting from a combination of grain-size, number of grain-pair interactions and the grain-pair intrinsic stiffness. Further, we observe that for materials composed of many grain sizes and grain compositions, it is useful to define an average product of branch length square and the grain-pair stiffness,  $l^2 K_n$ , as

$$l^2 K_n = \frac{\sum_{\alpha=1}^N (l^\alpha)^2 K_n^\alpha}{N}; \quad N = VN_p \quad (6.10)$$

where  $l$  may be regarded as the average branch length,  $K_n$  as the average grain-pair normal stiffness for the material, and  $N_p$  is the number density of grain-pair interactions. The second and the third terms of the stiffness tensor in Eq. 6.7 can be treated in a similar manner. Thus, Eq6. 6.7 through 6.10 can be combined and written in an integral form as follows

$$\begin{aligned} C_{ijkl} &= l^2 N_p \int_{\theta=0}^{\pi} \int_{\phi=0}^{2\pi} (K_n n_j n_l n_i n_k + K_s n_j n_l s_i s_k + K_t n_j n_l s_i s_k) \xi(\theta, \phi) \sin \theta d\phi d\theta \\ &= l^2 N_p \int_{\theta=0}^{\pi} \int_{\phi=0}^{2\pi} (K_{ik} n_j n_l) \xi(\theta, \phi) \sin \theta d\phi d\theta \end{aligned} \quad (6.11)$$

The fourth rank elastic stiffness tensor,  $C_{ijkl}$ , in its most general form has  $3^4=81$  independent constants. For the purposes of discussing material anisotropy, we consider symmetries of the stress and strain tensors (minor symmetries of stiffness tensor), thus reducing the number of independent constants to 36. Further, taking into account the *major* symmetries of stiffness tensor ( $C_{ijkl}=C_{klij}$ )

reduces the number of independent constants needed for completely anisotropic materials to 21 constants. The stiffness components are computed by imposing the symmetries of the stress and strain tensors as follows

$$\frac{\sigma_{pq} + \sigma_{qp}}{2} = \frac{(C_{pqrs} + C_{pqsr}) + (C_{qprs} + C_{qpsr})}{4} (\varepsilon_{rs} + \varepsilon_{sr}) + \frac{(C_{pqrs} + C_{pqsr}) - (C_{qprs} + C_{qpsr})}{4} (\varepsilon_{rs} - \varepsilon_{sr}) \quad (6.12)$$

where the left hand side is the average Cauchy stress and shear strain is taken as  $\gamma_{kl} = \varepsilon_{kl} + \varepsilon_{lk}$  and the anti-symmetric part ( $\varepsilon_{kl} - \varepsilon_{lk}$ ) is discarded. In Eq. 6.12, the indices p, q, r, and s do not follow the index notation conventions. Further reductions on the number of independent components in stiffness matrix are brought about due to the presence of elastic symmetries [156] as discussed in the previous section.

### 6.3.2 Density distribution function

It is clear from Eq. 6.11, that the directional density distribution function,  $\xi(\theta, \phi)$ , plays a key role in the determination of material anisotropy in granular micromechanics method. This function determines the density of number, stiffness, and grain-size of grain-pair interactions in different directions. The anisotropy arising from a smooth variation of grain-pair properties can be represented using a directional density distribution function expressed as spherical harmonic expansion given as

$$\xi(\theta, \phi) = \frac{1}{4\pi} \left\{ 1 + \sum_{k=2}^{\infty} \left[ a_{k0} P_k(\cos \theta) + \sum_{m=1}^{\infty} P_k^m(\cos \theta) (a_{km} \cos m\phi + b_{km} \sin m\phi) \right] \right\} \quad (6.13)$$

In the above equation, the summation over  $k$  (shown by  $\Sigma'$ ) is done only with respect to even indices of  $k$ .  $P_k(\cos \theta)$  is the  $k^{th}$ -degree Legendre polynomial with respect to  $\cos \theta$ ,  $P_k^m(\cos \theta)$  is its  $m^{th}$  associated Legendre function, and  $a_{k0}$ ,  $a_{km}$ , and  $b_{km}$  are directional density parameters representing the directional dependence of the mechanical behavior. The equation used for the

distribution function has the characteristic that all its terms are orthogonal to one, such that its integral over the surface of a unit sphere will always be equal to unity regardless of the number of terms included in the function, given as  $\int \int_{\theta \phi} \xi(\theta, \phi) \sin \theta d\theta d\phi = 1$ . This is consistent with the definition of the density distribution function,  $\xi$ , given in Eq. 6.9.

It is shown that inclusion of first three harmonics with the following parameters:  $a_{20}, a_{40}, a_{22}, a_{42}, a_{44}, a_{64}, b_{22}, b_{42}, b_{44}, b_{64}, b_{21}, b_{41}, b_{43}, b_{63}, a_{21}, a_{41}, a_{43},$  and  $a_{63}$ , is both necessary and sufficient to model completely anisotropic materials with a fully populated stiffness matrix in which all components are mutually independent. In addition to these 18 geometric parameters, 3 microscopic stiffness components,  $k_n, k_s,$  and  $k_t$  make-up the necessary 21 constants to form the completely anisotropic stiffness matrix. Chang and Misra [158] used a limited expansion to demonstrate the feasibility of this approach for modeling materials with orthotropic properties.

Substituting the directional distribution function presented in Eq. 6.13 into the relationship for stiffness matrix in Eq. 6.11, closed-form solutions for all stiffness components can be found as listed in Table 6.1. It can be seen that the derived components of stiffness matrix are mutually independent which is consistent with completely anisotropic materials and do not satisfy the Cauchy relations discussed by Love in [159] as one of the four tests for an adequate structure theory of solid bodies. It is also notable that by including appropriate terms in the distribution function,  $\xi(\theta, \phi)$ , materials with different levels of anisotropy ranging from completely isotropic to completely anisotropic can be modeled.

Table 6.1 Closed form equations of all components of stiffness matrix of a completely anisotropic material, derived based on the present method

$C_{11}$	$L^2 N_p \left\{ \frac{1}{15} (3k_n + 2k_s) + \frac{2}{105} a_{20} (6k_n + k_s) + \frac{8}{315} a_{40} (k_n - k_s) \right\}$
$C_{22}$	$L^2 N_p \left\{ \frac{1}{15} \left( 3k_n + \frac{3}{4} k_s + \frac{5}{4} k_t \right) + \frac{1}{140} a_{20} \left( -8k_n + k_s - \frac{7}{3} k_t \right) + \frac{1}{105} a_{40} (k_n - k_s) \right. \\ \left. + \frac{2}{35} a_{22} (6k_n + k_s) + \frac{4}{21} a_{42} (-k_n + k_s) + \frac{1}{3} a_{44} (8k_n + k_s - 9k_t) + 3a_{64} (k_s - k_t) \right\}$
$C_{33}$	$L^2 N_p \left\{ \frac{1}{15} \left( 3k_n + \frac{3}{4} k_s + \frac{5}{4} k_t \right) + \frac{1}{140} a_{20} \left( -8k_n + k_s - \frac{7}{3} k_t \right) + \frac{1}{105} a_{40} (k_n - k_s) + \frac{2}{35} a_{22} (-6k_n - k_s) + \frac{4}{21} a_{42} (k_n - k_s) + \frac{1}{3} a_{44} (8k_n + k_s - 9k_t) + 3a_{64} (k_s - k_t) \right\}$
$C_{12}$	$L^2 N_p \left\{ \frac{1}{15} (k_n - k_s) + \frac{1}{105} a_{20} (k_n - k_s) + \frac{4}{315} a_{40} (-k_n + k_s) + \frac{2}{35} a_{22} (k_n - k_s) + \frac{4}{21} a_{42} (k_n - k_s) \right\}$
$C_{13}$	$L^2 N_p \left\{ \frac{1}{15} (k_n - k_s) + \frac{1}{105} a_{20} (k_n - k_s) + \frac{4}{315} a_{40} (-k_n + k_s) + \frac{2}{35} a_{22} (-k_n + k_s) + \frac{4}{21} a_{42} (-k_n + k_s) \right\}$
$C_{23}$	$L^2 N_p \left\{ \frac{1}{15} \left( k_n + \frac{1}{4} k_s - \frac{5}{4} k_t \right) + \frac{1}{420} a_{20} (-8k_n + k_s + 7k_t) + \frac{1}{315} a_{40} (k_n - k_s) + \frac{1}{3} a_{44} (-8k_n - k_s + 9k_t) + 3a_{64} (k_t - k_s) \right\}$
$C_{44}$	$L^2 N_p \left\{ \frac{1}{15} \left( k_n + \frac{2}{8} k_s + \frac{10}{8} k_t \right) + \frac{1}{420} a_{20} (-8k_n + k_s - 7k_t) + \frac{1}{315} a_{40} (k_n - k_s) + \frac{1}{3} a_{44} (-8k_n - k_s + 9k_t) + 3a_{64} (k_t - k_s) \right\}$
$C_{55}$	$L^2 N_p \left\{ \frac{1}{15} \left( k_n + \frac{7}{8} k_s + \frac{5}{8} k_t \right) + \frac{1}{420} a_{20} (4k_n - 4k_s + 7k_t) + \frac{4}{315} a_{40} (-k_n + k_s) + \frac{1}{280} a_{22} (-16k_n - 19k_s + 7k_t) + \frac{1}{168} a_{42} (-32k_n + 11k_s + 21k_t) + \frac{1}{8} a_{62} (k_t - k_s) \right\}$
$C_{66}$	$L^2 N_p \left\{ \frac{1}{15} \left( k_n + \frac{7}{8} k_s + \frac{5}{8} k_t \right) + \frac{1}{420} a_{20} (4k_n - 4k_s + 7k_t) + \frac{4}{315} a_{40} (-k_n + k_s) + \frac{1}{280} a_{22} (16k_n + 19k_s - 7k_t) + \frac{1}{168} a_{42} (32k_n - 11k_s - 21k_t) + \frac{1}{8} a_{62} (k_t - k_s) \right\}$
$C_{14}$	$L^2 N_p \left\{ \frac{2}{35} b_{22} (k_n - k_s) + \frac{4}{21} b_{42} (k_n - k_s) \right\}$
$C_{24}$	$L^2 N_p \left\{ \frac{1}{35} b_{22} (6k_n + k_s) + \frac{2}{21} b_{42} (-k_n + k_s) + \frac{1}{3} b_{44} (8k_n + k_s - 9k_t) + 3b_{64} (k_t - k_s) \right\}$
$C_{34}$	$L^2 N_p \left\{ \frac{1}{35} b_{22} (6k_n + k_s) + \frac{2}{21} b_{42} (-k_n + k_s) + \frac{1}{3} b_{44} (-8k_n - k_s + 9k_t) + 3b_{64} (-k_t + k_s) \right\}$
$C_{56}$	$L^2 N_p \left\{ \frac{1}{280} b_{22} (16k_n + 19k_s - 7k_t) + \frac{1}{168} b_{42} (32k_n - 11k_s - 21k_t) \right\}$
$C_{15}$	$L^2 N_p \left\{ \frac{1}{70} b_{21} (-6k_n - k_s) + \frac{4}{63} b_{41} (-k_n + k_s) \right\}$
$C_{25}$	$L^2 N_p \left\{ \frac{1}{280} b_{21} (-8k_n + k_s + 7k_t) + \frac{1}{63} b_{41} (k_n - k_s) + \frac{1}{6} b_{43} (-4k_n + k_s + 3k_t) + \frac{1}{2} b_{63} (k_t - k_s) \right\}$
$C_{35}$	$L^2 N_p \left\{ \frac{1}{280} b_{21} (-24k_n + 3k_s - 7k_t) + \frac{1}{21} b_{41} (k_n - k_s) + \frac{1}{6} b_{43} (4k_n - k_s - 3k_t) + \frac{1}{2} b_{63} (k_t - k_s) \right\}$
$C_{46}$	$L^2 N_p \left\{ \frac{1}{280} b_{21} (-8k_n + k_s - 7k_t) + \frac{1}{63} b_{41} (k_n - k_s) + \frac{1}{6} b_{43} (-4k_n + k_s + 3k_t) + \frac{1}{2} b_{63} (k_t - k_s) \right\}$
$C_{16}$	$L^2 N_p \left\{ \frac{1}{70} a_{21} (-6k_n - k_s) + \frac{4}{63} a_{41} (-k_n + k_s) \right\}$
$C_{26}$	$L^2 N_p \left\{ \frac{1}{280} a_{21} (-24k_n + 3k_s - 7k_t) + \frac{1}{21} a_{41} (k_n - k_s) + \frac{1}{6} a_{43} (-4k_n + k_s + 3k_t) + \frac{1}{2} a_{63} (k_t - k_s) \right\}$
$C_{36}$	$L^2 N_p \left\{ \frac{1}{280} a_{21} (-8k_n + k_s + 7k_t) + \frac{1}{63} a_{41} (k_n - k_s) + \frac{1}{6} a_{43} (4k_n - k_s - 3k_t) + \frac{1}{2} a_{63} (k_t - k_s) \right\}$
$C_{45}$	$L^2 N_p \left\{ \frac{1}{280} a_{21} (-8k_n + k_s - 7k_t) + \frac{1}{63} a_{41} (k_n - k_s) + \frac{1}{6} a_{43} (4k_n - k_s - 3k_t) + \frac{1}{2} a_{63} (k_t - k_s) \right\}$

The necessary terms can be identified based upon the planes of elastic symmetry that determine the structure of the stiffness matrix. For isotropic materials, it is clear that the density distribution function should be a constant in all directions and thus all the directional density parameters in Eq. 6.13 should vanish. Further, the grain-pair stiffness coefficients in the two tangential directions

should also be equal. Applying these modifications to the stiffness tensor presented in Table 6.1, the expressions for isotropic elastic constants are obtained (see Eq. 2.16)

These expressions are consistent with the thermodynamic limits for isotropic elastic constants for appropriately specified inter-granular stiffness coefficients. For example, the expression for Poisson's ratio is  $\nu = (k_n - k_s)/(4k_n + k_s)$ , which varies in the classical thermodynamically admissible range of -1 for  $k_n=0$  to 0.5 for  $k_s=-2k_n/3$ . It is seen that if the grain-pair tangential stiffness coefficient were to be always positive, Poisson's ratio would take values between -1 and 0.25 as discussed in a previous works [18, 45]. However, the inter-granular tangential stiffness coefficient does not represent the stiffness of isolated grain-pair; instead, it represents the collective stiffness behavior of the grain-pair and its extended neighborhood [154, 160, 161]. In this case, a negative value for tangential stiffness coefficient is admissible. Alternatively, the normal grain-pair behavior can be treated using a volumetric-deviatoric split of the normal displacement and the conjugate normal forces as in the microplane model [40]. This split leads to two different normal stiffness coefficients for the normal force-displacement relationship (volumetric and deviatoric). Under this type of volumetric-deviatoric split, the current model will also yield Poisson's ratio ranging between -1 to 0.5.

For modeling transversely isotropic materials in which the  $1-1$  axis is the axis of rotational symmetry, it is known that material behavior within the  $2-3$  plane is independent of the direction. So the density distribution function should be a function of only the polar angle from the vertical,  $\theta$ , and independent of the azimuth angle,  $\phi$ . In this case, the terms in density distribution function will be only the Legendre polynomials. Thus, the only non-zero directional density parameters are  $a_{20}$  and  $a_{40}$ . Considering the anisotropy in the material behavior, different inter-granular

stiffness coefficients in tangential direction are needed, that is  $k_s \neq k_t$ . Thus, for transversely isotropic materials, following 5 constants are used:  $k_n$ ,  $k_s$ ,  $k_t$ ,  $a_{20}$ , and  $a_{40}$ , which is consistent with number of independent components in macroscopic elastic stiffness matrix. It can be readily verified from Table 6.1 that the symmetry requirements for this class of materials (shown in Eq. 6.3) are satisfied by the resultant expressions.

For materials with higher levels of anisotropy, the density distribution function should be a function of azimuthal angle,  $\phi$ , and will include terms with associated Legendre functions. For orthotropic materials, the behavior in each of its three principal directions is different and four additional directional density parameters,  $a_{22}$ ,  $a_{42}$ ,  $a_{44}$ , and  $a_{64}$ , are needed leading to the expected 9 independent constants in the macroscopic stiffness tensor. Again from Table 6.1, it can be seen that the resulting stiffness tensor satisfies the requirements for this class of materials (shown in Eq. 6.2).

For materials with only one plane of elastic symmetry, choice of directional density parameters depends upon the plane of elastic symmetry. For plane 2-3 as the plane of elastic symmetry, the relevant parameters are  $b_{22}$ ,  $b_{42}$ ,  $b_{44}$ , and  $b_{64}$ , for plane 1-3 as the plane of elastic symmetry, the relevant parameters are  $b_{21}$ ,  $b_{41}$ ,  $b_{43}$ , and  $b_{63}$ , and for plane 1-2 as the elastic symmetry plane, the needed parameters  $a_{21}$ ,  $a_{41}$ ,  $a_{43}$ , and  $a_{63}$ . For this class of materials, the model has 13 constants and from Table 6.1, it is seen that stiffness components obtained using these 13 constants satisfy the requirements for materials with one plane of elastic symmetry (shown in Eq. 6.1a, b, and c, respectively). Finally, if none of the planes act as planes of elastic symmetry, all of the aforementioned directional density parameters should be included in the formula resulting in altogether 21 independent microscopic constants which is equal to the number of components of a fully populated 6×6 stiffness matrix. The resulting stiffness components presented in Table 6.1,

can be easily shown to be mutually independent which is consistent with the requirement for completely anisotropic materials.

Table 6.2 gives the terms that should be included in the directional density distribution function,  $\xi(\theta, \phi)$ , for modeling materials with different levels of elastic symmetries. First row shows the  $\xi(\theta, \phi)$  function for isotropic materials, and the following rows show terms that should be progressively added for materials with diminishing elastic symmetries. In the case of a material with no plane of elastic symmetry and 21 independent constants in the stiffness tensor, all the terms in Table 6.2 should be included in the directional density distribution function.

Table 6.2 Directional density distribution function, used for materials with different levels of anisotropy

$\xi =$	$\frac{1}{4\pi}$	Isotropy	
	$+\frac{1}{4\pi} [a_{20}P_2(\cos \theta) + a_{40}P_4(\cos \theta)]$	Transverse Isotropy	
	$+\frac{1}{4\pi} \left\{ \left[ (a_{22}P_2^2(\cos \theta) + a_{42}P_4^2(\cos \theta)) \right] \cos 2\phi \right.$ $\left. + \left[ (a_{44}P_4^4(\cos \theta) + a_{64}P_6^4(\cos \theta)) \right] \cos 4\phi \right\}$	Orthotropy	
	$+\frac{1}{4\pi} \left\{ \left[ (b_{22}P_2^2(\cos \theta) + b_{42}P_4^2(\cos \theta)) \right] \sin 2\phi \right.$ $\left. + \left[ (b_{44}P_4^4(\cos \theta) + b_{64}P_6^4(\cos \theta)) \right] \sin 4\phi \right\}$	1 Plane of elastic symmetry: 2-3 Plane	No elastic symmetry
	$+\frac{1}{4\pi} \left\{ \left[ (b_{21}P_2^1(\cos \theta) + b_{41}P_4^1(\cos \theta)) \right] \sin \phi \right.$ $\left. + \left[ (b_{43}P_4^3(\cos \theta) + b_{63}P_6^3(\cos \theta)) \right] \sin 3\phi \right\}$	1 Plane of elastic symmetry: 1-3 Plane	
	$+\frac{1}{4\pi} \left\{ \left[ (a_{21}P_2^1(\cos \theta) + a_{41}P_4^1(\cos \theta)) \right] \cos \phi \right.$ $\left. + \left[ (a_{43}P_4^3(\cos \theta) + a_{63}P_6^3(\cos \theta)) \right] \cos 3\phi \right\}$	1 Plane of elastic symmetry: 1-2 Plane	

The shapes of directional density distribution functions for all of the aforementioned levels of anisotropy are presented in Figure 6.1. For each case, the isometric 3D view and also the views

from 2-3 plane, 1-3 plane, and 1-2 plane are shown. Note that the elastic symmetries that result in different levels of isotropy in the material, manifest themselves in the geometrical symmetries (or lack thereof) that are evident in the distribution functions for different classes of materials.



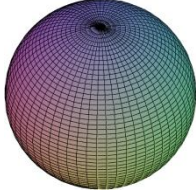
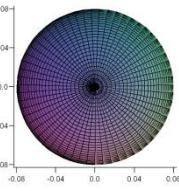
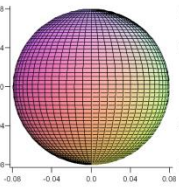
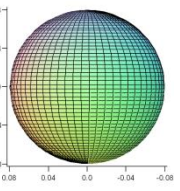
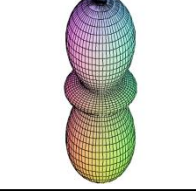
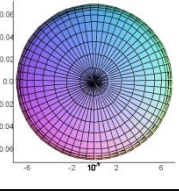
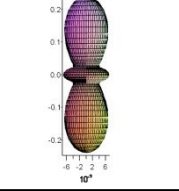
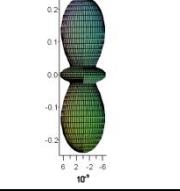
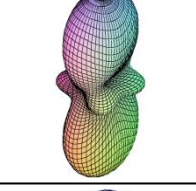
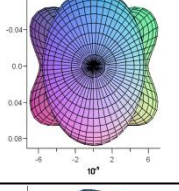
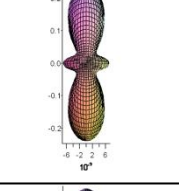
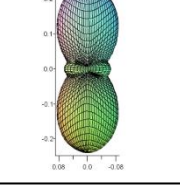
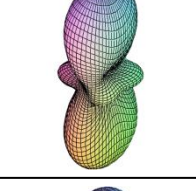
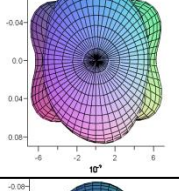
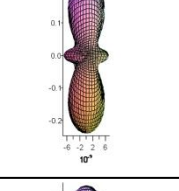
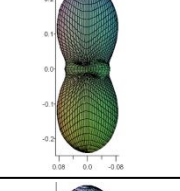
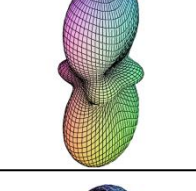
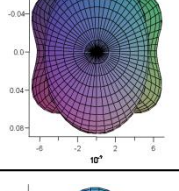
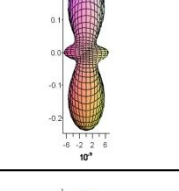
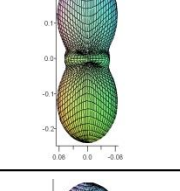
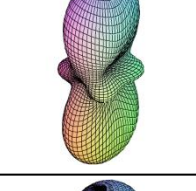
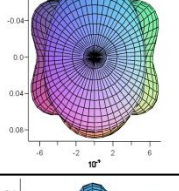
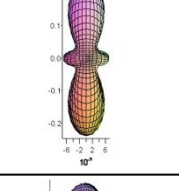
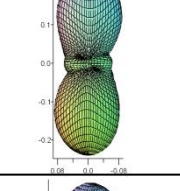
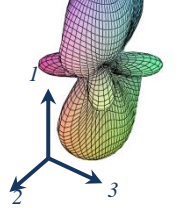
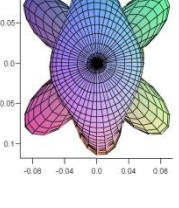
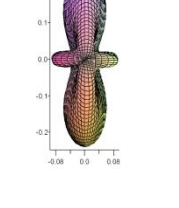
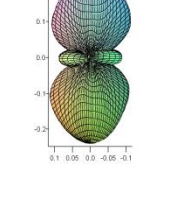
3D Perspective	23 Plane	13 Plane	12 Plane	Material type and $\xi$ function
				$\xi$ for isotropic materials $\xi=1/(4\pi)$
				$\xi$ for transversely isotropic materials $a_{20}=a_{40}=1.00$
				$\xi$ for orthotropic materials Additional parameters: $a_{22}=0.1$ ; $a_{42}=0.05$ $a_{44}=-0.0014$ ; $a_{64}=0.001$
				$\xi$ ; Symmetric about 23 plane; Additional parameters: $b_{22}=0.01$ ; $b_{42}=0.001$ $b_{44}=0.0008$ ; $b_{64}=0.0002$
				$\xi$ ; Symmetric about 13 plane: Parameters for orthotropy, plus $b_{21}=0.025$ ; $b_{41}=-0.008$ $b_{43}=0.0009$ ; $b_{63}=-0.0002$
				$\xi$ ; Symmetric about 12 plane: Parameters for orthotropy, plus $a_{21}=0.001$ ; $a_{41}=-0.005$ $a_{43}=-0.001$ ; $a_{63}=0.0008$
				$\xi$ for completely anisotropic materials. No elastic symmetry about any plane. Include all parameters above.

Figure 6.1 Density distribution function for materials with different levels of elastic symmetry and the parameters that need to be included in the harmonics expansion in order to show the required anisotropies

## 6.4 Modeling anisotropy using granular micromechanics with static constraint

### 6.4.1 Derivation of compliance and stiffness tensors

In chapter 2, the general derivation of the model with static (least square) assumption was presented resulting in Eq. 2.26b for the compliance tensor that is repeated here for convenience.

$$S_{ijkl} = \frac{l^2 N_{jr}^{-1} N_{ls}^{-1}}{V} \sum_{\alpha=1}^N S_{ik}^{\alpha} n_r^{\alpha} n_s^{\alpha} \quad (6.14)$$

Using Eq. 2.25 (showing the intergranular compliance matrix as a function of the normal and tangential components of inter-granular compliance coefficients), Eq. 6.14 can be expressed as

$$S_{ijkl} = \frac{N_{jr}^{-1} N_{lq}^{-1}}{V} \sum_{\alpha=1}^N n_r^{\alpha} n_q^{\alpha} \left( (l^{\alpha})^2 \frac{1}{k_n^{\alpha}} n_i^{\alpha} n_k^{\alpha} + (l^{\alpha})^2 \frac{1}{k_s^{\alpha}} s_i^{\alpha} s_k^{\alpha} + (l^{\alpha})^2 \frac{1}{k_t^{\alpha}} t_i^{\alpha} t_k^{\alpha} \right) \quad (6.15)$$

where summations are over all grain-pair interactions in the RVE. Note that throughout this work, the subscripts n, s, and t represent the inter-granular properties is normal ( $\mathbf{n}$ ), and tangential ( $\mathbf{s}$  and  $\mathbf{t}$ ) directions respectively and thus do not follow the index notation conventions.

For an RVE containing many ( $>10^6$ ) interacting grains, the exact knowledge of the material composition and properties, grain shapes and sizes, interfacial properties, etc. are unknown. Such detailed information is generally unattainable for almost all engineering materials. Therefore, the precise and true nature of every grain-pair interactions is unknown. However, this unfortunate missing information is compensated by the fortunate fact that generally for the determination of collective behavior we are not interested in the precise and detailed solution for exact motion of each and every grain in the RVE. In this work, we have chosen to treat the problem in a statistical sense by considering mean behaviors. Such statistical approximations are reasonably justified when firstly there is the absence of complete information about the microstructure and the micromechanical

parameters, and secondly, an incomplete solution, such as the mean behavior, based upon incomplete data is sufficient. With the aim of obtaining the estimate of the mean behavior, Eq. 6.15 can be rewritten observing that the terms in the summation are products of the direction cosines, the branch length and compliances associated with grain-pairs, which can be binned into discrete solid angles. Thus, the summation in Eq. 6.15, over the total number of contacts within the system, can be rewritten as a summation over  $\theta$  and  $\phi$  as

$$S_{ijkl} = \frac{N_{jr}^{-1} N_{lq}^{-1}}{V} \sum_{\theta} \sum_{\phi} \left[ \left( \sum_{\rho} \frac{(l^{\rho})^2}{k_n^{\rho}} \right) n_r n_q n_i n_k + \left( \sum_{\rho} \frac{(l^{\rho})^2}{k_s^{\rho}} \right) n_r n_q s_i s_k + \left( \sum_{\rho} \frac{(l^{\rho})^2}{k_t^{\rho}} \right) n_r n_q t_i t_k \right] \quad (6.16)$$

where the three summations over  $\rho$  represent summations over all inter-granular contacts whose orientation lies in a given solid angle range centered at  $\theta$  and  $\phi$ . For example, the term  $\sum_{\rho} (l^{\rho})^2 / k_n^{\rho}$  represents the sum of all  $(l^{\rho})^2 / k_n^{\rho}$  terms for all grain-pair interactions whose orientations are contained within a given solid angle range. For anisotropic materials, these sums will be different for different binned directions, which can be described using directional density distribution function,  $\xi(\theta, \phi)$ , that represents the directional distribution of the number, length, and stiffness of grain-pair interactions as

$$\frac{\sum_{\rho} (l^{\rho})^2 / k_n^{\rho}}{\sum_{\alpha=1}^N (l^{\alpha})^2 / k_n^{\alpha}} = \frac{\sum_{\rho} (l^{\rho})^2 / k_s^{\rho}}{\sum_{\alpha=1}^N (l^{\alpha})^2 / k_s^{\alpha}} = \frac{\sum_{\rho} (l^{\rho})^2 / k_t^{\rho}}{\sum_{\alpha=1}^N (l^{\alpha})^2 / k_t^{\alpha}} = \xi(\theta, \phi) \quad (6.17)$$

where it has been assumed that all the inter-granular compliances also follow the same distribution.

In addition, it is useful to define an average value of the terms  $(l^{\alpha})^2 / k_n^{\alpha}$  (and similarly for the shear terms) as

$$\frac{\sum_{\alpha=1}^N (l^\alpha)^2 / k_n^\alpha}{N} = l^2 / k_n; \quad \frac{\sum_{\alpha=1}^N (l^\alpha)^2 / k_s^\alpha}{N} = l^2 / k_s; \quad \frac{\sum_{\alpha=1}^N (l^\alpha)^2 / k_t^\alpha}{N} = l^2 / k_t \quad (6.18)$$

where  $l^2/k_n$ ,  $l^2/k_s$ , and  $l^2/k_t$  are average values for the RVE. Combining Eqs. 6.17 and 6.18 with Eq. 6.14, and defining  $\rho^c$  as the volume density of total number of grain-pair contacts ( $\rho^c = N/V$ ), the compliance tensor given in Eq. 15 can be written in integral form as

$$\begin{aligned} S_{ijkl} &= l^2 \rho^c N_{jr}^{-1} N_{lq}^{-1} \int_{\theta=0}^{\pi} \int_{\phi=0}^{2\pi} \left( \frac{1}{k_n} n_r n_q n_i n_k + \frac{1}{k_s} n_r n_q s_i s_k + \frac{1}{k_t} n_r n_q t_i t_k \right) \xi(\theta, \phi) \sin \theta d\phi d\theta \\ &= l^2 \rho^c N_{jr}^{-1} N_{lq}^{-1} \int_{\theta=0}^{\pi} \int_{\phi=0}^{2\pi} (S_{ik} n_r n_q) \xi(\theta, \phi) \sin \theta d\phi d\theta \end{aligned} \quad (6.19)$$

Now the fabric tensor,  $N_{ij}$ , introduced in Eq. 2.21 can also be treated from a statistical viewpoint such that the summation in Eq. 2.21, over the total number of contacts within the system, can be rewritten as a summation over  $\theta$  and  $\phi$  in a manner similar to Eq. 6.16

$$N_{ij} = \frac{1}{V} \sum_{\alpha=1}^N l_i^\alpha l_j^\alpha = \frac{1}{V} \sum_{\theta} \sum_{\phi} \left( \sum_{\rho} (l^\rho)^2 \right) n_i n_j \quad (6.20)$$

Subsequently the average branch length  $l$ , and directional density distribution of number and length of the grain-pair interactions,  $\xi'(\theta, \phi)$  may be introduced

$$\frac{\sum_{\alpha=1}^N (l^\alpha)^2}{N} = l; \quad \frac{\sum (l^\rho)^2}{\sum_{\alpha=1}^N (l^\alpha)^2} = \xi'(\theta, \phi) \quad (6.21)$$

As a result the second rank fabric tensor given in Eq. 6.20 can be written in an integral form as

$$N_{ij} = \rho^c \int_{\theta=0}^{2\pi} \int_{\phi=0}^{\pi} l_i l_j \xi'(\theta, \phi) \sin \theta d\theta d\phi = l^2 \rho^c \int_{\theta=0}^{2\pi} \int_{\phi=0}^{\pi} n_i n_j \xi'(\theta, \phi) \sin \theta d\theta d\phi \quad (6.22)$$

It is noteworthy that the two directional density distribution functions,  $\xi(\theta, \phi)$  and  $\xi'(\theta, \phi)$ , are distinct since they represent the distribution of different parameters, in contrast to the assumption

widely made in previous derivations of this type [45, 158, 162]. However for simplicity of subsequent discussion and calculations, the two directional density distribution functions are assumed to be the same in the remainder of this work where the focus is on elastic behavior. For inelastic behavior, the use of distinct distributions may be representative as observed from the analysis of regular grain assemblies using the described approach in [29], wherein the stiffness coefficients of grain-contacts in different direction evolves with loading whilst the micro-structure or fabric persists.

The fourth rank compliance tensor,  $S_{ijkl}$ , in its most general form has  $3^4=81$  independent constants. However, symmetry of stress and strain tensors leads to minor symmetries of compliance tensor and the constitutive equations can then be written in Voigt notation [163]. In this manner, the compliance tensor can be written as a  $6 \times 6$  matrix with 36 components. The components of such compliance matrix are calculated as follows

$$\gamma_{pq} = \varepsilon_{pq} + \varepsilon_{qp} = \left[ (S_{pqrs} + S_{pqsr}) + (S_{qprs} + S_{qpsr}) \right] \frac{\sigma_{rs} + \sigma_{sr}}{2} + \left[ (S_{pqrs} + S_{pqsr}) - (S_{qprs} + S_{qpsr}) \right] \frac{\sigma_{rs} - \sigma_{sr}}{2} \quad (6.23)$$

In this equation, shear strain is taken as  $\gamma_{ij} = \varepsilon_{ij} + \varepsilon_{ji}$ . Further, average value of the two shear stresses is taken as the Cauchy stress, and the difference,  $\sigma_{kl} - \sigma_{lk}$ , is discarded. Note that the indices p, q, r, and s used in Eq. 6.23 do not follow the index notation conventions.

After constructing the  $6 \times 6$  compliance matrix with this approach, major symmetry ( $S_{ijkl} = S_{klij}$ ) is also applied on the compliance matrix implying that the  $6 \times 6$  matrix is also symmetric and has only 21 independent constants. The macroscopic stiffness matrix can also be derived as the inverse of the global compliance tensor.

## 6.4.2 Density distribution function

The method using static constraint also uses the same form of density distribution function as that was presented in section 6.3.2 for the method with kinematic constraint. The expanded form of the density distribution function (in which all the coefficients and the Legendre polynomials and the Legendre associated functions have been expanded) is presented here.

$$\begin{aligned}
\xi_{(\theta,\phi)} = & \frac{1}{4\pi} \left( 1 + a_{20} \frac{3\cos^2\theta - 1}{2} + a_{40} \frac{35\cos^4\theta - 30\cos^2\theta + 3}{8} + a_{22}(3\sin^2\theta \cos 2\phi) \right. \\
& + a_{42} \left( \frac{105\cos^2\theta - 15}{2} \sin^2\theta \cos 2\phi \right) + a_{44}(105\sin^4\theta \cos 4\phi) \\
& + a_{64} \left( \frac{83160\cos^2\theta - 7560}{16} \sin^4\theta \cos 4\phi \right) + b_{22}(3\sin^2\theta \sin 2\phi) \\
& + b_{42} \left( \frac{105\cos^2\theta - 15}{2} \sin^2\theta \sin 2\phi \right) + b_{44}(105\sin^4\theta \sin 4\phi) \\
& + b_{64} \left( \frac{83160\cos^2\theta - 7560}{16} \sin^4\theta \sin 4\phi \right) + a_{21}(-3\sin\theta \cos\theta \cos\phi) \\
& + a_{41} \left( \frac{-35\cos^3\theta + 15\cos\theta}{2} \sin\theta \cos\phi \right) + a_{43}(-105\cos\theta \sin^3\theta \cos 3\phi) \\
& + a_{63} \left( -\frac{27720\cos^3\theta - 7560\cos\theta}{16} \sin^3\theta \cos 3\phi \right) + b_{21}(-3\sin\theta \cos\theta \sin\phi) \\
& + b_{41} \left( \frac{-35\cos^3\theta + 15\cos\theta}{2} \sin\theta \sin\phi \right) + b_{43}(-105\cos\theta \sin^3\theta \sin 3\phi) \\
& \left. + b_{63} \left( -\frac{27720\cos^3\theta - 7560\cos\theta}{16} \sin^3\theta \sin 3\phi \right) \right) \tag{6.24}
\end{aligned}$$

Note that the terms that should be used for modeling materials with all different levels of inherent anisotropy are the same for the two methods. Eq. 6.24 is in fact the expanded form of the distribution function used for completely anisotropic materials shown in a more compact form in Table 6.2.

Using the complete distribution function (that presented in Eq. 6.24) the components of the fabric tensor for the fully anisotropic material is derived as follows

$$N_{ij} = \frac{l^2 \rho^c}{15} \begin{pmatrix} 2a_{20} + 5 & -3a_{21} & -3b_{21} \\ -3a_{21} & -a_{20} + 6a_{22} + 5 & 6b_{22} \\ -3b_{21} & 6b_{22} & -a_{20} - 6a_{22} + 5 \end{pmatrix} \quad (6.25)$$

It is seen here that, although the complete  $\zeta(\theta, \phi)$  function given in Eq. 6.24 is used in calculating the fabric tensor, only the terms from the first harmonics expansion (terms with  $k=2$  in Eq. 6.13) appear in after the integration. The derived fabric tensor is used in Eq. 6.19 for calculating the compliance tensor for the completely anisotropic material. For modeling materials with any level of isotropy, the distribution function needs to be modified in the manner that was discussed in section 6.3.2 for the kinematic method and was summarized in Table 6.2.

Since, the closed-form solutions for triclinic materials will have very large number of terms, for illustration purposes only the stiffness coefficients for transversely isotropic and completely isotropic materials have been presented here. It is seen that by including the first two harmonics with coefficients  $a_{20}$  and  $a_{40}$  the method can produce all the five independent components of the stiffness matrix of a transversely isotropic material while satisfying the symmetry requirements.

The macroscopic stiffness matrix is found in the following form:

$$C = \frac{l^2 N_p}{90} \begin{bmatrix} \frac{A}{B} & \frac{E}{B} & \frac{E}{B} & 0 & 0 & 0 \\ \frac{E}{B} & \frac{C}{D} & \frac{F}{D} & 0 & 0 & 0 \\ \frac{E}{B} & \frac{F}{D} & \frac{C}{D} & 0 & 0 & 0 \\ 0 & 0 & 0 & \frac{C-F}{2D} & 0 & 0 \\ 0 & 0 & 0 & 0 & \frac{G}{H} & 0 \\ 0 & 0 & 0 & 0 & 0 & \frac{G}{H} \end{bmatrix} \quad (6.26)$$

Where parameters  $A \sim H$  are given in Table 6.3. Note that the parameters  $A \sim H$  are introduced here merely to simplify the representation of the stiffness matrix.

Table 6.3 List of parameters defined for showing components of stiffness matrix of anisotropic materials

A	$2k_n(2a_{20}+5)^2[21(k_n+4k_s)+k_n(3a_{20}-4a_{40})+k_s(4a_{40}-24a_{20})]$
B	$35(3k_n+2k_s)+k_n(15a_{20}-20a_{40})+k_s(20a_{20}+20a_{40}-14a_{20}^2)$
C	$k_n(a_{20}-5)^2[k_n^2(882(k_t+5k_s)+k_s(-252a_{20}-840a_{40}+168a_{20}a_{40}-126a_{20}^2))+k_t(252a_{20}-336a_{40}-48a_{20}a_{40}+168a_{20}^2+32a_{40}^2))+k_nk_s(k_s(6615+2457a_{20}+840a_{40}-168a_{20}a_{40}-756a_{20}^2)+k_t(18081+2321a_{20}-3108a_{40}+96a_{20}a_{40}-36a_{20}^2-64a_{40}^2))+k_s^2k_t(14112+4032a_{20}+3444a_{40}-48a_{20}a_{40}-2628a_{20}^2+32a_{40}^2)]$
D	$k_n^2[k_s(11025-630a_{20}-2100a_{40}+420a_{20}a_{40}-315a_{20}^2)+k_t(2205+630a_{20}-840a_{40}-120a_{20}a_{40}+45a_{20}^2+80a_{40}^2)]+k_nk_s[k_s(7350+630a_{20}+2100a_{40}-420a_{20}a_{40}-1890a_{20}^2+294a_{20}^3)+k_t(10290-630a_{20}-1120a_{40}+520a_{20}a_{40}-594a_{20}^2-160a_{40}^2+56a_{20}^2a_{40}-42a_{20}^3)]+k_s^2k_t(5880+1960a_{40}-400a_{20}a_{40}-1656a_{20}^2+80a_{40}^2-56a_{20}^2a_{40}+336a_{20}^3)$
E	$2k_n(k_n - k_s)(2a_{20}+5)(5-a_{20})(21+3a_{20}-4a_{40})$
F	$-k_n(a_{20}-5)^2[k_s^2k_t(3528+1008a_{20}+1596a_{40}+48a_{20}a_{40}-900a_{20}^2-32a_{40}^2)+k_nk_s[-k_s(6615+2457a_{20}+840a_{40}-168a_{20}a_{40}-756a_{20}^2)+k_t(8379+1449a_{20}-1932a_{40}-96a_{20}a_{40}+36a_{20}^2+64a_{40}^2)]]-k_n^2\{k_s(4410-252a_{20}-840a_{40}+168a_{20}a_{40}-126a_{20}^2)+k_t(882+252a_{20}-336a_{40}-48a_{20}a_{40}+18a_{20}^2+32a_{40}^2)\}]$
G	$252k_nk_s k_t (a_{20}-5)^2(2a_{20}+5)^2$
H	$k_n[k_s(2625-315a_{20}^2+42a_{20}^3)+k_t(3675+1710a_{20}+800a_{40}-160a_{20}a_{40}-477a_{20}^2+8a_{20}^2a_{40}-132a_{20}^3)]+k_tk_s(4200+1440a_{20}-800a_{40}-160a_{20}a_{40}+162a_{20}^2-8a_{20}^2a_{40}+6a_{40}^3)$

It is known that in transversely isotropic materials, the Poisson's ratios will be different based on the directions in which they are acting. In Figure 6.2, the variations of the two Poisson's ratios ( $\nu_{12}$  and  $\nu_{23}$ ) are shown with respect to the microscopic parameters, where the ratios of the tangential and normal inter-granular stiffness coefficients are defined as  $\beta_s=k_s/k_n$  and  $\beta_t=k_t/k_n$ . Figure 5.2 also shows for comparison the Poisson's ratios predicted using the alternative kinematic approach.

The closed-form solutions for Young's modulus, E, and Poisson's ratio,  $\nu$ , using least-squares approach will be as follows. Note that this closed form solution for isotropic materials has been presented previously (see for example [18, 45])

$$E = \frac{5l^2 \rho^c}{3} \frac{k_n k_s}{2k_n + 3k_s} \quad \text{and} \quad \nu = \frac{k_n - k_s}{2k_n + 3k_s} \quad (6.27)$$



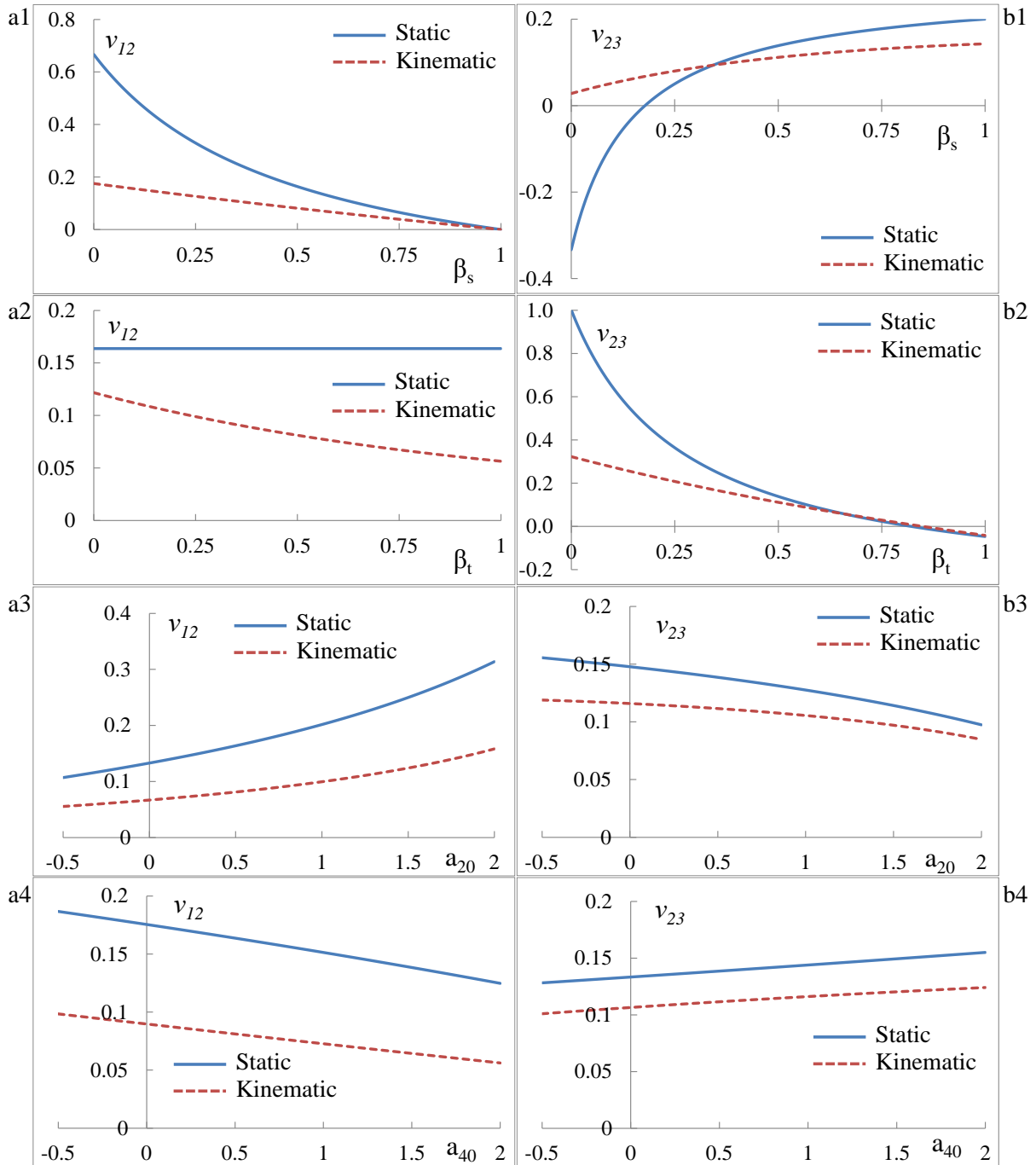


Figure 6.2 Variation of the two Poisson ratios of transversely isotropic materials with changing (sections a1 and b1)  $\beta_s$  while  $\beta_t=a_{20}=a_{40}=0.5$ ; (sections a2 and b2)  $\beta_t$  while  $\beta_s=a_{20}=a_{40}=0.5$ ; (sections a3 and b3)  $a_{20}$  while  $\beta_s= \beta_t= a_{40}=0.5$ ; (sections a4 and b4)  $a_{40}$  while  $\beta_s= \beta_t= a_{40}=0.5$

For the positive values of grain-pair stiffness coefficients, the Poisson ratio is predicted in the range of  $-1/3$  to  $1/2$  for least-squares approach and  $-1.0$  to  $1/4$  for the kinematic approach. From a

practical viewpoint, these ranges of Poisson's ratio are valid for many engineering materials. It is also noteworthy that from the viewpoint of positive semi-definiteness of macro-scale deformation energy, negative grain-pair stiffness could be admissible. In this case, the whole thermodynamically admissible range of Poisson's ratio (from -1.0 to 0.5) can be modeled with both approaches. At the inter-granular scales, the negative stiffness represents certain mechanisms that are manifested due to the immediate and extended neighborhood. For the least-squares approach, the normal stiffness must take negative values (up to  $-2k_n/3$  for  $\nu=-1$ ). The negative normal stiffness for these highly auxetic materials connotes severe dilation attributable to grain-pair as the grain neighborhood experiences shear. For the kinematic approach, the shear stiffness must take negative values (up to  $-2k_n/3$  for  $\nu=0.5$ ). In this case, the negative shear stiffness for these materials approaching incompressibility implies shear softening attributable to grain-pair as the grain neighborhood experiences compression or extension. It has been noted earlier that the inter-granular stiffness coefficients model the effects of immediate neighbors as well as the extended granular microstructure. Such a view is in contrast to the past derivations of these expressions, including expressions for anisotropic materials, in which the inter-granular stiffness coefficients were restrictively taken to represent the stiffness of two isolated grains interacting with each other. Furthermore, the grain-pair behavior can potentially be treated using a volumetric-deviatoric split of normal displacement as in the kinematic constrained microplane model [40]. Such split provides an alternative way to model the thermodynamically admissible range of Poisson's ratio. However, it leads to two different normal stiffness coefficients (volumetric and deviatoric) in the case of the kinematic approach. Similar volumetric-deviatoric split of shear displacement will likely result in two different shear stiffness in the case of the least-squares approach.

## 6.5 Elastic wave propagation and effects of model parameters

The velocity of elastic waves propagating within granular and porous media and the effects of material properties thereon has been studied extensively using experimental approaches [164-166] and numerical techniques [167-169]. In this section, the elastic wave propagation velocity is discussed with the view to show change of material macroscopic behavior resulting from changing microscopic parameters. The velocity surfaces that represent the velocity of waves propagating in different directions through the material have been calculated by varying the micro-scale parameters. These surfaces are composed of three sheets, one quasi-longitudinal ( $P$ ) and two quasi-shear waves ( $S1$  and  $S2$ ) [170]. The wave velocities in the material is obtained from the Christoffel equation

$$\det(\Gamma_{ik} - G\delta_{ik}) = 0 \quad (6.28)$$

where  $\Gamma_{ik}$  is the Christoffel matrix (acoustic tensor) which is derived by contracting the stiffness tensor with the unit normal vector twice given as  $C_{ijkl}n_jn_l$ . From Eq. 6.28, it is clear that  $G$  is the eigenvalue of the Christoffel matrix and represents phase velocity. By solving the above equation, three eigenvalues of the Christoffel matrix and their corresponding eigenvectors are derived. The biggest eigenvalue belongs to the quasi-longitudinal wave and the two others belong to the shear waves, one being pure shear and the other quasi-shear wave. For each case, the value of wave velocity can be derived as  $\Gamma_{ij}g_i g_j$  where  $\mathbf{g}$  is the corresponding eigenvector [171].

Here, the velocity surfaces for transversely isotropic materials for a range of micro-scale parameters have been presented. It is recalled that for transversely isotropic materials, 5 micro-scale parameters are used, namely,  $k_n$ ,  $k_s$ ,  $k_t$ ,  $a_{20}$ , and  $a_{40}$ . Stiffness tensors and subsequently the velocity surfaces have been calculated using both kinematic and static approaches. In figures 6.3-

6.6 sections of velocity surfaces with coordinate planes showing the change of elastic wave velocities resulting from varying the values of  $\beta_s=k_s/k_n$ ,  $\beta_t=k_t/k_n$ ,  $a_{20}$ , and  $a_{40}$ , respectively, are presented. For comparison, the wave velocities have been normalized by  $k_n$ . In all these figures, sections a, b, and c represent sections of the velocity surfaces (P, S1, and S2 waves respectively) with 1-2 plane while sections d, e, and f represent sections of the same surfaces with the 2-3 plane. It is noted that since the axis  $I$  is the axis of rotational symmetry, material behavior in all directions inside the plane whose normal vector is axis  $I$  are identical. Thus, sections of velocity surface only with 1-2 plane and 2-3 plane are provided and section of the surface with 3-1 plane will be exactly same as that with 1-2 plane. We also note that, because of this rotational symmetry, the velocity surface section with 2-3 plane will be always a circle regardless of the values of fabric parameters ( $a_{20}$  and  $a_{40}$ ) and ratios of inter-granular stiffness coefficients.

Sections a-f represent results calculated using kinematic approach while sections a'-f' show the same results from least-squares approach. It is evident that using same set of micro-scale stiffness, the wave velocity computed based on least-squares approach are smaller than those of kinematic approach. However, the trend of change of velocities resulting from change of microscopic properties is generally similar between the two methods. The exception is seen for the quasi-shear wave, in which discrepancies in the shape of the wave velocity profile derived from the two different methods can be observed. These differences in the results of the two approaches are due to the fact that the two methods use different approaches to link micro and macro scale kinematic measures, force/stress measures, and material properties. Thus the efficacy of the two approaches to represent different types of granular solids could be judged by a systematic variation of their average micro-scale parameters.

From Figures 6.3 and 6.4 we can observe that the tangential stiffness  $k_s$  appears to affect the longitudinal velocity more in the  $1$ -direction, while stiffness  $k_t$  primarily influences the behavior in the  $2$ - $3$  plane as seen from comparison of figures 6.3a (6.3a') with 5.4a (6.4a'). It is also interesting to see that the tangential stiffness  $k_t$  significantly affects the shape of the quasi-shear wave velocity surface as seen in figures 6.3c (6.3c') and 5.4c (6.4c'). The directional density parameters  $a_{20}$  and  $a_{40}$  also have a significant influence upon the shape of the velocity surfaces in the  $1$ - $2$  plane (see in Figure 6.5 and 6.6). Thus, by changing the micro-scale parameters (stiffness and directional density parameters) a wide range of transverse anisotropic behavior can be modeled. Similar anisotropy descriptions can be obtained for materials with other types of inherent anisotropies

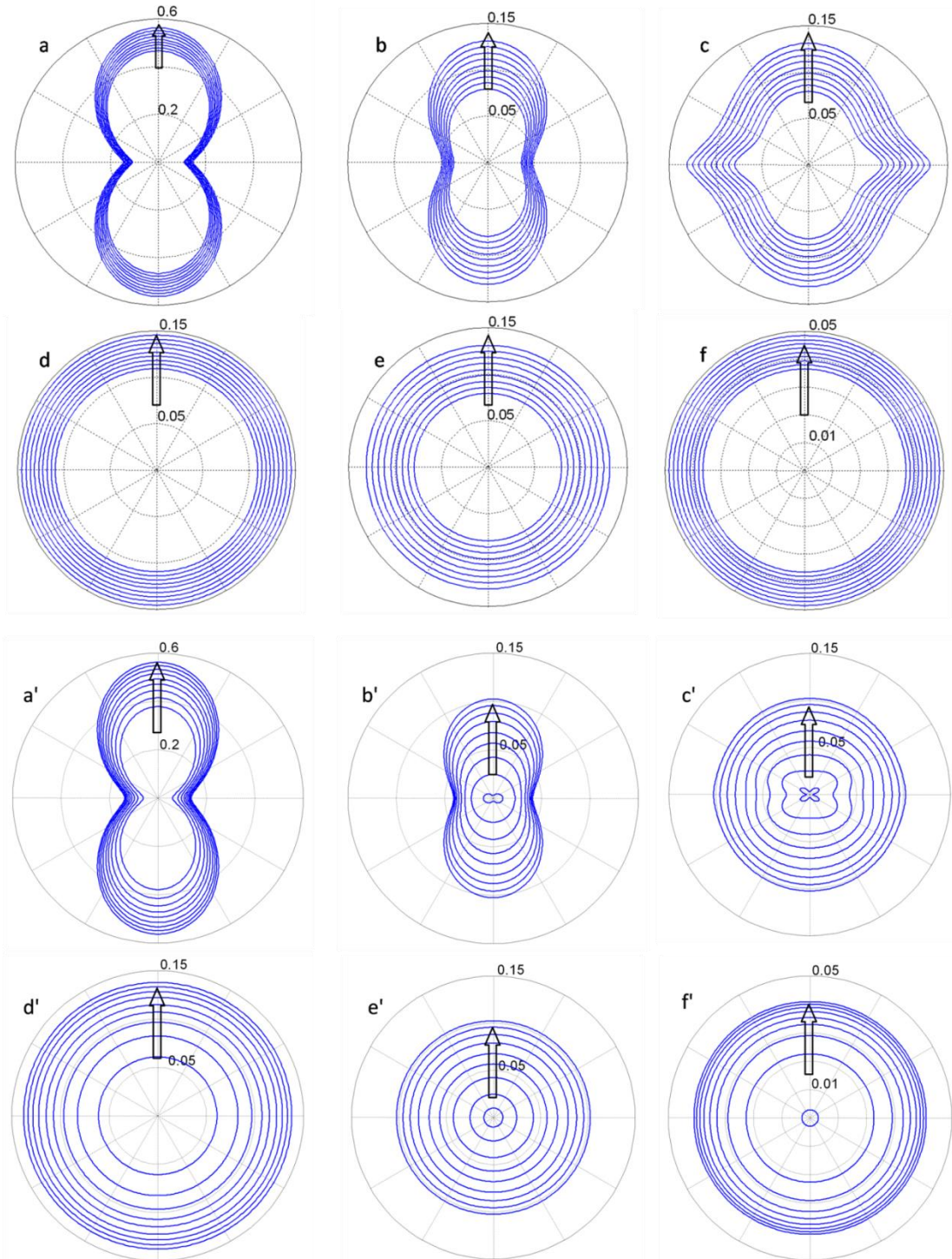


Figure 6.3 Sections of the quasi-longitudinal, pure shear and quasi-shear components of wave velocity surface with 12 plane (graphs a-c respectively) and with 23 plane (graphs d-f respectively) while changing ratio of  $\beta_s = 0.1 \sim 0.9$  with  $a_{20} = a_{40} = 2.0$ ,  $\beta_t = 0.5$ . Arrows represent the direction of variation of the surface while increasing  $\beta_s$ . For visualization purposes the values of wave velocities are reduced by 0.025. Calculations are done with kinematic approach (a-f) and static approach (a'-f').

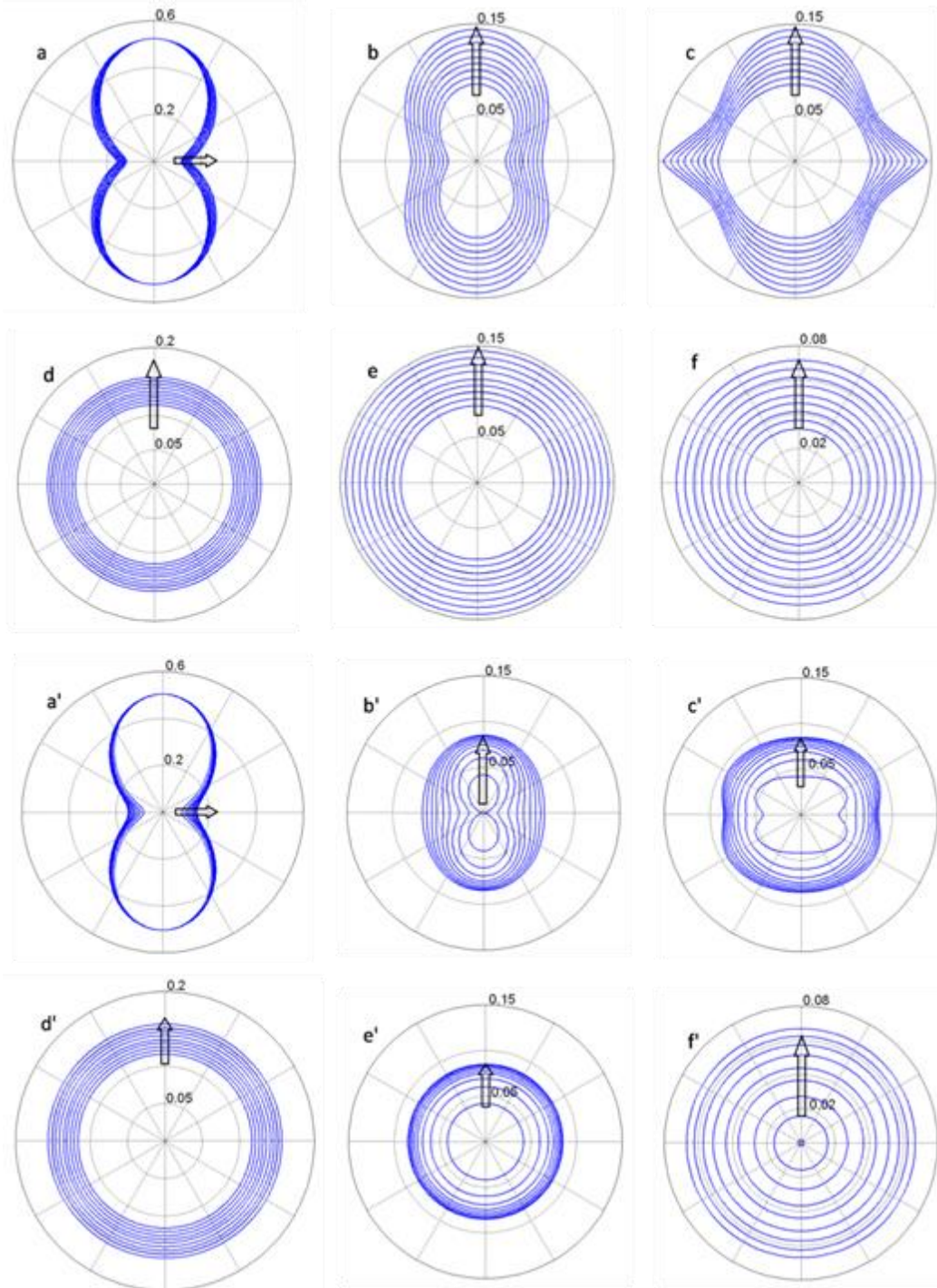


Figure 6.4 Sections of the quasi-longitudinal, pure shear and quasi-shear components of wave velocity surface with 12 plane (graphs a-c respectively) and with 23 plane (graphs d-f respectively) while changing ratio of  $\beta_t = 0.1 \sim 0.9$  with  $a_{20} = a_{40} = 2.0$ ,  $\beta_s = 0.5$ . Arrows represent the direction of variation of the surface while increasing  $\beta_t$ . For visualization purposes the values of wave velocities are reduced by 0.025. Calculations are done with kinematic approach (a-f) and static approach (a'-f')



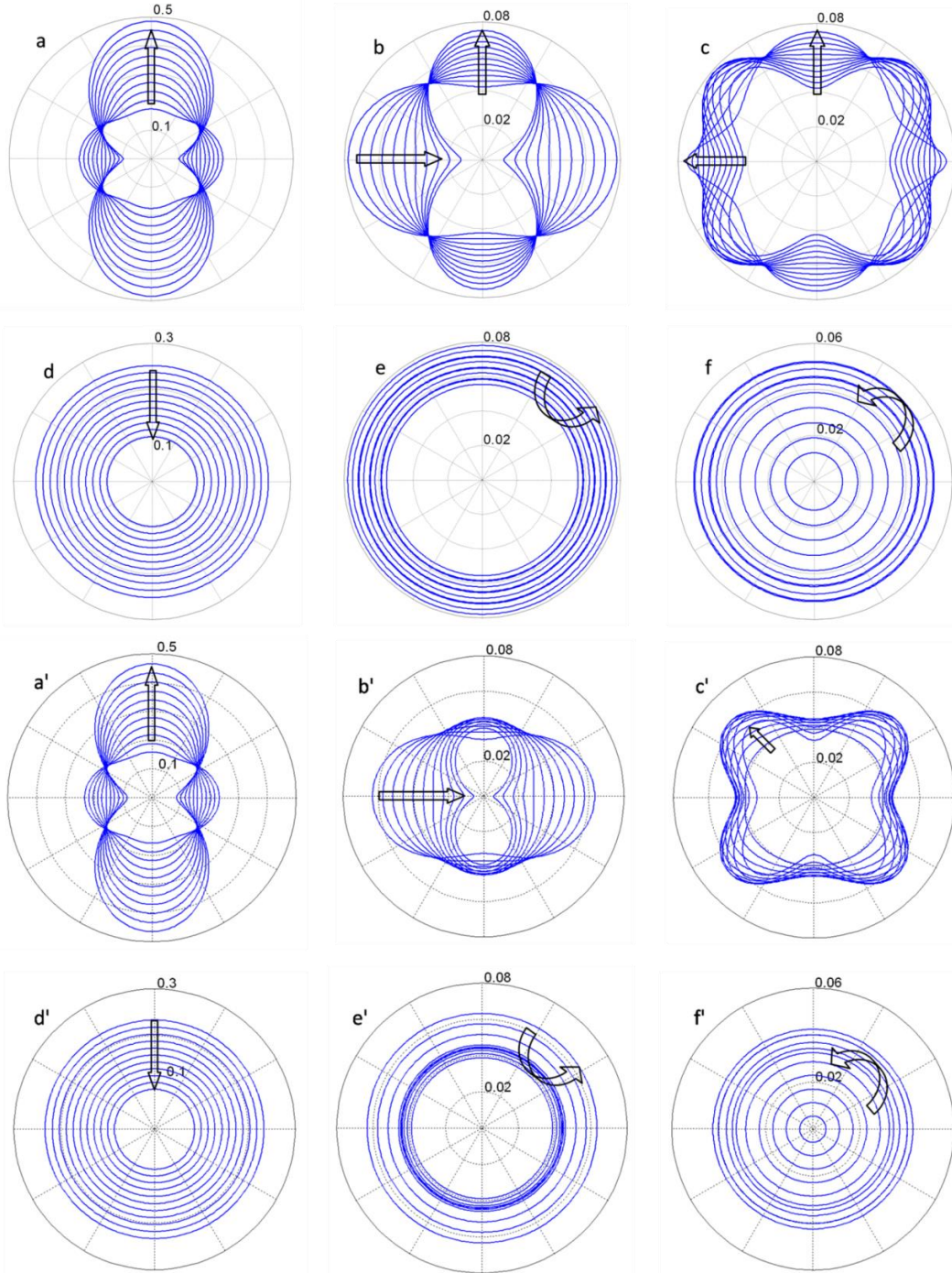


Figure 6.5 Sections of the quasi-longitudinal, pure shear and quasi-shear components of wave velocity surface with 12 plane (graphs a-c respectively) and with 23 plane (graphs d-f respectively) while changing ratio of  $a_{20}=-0.5\sim 2.0$  with  $a_{40}=2.0$ ,  $\beta_s = \beta_t = 0.5$ . Arrows represent the direction of variation of the surface while increasing  $a_{20}$ . For visualization purposes the values of wave velocities are reduced by 0.025. Calculations are done with kinematic approach (a-f) and static approach (a'-f')



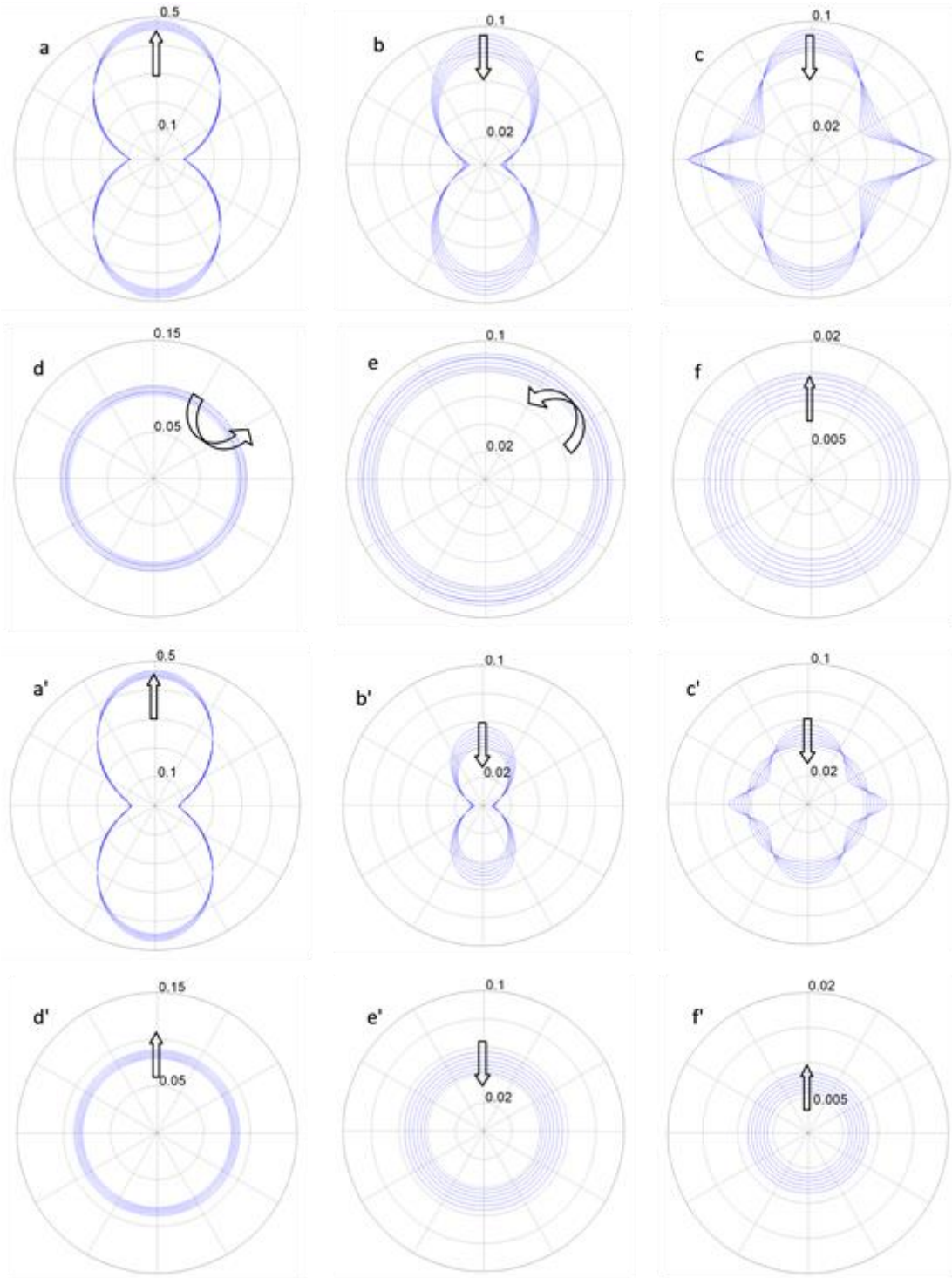


Figure 6.6 Sections of the quasi-longitudinal, pure shear and quasi-shear components of wave velocity surface with 12 plane (graphs a-c respectively) and with 23 plane (graphs d-f respectively) while changing ratio of  $a_{40}=-0.5\sim 2.0$  with  $a_{20}=2.0$ ,  $\beta_s = \beta_t = 0.5$ . Arrows represent the direction of variation of the surface while increasing  $a_{40}$ . For visualization purposes the values of wave velocities are reduced by 0.025. Calculations are done with kinematic approach (a-f) and static approach (a'-f')

## 6.6 Summary and conclusions

A method for modeling materials with different levels of anisotropy using granular micromechanics with both static and kinematic approaches has been developed. For isotropic materials, using a normal and a tangential microscopic stiffness coefficient, identical for all the inter-granular contacts, is sufficient for modeling the material behavior and finding the macroscopic stiffness components. For modeling materials with different levels of anisotropy, the present method uses two different microscopic stiffness coefficients for the two tangential directions and a directional density distribution function is introduced in the model which can sufficiently represent the anisotropy of the material. It is shown that using spherical harmonics expansion with sufficient number of terms can result in stiffness tensors consistent with materials with different levels of anisotropy.

The constitutive relationship is established by using inter-granular stiffness coefficients defined on the basis of the conjugate relationship of inter-granular displacement and forces. The clear implication of the inter-granular stiffness coefficients introduced in this manner is that they are different from that of isolated grain-pair and model the behavior of grain-pair embedded in a granular material and represent the effect of immediate neighbors as well as the extended micro-structure. They function as parameters that need to be determined as back-calculations from macro-scale measurements and not through direct measurements of two-isolated grains as in contact mechanics. Two directional density distribution functions are defined; one related to the average directional distribution of number, length, and stiffness/compliance of grain-pair interactions and the other related to average directional distribution of number, length of grain-pair interactions.

Subsequently for ensuring that the model is capable of reproducing different levels of anisotropy, the distribution density function is parameterized using spherical harmonics expansion with carefully selected terms. It is shown that using the density distribution function with 18 parameters is sufficient for modeling a completely anisotropic material. These 18 directional density parameters along with the three inter-granular stiffness coefficients make a total of 21 independent micro-scale constants and will result in 21 mutually independent, non-zero components of a  $6 \times 6$  stiffness matrix.

Different levels of isotropy in materials arise from the presence of planes of elastic symmetry and/or axes of rotational symmetry. In this study, the density distribution function is systematically modified for modeling materials with only 1 plane of elastic symmetry, orthotropic materials, and transversely isotropic materials. In all these cases, the derived stiffness matrices are consistent with the symmetry requirements of that particular material. For each anisotropy level, number of micromechanical parameters is equal to the number of independent constants in the stiffness tensor of that particular anisotropy level.

As a measure to demonstrate the effects of change of micromechanical properties included in the model on the macroscopic behavior of the material, acoustic wave propagation velocity through a transversely isotropic material is discussed within both kinematic and static approaches. Variation of wave velocity by changing microscopic properties is shown. It is found that the velocity surfaces quasi-shear can show different trends for the two methods suggesting that wave propagation can be applied to evaluate the efficacy of the two approaches to represent different types of granular solids.

## **7 Micromorphic granular micromechanics**

In usual continuum theories, the only kinematic measure used as strain is the average displacement gradient field. However, it is obvious that the displacement field within material point is not necessarily linear and the average displacement gradient will not be able to completely represent the kinematics of the material point. Experimental evidence for existence of non-affine grain movements and consequently fluctuations from the average in displacement gradient imply the necessity of including these fluctuations and their second gradient in the kinematics [47, 172, 173]. Also, experimental observations on granular assemblies prove existence of grain rotations and their effect in the macroscopic behavior of the material [47, 172, 174].

In this Chapter, the granular micromechanics approach is extended by incorporating, in addition to the traditionally used average displacement gradient, the following non-classical terms in the kinematics:

- 1- Fluctuations in displacement gradient
- 2- Second gradient of displacement fluctuations
- 3- Grain spins' average, fluctuation, and second gradient

The first two terms in the above list are added to the model considering the kinematic analyses of Mindlin-Eringen micro-structural elasticity [2] or micromorphic mechanics [4] and the third term is added due to the experimental and numerical observations implying their existence in granular assemblies. By including the aforementioned terms in defining the kinematic fields, kinematic measures in grain-scale are also enhanced. Conjugate to each one of the inter-granular kinematic

measures an inter-granular force (or moment) measure is introduced using a corresponding grain-scale stiffness coefficient defined separately for each kinematic measure. Macro-scale and Micro-scale deformation energy densities are defined in terms of macroscopic kinematics fields and inter-granular displacement measures respectively. Also different macro-scale stress measures are introduced as work conjugates of the different strain measures and are derived as derivatives of the strain energy density function with respect to their conjugate strain measure. Thus relationships for macro-scale stiffness tensors in terms of grain-scale stiffness parameters and geometric parameters are derived.

## 7.1 Kinematics of Granular Media

In order to model the material point as a continuum, a Volume Element (VE) defined as a collection of grains is considered in the global coordinate system,  $\mathbf{x}$ . For any grain,  $p$ , inside the VE, the vector field of displacement can be derived as a Taylor series expansion of the same vector field in a neighboring grain,  $n$ .

$$\phi_i^p = \phi_i^n + \phi_{i,j}^n l_j + \frac{1}{2} \phi_{i,jk}^n l_j l_k + \dots = \phi_i^n + \phi_{i,j}^n l_j + \phi_{i,jk}^n J_{jk} + \dots \quad (7.1)$$

where  $\phi_i$  is the displacement of grain,  $l_j$  is an inter-granular branch vector joining the centroids of grains  $n$  and  $p$ , and the tensor product  $l_j l_k / 2 = J_{jk}$  is a geometry moment tensor. First and second gradient terms have been included in the analysis and summation convention over repeated indices is implied unless noted otherwise.

It is known that, in general, finite rotations are not vectors and do not follow vector analysis rules [156]. However, for small rotation measures, which is of interest in this study, vector analysis rules can be applied to them. In order to study the rotation field within the VE, the same approach

as that used for studying the displacements is used. Thus the rotation of a grain,  $p$ , within the VE is written as the Taylor series expansion of the rotation of a neighbor grain,  $n$ .

$$\kappa_i^p = \kappa_i^n + \kappa_{i,j}^n l_j + \frac{1}{2} \kappa_{i,jk}^n l_j l_k + \dots = \kappa_i^n + \kappa_{i,j}^n l_j + \kappa_{i,jk}^n J_{jk} + \dots \quad (7.2)$$

where  $\kappa_i$  is the rotation of the grain,  $l_j$  is an inter-granular branch vector joining the centroids of grains  $n$  and  $p$ , and the tensor product  $l_j l_k / 2 = J_{jk}$  is a geometry moment tensor.

In a continuum model, the VE plays the role of a material point P, as depicted in Figure 7.1. In order to enable us to capture the non-uniformities of the displacement field within the VE, a local coordinate system,  $\mathbf{x}'$ , is defined for the material point with its axes parallel to those of the global coordinate axes and is attached to its barycenter. This local coordinate system is able to distinguish different grains inside the material point and thus the displacement of a grains are written as functions of not only the coordinates of the VE, but also the local coordinates of the grain within the material point, i.e.  $\phi_i(\mathbf{x}, \mathbf{x}')$ .

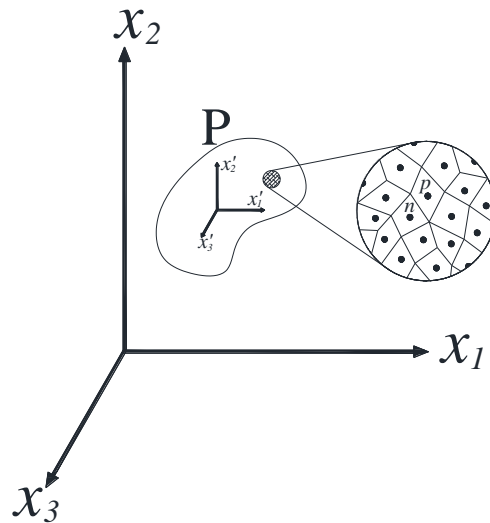


Figure 7.1 Schematic representation of the two coordinate systems,  $\mathbf{x}$  and  $\mathbf{x}'$  and the neighbor grains in the material point

As a development from the previous work on this issue, in this study in addition to the actual displacement field,  $u_i$ , (which consists of displacement of grains inside the material point) grains' pure spins field,  $\omega_i$ , is also taken into account. Total displacement of a point on the grain is derived as the sum of the displacement of grain's centroids and the cross product of its rotation with the position vector of the point under consideration.

$$\phi_i = u_i + e_{ijk} \kappa_j r_k \quad (7.3)$$

where  $r_k$  is the position vector of any point on the grain with respect to grains' centroids. Thus it is noted that at grains' centroids ( $r_i = 0$ ) total displacement is equal to the actual displacement field and grains' spins play no role in the displacement of its centroids. Further, each grain's total rotation field is also derived as the sum of grain's pure spin,  $\omega_i$ , and curl of the total displacement field. Thus the total rotation field is defined as

$$\kappa_i = e_{ijk} \phi_{k,j} + \omega_i \quad (7.4)$$

Along the lines of the methodology of micro-structural elasticity described by Mindlin [2] and micromorphic mechanics of Eringen [4], the total displacement and rotation fields are decomposed into two components, one representing an average field and the other representing the local fluctuations from average. Thus the displacement and rotation fields and their gradients can be rewritten as

$$\phi_i = \bar{\phi}_i - \tilde{\phi}_i \quad \Rightarrow \quad \psi_{ij}^\phi = \phi_{i,j} = \bar{\phi}_{i,j} - \tilde{\phi}_{i,j} = \bar{\phi}_{i,j} - \gamma_{ij}^\phi \quad (7.5a)$$

$$\kappa_i = \bar{\kappa}_i - \tilde{\kappa}_i \quad \Rightarrow \quad \psi_{ij}^\kappa = \kappa_{i,j} = \bar{\kappa}_{i,j} - \tilde{\kappa}_{i,j} = \bar{\kappa}_{i,j} - \gamma_{ij}^\kappa \quad (7.5b)$$

where the overhead bar and tilde represent the average and fluctuation fields respectively. In Eq. 7.3,  $\bar{\phi}_{i,j}$  and  $\tilde{\phi}_{i,j} = \gamma_{ij}^\phi$  are the average macro-scale and the fluctuations in displacement gradient (due to the combined effect of grains' displacement and spins). Also  $\bar{\kappa}_{i,j}$  and  $\tilde{\kappa}_{i,j} = \gamma_{ij}^\kappa$  are the

average macro-scale and the fluctuations in rotation gradient (due to the combined effect of grains' displacement and spins).

It should be noted here that the average displacement gradient field and the average rotation gradient field are constant for the material point and therefore their gradient (i.e. the second gradient of the average displacement and rotation fields) will be zero. Thus the second gradient of the total displacement and rotation fields are derived as

$$\phi_{i,jk} = \psi_{ij,k}^{\phi} = (\bar{\phi}_{i,j} - \gamma_{ij}^{\phi})_{,k} = -\gamma_{ij,k}^{\phi} \quad (7.6a)$$

$$\kappa_{i,jk} = \psi_{ij,k}^{\kappa} = (\bar{\kappa}_{i,j} - \tilde{\kappa}_{i,j})_{,k} = -\gamma_{ij,k}^{\kappa} \quad (7.6b)$$

In order to calculate the relative displacement of two neighbor grains, the first and second gradients of displacement, Eq. 7.5a and 7.6a, are substituted into Eq. 7.1

$$\delta_i^{mp} = \phi_i^p - \phi_i^n = \phi_{i,j}^n l_j + \phi_{i,jk}^n J_{jk} = \bar{\phi}_{i,j} l_j - \gamma_{ij}^{\phi} l_j + \frac{1}{2} \psi_{ij,k}^{\phi} l_j l_k = \delta_i^M - \delta_i^m + \delta_i^g \quad (7.7)$$

where

$$\delta_i^M = \bar{\phi}_{i,j} l_j; \quad \delta_i^m = \gamma_{ij}^{\phi} l_j; \quad \delta_i^g = \frac{1}{2} \psi_{ij,k}^{\phi} l_j l_k = \psi_{ij,k}^{\phi} J_{jk} \quad (7.8)$$

As seen from Eq. 7.8, the inter-granular relative displacements between two interacting (contacting) grains is decomposed into three terms: (1)  $\delta_i^M$  due to the average displacement gradient,  $\bar{\phi}_{i,j}$ , (2)  $\delta_i^m$  due to the gradients of the fluctuation in grain displacement,  $\gamma_{ij}(x)$ , and (3)

$\delta_i^g$  due to the second gradient of the total displacement field  $\psi_{ij,k}^{\phi}$ .

Further, the relative rotation of two grains is also derived by substituting the first and second gradients of the rotation field, Eq. 7.5b and 7.6b, into Eq. 7.2.

$$\theta_i^{mp} = \kappa_i^p - \kappa_i^n = \kappa_{i,j}^n l_j + \kappa_{i,jk}^n J_{jk} = \bar{\kappa}_{i,j} l_j - \gamma_{ij}^{\kappa} l_j + \frac{1}{2} \psi_{ij,k}^{\kappa} l_j l_k = \theta_i^M + \theta_i^m + \theta_i^g \quad (7.9)$$



where

$$\theta_i^M = \bar{\kappa}_{i,j} l_j; \quad \theta_i^m = \gamma_{ij}^\kappa l_j; \quad \theta_i^s = \frac{1}{2} \psi_{ij,k}^\kappa l_j l_k = \psi_{ij,k}^\kappa J_{jk} \quad (7.10)$$

Thus the relative inter-granular rotation field has been also decomposed into three terms: (1)  $\theta_i^M$  due to the gradients of the average rotations, (2)  $\theta_i^m$  due to the gradient of the fluctuations in grain rotations, and (3)  $\theta_i^s$  due to the second gradient of the total rotation field of the grains.

The fact that grains undergo relative rotations is also known from measurements of kinematic fields in grain assemblies [47, 172]. The above decomposition of both displacement and spins field within the RVE into average and fluctuation terms allows us to include both mean field grains' displacements and spins in addition to their fluctuations. Since the second rank tensors  $\gamma_{ij}^\phi(x_k)$  and  $\gamma_{ij}^\kappa(x_k)$  are independent of coordinates  $x'_k$  (homogeneous within the material point), the fluctuation modeled in this way is taken as linear within the material point which leads to a micromorphic theory of degree 1 in the terminology introduced by Germain [6]. The decomposition of displacement gradient in 6.5a is supported by the experimentally measured kinematic fields of grain assemblies [47, 172, 173] that show strong non-affine motions in a volume element comprising large number of grains. The presence of grain displacement fluctuations have also been recognized in previous works related to continuum modeling of grain packing within the rubric of classical continuum mechanics [19, 175]. The second and higher gradient of deformations have also been shown to be necessary for continuum modeling of pantographic trusses due to their unique structural arrangements and stiffness of the truss elements [176, 177].

## 7.2 Macro-scale and Micro-scale Dynamics

The kinematic measures contributing to the deformation energy are the gradients of the average and fluctuations of the displacement and rotation fields, in addition to the second gradients of the total displacement and rotation fields ( $\psi_{ij,k}^\phi = \phi_{i,jk}$  and  $\psi_{ij,k}^\kappa = \kappa_{i,jk}$ ). Thus the macro-scale deformation energy density of the granular continua can be defined as a function of these kinematic fields:  $W = W(\bar{\phi}_{i,j}, \gamma_{ij}^\phi, \psi_{ij,k}^\phi, \bar{\kappa}_{i,j}, \gamma_{ij}^\kappa, \psi_{ij,k}^\kappa)$ . Conjugate to each one of the above kinematic fields, a macro-scale stress measure is defined using the deformation energy density as:

$$\begin{aligned} \tau_{ij} &= \frac{\partial W}{\partial \bar{\phi}_{i,j}} = \frac{\partial W}{\partial \varepsilon_{ij}}; & \sigma_{ij} &= \frac{\partial W}{\partial \gamma_{ij}^\phi}; & \mu_{ijk} &= \frac{\partial W}{\partial \psi_{ij,k}^\phi} \\ M_{ij} &= \frac{\partial W}{\partial \bar{\kappa}_{i,j}}; & P_{ij} &= \frac{\partial W}{\partial \gamma_{ij}^\kappa}; & Q_{ijk} &= \frac{\partial W}{\partial \psi_{ij,k}^\kappa} \end{aligned} \quad (7.11)$$

where the stress measures conjugate to the displacement fields are shown with Greek letters while the moment stress measures conjugate to the spin fields are shown with Latin letters.  $\tau_{ij}$  and  $\sigma_{ij}$  are Cauchy stress and relative stress, while  $\mu_{ijk}$  is the double stress tensor conjugate to the second gradient of grains' displacement field. Also the two second rank tensors,  $M_{ij}$  and  $P_{ij}$  are the average and relative moment stress tensors conjugate to the average and fluctuations in grain rotations respectively, while the third rank tensor,  $Q_{ijk}$  is the double moment tensor conjugate to the second gradient of grains' rotations.

For a granular material system, the macro-scale deformation energy density,  $W$ , can be derived as the volume average of the micro-scale deformation energy components caused by the relative displacements and relative rotations of grain-pairs. The micro-scale deformation energy,  $W^\alpha$ , is defined as follows for the  $\alpha^{\text{th}}$  interacting pair as a function of the micro-scale kinematic measures:

$W^\alpha(\delta_i^M, \delta_i^m, \delta_i^g, \theta_i^M, \theta_i^m, \theta_i^g)$ , where for simplicity of presentation the superscript  $\alpha$  has been

dropped from the micro-scale kinematic variables. The macroscopic energy density of the RVE is thus given as

$$W = \frac{1}{V} \sum_{\alpha} W^{\alpha} \left( \delta_i^M, \delta_i^m, \delta_i^g, \theta_i^M, \theta_i^m, \theta_i^g \right) \quad (7.12)$$

Further, the inter-granular force and moment conjugates are introduced as derivatives of micro-scale energy function,  $W^{\alpha}$ , with respect to each of the inter-particle kinematic measures (displacements and rotations) as:

$$\begin{aligned} \frac{\partial W^{\alpha}}{\partial \delta_i^{\alpha \xi}} &= f_i^{\alpha \xi}; \quad \text{where } \xi: M, m, g \\ \frac{\partial W^{\alpha}}{\partial \theta_i^{\alpha \xi}} &= m_i^{\alpha \xi}; \quad \text{where } \xi: M, m, g \end{aligned} \quad (7.13)$$

Substituting Eq. 7.12 into Eq. 7.13, applying chain rule of differentiation, and making use of the definition of microscopic kinematic measures in terms of their macroscopic counterparts, Eq. 7.8 and 7.10, the following expressions for the macro-scale stress measures are derived:

$$\left. \begin{aligned} \tau_{ij} &= \frac{\partial W}{\partial \varepsilon_{ij}} = \frac{1}{V} \sum_{\alpha} \frac{\partial W^{\alpha}}{\partial \delta_k^M} \frac{\partial \delta_k^M}{\partial \varepsilon_{ij}} \\ \frac{\partial \delta_k^M}{\partial \varepsilon_{ij}} &= \frac{\partial (\varepsilon_{kq} l_q^{\alpha})}{\partial (\varepsilon_{ij})} = \delta_{ik} \delta_{jq} l_q^{\alpha} = \delta_{ik} l_j^{\alpha} \end{aligned} \right\} \Rightarrow \tau_{ij} = \frac{1}{V} \sum_{\alpha} \frac{\partial W^{\alpha}}{\partial \delta_k^M} \delta_{ik} l_j^{\alpha} = \frac{1}{V} \sum_{\alpha} f_i^M l_j^{\alpha} \quad (7.14)$$

$$\left. \begin{aligned} \sigma_{ij} &= \frac{\partial W}{\partial \gamma_{ij}^{\phi}} = \frac{1}{V} \sum_{\alpha} \frac{\partial W^{\alpha}}{\partial \delta_k^m} \frac{\partial \delta_k^m}{\partial \gamma_{ij}^{\phi}} \\ \frac{\partial \delta_k^m}{\partial \gamma_{ij}^{\phi}} &= \frac{\partial (\gamma_{kq}^{\phi} l_q^{\alpha})}{\partial \gamma_{ij}^{\phi}} = \delta_{ik} \delta_{jq} l_q^{\alpha} = \delta_{ik} l_j^{\alpha} \end{aligned} \right\} \Rightarrow \sigma_{ij} = \frac{1}{V} \sum_{\alpha} \frac{\partial W^{\alpha}}{\partial \delta_k^m} \delta_{ik} l_j^{\alpha} = \frac{1}{V} \sum_{\alpha} f_i^m l_j^{\alpha} \quad (7.15)$$

$$\left. \begin{aligned} \mu_{ijk} &= \frac{\partial W}{\partial \psi_{ij,k}^{\phi}} = \frac{1}{V} \sum_{\alpha} \frac{\partial W^{\alpha}}{\partial \delta_l^g} \frac{\partial \delta_l^g}{\partial \psi_{ij,k}^{\phi}} \\ \frac{\partial \delta_l^g}{\partial \psi_{ij,k}^{\phi}} &= \frac{\partial (\psi_{l,qr}^{\phi} J_{qr}^{\alpha})}{\partial \psi_{ij,k}^{\phi}} = \delta_{il} \delta_{jq} \delta_{kr} J_{qr}^{\alpha} = \delta_{il} J_{jk}^{\alpha} \end{aligned} \right\} \Rightarrow \mu_{ijk} = \frac{1}{V} \sum_{\alpha} \frac{\partial W^{\alpha}}{\partial \delta_k^g} \delta_{il} J_{jk}^{\alpha} = \frac{1}{V} \sum_{\alpha} f_i^g J_{jk}^{\alpha} \quad (7.16)$$

$$\left. \begin{aligned} M_{ij} &= \frac{\partial W}{\partial \bar{\kappa}_{i,j}} = \frac{1}{V} \sum_{\alpha} \left( \frac{\partial W^{\alpha}}{\partial \theta_k^M} \frac{\partial \theta_k^M}{\partial \bar{\kappa}_{i,j}} \right) \\ \frac{\partial \theta_k^M}{\partial \bar{\kappa}_{i,j}} &= \frac{\partial (\bar{\kappa}_{k,q} l_q)}{\partial \bar{\kappa}_{i,j}} = \delta_{ik} \delta_{jq} l_q^{\alpha} = \delta_{ik} l_j^{\alpha} \end{aligned} \right\} \Rightarrow M_{ij} = \frac{1}{V} \sum_{\alpha} \left( \frac{\partial W^{\alpha}}{\partial \theta_k^M} \delta_{ik} l_j^{\alpha} \right) = \frac{1}{V} \sum_{\alpha} m_i^M l_j^{\alpha} \quad (7.17)$$

$$\left. \begin{aligned} P_{ij} &= \frac{\partial W}{\partial \gamma_{i,j}^{\kappa}} = \frac{1}{V} \sum_{\alpha} \left( \frac{\partial W^{\alpha}}{\partial \theta_k^m} \frac{\partial \theta_k^m}{\partial \gamma_{i,j}^{\kappa}} \right) \\ \frac{\partial \theta_k^m}{\partial \gamma_{i,j}^{\kappa}} &= \frac{\partial (\gamma_{kq}^{\kappa} l_q)}{\partial \gamma_{i,j}^{\kappa}} = \delta_{ik} \delta_{jq} l_q^{\alpha} = \delta_{ik} l_j^{\alpha} \end{aligned} \right\} \Rightarrow P_{ij} = \frac{1}{V} \sum_{\alpha} \left( \frac{\partial W^{\alpha}}{\partial \theta_k^m} \delta_{ik} l_j^{\alpha} \right) = \frac{1}{V} \sum_{\alpha} m_i^m l_j^{\alpha} \quad (7.18)$$

$$\left. \begin{aligned} Q_{ijk} &= \frac{\partial W}{\partial \psi_{ij,k}^{\kappa}} = \frac{1}{V} \sum_{\alpha} \left( \frac{\partial W^{\alpha}}{\partial \theta_l^g} \frac{\partial \theta_l^g}{\partial \psi_{ij,k}^{\kappa}} \right) \\ \frac{\partial \theta_l^g}{\partial \psi_{ij,k}^{\kappa}} &= \frac{\partial (\psi_{lq,r}^{\kappa} J_{qr}^{\alpha})}{\partial \psi_{ij,k}^{\kappa}} = \delta_{il} \delta_{jq} \delta_{rk} J_{qr}^{\alpha} = \delta_{il} J_{jk}^{\alpha} \end{aligned} \right\} \Rightarrow Q_{ijk} = \frac{1}{V} \sum_{\alpha} \frac{\partial W^{\alpha}}{\partial \theta_l^g} \delta_{il} J_{jk}^{\alpha} = \frac{1}{V} \sum_{\alpha} m_i^g J_{jk}^{\alpha} \quad (7.19)$$

where the superscript  $\alpha$  has been dropped from the micro-scale kinematic and force measures. Thus, the macro-scale stress measures have been defined in terms of the inter-granular force measures and the local geometry represented by the branch vector,  $l_j$ , and geometry moment tensor,  $J_{jk}$ . We observe that the inter-granular forces  $f_i^M$ ,  $f_i^m$ , and  $f_i^g$  are related to the Cauchy, the relative, and double moment stresses, respectively. Further, the inter-granular moments,  $m_i^M$ ,  $m_i^m$ , and  $m_i^g$  contribute to the average and relative moment stresses and double moment stress tensors respectively.

### 7.3 Micro-scale and Macro-scale Constitutive Equations

For formulating micro-scale constitutive equations that relates the micro-scale kinematic measures to the conjugate inter-granular force measures, all displacement and rotation terms are decomposed

into components in the contact's coordinate system,  $\mathbf{nst}$ , defined previously in Eq. 2.2. Thus, the micro-scale deformation energy,  $W^\alpha$ , is written in the following simple form

$$W^\alpha = \left. \begin{aligned} & \sum_{\xi \text{ and } \zeta} \left( f_n^{\alpha\xi} \delta_n^{\alpha\xi} + f_s^{\alpha\xi} \delta_s^{\alpha\xi} + f_t^{\alpha\xi} \delta_t^{\alpha\xi} \right. \\ & \left. + m_n^{\alpha\zeta} \theta_n^{\alpha\zeta} + m_s^{\alpha\zeta} \theta_s^{\alpha\zeta} + m_t^{\alpha\zeta} \theta_t^{\alpha\zeta} \right) \end{aligned} \right\}; \quad \begin{array}{l} \xi: \mathbf{M}, \mathbf{m}, \mathbf{g} \\ \zeta: \mathbf{M}, \mathbf{m}, \mathbf{g} \end{array} \quad (7.20)$$

where the subscripts  $n$ ,  $s$ , and  $t$  represent the components in the local coordinate system and do not follow the tensor summation convention. For modeling elastic isotropic materials cross-linking terms implying interaction between normal and tangential components of force-displacement and moment-rotation pairs are ignored. Furthermore, in order to guarantee linear elasticity in macro-scale, all the terms of the micro-scale deformation energy are quadratic in terms of the kinematic measures. Thus for linear isotropic elasticity, the micro-scale deformation energy is defined as

$$W^\alpha = \frac{1}{2} \left[ \sum_{\xi \text{ and } \zeta} \left( K_n^{\alpha\xi} (\delta_n^{\alpha\xi})^2 + K_w^{\alpha\xi} (\delta_s^{\alpha\xi})^2 + K_w^{\alpha\xi} (\delta_t^{\alpha\xi})^2 + G_n^{\alpha\zeta} (\theta_n^{\alpha\zeta})^2 + G_w^{\alpha\zeta} (\theta_s^{\alpha\zeta})^2 + G_w^{\alpha\zeta} (\theta_t^{\alpha\zeta})^2 \right) \right]; \quad \begin{array}{l} \xi: \mathbf{M}, \mathbf{m}, \mathbf{g} \\ \zeta: \mathbf{M}, \mathbf{m}, \mathbf{g} \end{array} \quad (7.21)$$

where  $K$  and  $G$  represent the inter-granular stiffness parameters for forces and moments, respectively. Note that the subscripts,  $n$ ,  $s$ ,  $t$ , and  $w$  represent kinematic and stiffness terms in local coordinate system defined in Eq. 2.2 and do *not* follow the summation convention for repeated indices. Since the material is assumed to be isotropic, the behavior of grain interactions in different directions within the tangential plane are similar leading to a single stiffness coefficient ( $K_w$  for forces and  $G_w$  for moments) for the two directions  $s$  and  $t$ . For inherently isotropic materials, different stiffness coefficients should be used for the two tangential directions (See Chapter 5). It is also noted that the terms that cross-link the different micro-scale kinematic measures have been ignored for simplicity. The introduced grain-pair stiffness parameters define the force components conjugate to different micro-scale kinematic measures that contribute to inter-granular relative

displacements and rotations. These stiffness parameters do not represent the stiffness of two isolated interacting grains. In the derived model we have introduced 3 types of inter-granular stiffness parameters for force-displacement equation, namely, the average, the fluctuation, and the second gradient, distinguished by their superscripts  $\xi$ :  $M$ ,  $m$ , and  $g$ , respectively. Also for moment-rotation equations, three stiffness parameters are used in local scale, namely the average, fluctuation, and the second gradient term, distinguished by their superscripts  $\zeta$ :  $M$ ,  $m$ , and  $g$ , respectively. The typical micro-scale constitutive equations for forces and moments in terms of displacements and rotations in the contact local coordinate system  $nst$ , after dropping the aforementioned superscripts, can be written in matrix form as

$$\begin{Bmatrix} f_n \\ f_s \\ f_t \end{Bmatrix} = \begin{bmatrix} K_n & 0 & 0 \\ 0 & K_w & 0 \\ 0 & 0 & K_w \end{bmatrix} \begin{Bmatrix} \delta_n \\ \delta_s \\ \delta_t \end{Bmatrix}; \quad \begin{Bmatrix} m_n \\ m_s \\ m_t \end{Bmatrix} = \begin{bmatrix} G_n & 0 & 0 \\ 0 & G_w & 0 \\ 0 & 0 & G_w \end{bmatrix} \begin{Bmatrix} \theta_n \\ \theta_s \\ \theta_t \end{Bmatrix} \quad (7.22)$$

Having found the force and moment vectors components in  $nst$  coordinate, they are rotated along with their corresponding stiffness tensors in the direction of the material point coordinate system. Local constitutive equations and stiffness tensors in the material point coordinate system are found using the tensors and vectors rotation as

$$\begin{aligned} f_i^{\alpha\xi} &= K_{ij}^{\alpha\xi} \delta_j^{\alpha\xi}; & K_{ij}^{\alpha\xi} &= K_n^{\alpha\xi} n_i n_j + K_w^{\alpha\xi} (s_i s_j + t_i t_j); & \text{where } \xi: M, m, g \\ m_i^{\alpha\zeta} &= G_{ij}^{\alpha\zeta} \theta_j^{\alpha\zeta}; & G_{ij}^{\alpha\zeta} &= G_n^{\alpha\zeta} n_i n_j + G_w^{\alpha\zeta} (s_i s_j + t_i t_j); & \text{where } \zeta: M, m, g \end{aligned} \quad (7.23)$$

By substituting the micro-scale constitutive equations, Eq. 7.23, into Eq. 7.14-7.19, the macro-scale constitutive relationships are derived linking the macro-scale kinematic measures to their conjugate stress tensors as follows

$$\tau_{ij} = \frac{1}{V} \sum_{\alpha} f_i^M l_j^{\alpha} = \frac{1}{V} \sum_{\alpha} K_{ik}^M \delta_k^M l_j^{\alpha} = \left( \frac{1}{V} \sum_{\alpha} K_{ik}^M l_l^{\alpha} l_j^{\alpha} \right) \varepsilon_{kl} = C_{ijkl}^M \varepsilon_{kl} \quad (7.24)$$

$$\sigma_{ij} = \frac{1}{V} \sum_{\alpha} f_i^m l_j^{\alpha} = \frac{1}{V} \sum_{\alpha} K_{ik}^m \delta_k^m l_j^{\alpha} = \left( \frac{1}{V} \sum_{\alpha} K_{ik}^m l_l^{\alpha} l_j^{\alpha} \right) \gamma_{kl}^{\phi} = C_{ijkl}^m \gamma_{kl}^{\phi} \quad (7.25)$$

$$\mu_{ijk} = \frac{1}{V} \sum_{\alpha} f_i^g J_{jk}^{\alpha} = \frac{1}{V} \sum_{\alpha} K_{il}^g \delta_l^g J_{jk}^{\alpha} = \left( \frac{1}{V} \sum_{\alpha} K_{il}^g J_{mn}^{\alpha} J_{jk}^{\alpha} \right) \psi_{lm,n}^{\phi} = A_{ijklmn} \psi_{lm,n}^{\phi}$$

(7.26)

$$M_{ij} = \frac{1}{V} \sum_{\alpha} m_i^M l_j^{\alpha} = \frac{1}{V} \sum_{\alpha} G_{ik}^M \theta_k^M l_j^{\alpha} = \left( \frac{1}{V} \sum_{\alpha} G_{ik}^M l_l^{\alpha} l_j^{\alpha} \right) \bar{\kappa}_{k,l} = D_{ijkl}^M \bar{\kappa}_{k,l} \quad (7.27)$$

$$P_{ij} = \frac{1}{V} \sum_{\alpha} m_i^m l_j^{\alpha} = \frac{1}{V} \sum_{\alpha} G_{ik}^m \theta_k^m l_j^{\alpha} = \left( \frac{1}{V} \sum_{\alpha} G_{ik}^m l_l^{\alpha} l_j^{\alpha} \right) \gamma_{kl}^{\kappa} = D_{ijkl}^m \gamma_{kl}^{\kappa} \quad (7.28)$$

$$Q_{ijk} = \frac{1}{V} \sum_{\alpha} m_i^g J_{jk}^{\alpha} = \frac{1}{V} \sum_{\alpha} G_{il}^g \theta_l^g J_{jk}^{\alpha} = \left( \frac{1}{V} \sum_{\alpha} G_{il}^g J_{mn}^{\alpha} J_{jk}^{\alpha} \right) \psi_{lm,n}^{\kappa} = B_{ijklmn} \psi_{lm,n}^{\kappa} \quad (7.29)$$

It is seen that following this approach leads to four fourth rank stiffness tensors (2 for average and fluctuation terms in displacement and 2 for average and fluctuation terms in rotation) and two sixth rank tensors for the second gradient terms in displacement and rotation. It is notable that the derived constitutive relationships in Eq. 7.24-7.29 are uncoupled as a consequence of the assumption made to ignore the coupling terms between the different kinematic measures in the micro-scale deformation energy,  $W^{\alpha}$ , given in Eq. 7.20 and 7.21. The inclusion of cross-linking between different microscopic kinematic and force measures will lead to coupling terms in the macro-scale constitutive equations. Were the interactions between different kinematic and stress measures to be taken into account, the analysis would have led to extra stiffness tensors. Those extra stiffness tensors will include fourth, fifth, and sixth rank tensors. It is, however, known that there are no isotropic tensors of odd rank. So the fifth rank tensors implying cross-linking either between the second gradient kinematic measures and the second rank stress measures or between the first gradient kinematic measures and the third rank stress measures will be always zero for

isotropic materials. The other cross-linking terms might be included in the model by taking into account the interactions in the micro-scale which will be pursued in the future.

Note that the summations in Eq. 7.24-7.29 are over all grain-pair interactions within the material point. The quantities within the summation can be evaluated provided we know the grain-pair stiffness and branch vectors. In principle these properties are different for every interacting grain-pair. However, the spatial distribution of these properties within the material point is not known. It is notable though that the quantities within the summation are functions of the orientations of the branch vector and the product of grain-pair stiffness and branch length. For describing the mean behavior of a random granular material, the micro-scale parameter, represented by the product of grain-pair stiffness and branch length, can be taken to be averages for a given branch vector direction.

In principal, the distribution of grain-pair interactions and their properties (length of the interaction line and also the inter-granular stiffness coefficients) depend on the direction of the contact. Thus the directional distribution of the inter-granular interactions plays an important role in defining the constitutive tensors. In order to approach the directional dependency in a systematic way, a directional density distribution function,  $\xi(\theta, \phi)$ , is introduced. This distribution function is intended to represent the directional dependence of number and stiffness of the interacting grain-pairs. In isotropic materials all directions have the same properties and bond length and stiffness for all directions are equal. Thus the directional density distribution function is just a constant of normalization in all directions

$$\xi(\theta, \phi) = \frac{1}{4\pi} \Rightarrow \int_{\Omega} \xi d\Omega = \int_{\theta} \int_{\phi} \xi \sin \theta d\theta d\phi = 1 \quad (7.30)$$



where  $d\Omega = d\theta \sin\theta d\phi$  denotes the solid angle corresponding to given  $\theta$  and  $\phi$  values. Using a properly defined density distribution function can lead to models for materials with different levels of inherent anisotropy satisfying all symmetry requirements due to the presence and lack of elastic symmetries (See Chapter 6). Other efforts for modeling anisotropic materials using other forms of directional density distribution functions can be found in [18, 46, 178]. Considering the volume density of grain-pair interactions in a material point to be  $N_p$ , and assuming an average grain-pair stiffness within a solid angle  $d\Omega$ , the stiffness tensors derived in Eq. 7.24-7.29 can be rewritten in the following form by converting the summations to integrations

$$C_{ijkl}^M = \frac{1}{V} \sum_{\alpha} K_{ik}^M l_l^{\alpha} l_j^{\alpha} = l^2 N_p \int_{\theta=0}^{\pi} \int_{\phi=0}^{2\pi} (K_{ik}^M n_j n_l) \xi \sin\theta d\phi d\theta \quad (7.31)$$

$$C_{ijkl}^m = \frac{1}{V} \sum_{\alpha} K_{ik}^m l_l^{\alpha} l_j^{\alpha} = l^2 N_p \int_{\theta=0}^{\pi} \int_{\phi=0}^{2\pi} (K_{ik}^m n_j n_l) \xi \sin\theta d\phi d\theta \quad (7.32)$$

$$A_{ijklmn} = \frac{1}{V} \sum_{\alpha} K_{il}^g J_{mn}^{\alpha} J_{jk}^{\alpha} = \frac{l^4 N_p}{4} \int_{\theta=0}^{\pi} \int_{\phi=0}^{2\pi} (K_{il}^g n_j n_k n_m n_n) \xi \sin\theta d\phi d\theta \quad (7.33)$$

$$D_{ijkl}^M = \frac{1}{V} \sum_{\alpha} G_{ik}^M l_l^{\alpha} l_j^{\alpha} = l^2 N_p \int_{\theta=0}^{\pi} \int_{\phi=0}^{2\pi} (G_{ik}^M n_j n_l) \xi \sin\theta d\phi d\theta \quad (7.34)$$

$$D_{ijkl}^m = \frac{1}{V} \sum_{\alpha} G_{ik}^m l_l^{\alpha} l_j^{\alpha} = l^2 N_p \int_{\theta=0}^{\pi} \int_{\phi=0}^{2\pi} (G_{ik}^m n_j n_l) \xi \sin\theta d\phi d\theta \quad (7.35)$$

$$B_{ijklmn} = \frac{1}{V} \sum_{\alpha} G_{il}^g J_{mn}^{\alpha} J_{jk}^{\alpha} = \frac{l^4 N_p}{4} \int_{\theta=0}^{\pi} \int_{\phi=0}^{2\pi} (G_{il}^g n_j n_k n_m n_n) \xi \sin\theta d\phi d\theta \quad (7.36)$$

It is seen from the above equations that the granular micromechanical view of the material behavior gives rise to six constitutive tensors. These include three fourth rank constitutive tensors,  $C_{ijkl}^M$ ,  $C_{ijkl}^m$ , and  $D_{ijkl}^m$ , and two sixth rank constitutive tensors,  $A_{ijklmn}$  and  $B_{ijklmn}$ . The grain-pair stiffness parameters in these constitutive tensors are conceived, in a statistical sense, to describe

the essential grain-scale mechanisms in a collective granular system and do not represent the behavior of two interacting grains, isolated from the entire assembly. This view is in contrast to the previous continuum models of granular media in which the grain-pair stiffness coefficients are often taken to be those of isolated interacting grains (see for example [19, 31, 32, 179]). In the current model, these stiffness parameters function as the fundamental material properties which are related to their measurable continuum counterparts. Needless to say, results of classical continuum model will be recovered if the fluctuation, the second gradient and the rotational inter-granular stiffness parameters vanish. However, it is clear from the kinematic analyses presented here that these mechanisms should have non vanishing contributions. The need for including the fluctuation and second gradient terms is supported by analyses of grain packing [19, 175] as well as computer simulations and experiments of grain assemblies [47, 172, 173] that show strong non-affine motions in a volume element comprising large number of grains.

It is clear from Eqs. 7.31, 7.32, 7.34, and 7.35, that the four tensors  $C_{ijkl}^M$ ,  $C_{ijkl}^m$ ,  $D_{ijkl}^M$ , and  $D_{ijkl}^m$ , are formally similar. The difference between them is merely due to the difference between the micro-scale stiffness coefficients of the grain-pair. For isotropic elasticity the following closed form expressions for the fourth rank stiffness tensors are derived by performing the integrations

$$\left. \begin{aligned} C_{iiii}^{\xi} &= \frac{l^2 N_p}{15} (3K_n^{\xi} + 2K_w^{\xi}); & C_{ijij}^{\xi} &= \frac{l^2 N_p}{15} (K_n^{\xi} - K_w^{\xi}) \\ C_{ijij}^{\xi} &= \frac{l^2 N_p}{15} (K_n^{\xi} + 4K_w^{\xi}) & C_{ijji}^{\xi} &= \frac{l^2 N_p}{15} (K_n^{\xi} - K_w^{\xi}); & i \neq j \\ C_{ijkl}^{\xi} &= 0; & & \text{otherwise} \end{aligned} \right\}; \quad \xi = M \text{ and } m \quad (7.37)$$

$$\left. \begin{aligned}
D_{iii}^{\xi} &= \frac{l^2 N_p}{15} (3G_n^{\xi} + 2G_w^{\xi}); & D_{ijj}^{\xi} &= \frac{l^2 N_p}{15} (G_n^{\xi} - G_w^{\xi}) \\
D_{ijj}^{\xi} &= \frac{l^2 N_p}{15} (G_n^{\xi} + 4G_w^{\xi}) & D_{iji}^{\xi} &= \frac{l^2 N_p}{15} (G_n^{\xi} - G_w^{\xi}); & i \neq j \\
D_{ijkl}^{\xi} &= 0; & & & \text{otherwise}
\end{aligned} \right\}; \quad \xi = M \text{ and } m \quad (7.38)$$

In Eq. 7.37 and 7.38, the subscripts take values 1, 2, or 3 and summation over repeated indices is not implied. A closed form presentation of all components of the sixth rank tensors  $A_{ijklmn}$  and  $B_{ijklmn}$  are also calculated for isotropic elasticity by calculating Eq. 7.33, and 7.36 respectively.

$$\left\{ \begin{aligned}
A_{111111} &= A_{222222} = A_{333333} = l^4 N_p \frac{5K_n^g + 2K_w^g}{35} \\
A_{111122} &= A_{111133} = A_{112112} = A_{113113} = A_{122111} = A_{133111} = A_{221221} = A_{222233} = A_{222211} = A_{223223} \\
&= A_{233222} = A_{331331} = A_{332332} = A_{333311} = A_{333322} = A_{211222} = A_{311333} = A_{322333} = l^4 N_p \frac{3K_n^g + 4K_w^g}{105} \\
A_{111221} &= A_{111313} = A_{112222} = A_{112211} = 3A_{112233} = 3A_{112332} = A_{113333} = A_{113311} = 3A_{113223} = 3A_{113322} \\
&= A_{122221} = 3A_{122331} = 3A_{123231} = 3A_{123312} = A_{133331} = 3A_{133221} = A_{221111} = A_{221122} = 3A_{221133} \\
&= 3A_{221331} = A_{222112} = A_{222332} = A_{223333} = A_{223322} = 3A_{223113} = 3A_{223311} = 3A_{231123} = 3A_{231321} \\
&= A_{233332} = 3A_{233112} = A_{331111} = A_{331133} = 3A_{331122} = 3A_{331221} = A_{332222} = A_{332233} = 3A_{332112} \\
&= 3A_{332211} = A_{333113} = A_{333223} = A_{211112} = 3A_{211332} = A_{311113} = 3A_{311223} = 3A_{312123} = 3A_{312231} \\
&= A_{322223} = 3A_{322113} = l^4 N_p \frac{K_n^g - K_w^g}{35} \\
A_{122122} &= 3A_{122133} = 3A_{123123} = A_{133133} = 3A_{133122} = 3A_{231213} = A_{233233} = 3A_{233211} = A_{211211} \\
&= 3A_{211233} = A_{311311} = 3A_{311322} = 3A_{312312} = A_{322322} = 3A_{322311} = l^4 N_p \frac{K_n^g + 6K_w^g}{35} \\
A_{ijklmn} &= A_{ikjlmn} = A_{ijklnm} = A_{ikjlmm} \\
A_{ijklmn} &= 0; & & & \text{otherwise}
\end{aligned} \right\} \quad (7.39)$$

$$\left\{ \begin{aligned}
& B_{111111} = B_{222222} = B_{333333} = l^4 N_p \frac{5G_n^g + 2G_w^g}{35} \\
& B_{111122} = B_{111133} = B_{112112} = B_{113113} = B_{122111} = B_{133111} = B_{221221} = B_{222233} = B_{222211} = B_{223223} \\
& = B_{233222} = B_{331331} = B_{332332} = B_{333311} = B_{333322} = B_{211222} = B_{311333} = B_{322333} = l^4 N_p \frac{3G_n^g + 4G_w^g}{105} \\
& B_{111221} = B_{111313} = B_{112222} = B_{112211} = 3B_{112233} = 3B_{112332} = B_{113333} = B_{113311} = 3B_{113223} = 3B_{113322} \\
& = B_{122221} = 3B_{122331} = 3B_{123231} = 3B_{123312} = B_{133331} = 3B_{133221} = B_{221111} = B_{221122} = 3B_{221133} \\
& = 3B_{221331} = B_{222112} = B_{222332} = B_{223333} = B_{223322} = 3B_{223113} = 3B_{223311} = 3B_{231123} = 3B_{231321} \\
& = B_{233332} = 3B_{233112} = B_{331111} = B_{331133} = 3B_{331122} = 3B_{331221} = B_{332222} = B_{332233} = 3B_{332112} \\
& = 3B_{332211} = B_{333113} = B_{333223} = B_{211112} = 3B_{211332} = B_{311113} = 3B_{311223} = 3B_{312123} = 3B_{312231} \\
& = B_{322223} = 3B_{322113} = l^4 N_p \frac{G_n^g - G_w^g}{35} \\
& B_{122122} = 3B_{122133} = 3B_{123123} = B_{133133} = 3B_{133122} = 3B_{231213} = B_{233233} = 3B_{233211} = B_{211211} \\
& = 3B_{211233} = B_{311311} = 3B_{311322} = 3B_{312312} = B_{322322} = 3B_{322311} = l^4 N_p \frac{G_n^g + 6G_w^g}{35} \\
& B_{ijklmn} = B_{ikjlmn} = B_{ijklnm} = B_{ikjlnm} \\
& B_{ijklmn} = 0; \quad \textit{otherwise}
\end{aligned} \right. \tag{7.40}$$

We note here that the six stiffness tensors presented in Eq. 7.37-7.40 comply, in form, with the general form of fourth and sixth rank isotropic tensors that can be derived based only on mathematical considerations (see for example [2, 180]). In order to facilitate the following discussion and, in particular, deriving the equations of motion for the micromorphic media under consideration, it is advantageous to write these stiffness tensors (given in Eq. 7.37-7.40) in the indicial notation used by Mindlin [2]. Using the definition of the most general form of fourth and sixth rank isotropic tensors, the stiffness tensors corresponding to the displacement field (given in Eq. 7.37 and 7.39) are rewritten as follows

$$\begin{aligned}
C_{ijkl}^M &= \lambda \delta_{ij} \delta_{kl} + \mu_1 \delta_{ik} \delta_{jl} + \mu_2 \delta_{il} \delta_{jk} \\
C_{ijkl}^m &= b_1 \delta_{ij} \delta_{kl} + b_2 \delta_{ik} \delta_{jl} + b_3 \delta_{il} \delta_{jk} \\
A_{ijklmn} &= a_1 \delta_{ij} \delta_{kl} \delta_{mn} + a_2 \delta_{ij} \delta_{km} \delta_{nl} + a_3 \delta_{ij} \delta_{kn} \delta_{ml} + a_4 \delta_{jk} \delta_{il} \delta_{mn} + a_5 \delta_{jk} \delta_{im} \delta_{nl} \\
&\quad + a_6 \delta_{jk} \delta_{in} \delta_{lm} + a_7 \delta_{ki} \delta_{jl} \delta_{nm} + a_8 \delta_{ki} \delta_{jm} \delta_{nl} + a_9 \delta_{ki} \delta_{jn} \delta_{lm} + a_{10} \delta_{il} \delta_{jm} \delta_{kn} \\
&\quad + a_{11} \delta_{jl} \delta_{km} \delta_{in} + a_{12} \delta_{kl} \delta_{im} \delta_{jn} + a_{13} \delta_{il} \delta_{jn} \delta_{km} + a_{14} \delta_{jl} \delta_{kn} \delta_{im} + a_{15} \delta_{kl} \delta_{in} \delta_{jm}
\end{aligned} \tag{7.41}$$

while those corresponding to the rotation field (given in Eq. 7.38 and 7.40) are given as

$$\begin{aligned}
D_{ijkl}^M &= \eta \delta_{ij} \delta_{kl} + \nu_1 \delta_{ik} \delta_{jl} + \nu_2 \delta_{il} \delta_{jk} \\
D_{ijkl}^m &= d_1 \delta_{ij} \delta_{kl} + d_2 \delta_{ik} \delta_{jl} + d_3 \delta_{il} \delta_{jk} \\
B_{ijklmn} &= e_1 \delta_{ij} \delta_{kl} \delta_{mn} + e_2 \delta_{ij} \delta_{km} \delta_{nl} + e_3 \delta_{ij} \delta_{kn} \delta_{ml} + e_4 \delta_{jk} \delta_{il} \delta_{mn} + e_5 \delta_{jk} \delta_{im} \delta_{nl} \\
&\quad + e_6 \delta_{jk} \delta_{in} \delta_{lm} + e_7 \delta_{ki} \delta_{jl} \delta_{mn} + e_8 \delta_{ki} \delta_{jm} \delta_{nl} + e_9 \delta_{ki} \delta_{jn} \delta_{lm} + e_{10} \delta_{il} \delta_{jm} \delta_{kn} \\
&\quad + e_{11} \delta_{jl} \delta_{km} \delta_{in} + e_{12} \delta_{kl} \delta_{im} \delta_{jn} + e_{13} \delta_{il} \delta_{jn} \delta_{km} + e_{14} \delta_{jl} \delta_{kn} \delta_{im} + e_{15} \delta_{kl} \delta_{in} \delta_{jm}
\end{aligned} \tag{7.42}$$

The parameters used in Eq. 7.41 and 7.42 are macroscopic stiffness parameters that define the linear elastic behavior of isotropic micromorphic media. By equating the components of the stiffness tensors derived in Eq. 7.37-7.40 with those given in the index form in Eq. 7.41 and 7.42, the parameters used in the index form are derived based on the micro-scale intergranular stiffness coefficients. The stiffness parameters corresponding to displacement field are derived as

$$\lambda = \mu_2 = \frac{l^2 N_p}{15} (K_n^M - K_w^M); \quad \mu_1 = \frac{l^2 N_p}{15} (K_n^M + 4K_w^M) \tag{7.43a}$$

$$b_1 = b_3 = \frac{l^2 N_p}{15} (K_n^m - K_w^m); \quad b_2 = \frac{l^2 N_p}{15} (K_n^m + 4K_w^m) \tag{7.43b}$$

$$\begin{cases} a_1 = a_2 = a_3 = a_5 = a_7 = a_6 = a_8 = a_9 = a_{10} = a_{11} = a_{12} = a_{14} = \frac{l^4 N_p}{105} (K_n^g - K_w^g) \\ a_4 = a_{10} = a_{13} = \frac{l^4 N_p}{105} (K_n^g + 6K_w^g) \end{cases} \tag{7.43c}$$

while those corresponding to the rotation field are

$$\eta = \nu_2 = \frac{l^2 N_p}{15} (G_n^M - G_w^M); \quad \nu_1 = \frac{l^2 N_p}{15} (G_n^M + 4G_w^M) \tag{7.44a}$$

$$d_1 = d_3 = \frac{l^2 N_p}{15} (G_n^m - G_w^m); \quad d_2 = \frac{l^2 N_p}{15} (G_n^m + 4G_w^m) \tag{7.44b}$$

$$\begin{cases} e_1 = e_2 = e_3 = e_5 = e_6 = e_7 = e_8 = e_9 = e_{11} = e_{12} = e_{14} = e_{15} = \frac{l^4 N_p}{105} (G_n^g - G_w^g) \\ e_4 = e_{10} = e_{13} = \frac{l^4 N_p}{105} (G_n^g + 6G_w^g) \end{cases} \tag{7.44c}$$

Note here that the parameters  $\lambda$  and  $\mu = (\mu_1 + \mu_2)/2$  in Eq. 7.43a are the well-known Lamé parameters used in first gradient isotropic elasticity.

## 7.4 Summary

The granular micromechanics approach has been applied to find a micromorphic continuum model for elasticity of granular media. In this approach, continuum model of granular materials is obtained by considering the interactions of grain pairs. Since the complete granular microstructure and micromechanics of a material is seldom known, it is impossible to know the displacement of all the grains within a material point.

The relative displacement of interacting grain-pairs are decomposed into an average term compatible with the macro-scale field, a micro-scale fluctuation term defined within a material point, and its second gradient. In addition, the second gradient terms are found to give rise to relative rotations between grain pairs. Further grains' spins and their effect on the inter-granular relative displacement and rotations are also taken into account.

The macro-scale deformation energy density is thus modeled as a summation of micro-scale deformation energy defined for each grain-pair as a function of inter-granular relative displacements and rotations. Consequently, inter-granular force conjugates are defined for each micro-scale kinematic measure and the macro-scale stress conjugates are obtained in terms of these inter-granular forces. Furthermore, for linear elasticity, the micro-scale deformation energy is formulated as a quadratic function of the kinematic measures, which requires introduction of different inter-granular stiffness measures.

In the macro-scale, conjugate to the different strain measures, a stress field has been introduced. Helmholtz free energy density has been defined as a function of all the strain measures (average displacement gradient, displacement fluctuation gradient and second gradient, average spin gradient, spin fluctuation gradient and second gradient). The different terms are assumed not to be interacting in the formation of energy (No coupling terms in the energy functional are allowed). Finally by equating the Helmholtz free energy with the average deformation energy of all grain-pair interactions, macroscopic stress tensors and stiffness tensors have been derived as based on microscopic inter-granular stiffness coefficients.

Close form solutions for all components of all the defined stiffness tensors have been presented for elastic isotropy and the equations in index form have also been formulated. This formulation will be useful for deriving the equations of motion for solving wave propagation problem which is the topic of next chapter.

## **8 IDENTIFICATION OF HIGHER ORDER MICRO- AND MACRO-SCALE STIFFNESS COMPONENTS USING GRANULAR MICROMECHANICS**

### **8.1 Introduction**

One of the most common critiques on extended continuum models, methods that include higher order and fluctuation terms, is the lack of a practical approach for calibrating the relevant material properties. Especially for the second gradient terms, since the number of the components in the 6<sup>th</sup> rank stiffness tensor is very large, the task of calibration of material properties becomes increasingly difficult.

In this chapter, a practical approach has been presented that can be a beginning point for calibrating the stiffness components for higher order and micromorphic models. Using this approach, it is possible to calibrate all the inter-granular stiffness coefficients corresponding to all kinematic measures (average, fluctuation, and second gradient) for any given grain assembly. However, in order to apply it to a material system that cannot be identified as an exact grain assembly with identifiable grains, grain boundaries, contacts, etc., more work needs to be done.

The presented approach is based on the concept of deformation energy. All components of the inter-granular relative displacement and rotation contribute separately to the internal deformation energy in the material. In this approach, the boundary conditions pertinent to each component of the total displacement are applied on the material point separately. Using a discrete analysis, equilibrium (minimum energy state) is enforced on the granular assembly. As a result the total energy of the assembly is calculated and the stress measure that is conjugate to the applied



boundary condition can be derived. Performing this analysis for different boundary conditions, all components of the macroscopic stiffness tensors corresponding to all kinematic measures can be derived.

The analysis is performed with a slightly different micromorphic theory compared to the theory presented in Chapter 7. In the micromorphic theory that was used for this analysis, the effects of grain spins are neglected. However, note that the same analysis can be performed on the complete micromorphic theory presented in Chapter 7, which can be a topic of a future work.

In this chapter, first the micromorphic theory without considering the effects of grain spins is presented. Following that, the equilibrium conditions and the corresponding boundary conditions for the micromorphic theory are presented. Then a brief description of the discrete analysis performed on the assembly is given. Finally, for different grain assemblies, the discrete analysis is performed and the material parameters for the micromorphic theory are calibrated. The grain-pair stiffness coefficients relevant to the effective continuum medium are then back-calculated treating the assembly as a unit cell which is randomly oriented to yield an isotropic material.

The identification process shows the clear need for the additional macro-scale deformation measures for the continuum modeling of granular materials and exemplifies the need for partitioning the grain-pair (micro-scale) deformation energy into the corresponding micro-scale mechanisms. The work presented in this chapter is published in 2015 and 2016 [160, 161].

## **8.2 Micromorphic Granular Micromechanics, without grain spins**

### **8.2.1 Kinematics of Granular Media**

To develop the measures that describe the kinematics of a granular assembly, while neglecting the effects of grain spins, the relative displacement of two contacting neighbor grains,  $n$  and  $p$ , within a continuum material point in the coordinate system of  $\mathbf{x}$  is considered. Displacement of grain  $p$

is written using a Taylor series expansion of the displacement of the neighbor grain,  $n$ , with terms up to 2<sup>nd</sup> order as follows

$$\phi_i^p = \phi_i^n + \phi_{i,j}^n l_j + \frac{1}{2} \phi_{i,jk}^n l_j l_k + \dots \quad (8.1)$$

where  $\phi_i$  is the displacement of grain centroids,  $l_j$  is the vector joining the centroids of the two grains,  $n$  and  $p$ . The gradient of the displacement field,  $\phi_{i,j}$ , (the micro-scale displacement gradient) is decomposed here into two parts, one representing the average or macro-scale displacement gradient,  $\bar{\phi}_{i,j}$ , and the other,  $\gamma_{ij}$ , representing the gradient, with respect to  $\mathbf{x}'$ , of the displacement fluctuations in the following manner

$$\psi_{ij} \equiv \phi_{i,j} = \bar{\phi}_{i,j} - \gamma_{ij} \quad (8.2)$$

Figure 8.1 shows the schematic representation of a material point in 2D coordinate system and the macroscopic coordinate system,  $\mathbf{x}$ , as well as the microscopic coordinate system,  $\mathbf{x}'$ .

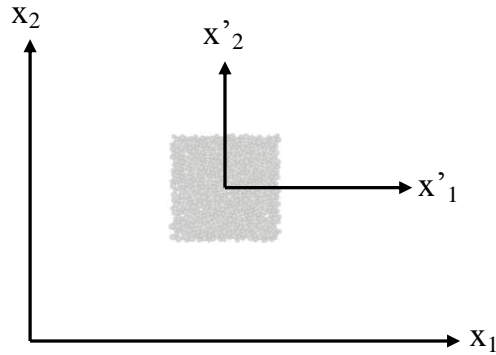


Figure 8.1- Representation of material point and the global coordinate system,  $\mathbf{x}$ , and the local coordinate system,  $\mathbf{x}'$ , located at the material point's center of mass

Note that the macro-scale displacement gradient,  $\bar{\phi}_{i,j}$ , is independent of coordinates  $x_k$ . Grain displacement fluctuations are assumed to be linear functions of the local coordinate system,  $\mathbf{x}'$  and this leads to a micromorphic theory of degree 1 in the terminology introduced by Germain [6, 181]. This implies that the second rank tensor  $\gamma_{ij}$  is independent of the local coordinates (it is

homogeneous within the material point) and is a function only of  $\mathbf{x}$ . Now considering the second gradient terms in the formulation and using Eq. 8.1 and Eq. 8.2 the relative displacement of two neighbor grains,  $n$  and  $p$ , is derived as

$$\delta_i^{np} = \phi_i^p - \phi_i^n = (\bar{\phi}_{i,j} - \gamma_{ij})l_j + \frac{1}{2}\phi_{i,jk}l_jl_k = \bar{\phi}_{i,j}l_j - \gamma_{ij}l_j + \frac{1}{2}\phi_{i,jk}l_jl_k = \delta_i^M - \delta_i^m + \delta_i^s \quad (8.3)$$

where

$$\delta_i^M = \bar{\phi}_{i,j}l_j; \quad \delta_i^m = \gamma_{ij}l_j; \quad \delta_i^s = \frac{1}{2}\phi_{i,jk}l_jl_k = \phi_{i,jk}J_{jk} = \psi_{ij,k}J_{jk} \quad (8.4)$$

In this equation, the tensor  $J_{ij} = l_i l_j / 2$  represents a moment tensor which is introduced for simplifying further derivations. As seen from Eq. 8.3, the inter-granular relative displacements between two interacting (contacting) grains is decomposed into three terms: (1)  $\delta_i^M$  due to the macro-scale displacement gradient,  $\bar{\phi}_{i,j}$ , (2)  $\delta_i^m$  due to the gradients of the fluctuation in grain displacement,  $\gamma_{ij}(x)$ , and (3)  $\delta_i^s$  due to the second gradient term,  $\phi_{i,jk}$ , which is same as the gradient of the relative displacements,  $\gamma_{ij,k}$ . A similar analysis could be done for the contact problem [182, 183].

Further, the relative rotation of grains within the granular assembly can be related to the rotation field within the material point defined as the curl of displacement field [154]. Now using this definition of rotation and applying Taylor series expansion, the relative rotation of two neighbor grains,  $n$  and  $p$ , denoted as  $\theta$  is obtained as

$$\theta_i^{np} = \kappa_i^p - \kappa_i^n = \kappa_{i,p}^n l_p = (e_{ijk} \phi_{k,j})_{,p} l_p = e_{ijk} \phi_{k,jp} l_p \quad (8.5)$$

The inter-granular relative rotation between two interacting grains is, thus, related to the second gradient term,  $\phi_{i,jk}$ . That grains undergo relative rotations is also known from measurements of kinematic fields in grain assemblies [47, 172].

## 8.2.2 Macro-scale Stress and Micro-scale Force Conjugates

In the formulation presented hereafter, anti-symmetric part of the average displacement gradient tensor,  $\bar{\phi}_{i,j}$ , is discarded and only the symmetric part,  $\bar{\phi}_{(i,j)}$ , is retained as the classical small deformation strain tensor. The macro-scale deformation energy density of the granular continua can now be defined as a function of the continuum kinematic measures as:  $W = W(\bar{\phi}_{(i,j)}, \gamma_{ij}, \phi_{i,jk})$ . Consequently, the macro-scale stress components conjugate to these kinematic measures are obtained as

$$\tau_{ij} = \frac{\partial W}{\partial \bar{\phi}_{(i,j)}} = \frac{\partial W}{\partial \varepsilon_{ij}}; \quad \sigma_{ij} = \frac{\partial W}{\partial \gamma_{ij}}; \quad \mu_{ijk} = \frac{\partial W}{\partial \gamma_{ij,k}} \quad (8.6)$$

where  $\tau_{ij}$ ,  $\sigma_{ij}$ , and  $\mu_{ijk}$  are Cauchy stress, relative stress, and double stress respectively. It is now noted that the macroscopic strain energy density function can be obtained as the volume average of the deformation energies of the grain-pair interactions written as

$$W = \frac{1}{V} \sum_{\alpha} W^{\alpha}(\delta_i^M, \delta_i^m, \delta_i^g, \theta_i^{\mu}) \quad (8.7)$$

where the superscript  $\alpha$  denoted the  $\alpha^{\text{th}}$  grain-pair interaction and it has been intentionally dropped from the kinematic measures to simplify the equations. Now conjugate to each one of these displacement measures and the rotation measures, force and moment vectors are defined as derivatives of the strain energy function with respect to the corresponding kinematic measure

$$\frac{\partial W^\alpha}{\partial \delta_i^{\alpha\xi}} = f_i^{\alpha\xi}; \quad \text{where } \xi: \text{M, m, g} \quad (8.8)$$

$$\frac{\partial W^\alpha}{\partial \theta_i^{\alpha u}} = m_i^{\alpha u}$$

Now substituting Eq. 8.8 and Eq. 8.7 into Eq. 8.6 and using the definition of inter-granular displacement and rotation measures presented in Eq. 8.4 and Eq. 8.5 respectively, macroscopic stress tensors conjugate to each one the macro-scale kinematic measures can be derived as follows

$$\tau_{ij} = \frac{\partial W}{\partial \varepsilon_{ij}} = \frac{1}{V} \sum_\alpha \frac{\partial W^\alpha}{\partial \delta_k^M} \frac{\partial \delta_k^M}{\partial \varepsilon_{ij}} = \frac{1}{V} \sum_\alpha f_i^M l_j^\alpha \quad (8.9)$$

$$\sigma_{ij} = \frac{\partial W}{\partial \gamma_{ij}} = \frac{1}{V} \sum_\alpha \frac{\partial W^\alpha}{\partial \delta_k^m} \frac{\partial \delta_k^m}{\partial \gamma_{ij}} = \frac{1}{V} \sum_\alpha f_i^m l_j^\alpha \quad (8.10)$$

$$\mu_{ijk} = \frac{\partial W}{\partial \phi_{i,jk}} = \frac{1}{V} \sum_\alpha \left( \frac{\partial W^\alpha}{\partial \delta_l^s} \frac{\partial \delta_l^s}{\partial \phi_{i,jk}} + \frac{\partial W^\alpha}{\partial \theta_l^u} \frac{\partial \theta_l^u}{\partial \phi_{i,jk}} \right) = \frac{1}{V} \left( \sum_\alpha f_i^s J_{jk}^\alpha + \sum_\alpha m_l^u e_{jil} l_k^\alpha \right) \quad (8.11)$$

In Eqs. 8.9-8.11, the superscript  $\alpha$  has been dropped from the micro-scale kinematic and force measures. We contrast the expressions for the stress tensor conjugates obtained here with those reported in literature [184] that are typically based upon the virial theorem [185]. Here, we have introduced separate force measures conjugate to the grain-pair (micro-scale) counterparts of the continuum deformation measures.

### 8.2.3 Micro-scale and Macro-scale Constitutive Equations

A set of constitutive equations is now introduced at the micro-scale that link the micro-scale kinematics measures to their conjugate force and moment measures as

$$\begin{aligned} f_i^{\alpha\xi} &= K_{ij}^{\alpha\xi} \delta_j^{\alpha\xi}; & \text{where } \xi: \text{M, m, g} \\ m_i^{\alpha u} &= G_{ij}^{\alpha u} \theta_j^{\alpha u}; \end{aligned} \quad (8.12)$$

Here, we note that for simplicity and without the loss of generality, the cross coupling between different force and kinematic measures has been ignored. Thus each of the inter-granular force and moment components are dependent only on their conjugated displacement measure. The consequence of this assumption will be that uncoupled constitutive relationships will be obtained for the continuum model. Further, it should be noted that the micro-scale stiffness coefficients in Eq. 8.12 represent inter-granular stiffness measures in a statistical sense. Since the total relative displacement between two neighbor grains were previously decomposed into different terms, representing the average and fluctuation displacement gradients and also second gradient terms, the stiffness coefficients corresponding to them will all contribute, in a statistical sense, to form the overall response of the interaction to the grains' relative displacements. Now substituting the micro-scale constitutive equations, Eq. 8.12, into Eq. 8.9-8.11 and noting that the macro-scale strain measures are constant throughout the material point, macro-scale constitutive equations are derived as

$$\tau_{ij} = \frac{1}{V} \sum_{\alpha} f_i^M l_j^{\alpha} = \frac{1}{V} \sum_{\alpha} K_{ik}^M \delta_k^M l_j^{\alpha} = \left( \frac{1}{V} \sum_{\alpha} K_{ik}^M l_l^{\alpha} l_j^{\alpha} \right) \varepsilon_{kl} = C_{ijkl}^M \varepsilon_{kl} \quad (8.13)$$

$$\sigma_{ij} = \frac{1}{V} \sum_{\alpha} f_i^m l_j^{\alpha} = \frac{1}{V} \sum_{\alpha} K_{ik}^m \delta_k^{\alpha} l_j^{\alpha} = \left( \frac{1}{V} \sum_{\alpha} K_{ik}^m l_l^{\alpha} l_j^{\alpha} \right) \gamma_{kl} = C_{ijkl}^m \gamma_{kl} \quad (8.14)$$

$$\begin{aligned} \mu_{ijk} &= \frac{1}{V} \sum_{\alpha} (f_i^s J_{jk}^{\alpha} + m_l^u e_{jil} l_k) = \left( \frac{1}{V} \sum_{\alpha} K_{il}^s J_{mn}^{\alpha} J_{jk}^{\alpha} + \frac{1}{V} \sum_{\alpha} G_{pq}^u e_{mlq} e_{jip} l_k l_n \right) \phi_{l,mn} \\ &= (A_{ijklmn}^s + A_{ijklmn}^u) \phi_{l,mn} = A_{ijklmn} \phi_{l,mn} \end{aligned} \quad (8.15)$$

Here it should be noted that the summations in Eq. 8.13-8.15 are performed over all grain-pair interactions inside the material point. The quantities inside the summation (stiffness coefficients and geometric parameters  $l_i$  and  $J_{ij}$ ) are all different for every single grain-pair interaction. It is, however, possible to find an average value for all these quantities for grain-pair interactions in any

given orientation. Using these average values, the summation over all grain interactions can be changed to integration over all generic orientations. This is done using two new parameters,  $N_p$ , representing the number density of grain interactions defined as the number of grain-pair interactions divided by the volume of the VE, and a normalized directional density distribution function,  $\xi$ , defining the density of contacts in different orientations within the material point (See Chapter 6 for a complete description). For isotropic materials (or for randomly distributed grain assemblies) the density distribution function in 2D and 3D domains will be

$$\xi(\theta) = \frac{1}{2\pi} \Rightarrow \int_{\theta} \xi d\theta = \frac{1}{2\pi} 2\pi = 1; \quad \text{for 2D} \quad (8.16a)$$

$$\xi(\theta, \phi) = \frac{1}{4\pi} \Rightarrow \int_{\theta} \int_{\phi} \xi(\sin \theta d\theta d\phi) = \frac{1}{4\pi} (2\pi)(2) = 1; \quad \text{for 3D} \quad (8.16b)$$

In Eq. 8.16a,  $\theta$  is the polar angle of the 2D polar coordinate system while in Eq. 16b,  $\theta$  and  $\phi$  are the polar angle measured from the vertical axis and the azimuth angle in the 3D spherical coordinate system respectively.

#### 8.2.4 Constitutive coefficients for 2D Granular System

For further development in this chapter, the focus will be on two dimensional (2D) material systems and grain assemblies for demonstrating and visualizing the model applicability. In two-dimensions, the local coordinate system is composed of a unit normal vector,  $n_i$ , in the direction of the branch vector joining the two grains' centroids and another unit vector,  $s_i$ , lying in the direction of the tangential plane, whose normal vector is  $\mathbf{n}$ . These Cartesian components of the unit vectors are defined as

$$\begin{aligned} n_i &= \langle \cos \theta, \sin \theta \rangle \\ s_i &= \langle -\sin \theta, \cos \theta \rangle \end{aligned} \quad (8.17)$$

Following the previous discussion about using an average value for the geometric tensors  $l_i$  and  $J_{ij}$  in any given orientation, and using the 2D density distribution function introduced in Eq. 8.16a, the summations in Eq. 8.13-8.15 are rewritten as integrations in the following form

$$C_{ijkl}^M = \frac{1}{V} \sum_{\alpha} K_{ik}^M l_l^{\alpha} l_j^{\alpha} = l^2 N_p \int_{\theta=0}^{2\pi} (K_{ik}^M n_j n_l) \xi d\theta \quad (8.18)$$

$$C_{ijkl}^m = \frac{1}{V} \sum_{\alpha} K_{ik}^m l_l^{\alpha} l_j^{\alpha} = l^2 N_p \int_{\theta=0}^{2\pi} (K_{ik}^m n_j n_l) \xi d\theta \quad (8.19)$$

$$A_{ijklmn}^s = \frac{1}{V} \sum_{\alpha} K_{il}^s J_{mn}^{\alpha} J_{jk}^{\alpha} = \frac{l^4 N_p}{4} \int_{\theta=0}^{2\pi} (K_{il}^s n_j n_k n_m n_n) \xi d\theta \quad (8.20a)$$

$$A_{ijklmn}^u = \frac{1}{V} \sum_{\alpha} G_{pq}^u e_{mlq} e_{jip} l_k l_n = l^2 N_p \int_{\theta=0}^{2\pi} (G_{pq}^u e_{lmq} e_{ijp} n_k n_n) \xi d\theta \quad (8.20b)$$

Note that since the method is applied here for only 2D modeling, the indices  $i, j, k, l, m$ , and  $n$  take the value of either 1 or 2. It should be noted here that in a 2D domain (with in-plane coordinate axes 1 and 2) the only possible rotation is the rotation about the axis normal to the plane under consideration, 3 axis, denoted as  $\theta_3$  which gives rise to the moment component  $m_3$ . Now, In Eq. 20b,  $e_{ijp}$  and  $e_{lmq}$  denote permutation symbol and since the indices  $i, j, l$ , and  $m$  can take only values of 1 and 2, the indices  $p$  and  $q$  should only take the value 3. So the rotational stiffness tensor,  $\mathbf{G}$ , can have only one component,  $G_{pq} = G_{33} = G$ . Having this in mind and considering Eq. 8.12 defining the general constitutive equations in inter-granular scale, the moment-rotation constitutive equation in grain-scale can thus be written simply as

$$m_3 = G \theta_3 \quad (8.21)$$

For the force-displacement constitutive equations in micro-scale, inter-granular force and displacement vectors are decomposed in the local directions into two components, one normal and



one tangential. Constitutive equations, in its most general case, in the local level are then defined in this coordinate system as

$$\begin{Bmatrix} f_n \\ f_s \end{Bmatrix} = \begin{pmatrix} K_n & K_{ns} \\ K_{ns} & K_s \end{pmatrix} \begin{Bmatrix} \delta_n \\ \delta_s \end{Bmatrix} \quad (8.22)$$

where we have for convenience not shown the superscripts. As it is seen in Eq. 8.22, in the model presented here, the interaction between normal and tangential components of inter-granular force and displacement vectors is included. In the previous versions of the method of granular micromechanics this coupling term was ignored and the stiffness tensor was composed of one normal component,  $K_n$ , and one tangential component,  $K_s$ . It should be pointed, however, that the stiffness tensor is still kept symmetric. The stiffness tensor used in Eq. 8.22 should then be rotated to the VE coordinate system to result in the stiffness tensor  $K_{ij}$  which will be used in the grain-scale constitutive equation  $f_i = K_{ij}\delta_j$  and also in Eq. 8.18, 8.19, and 8.20a.

$$K_{ij} = \begin{pmatrix} K_{11} & K_{12} \\ K_{21} & K_{22} \end{pmatrix} = \begin{pmatrix} n_1 & s_1 \\ n_2 & s_2 \end{pmatrix} \begin{pmatrix} K_n & K_{ns} \\ K_{ns} & K_s \end{pmatrix} \begin{pmatrix} n_1 & n_2 \\ s_1 & s_2 \end{pmatrix} \quad (8.23)$$

For isotropic materials and in linear elastic limit, constitutive equations and their corresponding stiffness tensors can be derived in close-form by performing the integrations presented in Eq. 8.18-8.20. The 2D form of constitutive equations and corresponding stiffness tensors are thus derived as follows

$$\begin{Bmatrix} \tau_{11} \\ \tau_{22} \\ \tau_{12} \end{Bmatrix} = \begin{pmatrix} C_{11}^M & C_{12}^M & 0 \\ C_{12}^M & C_{11}^M & 0 \\ 0 & 0 & C_{33}^M \end{pmatrix} \begin{Bmatrix} \varepsilon_{11} \\ \varepsilon_{22} \\ \varepsilon_{12} \end{Bmatrix}; \quad \text{where} \quad \begin{cases} C_{11}^M = \frac{l^2 N_p}{8} (3k_n^M + k_s^M) \\ C_{33}^M = \frac{l^2 N_p}{8} (k_n^M + k_s^M) \\ C_{12}^M = \frac{l^2 N_p}{8} (k_n^M - k_s^M) \end{cases} \quad (8.24)$$

$$\left\{ \begin{matrix} \sigma_{11} \\ \sigma_{22} \\ \sigma_{12} \\ \sigma_{21} \end{matrix} \right\} = \begin{pmatrix} C_{11}^m & C_{12}^m & C_{13}^m & C_{14}^m \\ C_{12}^m & C_{11}^m & C_{13}^m & C_{14}^m \\ C_{13}^m & C_{13}^m & C_{33}^m & C_{12}^m \\ C_{14}^m & C_{14}^m & C_{12}^m & C_{33}^m \end{pmatrix} \left\{ \begin{matrix} \gamma_{11} \\ \gamma_{22} \\ \gamma_{12} \\ \gamma_{21} \end{matrix} \right\}; \quad \text{where} \quad \left\{ \begin{matrix} C_{11}^m = \frac{l^2 N_p}{8} (3k_n^m + k_s^m) \\ C_{33}^m = \frac{l^2 N_p}{8} (k_n^m + 3k_s^m) \\ C_{12}^m = \frac{l^2 N_p}{8} (k_n^m - k_s^m) \\ C_{13}^m = -C_{14}^m = \frac{-l^2 N_p}{4} k_{ns}^m \end{matrix} \right. \quad (8.25)$$

$$\left\{ \begin{matrix} \mu_{111} \\ \mu_{112} \\ \mu_{121} \\ \mu_{122} \\ \mu_{211} \\ \mu_{212} \\ \mu_{221} \\ \mu_{222} \end{matrix} \right\} = \left( \left[ A_{ijklmn}^g \right]_{8 \times 8} + \left[ A_{ijklmn}^u \right]_{8 \times 8} \right) \left\{ \begin{matrix} \phi_{1,11} \\ \phi_{1,12} \\ \phi_{1,21} \\ \phi_{1,22} \\ \phi_{2,11} \\ \phi_{2,12} \\ \phi_{2,21} \\ \phi_{2,22} \end{matrix} \right\} = \left[ A_{ijklmn} \right]_{8 \times 8} \left\{ \begin{matrix} \phi_{1,11} \\ \phi_{1,12} \\ \phi_{1,21} \\ \phi_{1,22} \\ \phi_{2,11} \\ \phi_{2,12} \\ \phi_{2,21} \\ \phi_{2,22} \end{matrix} \right\} \quad (8.26a)$$

where

$$\left[ A_{ijklmn}^g \right]_{8 \times 8} = \frac{l^4 N_p}{16} \begin{pmatrix} 5k_n^g + k_s^g & -2k_{ns}^g & -2k_{ns}^g & k_n^g + k_s^g & 4k_{ns}^g & k_n^g - k_s^g & k_n^g - k_s^g & 0 \\ -2k_{ns}^g & k_n^g + k_s^g & k_n^g + k_s^g & -2k_{ns}^g & k_n^g - k_s^g & 0 & 0 & k_n^g - k_s^g \\ -2k_{ns}^g & k_n^g + k_s^g & k_n^g + k_s^g & -2k_{ns}^g & k_n^g - k_s^g & 0 & 0 & k_n^g - k_s^g \\ k_n^g + k_s^g & -2k_{ns}^g & -2k_{ns}^g & k_n^g + 5k_s^g & 0 & k_n^g - k_s^g & k_n^g - k_s^g & -4k_{ns}^g \\ 4k_{ns}^g & k_n^g - k_s^g & k_n^g - k_s^g & 0 & k_n^g + 5k_s^g & -2k_{ns}^g & -2k_{ns}^g & k_n^g + k_s^g \\ k_n^g - k_s^g & 0 & 0 & k_n^g - k_s^g & -2k_{ns}^g & k_n^g + k_s^g & k_n^g + k_s^g & -2k_{ns}^g \\ k_n^g - k_s^g & 0 & 0 & k_n^g - k_s^g & -2k_{ns}^g & k_n^g + k_s^g & k_n^g + k_s^g & -2k_{ns}^g \\ 0 & k_n^g - k_s^g & k_n^g - k_s^g & -4k_{ns}^g & k_n^g + k_s^g & -2k_{ns}^g & -2k_{ns}^g & 5k_n^g + k_s^g \end{pmatrix} \quad (8.26b)$$

$$\left[ A_{ijklmn}^u \right]_{8 \times 8} = \frac{l^2 N_p}{2} \begin{pmatrix} 0 & 0 & 0 & 0 & 0 & 0 & 0 & 0 \\ 0 & 0 & 0 & 0 & 0 & 0 & 0 & 0 \\ 0 & 0 & G & 0 & -G & 0 & 0 & 0 \\ 0 & 0 & 0 & G & 0 & -G & 0 & 0 \\ 0 & 0 & -G & 0 & G & 0 & 0 & 0 \\ 0 & 0 & 0 & -G & 0 & G & 0 & 0 \\ 0 & 0 & 0 & 0 & 0 & 0 & 0 & 0 \\ 0 & 0 & 0 & 0 & 0 & 0 & 0 & 0 \end{pmatrix} \quad (8.26c)$$

It is noteworthy that the two fourth rank stiffness tensors,  $C_{ijkl}^M$  and  $C_{ijkl}^m$ , are formally similar. The only difference between the two tensors is that their components are derived based on grain-pair stiffness coefficients corresponding to different inter-granular phenomena. It should also be noted that since the average strain tensor is the symmetric part of the macro-scale displacement gradient, the strain and its conjugate stress tensor have 3 components. Thus the stiffness matrix linking the average strain tensor to Cauchy stress,  $C_{ijkl}^M$ , is also symmetrized into a 3×3 matrix while  $C_{ijkl}^m$  is a 4×4 matrix.

### 8.3 Variational principle and balance equations

To complete the governing equations of the system we derive the balance equations and the boundary conditions applicable to the current modeling approach. Using the definition of different kinematic measures introduced in Eq. 8.2 and Gauss's divergence theorem, the variational of the macro-scale deformation energy functional is derived as

$$\begin{aligned}
\delta \mathcal{W} &= \int_v \delta W dV = \int_v \left( \tau_{ij} \delta \varepsilon_{ij} + \sigma_{ij} \delta \gamma_{ij} + \mu_{ijk} \delta \phi_{i,jk} \right) dV \\
&= - \int_v \left( \tau_{ij} + \sigma_{ij} \right)_{,j} \delta \bar{\phi}_i dV - \int_v \left( \mu_{ijk,k} + \sigma_{ij} \right) \delta \psi_{ij} dV \\
&\quad + \int_s \left( \tau_{ij} + \sigma_{ij} \right) n_j \delta \bar{\phi}_i dS + \int_s \mu_{ijk} n_k \delta \psi_{ij} dS
\end{aligned} \tag{8.27}$$

If the system is to be in static equilibrium, the internal potential energy should be equal to the external energy created by all the external forces applied on the system. The variational of external energy is written as

$$\delta \mathcal{W}^{ext} = \int_v f_i \delta \bar{\phi}_i dV + \int_v \Phi_{ij} \delta \psi_{ij} dV + \int_s t_i \delta \bar{\phi}_i dS + \int_s T_{ij} \delta \psi_{ij} dS \tag{8.28}$$

where  $f_i$  is the non-contact volumic (body) force per unit volume,  $t_i$  is the contact traction defined as a surface force per unit area,  $\Phi_{ij}$  is the non-contact volumic (body) double force per unit volume, and  $T_{ij}$  is the contact double traction defined as double force per unit area. Now equating the external energy performed by external forces (given in Eq. 8.28) and the internal potential energy (given in Eq. 8.27), results in

$$\begin{aligned} \int_v \left[ f_i + (\tau_{ij} + \sigma_{ij})_{,j} \right] \delta\bar{\phi}_i dV + \int_v \left[ \Phi_{i,j} + (\mu_{ijk,k} + \sigma_{ij}) \right] \delta\psi_{ij} dV \\ + \int_s \left[ t_i - (\tau_{ij} + \sigma_{ij}) n_j \right] \delta\bar{\phi}_i dS + \int_s \left[ T_{ij} - \mu_{ijk} n_k \right] \delta\psi_{ij} dS = 0 \end{aligned} \quad (8.29)$$

Now it is noted that Eq. 29 should be satisfied for any arbitrary set of variational of kinematic measures,  $\delta\bar{\phi}_i$  and  $\delta\psi_{ij}$ . This implies that the terms inside square brackets in Eq. 8.29 should always be identical to zero resulting in the following balance equations and boundary conditions

$$\begin{cases} (\tau_{ij} + \sigma_{ij})_{,j} + f_i = 0 \\ \mu_{ijk,i} + \sigma_{jk} + \Phi_{jk} = 0 \end{cases} \quad (8.30)$$

$$\begin{cases} (\tau_{ij} + \sigma_{ij}) n_j = t_i \\ \mu_{ijk} n_k = T_{jk} \end{cases} \quad (8.31)$$

where the stress measures  $\tau_{ij}$ ,  $\sigma_{ij}$ , and  $\mu_{ijk}$  are defined using the constitutive equations given in Eq. 24-26 respectively.

#### 8.4 Identification of macro and micro-scale constitutive coefficients

To show the applicability of the derived continuum model, a methodology for identification of the constitutive coefficients for particular instance of granular materials is developed. To this end, we perform discrete simulations or ‘*numerical experiments*’ as controlled surrogates to physical

experiments. Here, the numerical experiments are performed using a randomly generated assembly of disks whose heterogeneity is impacted by varying the disk size (See Figure 8.2).

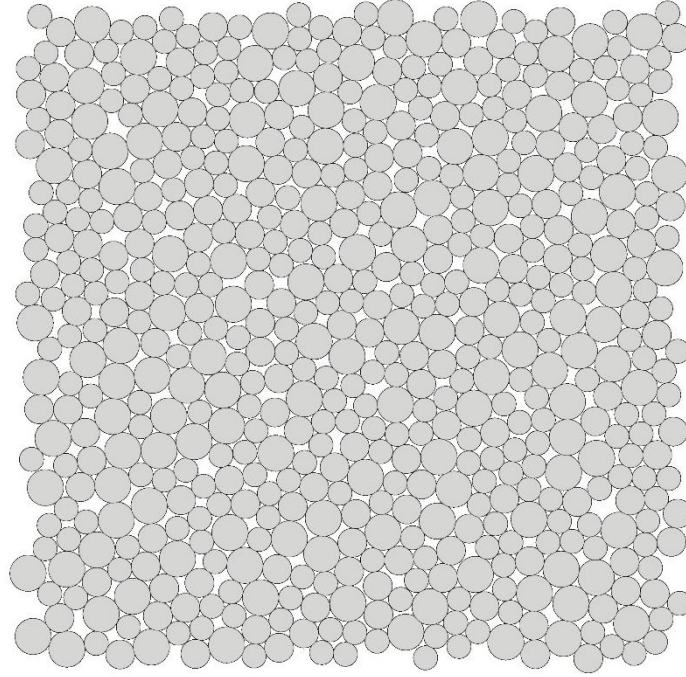


Figure 8.2 The granular assembly used in this study

#### 8.4.1 Numerical simulation methodology for discrete 2D granular system

For each grain within the assembly, say  $n^{\text{th}}$  grain, the variational of the total potential energy can be written as

$$\delta W^n = \sum_{\alpha} \delta W^{n\alpha}(\delta_i^{n\alpha}, \theta_i^{n\alpha}) = \sum_{\alpha} f_i^{n\alpha} \delta \delta_i^{n\alpha} + \sum_{\alpha} (m_i^{n\alpha} + e_{ijk} f_j^{n\alpha} r_k^n) \delta \theta_i^{n\alpha} \quad (8.32)$$

where the summation over  $\alpha$  denotes summation over all grains which have interaction with  $n^{\text{th}}$  grain. So  $f^{n\alpha}$ ,  $m^{n\alpha}$ ,  $\delta^{n\alpha}$ , and  $\theta^{n\alpha}$  denote the inter-granular force, moment, relative displacement, and relative rotation between grains  $n$  and  $\alpha$  respectively. Now denoting the total force exerted on the  $n^{\text{th}}$  grain  $F_i$  and the total moment  $M_i$ , the variational of the total potential energy can be equally written as

$$\delta W^n = F_i^n \delta \phi_i^n + M_i^n \delta \kappa_i^n \quad (8.33)$$

Now considering the definitions of inter-granular kinematic measures  $\delta_i^{n\alpha}$  and  $\theta_i^{n\alpha}$  given in Eq. 8.3 and 8.5 respectively, the variation of these relative kinematic measures can be derived based on the variation of displacement and rotations fields.

$$\begin{aligned} \delta_i^{n\alpha} = \phi_i^\alpha - \phi_i^n &\Rightarrow \delta \delta_i^{n\alpha} = -\delta \phi_i^n \\ \theta_i^{n\alpha} = \kappa_i^\alpha - \kappa_i^n &\Rightarrow \delta \theta_i^{n\alpha} = -\delta \kappa_i^n \end{aligned} \quad (8.34)$$

Setting the right hand sides of Eq. 8.32 and Eq. 8.33 equal and substituting Eq. 8.34 results in

$$F_i^n \delta \phi_i^n + M_i^n \delta \kappa_i^n = -\sum_\alpha f_i^{n\alpha} \delta \phi_i^n - \sum_\alpha (m_i^{n\alpha} + e_{ijk} f_j^{n\alpha} r_k^n) \delta \kappa_i^n \quad (8.35)$$

Now it should be noted that the above equality should hold for any arbitrary set of kinematic variables. This results in the following balance equations for the particular grain,  $n$ .

$$\begin{cases} F_i^n = -\sum_\alpha f_i^{n\alpha} \\ M_i^n = -\sum_\alpha (m_i^{n\alpha} + e_{ijk} f_j^{n\alpha} r_k^n) \end{cases} \quad (8.36)$$

Further, we know that these inter-granular force and moments tensors are attainable using grain-scale constitutive relationships relating them to inter-granular kinematic measures. If the inter-granular stiffness coefficients in normal, tangential, and normal-tangential coupling are taken to be  $\bar{K}_n$ ,  $\bar{K}_s$ , and  $\bar{K}_{ns}$  respectively and the inter-granular moment stiffness is taken to be  $\bar{G}$ , grain-scale constitutive equations are written as

$$\begin{cases} f_i^{n\alpha} = \bar{K}_{ij}^\alpha \delta_j^{n\alpha}; & \text{where } \bar{K}_{ij}^{n\alpha} = \bar{K}_n^\alpha n_i^\alpha n_j^\alpha + \bar{K}_s^\alpha s_i^\alpha s_j^\alpha + \bar{K}_{ns}^\alpha (n_i^\alpha s_j^\alpha + s_i^\alpha n_j^\alpha) \\ m^{n\alpha} = \bar{G}^\alpha \theta^{n\alpha} \end{cases} \quad (8.37)$$

It should be noted here that these stiffness parameters represent the stiffness of an interacting grain-pair isolated from the assembly. Now by combining Eq. 8.36 and Eq. 8.37, the total force and moment vectors acting on the  $n^{\text{th}}$  grain can be derived as a function the relative inter-granular

displacements and rotations that are in turn defined as the difference of the displacement and rotation of the grain-pair as in Eq. 8.3 and Eq. 8.5, respectively. In view of this, expressions for the total force and moment in the terms of grain motions can be established. These expressions can be assembled to form an overall force-displacement equation governing the behavior of the assembly as a whole written as [186]

$$\{F\}_{3M \times 1} = [S]_{3M \times 3M} \{u\}_{3M \times 1} \quad (8.38)$$

where  $M$  denotes the total number of grains within the whole assembly. For each grain there are 3 kinematic measures (2 displacements and 1 rotation) resulting in a total number of  $3M$  kinematic variables represented in  $\mathbf{u}$ . Also each grain has 3 force measures (2 forces and 1 moment) resulting in a total number of  $3M$  force variables represented in  $\mathbf{F}$ . So the overall number of variables in Eq. 8.38 is  $6M$ , knowing any  $3M$  of which the other  $3M$  can be derived by solving the system of equations represented in matrix form in Eq. 8.38.

#### 8.4.2 Methodology for identification of constitutive coefficients

As it is seen in Eq. 8.13-8.15, constitutive equations governing the behavior of micromorphic materials and grain assemblies are characterized by three different stiffness tensors,  $C_{ijkl}^M$ ,  $C_{ijkl}^m$ , and  $A_{ijklmn} = A_{ijklmn}^u + A_{ijklmn}^g$ . These stiffness tensors correspond to the average displacement gradient field, the fluctuations in displacement gradient, and second gradient of displacement, respectively. From a continuum viewpoint, the strain energy can be written as the sum of the energies derived from these three terms as

$$W = C_{ijkl}^M \varepsilon_{ij} \varepsilon_{kl} + C_{ijkl}^m \gamma_{ij} \gamma_{kl} + A_{ijklmn} \psi_{ij,k} \psi_{lm,n} \quad (8.39)$$

For finding the components of these stiffness tensors, numerical experiments are performed with the 2D grain assembly using the simulation methodology presented in section 8.4.1. These numerical experiments are performed in a manner akin to physical experiments by applying boundary conditions on the grain assemblies. Thus to obtain the components of  $C_{ijkl}^M$ , we purely apply on the boundary of the grain assembly a specified macro-scale displacement gradient while holding the fluctuation displacement gradient,  $\gamma_{ij}$ , and the second gradient term,  $\psi_{ij,k}$ , to be zero. In order to achieve this type of displacement at the boundary, boundary grains and their immediate neighbors are displaced by the amount that is compatible with the specified macro-scale displacement gradient. In this manner, the fluctuations in the displacement gradient and the second gradient of displacement are ensured to be zero. The schematic of the movement applied on the boundary grains for this type of loading is seen in Figure 8.3.a1. For the assembly loaded in this manner, the strain energy will be

$$W \Big|_{(\gamma_{ij}=0, \psi_{ij,k}=0)} = C_{ijkl}^M \epsilon_{kl} \epsilon_{ij} \quad (8.40)$$

Applying any component of strain on the assembly and deriving the energy using Eq. 8.32 and equating it with the right hand side of Eq. 8.40 results in an equation based on the corresponding components of the stiffness tensor. Before symmetrizing the stiffness tensor, it can be written as a 4×4 matrix with major symmetry. Thus it has 10 independent components. So in order to calculate all its 10 independent components, 10 different displacement fields on the boundary need to be applied on the assembly.



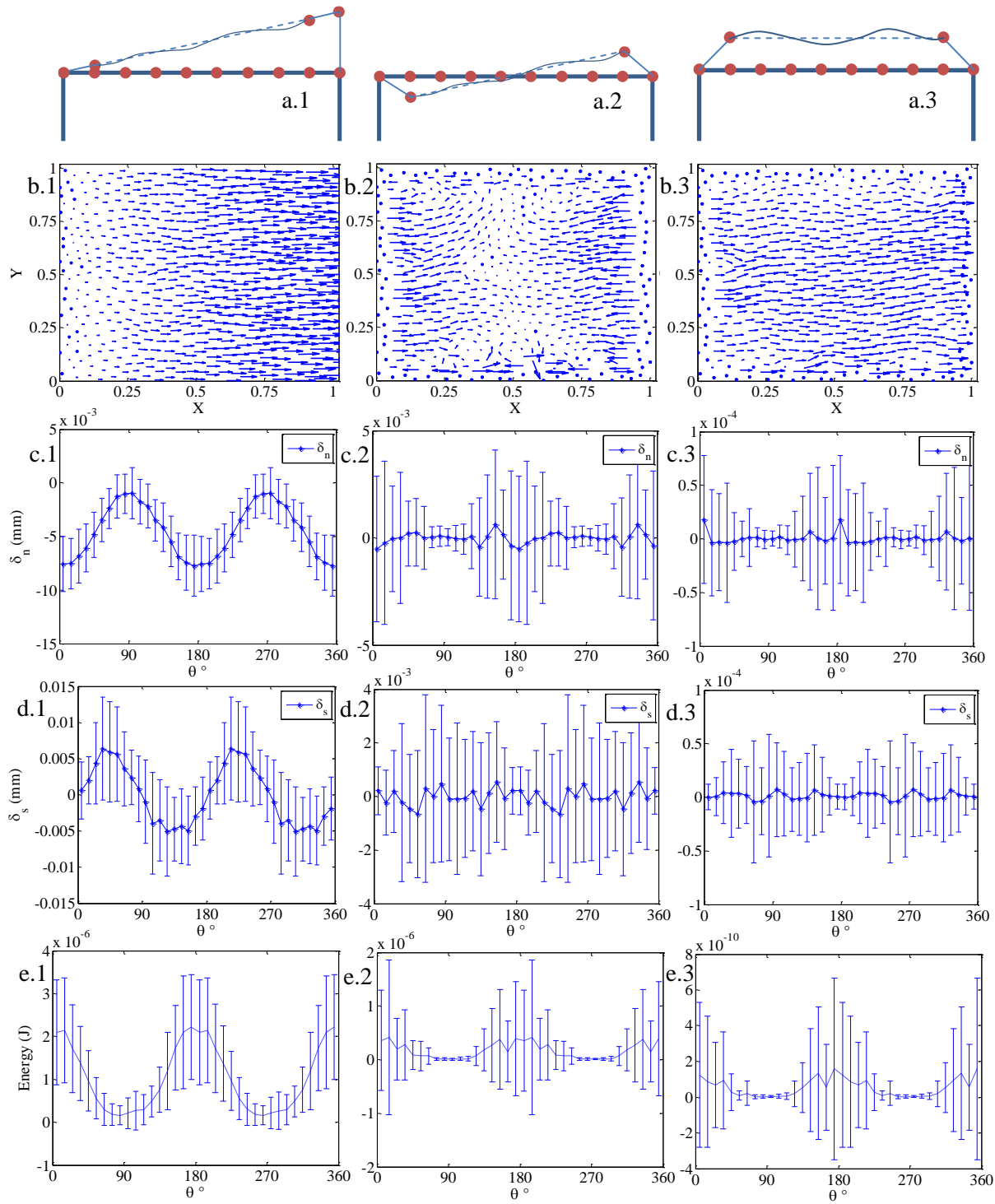


Figure 8.3 Schematics of the boundary grains' displacement applying average strain, fluctuation strain, and second gradient strain (a.1, a.2, and a.3 respectively), grains displacement in the three loading schemes (b.1, b.2, and b.3), histogram of normal component of inter-granular displacement (c.1, c.2, and c.3), histogram of tangential component of inter-granular displacement (d.1, d.2, and d.3), and histogram of grain interactions' energies (e.1, e.2, and e.3)

Four of the above loading scenarios will include applying displacement gradient only in 11, 22, 12 and 21 directions while the next six will be in the direction of combinations of those. Writing Eq. 40 for all these 10 cases will lead to a system of 10 equations and 10 unknowns solving which will result in all components of  $C_{ijkl}^M$ . The 4×4 stiffness matrix is then reduced to the 3×3 stiffness matrix by imposing symmetry of strain and conjugate stress.

For finding the components of  $C_{ijkl}^m$ , we purely apply fluctuations in displacement gradient while keeping the macro-scale displacement gradient and the second gradient of displacement to be zero. For this type of boundary condition, the boundary grains are kept stationary while their immediate neighbors are moved according to a fluctuation in displacement gradient and using Eq. 8.3. The schematic of the movement applied on the boundary grains for this type of loading is seen in Figure 8.3.a2. By loading the assembly in this manner the strain energy of the assembly will be

$$W \Big|_{(\varepsilon_{ij}=0, \psi_{ij,k}=0)} = C_{ijkl}^m \gamma_{ij} \gamma_{kl} \quad (8.41)$$

Applying the same components of fluctuation strain as it was done for finding  $C_{ijkl}^m$  and loading the assembly in 10 different directions and solving the energy equation from Eq. 8.41, all the 10 components of the tensor  $C_{ijkl}^m$  are derived.

And finally for finding the components of the sixth rank stiffness tensors, second gradients of displacement fluctuations are applied on the assembly while keeping the average and fluctuations in displacement gradient to be equal to zero. For this purpose the boundary grains are kept stationary while their immediate neighbors are moved in consistence with the second gradient in the displacement fluctuations. Boundary grains' neighbors' movements are derived using Eq. 8.3 with the desired value of  $\psi_{ij,k}$ . The schematic movement of boundary grains for this type of

loading is presented in Figure 8.3.a3. In this loading scheme the internal strain energy will be derived as

$$W \Big|_{(\varepsilon_{ij}=0, \gamma_{ij}=0)} = A_{ijklmn} \psi_{ij,k} \psi_{lm,n} \quad (8.42)$$

As it is seen in Eq. 8.26, in a 2D granular system, the sixth rank stiffness tensor  $A_{ijklmn}$  can be written as an 8×8 matrix with 36 independent components. To find all these components, second gradient of displacement in 36 different combinations need to be applied on the material. Eight of these combinations are indicated by the eight different components of  $\psi_{ijk}$  and the 26 remaining ones are composed of their combinations. Finding the energy for each one of these cases using Eq. 8.32 and writing Eq. 8.42 result in a system of 36 equations and 36 unknowns that when solved will yield all components of the second gradient stiffness tensor.

## 8.5 Results and Discussions

Random assembly of 3 sized disks was generated with 576 total disks composed of 301 disks of size 19  $\mu\text{m}$ , 150 disks of 22  $\mu\text{m}$ , and 125 disks of 28  $\mu\text{m}$ , within a cell of period 1mmx1mm as depicted in Figure 3. The total number of grain-pair interactions is 1384. Two sets of simulation were performed: in case 1 the stiffness were specified as  $\bar{K}_n = \bar{K}_s = 17.5 \text{ KN/mm}$  and  $\bar{K}_{ns} = \bar{G} = 0.0$ ; while in case 2  $\bar{K}_n = 100\bar{K}_s = 17.5 \text{ KN/mm}$  and  $\bar{K}_{ns} = \bar{G} = 0.0$ . It is noteworthy that for case 1, the normal and tangential stiffness coefficients are same, while for case 2, the tangential stiffness is negligible thus potentially generating contrast in the emphasis of fluctuation and second gradient terms.

To illustrate the identification process, in Figure 8.3 sample results from three different types of boundary conditions described in section 8.4.2 are presented. Figure 8.3(a1-e1) present the results

from application of  $\varepsilon_{11}=0.01$ , while all other components are held zero. Figure 8.3(a2-e2) present the results from application of  $\gamma_{11}=0.01$ , while all other components are held zero. Figure 8.3(a3-e3) present the results from application of  $\psi_{11,1}=0.1/\text{mm}$ , while all other components are held zero. A schematic of boundary grains' movement applied to the grain assembly in these three different loadings can be seen in Figure 8.3(a1-a3). Figures 8.3(b1-b3) show the movement of grains due to the applied strain component while Figures 8.3(c1-c3) and 8.3(d1-d3) present the average and standard deviation of the normal and tangential components, respectively, of the relative displacement for grain-pair contacts in different directions.

Figure 8.3(e1-e3) present the average and standard deviation of the strain energy created in grain-pair interactions in different directions. It is remarkable that in the cases where the average displacement gradient applied on the assembly is zero, (cases in Figures 8.3b and 8.3c) the average of both normal and tangential components of relative inter-granular displacement vectors are zero for contacts in all different directions. The standard deviations are, however, not negligible compared to the case where average displacement gradient is applied. Most importantly, the overall energies for the type 2 boundary conditions are similar to type 1 at the given strain-level. Further, the second gradient deformation also results in comparable energy-level at the given level of deformation. There is a clear need for partitioning the grain-pair (micro-scale) deformation energy into the corresponding micro-scale mechanisms.

The identified constitutive coefficients are listed in Table 8.1 and 8.2 in column titled unit cell. Due to the finite size, the disk assembly show small degree of anisotropy and has completely populated constitutive matrices although, quite evidently, the minor terms have a small numerical value. For identification of the grain-pair stiffness relevant to the effective micromorphic continuum medium which is isotropic, we consider that the unit cell (Figure 8.2) is randomly

oriented as in polycrystals. As a result, an isotropic stiffness tensor of an RVE with many unit cells through the VRH directional averaging process [187] is estimated, which are listed in Table 8.1 and 8.2 in column titled RVE.

Table 8.1 Components of two fourth rank stiffness tensors ( $C^M$  and  $C^m$ ) for the two sets of grain properties, derived for the unit cell, the RVE, and using the present model

Component	Case 1			Case 2		
	Unit cell (GPa)	RVE (GPa)	Model results (GPa)	Unit cell (GPa)	RVE (GPa)	Model results (GPa)
$C_{11}^M$	42.6	42.6	42.6	27.3	27.9	27.9
$C_{22}^M$	42.8	42.6	42.6	28.1	27.9	27.9
$C_{33}^M$	20.4	20.5	20.5	7.8	7.6	7.6
$C_{12}^M$	1.6	1.6	1.6	13.0	12.8	12.8
$C_{13}^M$	0.3	0.0	0.0	0.5	0.0	0.0
$C_{23}^M$	0.1	0.0	0.0	0.4	0.0	0.0
$C_{11}^m$	7.8	7.3	7.3	4.5	4.1	4.1
$C_{22}^m$	6.8	7.3	7.3	4.1	4.1	4.1
$C_{33}^m$	6.7	7.2	7.2	2.6	3.1	3.1
$C_{44}^m$	7.6	7.2	7.2	3.1	3.1	3.1
$C_{12}^m$	0.1	0.1	1.6	0.3	0.5	12.8
$C_{13}^m$	0.2	0.0	0.0	0.2	0.1	0.0
$C_{14}^m$	0.1	0.0	0.0	0.0	-0.1	-0.1
$C_{23}^m$	0.0	0.0	0.0	0.1	0.1	0.0
$C_{24}^m$	0.1	0.0	0.0	-0.1	-0.1	-0.1
$C_{34}^m$	0.1	0.1	0.1	0.2	0.5	0.5

It is noteworthy, that the unit cell and the estimated RVE have small differences, implying that the unit cell (shown in Figure 8.2) is only slightly anisotropic. Subsequently, grain-pair stiffness coefficients relevant to the effective micromorphic using Eq. 8.24-8.26 are calculated and provided in Table 8.3. The parameters thus found are then substituted into Eq. 8.24-8.26 and the constitutive

coefficients from the method of granular micromechanics derived and listed in Tables 8.1 and 8.2 in column titled model.

Table 8.2 Components of the sixth rank stiffness tensor for the two sets of grain properties, derived for the unit cell, the RVE, and using the present model

Component	Case 1			Case 2		
	Unit cell (10 <sup>-5</sup> KN)	RVE (10 <sup>-5</sup> KN)	Model results (10 <sup>-5</sup> KN)	Unit cell (10 <sup>-5</sup> KN)	RVE (10 <sup>-5</sup> KN)	Model results (10 <sup>-5</sup> KN)
A <sub>111111</sub>	241	253	253	145	144	144
A <sub>112112</sub>	142	128	84	68	62	41
A <sub>122122</sub>	239	254	254	89	104	104
A <sub>211211</sub>	243	254	254	94	104	104
A <sub>212212</sub>	140	128	84	66	62	41
A <sub>222222</sub>	238	253	253	146	144	144
A <sub>111112</sub>	-12	0	0	-3	2	2
A <sub>111122</sub>	10	-3	84	4	1	41
A <sub>111211</sub>	0	0	0	-3	-3	-3
A <sub>111212</sub>	1	1	0	8	10	10
A <sub>111222</sub>	0	0	0	3	0	0
A <sub>112122</sub>	16	0	0	9	2	2
A <sub>112211</sub>	-1	-1	0	7	10	10
A <sub>112212</sub>	0	0	0	-1	0	0
A <sub>112222</sub>	1	1	0	6	10	10
A <sub>122211</sub>	0	0	0	3	0	0
A <sub>122212</sub>	-1	-1	0	5	10	10
A <sub>122222</sub>	0	0	0	2	3	3
A <sub>211212</sub>	-11	0	0	-8	-2	-2
A <sub>211222</sub>	10	-3	84	10	1	41
A <sub>212222</sub>	15	0	0	6	-2	-2
A <sub>221222</sub>	15	0	0	6	-2	-2

The model results have a perfect match with discrete simulation for the constitutive coefficients associated to macro-scale displacement gradients and the fluctuations in displacement gradient. Since the number of independent material properties used in the method of granular

micromechanics is less than the number of independent components in the second gradient stiffness tensors, an optimization scheme is used to find the microscopic stiffness parameters.

Table 8.3 Table of micro-scale constitutive coefficients derived for the assembly (units: K in kN/mm and G in N.mm)

Case	Discrete Simulations	$K_n^M$	$K_s^M$	$K_n^m$	$K_s^m$	$K_{ns}^m$	$K_n^g$	$K_s^g$	$K_{ns}^g$	G
1	$\bar{K}_n = \bar{K}_s = 17.5$ $\bar{K}_{ns} = \bar{G} = 0.0$	16.8	14.3	2.8	2.7	6.6E-03	0.67	0.68	8.6E-05	Neg.
2	$\bar{K}_n = 100\bar{K}_s = 17.5$ $\bar{K}_{ns} = \bar{G} = 0.0$	15.5	-4.0	1.7	1.0	-5.4E-02	0.41	0.25	-1.4E-02	Neg.

A good agreement is also found for the constitutive coefficients associated to the 2nd gradient of displacement. Most importantly, the orders of different terms and the major non-zero terms are in concurrence. It is also remarkable that there are non-zero coupling terms,  $K_{ns}$  (the terms which are responsible for the coupling between normal and shear components of force and displacement vectors and vice-versa) in the micro-scale constitutive relationships which affect the macroscopic stiffness tensors. Although their effects are of smaller order compared to that of the diagonal stiffness coefficients,  $K_n$  and  $K_s$ , nevertheless they conform to the relationships derived from the present model. As seen from Eq. 8.25 and 8.26, some macro-scale constitutive coefficients include these coupling coefficients. In traditional continuum models, these components are zero for isotropic materials. However, it is seen that the relationships between them are satisfied in the results derived here. It is also noted that the micro-scale moment stiffness coefficients, G, are negligible (of the order  $10^{-16}$  N.mm), which implies that for this particular simulations the grain rotations do not have a insignificant role. However, this is likely a result of assumed zero rotational stiffness in the discrete simulations.

Finally, the back calculated micro-scale constitutive coefficients in Table 8.3 are compared with those assigned in the discrete simulations. It is clear that the needed micro-scale constitutive coefficients are significantly affected by heterogeneity introduced by microstructure, such that the continuum modeling with only macro-scale displacement gradients is not sufficient even for the relatively uniform system analyzed here, wherein the stiffness coefficients assigned to all grain-pairs all identical. Grain neighborhoods affect the behavior of grain interactions significantly, such that the effective grain-pair stiffness cannot be just estimated from the stiffness of two isolated grains. Additional macro-scale deformation measures are, therefore, necessary for the continuum modeling of granular materials. Similar observations have been made for other material systems such as pantographic trusses [176, 177], biomaterials [188, 189], and in fiber composites [190]. It is also noted that the application of isolated grain-pair stiffness to estimate the energies and stresses associated with different deformation measures as have been proposed in some multi-scale modeling that aim to bridge discrete-continuum models also need to be carefully considered.

## **8.6 Summary and conclusion**

In the present chapter the granular micromechanics approach, previously derived in three dimensions and with considering the effects of grain spins, has been derived in two dimensions and with neglecting the effects of grain spins. By equating the macroscopic strain energy density to the volume average of inter-granular energy functions, macroscopic stiffness tensors corresponding to each of the kinematic measures have been derived based on the inter-granular stiffness coefficients and the geometrical properties of the grain assembly. For isotropic 2D assemblies, closed-form expressions of the stiffness tensors components have been obtained.



A practical method to identify the macro- and micro-scale constitutive coefficients from discrete simulation has been described. The procedure was applied to obtain the stiffness tensors corresponding to the macro-scale displacement gradient, fluctuations in displacement gradient and second gradient of displacement for a particular grain assembly. This kind of approach can be used for any given material system or grain assembly.

Based upon the identification results it can be concluded that the effective grain-pair stiffness coefficients in the method of granular micromechanics, or perhaps any micromechanically-based continuum model, are different from the isolated grain-pair stiffness coefficients used in discrete simulations. In the continuum models, the stiffness coefficients represent, in a collective manner, the average behavior of grain-pair interactions. These effective stiffness coefficients are unique for each material or granular assembly since, the inter-granular mechanisms are affected not only by the two grains under consideration, but also by the grains in the neighborhood and by extension the whole assembly. It is also found that the stiffness coefficients corresponding to the average displacement gradient terms have the largest values but the coefficients corresponding to displacement gradient fluctuations are also significant and of a similar order.

It is seen that using the method of granular micromechanics, results that are equally accurate compared to results of discrete analyses and it is achieved by much less computational effort. This makes the method applicable for more complex and realistic materials and grain assemblies. The micromorphic and second gradient terms are necessary for modeling some frequency dependent wave transmission/reflection phenomena at material interfaces [154, 191-193]. The micromorphic behavior of granular materials indicates the possibility of realizing materials with alternate synthesis pathways which show specific wave propagation behaviors that can be used for vibration control as alternative to piezoelectric materials [194-200] or for identification [190, 201, 202].

Alternatively, such materials can be applied to help the optimize control procedures [188, 189] or for optimal biomaterial design [203] in bone mechanics.

The identification process described herein can be used for extending the applicability of micromorphic models or its micropolar and second gradient simplifications to describe post-instability macro-scale behavior, such as boundary and localization layers in micro-structured media [33, 60, 204, 205].

## **9 BALANCE EQUATIONS AND WAVE PROPAGATION**

### **9.1 Introduction**

As the last step for completing the formulation of the micromorphic theory with considering grain spins, within the framework of the method of granular micromechanics, in this chapter, the differential equations governing the equilibrium of these materials are derived. For this purpose, all the sources of energy are calculated. These include 1) the internal potential energy due to the different strain measures and their conjugate stress measures, 2) the external work performed on the material by the body forces and moments, and 3) the kinetic energy due to the different sources of deformations in the material point.

Utilizing the action functional [2, 159], imposing the balance of internal, external, and kinetic energies, equilibrium equations and relevant boundary conditions are derived. By substituting the constitutive equations for linear elastic isotropic micromorphic materials (derived in Chapter 7) into the balance equations, displacement equations of motion for isotropic materials are derived. Using these equations propagation plane waves through the material is studied.

Propagation of waves within isotropic and anisotropic media are fundamentally different. If the material studied is isotropic, the direction of wave propagation will not affect the results. Whereas, for anisotropic materials, for which the formulation was presented in Chapter 6, the direction of wave propagation will change the results. Waves propagating in different directions will behave differently.

In this chapter, plane wave propagation within both isotropic and transversely isotropic materials has been studied. Dispersion graphs representing the relationship between the wave frequency and wave number have been derived showing interesting phenomena that cannot be captured with usual first gradient continuum theories. Some parts of the results presented here have been published [154], and the study of wave propagation within micromorphic media with grain spins, and also for anisotropic materials will be published later. Moreover, a parametric study has been performed showing the effect of model parameters on the wave-propagation behavior of anisotropic materials.

## 9.2 Variational principle and balance equations

In this section, the balance of internal potential energy, external work, and the kinetic energy, for a general micromorphic medium is studied in order to derive the equilibrium equations and boundary conditions for such media. Then using the constitutive relationships derived in chapter 7, equations of motion in terms of the kinematic measures are derived. For this purpose, the variation of internal potential energy is defined using the definition of the stress measures for the micromorphic media and the conjugate kinematic measures presented in Eq. 7.11.

$$\begin{aligned}
\delta W &= \tau_{ij} \delta \varepsilon_{ij} + \sigma_{ij} \delta \gamma_{ij}^{\phi} + \mu_{ijk} \delta \psi_{ij,k}^{\phi} + M_{ij} \delta \bar{\kappa}_{i,j} + P_{ij} \delta \gamma_{ij}^{\kappa} + Q_{ijk} \delta \psi_{ij,k}^{\kappa} \\
&= \tau_{ij} \delta \bar{\phi}_{i,j} + \sigma_{ij} (\delta \bar{\phi}_{i,j} - \delta \psi_{ij}^{\phi}) + \mu_{ijk} \delta \psi_{ij,k}^{\phi} + M_{ij} \delta \bar{\kappa}_{i,j} + P_{ij} (\delta \bar{\kappa}_{ij} - \delta \psi_{ij}^{\kappa}) + Q_{ijk} \delta \psi_{ij,k}^{\kappa} \\
&= \left[ (\tau_{ij} + \sigma_{ij}) \delta \bar{\phi}_i \right]_{,j} - (\tau_{ij} + \sigma_{ij})_{,j} \delta \bar{\phi}_i - \sigma_{ij} \delta \psi_{ij}^{\phi} + \left[ \mu_{ijk} \delta \psi_{ij}^{\phi} \right]_{,k} - \mu_{ijk,k} \delta \psi_{ij}^{\phi} \\
&\quad + \left[ (M_{ij} + P_{ij}) \delta \bar{\kappa}_i \right]_{,j} - (M_{ij} + P_{ij})_{,j} \delta \bar{\kappa}_i - P_{ij} \delta \psi_{ij}^{\kappa} + \left[ Q_{ijk} \delta \psi_{ij}^{\kappa} \right]_{,k} - Q_{ijk,k} \delta \psi_{ij}^{\kappa}
\end{aligned} \tag{9.1}$$

where, using Eq. 7.5a and 7.5b, the microstrain tensors corresponding to displacement and rotation,

$\gamma_{ij}^{\phi}$  and  $\gamma_{ij}^{\omega}$ , have been replaced with  $\delta \bar{\phi}_{i,j} - \delta \psi_{ij}^{\phi}$  and  $\delta \bar{\omega}_{ij} - \delta \psi_{ij}^{\omega}$  respectively. The variational of

the macro-scale deformation energy functional is thus derived as the integral of the variation of internal potential energy over the volume,  $V$ , which using Gauss's divergence theorem can be rewritten as

$$\begin{aligned} \delta \mathcal{W} &= \int_v \delta W dV \\ &= - \int_v (\tau_{ij} + \sigma_{ij})_{,j} \delta \bar{\phi}_i dV - \int_v (\sigma_{ij} + \mu_{ijk,k}) \delta \psi_{ij}^\phi dV - \int_v (M_{ij} + P_{ij})_{,j} \delta \bar{\kappa}_i dV - \int_v (P_{ij} + Q_{ijk,k}) \delta \psi_{ij}^\kappa dV \quad (9.2) \\ &+ \int_s [(\tau_{ij} + \sigma_{ij}) n_j] \delta \bar{\phi}_i dS + \int_s [\mu_{ijk} n_k] \delta \psi_{ij}^\phi dS + \int_s [(M_{ij} + P_{ij}) n_j] \delta \bar{\kappa}_i dS + \int_s [Q_{ijk} n_k] \delta \psi_{ij}^\kappa dS \end{aligned}$$

where  $S$  is the surface covering the volume element  $V$  and its outward unit normal at any point is the vector  $\mathbf{n}$ .

In order to calculate the kinetic energy of the micromorphic material, it is divided into two main components,  $T^\phi$ , which is due to grains' displacements,  $T^\kappa$ , which is due to grains' rotations. In order to calculate the different components of kinetic energy of the material point, one needs to define the material's mass and its moments of inertia. For this purpose, the parameter  $\rho'$  is defined as the density of the grains (solid particles) in the material point. On the other hand, density of the unit cell that is made of grains and its surroundings (i.e. the density of the grain and its surrounding space) is referred to using the parameter  $\rho$ . Using these parameters, material point's mass and second rank moment of inertia are derived as

$$\begin{aligned} m' &= \int_{v'} \rho dV' \\ I_{ij} &= \int_{v'} \rho x'_i x'_j dV' \end{aligned} \quad (9.3)$$

While it is noted that since the local coordinate system is placed at the material point's center of mass the moments of inertia of odd rank will vanish ( $\int_{v'} \rho x'_i dV' = \int_{v'} \rho x'_i x'_j x'_k dV' = \dots = 0$ ).

In calculating the kinetic energy due to both kinematic components of grains (their displacement and rotation) one needs to take into account both the average and the total gradient of the total kinematic measures. Thus the kinetic energy due to displacement, which herein is called  $T^\phi$ , will have two terms, one due to rate of  $\bar{\phi}_i$  and one due to rate of  $\psi_{ij}^\phi$ . In the same way, the kinetic energy due to displacement, which herein is called  $T^\kappa$ , will have two terms, one due to rate of  $\bar{\kappa}_i$  and one due to rate of  $\psi_{ij}^\kappa$ . Considering all these terms, the kinetic energy is formulated as

$$T = T^\phi + T^\kappa = \frac{1}{2} \left( \dot{\bar{\phi}}_i \dot{\bar{\phi}}_i + \frac{I_{jk}}{m'} \dot{\psi}_{ij}^\phi \dot{\psi}_{ik}^\phi + \frac{J}{m'} \dot{\bar{\kappa}}_i \dot{\bar{\kappa}}_i + \frac{\chi}{m'} \dot{\psi}_{ij}^\kappa \dot{\psi}_{ij}^\kappa \right) \quad (9.4)$$

where  $J = \int_{v'} \rho r^2 dV'$  and  $\chi = \int_{v'} \rho r^4 dV'$  are the second and fourth order polar moments of inertia.

So the variation of the kinetic energy over the material point can be written as

$$\begin{aligned} \delta \mathcal{T} &= \delta \int_{oV} \int_{oV} \rho T dt dV = \frac{1}{2} \rho \delta \int_{oV} \int_{oV} \left( \dot{\bar{\phi}}_i \dot{\bar{\phi}}_i + \frac{I_{jk}}{m'} \dot{\psi}_{ij}^\phi \dot{\psi}_{ik}^\phi + \frac{J}{m'} \dot{\bar{\kappa}}_i \dot{\bar{\kappa}}_i + \frac{\chi}{m'} \dot{\psi}_{ij}^\kappa \dot{\psi}_{ij}^\kappa \right) dt dV \\ &= \frac{1}{2} \rho \int_{oV} \int_{oV} \left( \left( \delta \dot{\bar{\phi}}_i \dot{\bar{\phi}}_i + \dot{\bar{\phi}}_i \delta \dot{\bar{\phi}}_i \right) + \frac{I_{jk}}{m'} \left( \delta \dot{\psi}_{ij}^\phi \dot{\psi}_{ik}^\phi + \dot{\psi}_{ij}^\phi \delta \dot{\psi}_{ik}^\phi \right) + \frac{J}{m'} \left( \delta \dot{\bar{\kappa}}_i \dot{\bar{\kappa}}_i + \dot{\bar{\kappa}}_i \delta \dot{\bar{\kappa}}_i \right) + \frac{\chi}{m'} \left( \delta \dot{\psi}_{ij}^\kappa \dot{\psi}_{ij}^\kappa + \dot{\psi}_{ij}^\kappa \delta \dot{\psi}_{ij}^\kappa \right) \right) dt dV \quad (9.5) \\ &= \rho \int_{oV} \int_{oV} \left( \frac{\partial \delta \bar{\phi}_i}{\partial t} \dot{\bar{\phi}}_i + \frac{\partial \dot{\bar{\phi}}_i}{\partial t} \delta \bar{\phi}_i + \frac{I_{jk}}{m'} \frac{\partial \delta \psi_{ij}^\phi}{\partial t} \dot{\psi}_{ik}^\phi + \frac{\partial \dot{\psi}_{ij}^\phi}{\partial t} \delta \psi_{ik}^\phi + \frac{J}{m'} \frac{\partial \delta \bar{\kappa}_i}{\partial t} \dot{\bar{\kappa}}_i + \frac{\partial \dot{\bar{\kappa}}_i}{\partial t} \delta \bar{\kappa}_i + \frac{\chi}{m'} \frac{\partial \delta \psi_{ij}^\kappa}{\partial t} \dot{\psi}_{ij}^\kappa + \frac{\partial \dot{\psi}_{ij}^\kappa}{\partial t} \delta \psi_{ij}^\kappa \right) dt dV \end{aligned}$$

which using integration by parts, can be rewritten as

$$\begin{aligned} \delta \mathcal{T} &= \int_V \rho \left( \left[ \delta \bar{\phi}_i \frac{\partial \bar{\phi}_i}{\partial t} \right]_0^{t_1} - \int_0^{t_1} \delta \bar{\phi}_i \frac{\partial^2 \bar{\phi}_i}{\partial t^2} dt \right) dV \\ &+ \int_V \rho \left( \left[ \frac{I_{jk}}{m'} \delta \psi_{ij}^\phi \frac{\partial \psi_{ik}^\phi}{\partial t} \right]_0^{t_1} - \int_0^{t_1} \frac{I_{jk}}{m'} \delta \psi_{ij}^\phi \frac{\partial^2 \psi_{ik}^\phi}{\partial t^2} dt \right) dV \\ &+ \int_V \rho \left( \left[ \frac{J}{m'} \delta \bar{\kappa}_i \frac{\partial \bar{\kappa}_i}{\partial t} \right]_0^{t_1} - \int_0^{t_1} \frac{J}{m'} \delta \bar{\kappa}_i \frac{\partial^2 \bar{\kappa}_i}{\partial t^2} dt \right) dV \\ &+ \int_V \rho \left( \left[ \frac{\chi}{m'} \delta \psi_{ij}^\kappa \frac{\partial \psi_{ij}^\kappa}{\partial t} \right]_0^{t_1} - \int_0^{t_1} \frac{\chi}{m'} \delta \psi_{ij}^\kappa \frac{\partial^2 \psi_{ij}^\kappa}{\partial t^2} dt \right) dV \quad (9.6) \end{aligned}$$

Now noting that all kinematic measures  $(\bar{\phi}_i, \psi_{ij}^\phi, \bar{\kappa}_i, \text{ and } \psi_{ij}^\kappa)$ , and their rates vanish at the initial and final time values [159], variation of kinetic energy will be simplified to

$$\delta\mathcal{T} = -\int_V \int_0^{t_1} \left( \rho \ddot{\bar{\phi}}_i \delta\bar{\phi}_i + \rho \frac{I_{jk}}{m'} \ddot{\psi}_{ik}^\phi \delta\psi_{ij}^\phi + \rho \frac{J}{m'} \ddot{\bar{\kappa}}_i \delta\bar{\kappa}_i + \rho \frac{\chi}{m'} \ddot{\psi}_{ij}^\kappa \delta\psi_{ij}^\kappa \right) dt dV \quad (9.7)$$

Now the only remaining source of energy is the external work of long range forces and moments. One needs to calculate the variational of the external works done by long range body (volume), surface, and edge forces and moments acting on the material point to have the complete formulation for the energy of the material point.

$$\begin{aligned} \delta\mathcal{W}^{ext} = & \int_V f_i \delta\bar{\phi}_i dV + \int_V m_i \delta\bar{\kappa}_i dV + \int_V \Phi_{ij} \delta\psi_{ij}^\phi dV + \int_V \Omega_{ij} \delta\psi_{ij}^\kappa dV \\ & + \int_S t_i \delta\bar{\phi}_i dS + \int_S q_i \delta\bar{\kappa}_i dS + \int_S T_{ij} \delta\psi_{ij}^\phi dS + \int_V \Gamma_{ij} \delta\psi_{ij}^\kappa dV \end{aligned} \quad (9.8)$$

In Eq. 9.8,  $f_i$  is the non-contact volumic (body) force per unit volume,  $t_i$  is the contact traction defined as a surface force per unit area, while  $m_i$  is the volumic moment per unit volume and  $q_i$  is the contact moment per unit area.  $\Phi_{ij}$  is the non-contact volumic (body) double force per unit volume, and  $T_{ij}$  is the contact double traction defined as double force per unit area, both associated with the total displacement gradient. The two tensors  $\Omega_{ij}$  and  $\Gamma_{ij}$  are the non-contact volumic (body) double force per unit volume and contact double traction both associated with the total gradient of spins. Now utilizing the action functional, the variational equation of motion is written using Hamilton's principle as

$$\delta A = \int_0^t \int_V (\delta\mathcal{T} - \delta\mathcal{W}) dV dt + \int_0^t \delta\mathcal{W}^{ext} dt = \int_0^t (\delta\mathcal{W}^{ext} - \delta\mathcal{W} + \delta\mathcal{T}) dt = 0 \quad (9.9)$$

Substituting Eq. 9.2, 9.7, and 9.8 into Eq. 9.9, and dropping the integration over time yields the following equation for the balance of potential and kinetic energies of the material point.

$$\begin{aligned}
\delta A = & \int_v \left[ f_i + (\tau_{ij} + \sigma_{ij})_{,j} - \rho \ddot{\phi}_i \right] \delta \bar{\phi}_i dV + \int_v \left[ \Phi_{ij} + (\sigma_{ij} + \mu_{ijk,k}) - \rho \frac{I^{jk}}{m'} \ddot{\psi}_{ik}^\phi \right] \delta \psi_{ij}^\phi dV \\
& + \int_v \left[ m_i + (M_{ij} + P_{ij})_{,j} - \rho \frac{J}{m'} \ddot{\kappa}_i \right] \delta \bar{\kappa}_i dV + \int_v \left[ \Omega_{ij} + (P_{ij} + Q_{ijk,k}) - \rho \frac{\chi}{m'} \ddot{\psi}_{ij}^\kappa \right] \delta \psi_{ij}^\kappa dV \\
& + \int_s \left[ t_i - (\tau_{ij} + \sigma_{ij}) n_j \right] \delta \bar{\phi}_i dS + \int_s \left[ T_{ij} - \mu_{ijk} n_k \right] \delta \psi_{ij}^\phi dS \\
& + \int_s \left[ q_i - (M_{ij} + P_{ij}) n_j \right] \delta \bar{\kappa}_i dS + \int_s \left[ \Gamma_{ij} - Q_{ijk} n_k \right] \delta \psi_{ij}^\kappa dS = 0
\end{aligned} \tag{9.10}$$

For the variational of the action functional to be always equal to zero, all the integrals in Eq. 9.10 should simultaneously be equal to zero. Setting the volume integrals equal to zero results in equilibrium equations, while setting the surface integrals equal to zero results in the corresponding boundary conditions. It is also noted that these integral should be equal to zero for arbitrary kinematic measures. So all the terms inside square brackets in Eq. 9.10 should vanish simultaneously.

The four equilibrium equations, in terms of stress measures, for micromorphic media with grain spins are therefore derived as

$$(\tau_{ij} + \sigma_{ij})_{,j} + f_i = \rho \ddot{\phi}_i \tag{9.11a}$$

$$\sigma_{ij} + \mu_{ijk,k} + \Phi_{ij} = \rho \frac{I^{jk}}{m'} \ddot{\psi}_{ik}^\phi \tag{9.11b}$$

$$(M_{ij} + P_{ij})_{,j} + m_i = \rho \frac{J}{m'} \ddot{\kappa}_i \tag{9.11c}$$

$$P_{ij} + Q_{ijk,k} + \Omega_{ij} = \rho \frac{\chi}{m'} \ddot{\psi}_{ij}^\kappa \tag{9.11d}$$

and the four boundary conditions given in terms of the stress measures and body forces are

$$(\tau_{ij} + \sigma_{ij}) n_j = t_i \tag{9.12a}$$

$$\mu_{ijk} n_k = T_{ij} \tag{9.12b}$$



$$(M_{ij} + P_{ij})n_j = q_i \quad (9.12c)$$

$$Q_{ijk}n_k = \Gamma_{ij} \quad (9.12d)$$

### 9.3 Displacement equations of motion

The objective of this section is to derive the general form of displacement equations of motion, i.e. the equilibrium equations in terms of kinematic variables, for elastic micromorphic media. For this purpose, the macroscopic constitutive equations derived in 7.24-7.29 are substituted into the equilibrium equations, Eq. 9.11, resulting in the following equations of motion

$$\left[ C_{ijkl}^M + C_{ijkl}^m \right] \bar{\phi}_{k,lj} - C_{ijkl}^m \psi_{kl,j}^\phi = \rho \ddot{\bar{\phi}}_i \quad (9.13a)$$

$$C_{ijkl}^m (\bar{\phi}_{k,l} - \psi_{kl}^\phi) + A_{ijklmn} \psi_{lm,nk}^\phi = \rho \frac{I_{jk}}{m'} \ddot{\psi}_{ik}^\phi \quad (9.13b)$$

$$\left[ D_{ijkl}^M + D_{ijkl}^m \right] \bar{\kappa}_{k,lj} - D_{ijkl}^m \psi_{kl,j}^\kappa = \rho \frac{J}{m'} \ddot{\bar{\kappa}}_i \quad (9.13c)$$

$$D_{ijkl}^m (\bar{\kappa}_{k,l} - \psi_{kl}^\kappa) + B_{ijklmn} \psi_{lm,nk}^\kappa = \rho \frac{\mathcal{X}}{m'} \ddot{\psi}_{ij}^\kappa \quad (9.13d)$$

where the noncontact volumic forces and moments corresponding to grain displacements and rotations,  $f_i$  and  $m_i$ , and the double forces and moments,  $\Phi_{ij}$  and  $\Omega_{ij}$ , are assumed to be absent.

It is notable that the first two equations, Eq. 9.13a and 9.13b, only contain terms corresponding to the kinematic measures associated with grain displacement ( $\bar{\phi}_i$  and  $\psi_{ij}^\phi$ ). Also the third and fourth equations, Eq. 9.13c and 9.13d, just contain terms corresponding to the kinematic measures associated with grain spins ( $\bar{\kappa}_i$  and  $\psi_{ij}^\kappa$ ). Therefore, the four equations of motion can be

decomposed into two sets of equations, one for the displacement terms (Eq. 9.13a and 9.13b) and one for rotation terms (Eq. 9.13c and 9.13d).

In order to further simplify the equations of motion, the second and fourth rank moments of inertia are calculated. For regular 3D shapes that can be used to represent a unit-cell, the second rank moment of inertia tensor is a diagonal matrix whose diagonal elements are all equal ( $I = \alpha_1 m' R^2$ ) while the polar and the fourth rank moments of inertia are also equal to  $J = \alpha_2 m' R^2$  and  $\chi = \alpha_3 m' R^4$  respectively, where  $m'$  and  $R$  represent the unit cell's mass and radius and  $\alpha_1$ ,  $\alpha_2$ , and  $\alpha_3$  are shape factors (See Table 9.1 for values of the shape factors  $\alpha_1$ ,  $\alpha_2$ , and  $\alpha_3$  for spherical and cubic unit cells)

Table 9.1 Shape factors for spherical and cubic unit cells

Shape	Characteristic length	$\alpha_1$	$\alpha_2$	$\alpha_3$
Sphere	r (radius)	1/5	2/5	12/35
Cube	d (edge length)	1/12	1/6	7/360

Now substituting the stiffness tensors of an isotropic micromorphic media, given in index form in Eq. 7.41 and 7.42, into Eq. 9.13, the equations of motion in terms of the stiffness coefficients are derived as

$$\left\{ \begin{aligned} & (\lambda + \mu_2 + b_1 + b_3) \bar{\phi}_{j,ji} + (\mu_1 + b_2) \bar{\phi}_{i,jj} - b_1 \psi_{jj,i}^\phi - b_2 \psi_{ij,j}^\phi - b_3 \psi_{ji,j}^\phi = \rho \ddot{\phi}_i \\ & a_1 \left[ \delta_{ij} (2\psi_{kn,nk}^\phi + \psi_{kk,mn}^\phi) + 2(\psi_{kk,ij}^\phi + \psi_{ki,jk}^\phi + \psi_{jk,ki}^\phi + \psi_{kj,ik}^\phi) + \psi_{ji,kk}^\phi \right] + a_4 (2\psi_{ik,kj}^\phi + \psi_{ij,kk}^\phi) \\ & + (b_1 \delta_{ij} (\bar{\phi}_{k,k} - \psi_{kk}^\phi) + b_2 (\bar{\phi}_{i,j} - \psi_{ij}^\phi) + b_3 (\bar{\phi}_{j,i} - \psi_{ji}^\phi)) = \rho (\alpha_1 R^2) \ddot{\psi}_{ij}^\phi \end{aligned} \right. \quad (9.14a)$$

$$\left\{ \begin{array}{l} (\eta + \nu_2 + d_1 + d_3) \bar{\kappa}_{j,ji} + (\nu_1 + d_2) \bar{\kappa}_{i,jj} - d_1 \psi_{jj,i}^\kappa - d_2 \psi_{ij,j}^\kappa - d_3 \psi_{ji,j}^\kappa = \rho (\alpha_2 R^2) \ddot{\bar{\kappa}}_j \\ e_1 \left[ \delta_{ij} (2\psi_{kn,nk}^\kappa + \psi_{kk,nn}^\kappa) + 2(\psi_{kk,ij}^\kappa + \psi_{ki,jk}^\kappa + \psi_{jk,ki}^\kappa + \psi_{kj,ik}^\kappa) + \psi_{ji,kk}^\kappa \right] + e_4 (2\psi_{ik,kj}^\kappa + \psi_{ij,kk}^\kappa) \\ + (d_1 \delta_{ij} (\bar{\kappa}_{k,k} - \psi_{kk}^\kappa) + d_2 (\bar{\kappa}_{i,j} - \psi_{ij}^\kappa) + d_3 (\bar{\kappa}_{j,i} - \psi_{ji}^\kappa)) = \rho (\alpha_3 R^4) \ddot{\psi}_{ij}^\kappa \end{array} \right. \quad (9.14b)$$

These two sets of equations are decoupled from each other and should be solved separately. However, it is noted that the two equations in Eq. 9.14a contain both the average and the total gradient of the displacement field. Also the two equations in Eq. 9.14b contain both the average and the total gradient of grains' spins field.

First equation in each one of the above system of equations represents 3 equations for the three components of  $\bar{\phi}_i$  and  $\bar{\kappa}_i$ , while the second equations represent 9 equations for the 9 components of  $\psi_{ij}^\phi$  and  $\psi_{ij}^\kappa$ . So the 12 equations contained in Eq. 9.14a should be solved simultaneously for all components of  $\bar{\phi}_i$  and  $\psi_{ij}^\phi$  and the 12 equations contained in Eq. 9.14b should be solved simultaneously for all components of  $\bar{\kappa}_i$  and  $\psi_{ij}^\kappa$ .

In order to solve these problems, two types of waves, one displacement wave and one rotation wave are considered. What follows contains a complete analysis of the propagation of these two types of waves.

#### 9.4 Plane wave propagation within isotropic micromorphic media

For studying wave propagation in isotropic media, wave propagation in all directions are identical and hence, study of the propagation of waves in only one direction will be sufficient. Here, without loss of generality, propagation of waves along  $x_1$  axis is studied. In this case for a plane wave

solution, all kinematic measures should be only functions of the axis  $x_1$  and time in the following manner.

$$\bar{\phi}_i = \bar{\phi}_i(x_1, t) \quad \text{and} \quad \psi_{ij}^\phi = \psi_{ij}^\phi(x_1, t) \quad (9.15a)$$

$$\bar{\kappa}_i = \bar{\kappa}_i(x_1, t) \quad \text{and} \quad \psi_{ij}^\kappa = \psi_{ij}^\kappa(x_1, t) \quad (9.15b)$$

Due to material's isotropic behavior, the two directions perpendicular to the direction of wave propagation, 2 and 3, are identical. Having this in mind, a linear decomposition of second rank tensors has been applied on both  $\psi_{ij}^\phi$  and  $\psi_{ij}^\kappa$  (total gradients of the displacement and rotation fields) as follows

$$\psi^\phi = \psi_{ii}^\phi/3 \quad \text{and} \quad \psi_{11}^{\phi D} = \psi_{11}^\phi - \psi^\phi \quad (9.16a)$$

$$\psi^\kappa = \psi_{ii}^\kappa/3 \quad \text{and} \quad \psi_{11}^{\kappa D} = \psi_{11}^\kappa - \psi^\kappa \quad (9.16b)$$

where  $\psi^\phi$  and  $\psi^\kappa$  represent the volumetric component of the total gradients of displacement and rotation respectively, while  $\psi_{11}^{\phi D}$  and  $\psi_{11}^{\kappa D}$  are the deviatoric components of the total gradients of displacement and rotation respectively. Using this decomposition, the diagonal components of the aforementioned second rank tensors can be rewritten in terms of the volumetric and deviatoric components as follows

$$\psi_{11}^\phi = \psi^\phi + \psi_{11}^{\phi D} \quad \text{and} \quad \psi_{22}^\phi + \psi_{33}^\phi = 2\psi^\phi - \psi_{11}^{\phi D} \quad (9.17a)$$

$$\psi_{11}^\kappa = \psi^\kappa + \psi_{11}^{\kappa D} \quad \text{and} \quad \psi_{22}^\kappa + \psi_{33}^\kappa = 2\psi^\kappa - \psi_{11}^{\kappa D} \quad (9.17b)$$

A set of general solutions for the differential equations of motion are given by the Harmonic wave functions below

$$\bar{\phi}_i = A_i e^{i(\xi x_1 - \omega t)}; \quad \psi_{ij}^\phi = B_{ij} e^{i(\xi x_1 - \omega t)}; \quad (9.18a)$$

$$\bar{\kappa}_i = C_i e^{i(\xi x_1 - \omega t)}; \quad \psi_{ij}^\kappa = D_{ij} e^{i(\xi x_1 - \omega t)}; \quad (9.18b)$$

where  $\zeta$  is the wave number with units of 1/m,  $\omega$  is the frequency with units of rad/s, and the coefficients  $A_i$ ,  $B_{ij}$ ,  $C_i$ , and  $D_{ij}$  represent wave amplitudes corresponding to the average displacement, displacement gradient, average spin, and spin gradient fields respectively. The volumetric-deviatoric decomposition is applied on the solutions presented in Eq. 9.18a and the result is substituted into the displacement equations of motion (Eq. 9.14a) resulting in dispersion relationships for different components of displacement waves. The same decomposition is applied on the solutions presented in Eq. 9.18b and the result is substituted into the spins equations of motion (Eq. 9.14b) resulting in dispersion relationships for different components of spin waves. Since the two sets of equations of motion (Eq. 9.17a and Eq. 9.14b) are formally identical, the solutions and the dispersion relationships will be identical as well. The only difference between the two waves originates from the difference in the kinetic energy corresponding to the two terms (See Eq. 9.7) and also the difference between the values of stiffness coefficients corresponding to the two fields. What follows contains the derivation of dispersion relationships for different components of both displacement and spin waves within isotropic micromorphic media.

#### 9.4.1 Displacement waves in isotropic media

The proposed solutions for the average displacement field and the total gradient, given in Eq. 9.18a, are substituted into the corresponding equations of motion, Eq. 9.14a. Using the volumetric-deviatoric decomposition of the total gradient of the displacement, the equations of motion are decomposed into four parts:

- I. *Longitudinal waves*; for which the kinematic components are  $\bar{\phi}_1$ ,  $\psi^\phi$ , and  $\psi_{11}^{\phi D}$

II. *Transverse waves* in 2- or 3-direction; for which the kinematic components are either

$$\left(\bar{\phi}_2, \psi_{(12)}^\phi, \text{ and } \psi_{[12]}^\phi\right) \text{ or } \left(\bar{\phi}_3, 2\psi_{(13)}^\phi, \text{ and } 2\psi_{[13]}^\phi\right)$$

III. *In-Plane shear waves*; concerning the shear waves inside the plane perpendicular to the direction of wave propagation, 23-plane here. The kinematic components here are

$$2\psi_{(23)}^\phi \text{ and } 2\psi_{[23]}^\phi$$

IV. *Relative in-plane normal wave*; for which the kinematic component that is being studied is

$$\psi_{22}^\phi - \psi_{33}^\phi.$$

The above decomposition guarantees that the differential equations corresponding to the four groups of waves are mutually independent and can be solved separately.

### I. Longitudinal waves

This system of equations belongs to the components of the displacement field which are in the direction of propagation of the wave (direction 1). The system of equations and unknowns can be written in the following matrix form

$$\left( \begin{array}{ccc} L_{11}\xi^2 - \rho\omega^2 & L_{12}\xi & L_{13}\xi \\ L_{12}\xi & L_{22}\xi^2 + L'_{22} - 3\rho\alpha_1 R^2 \omega^2 & L_{23}\xi^2 \\ L_{13}\xi & L_{32}\xi^2 & L_{33}\xi^2 + L'_{33} - \frac{3}{2}\rho\alpha_1 R^2 \omega^2 \end{array} \right) \times \left\{ \begin{array}{c} \bar{\phi}_1 \\ \psi^\phi \\ \psi^{\phi D}_{11} \end{array} \right\} = \left\{ \begin{array}{c} 0 \\ 0 \\ 0 \end{array} \right\} \quad (9.19)$$

where

$$\begin{aligned} L_{11} &= l^2 N_p (3K_n^M + 2K_w^M + 3K_n^m + 2K_w^m) / 15 \\ L_{12} &= l^2 N_p K_n^m / 3; \quad L_{13} = l^2 N_p (2K_n^m + 3K_w^m) / 15 \\ L_{22} &= l^4 N_p K_n^g / 3; \quad L'_{22} = l^2 N_p K_n^m; \quad L_{23} = 2l^4 N_p K_n^g / 15 \\ L_{33} &= l^2 N_p (22K_n^g + 27K_w^g) / 210; \quad L'_{33} = l^4 N_p (2K_n^m + 3K_w^m) / 10 \end{aligned} \quad (9.20)$$

In order for the system of equations and unknowns presented in Eq. 9.19 to have non-trivial solutions, the determinant of the coefficients matrix should be zero. The matrix is evaluated at any given wave number ( $\xi$ ) and the determinant is set equal to zero resulting in a sixth order algebraic equation in terms of frequency ( $\omega$ ) with 6 real-valued solutions, three negative valued and three positive valued. The three positive values represent the frequency of the three wave components in the longitudinal direction. The results are presented in form of dispersion graphs (frequency vs. wave-number) later.

## II. Transverse waves

This system of equations belongs to the components of the displacement field which are inside the plane perpendicular to the direction of propagation of the wave. The plane can be either the 12 plane or the 13 plane. The system of equations and unknowns can be written in the following matrix form

$$\begin{pmatrix} T_{11}\xi^2 - \rho\omega^2 & T_{12}\xi & T_{13}\xi \\ T_{12}\xi & T_{22}\xi^2 + T'_{22} - 2\rho\alpha_1 R^2 \omega^2 & T_{23}\xi^2 \\ T_{13}\xi & T_{23}\xi^2 & T_{33}\xi^2 + T'_{33} - 2\rho\alpha_1 R^2 \omega^2 \end{pmatrix} \times \begin{Bmatrix} \bar{\phi}_i \\ \psi_{(1i)}^\phi \\ \psi_{[1i]}^\phi \end{Bmatrix} = \begin{Bmatrix} 0 \\ 0 \\ 0 \end{Bmatrix} \quad (9.21)$$

where  $i = 2$  and  $3$  and

$$\begin{aligned} T_{11} &= l^2 N_p (K_n^M + 4K_w^M + K_n^m + 4K_w^m) / 15; \\ T_{12} &= l^2 N_p (2K_n^m + 3K_w^m) / 15; \quad T_{13} = -l^2 N_p K_w^m / 3 \\ T_{22} &= 4l^4 N_p (3K_n^g + 4K_w^g) / 105; \quad T'_{22} = l^2 N_p (4K_n^m + 6K_w^m) / 15; \quad T_{23} = -2l^4 N_p K_w^g / 15 \\ T_{33} &= 4l^4 N_p K_w^g / 15; \quad T'_{33} = 2l^2 N_p K_w^m / 3 \end{aligned} \quad (9.22)$$

Note that due to the isotropy of the material, wave components in the two transverse directions (2 and 3) are identical. In order to ensure having non-trivial solution, the determinant of the coefficients matrix in Eq. 9.21 is set equal to zero at any given wave number ( $\xi$ ). This results in a

sixth order algebraic equation in terms of frequency ( $\omega$ ) with six real-valued solutions, three negative valued and three positive valued. The three positive values represent the frequency of the three wave components in the transverse direction.

### III. In-plane shear waves

This system of equations belongs to the symmetric and anti-symmetric shear components of waves inside the plane perpendicular to the direction of propagation of the wave. The system of equations and unknowns can be written in the following matrix form

$$\begin{pmatrix} S_{11}\xi^2 + S'_{11} - \rho\alpha_1 R^2 \omega^2 & 0 \\ 0 & S_{22}\xi^2 + S'_{22} - \rho\alpha_1 R^2 \omega^2 \end{pmatrix} \times \begin{Bmatrix} 2\psi_{(23)}^\phi \\ 2\psi_{[23]}^\phi \end{Bmatrix} = \begin{Bmatrix} 0 \\ 0 \end{Bmatrix} \quad (9.23)$$

where

$$\begin{aligned} S_{11} &= l^4 N_p (2K_n^g + 5K_w^g) / 105; & S'_{11} &= l^2 N_p (2K_n^m + 3K_w^m) / 15; \\ S_{22} &= l^4 N_p K_w^g / 105; & S'_{22} &= l^2 N_p K_w^m / 3; \end{aligned} \quad (9.24)$$

It can be noted from Eq. 9.23 that the symmetric and anti-symmetric parts of the in-plane shear component of the total gradient of the displacement field are fully decoupled from each other. In order to ensure non-trivial solution to the problem, the frequencies should be

$$\begin{aligned} \omega &= \sqrt{\frac{S_{11}\xi^2 + S'_{11}}{\rho\alpha_1 R^2}} \\ \omega &= \sqrt{\frac{S_{22}\xi^2 + S'_{22}}{\rho\alpha_1 R^2}} \end{aligned} \quad (9.25)$$

### IV. Relative in-plane normal wave

The only remaining equation will be concerning the difference between the two in-plane normal components of the total gradient of the displacement,  $\psi_{22}^\phi - \psi_{33}^\phi$ , and is formulated as



$$(D_{11}\xi^2 + D'_{11} - \rho\alpha_1 R^2 \omega^2) \times (\psi_{22}^\phi - \psi_{33}^\phi) = 0 \quad (9.26)$$

where

$$D_{11} = l^4 N_p (2K_n^g + 5K_w^g) / 105; \quad D'_{11} = l^2 N_p (2K_n^m + 3K_w^m) / 15 \quad (9.27)$$

The trivial solution for Eq. 9.26 is obviously  $\psi_{22}^\phi - \psi_{33}^\phi = 0$ . This, however, implies that there is no such wave since its amplitude will be always zero. Thus, for the equation to have non-trivial solution, the frequency should be

$$\omega = \sqrt{\frac{D_{11}\xi^2 + D'_{11}}{\rho\alpha_1 R^2}} \quad (9.28)$$

#### 9.4.2 Spin waves in isotropic media

As it was stated before, the analysis of spins waves is identical to that of displacement waves. However, for completeness purposes, results of the analysis of different components of spins waves are presented here.

Applying the volumetric-deviatoric decomposition to the spin waves (see Eq. 9.16b and 9.17b), equations of motion are decomposed into four parts:

- I. *Longitudinal waves*; where the kinematic components are  $\bar{\kappa}_1$ ,  $\psi^\kappa$ , and  $\psi_{11}^{\kappa D}$
- II. *Transverse waves* in 2- or 3-direction; where the kinematic components are either  $(\bar{\kappa}_2, \psi_{(12)}^\kappa, \text{ and } \psi_{[12]}^\kappa)$  or  $(\bar{\kappa}_3, \psi_{(13)}^\kappa, \text{ and } \psi_{[13]}^\kappa)$
- III. *In-Plane shear waves*; concerning the shear waves inside the plane perpendicular to the direction of wave propagation, 23-plane here. The kinematic components here are  $2\psi_{(23)}^\kappa$  and  $2\psi_{[23]}^\kappa$

IV. *Relative in-plane normal wave*; where the kinematic component that is being studied is  $\psi_{22}^{\kappa} - \psi_{33}^{\kappa}$

With this decomposition, the dispersion equations are fully decoupled and can be solved independently.

### I. Longitudinal waves

This system of equations belongs to the components of the kinematic fields which are in the direction of propagation of the wave (direction 1).

$$\left( \begin{array}{ccc} L_{11}\xi^2 - \rho\alpha_2 R^2 \omega^2 & L_{12}\xi & L_{13}\xi \\ L_{12}\xi & L_{22}\xi^2 + L'_{22} - 3\rho\alpha_3 R^4 \omega^2 & L_{23}\xi^2 \\ L_{13}\xi & L_{32}\xi^2 & L_{33}\xi^2 + L'_{33} - \frac{3}{2}\rho\alpha_3 R^4 \omega^2 \end{array} \right) \times \left\{ \begin{array}{c} \bar{\kappa}_1 \\ \psi^{\kappa} \\ \psi_{11}^{\kappa D} \end{array} \right\} = \left\{ \begin{array}{c} 0 \\ 0 \\ 0 \end{array} \right\} \quad (9.29)$$

where

$$\begin{aligned} L_{11} &= l^2 N_p (3G_n^M + 2G_w^M + 3G_n^m + 2G_w^m) / 15 \\ L_{12} &= l^2 N_p G_n^m / 3; \quad L_{13} = l^2 N_p (2G_n^m + 3G_w^m) / 15 \\ L_{22} &= l^4 N_p G_n^s / 3; \quad L'_{22} = l^2 N_p G_n^m; \quad L_{23} = 2l^4 N_p G_n^s / 15 \\ L_{33} &= l^2 N_p (22G_n^s + 27G_w^s) / 210; \quad L'_{33} = l^4 N_p (2G_n^m + 3G_w^m) / 10 \end{aligned} \quad (9.30)$$

Dispersion relationships for the longitudinal spin waves are derived by setting the determinant of the coefficients matrix in Eq. 9.29 equal to zero.

### II. Transverse waves

The system of equations belonging to the components of the spin field which are inside the plane perpendicular to the direction of propagation of the wave can be written in matrix form as

$$\begin{pmatrix} T_{11}\xi^2 - \rho\alpha_2 R^2 \omega^2 & T_{12}\xi & T_{13}\xi \\ T_{12}\xi & T_{22}\xi^2 + T'_{22} - 2\rho\alpha_3 R^4 \omega^2 & T_{23}\xi^2 \\ T_{13}\xi & T_{23}\xi^2 & T_{33}\xi^2 + T'_{33} - 2\rho\alpha_3 R^4 \omega^2 \end{pmatrix} \times \begin{Bmatrix} \bar{\kappa}_i \\ \psi_{(li)}^\kappa \\ \psi_{[li]}^\kappa \end{Bmatrix} = \begin{Bmatrix} 0 \\ 0 \\ 0 \end{Bmatrix} \quad (9.31)$$

where  $i = 2$  and  $3$  and

$$\begin{aligned} T_{11} &= l^2 N_p (G_n^M + 4G_w^M + G_n^m + 4G_w^m)/15; \\ T_{12} &= l^2 N_p (2G_n^m + 3G_w^m)/15; \quad T_{13} = -l^2 N_p G_w^m/3 \\ T_{22} &= 4l^4 N_p (3G_n^g + 4G_w^g)/105; \quad T'_{22} = l^2 N_p (4G_n^m + 6G_w^m)/15; \quad T_{23} = -2l^4 N_p G_w^g/15 \\ T_{33} &= 4l^4 N_p G_w^g/15; \quad T'_{33} = 2l^2 N_p G_w^m/3 \end{aligned} \quad (9.32)$$

Note that due to the isotropy of the material, wave components in the two transverse directions (2 and 3) are identical. The dispersion relationships concerning this group of waves is derived by setting the determinant of the coefficients matrix in Eq. 9.31 equal to zero.

### III. In-plane shear waves

Equations of motion belonging to the in-plane shear spin waves are written in matrix form in the following fashion.

$$\begin{pmatrix} S_{11}\xi^2 + S'_{11} - \rho\alpha_3 R^4 \omega^2 & 0 \\ 0 & S_{22}\xi^2 + S'_{22} - \rho\alpha_3 R^4 \omega^2 \end{pmatrix} \times \begin{Bmatrix} 2\psi_{(23)}^\kappa \\ 2\psi_{[23]}^\kappa \end{Bmatrix} = \begin{Bmatrix} 0 \\ 0 \end{Bmatrix} \quad (9.33)$$

where

$$\begin{aligned} S_{11} &= l^4 N_p (2G_n^g + 5G_w^g)/105; \quad S'_{11} = l^2 N_p (2G_n^m + 3G_w^m)/15; \\ S_{22} &= l^4 N_p G_w^g/105; \quad S'_{22} = l^2 N_p G_w^m/3; \end{aligned} \quad (9.34)$$

Since the two equations inside Eq. 9.33 are fully decoupled, a closed form solution for the dispersion relationships is derived as

$$\omega = \sqrt{\frac{S_{11}\xi^2 + S'_{11}}{\rho\alpha_3 R^4}}$$

$$\omega = \sqrt{\frac{S_{22}\xi^2 + S'_{22}}{\rho\alpha_3 R^4}}$$
(9.35)

#### IV. Relative in-plane normal wave

The only remaining equation will be concerning the difference between the two in-plane normal components of the total gradient of the spins,  $\psi_{22}^\chi - \psi_{33}^\chi$ , and is stated as

$$\left(D_{11}\xi^2 + D'_{11} - \rho\alpha_3 R^4 \omega^2\right) \times \left(\psi_{22}^\chi - \psi_{33}^\chi\right) = 0$$
(9.36)

where

$$D_{11} = l^4 N_p \left(2G_n^g + 5G_w^g\right) / 105; \quad D'_{11} = l^2 N_p \left(2G_n^m + 3G_w^m\right) / 15$$
(9.37)

In order to ensure a non-trivial solution, the dispersion relationship for this component of spin waves will be derived as

$$\omega = \sqrt{\frac{D_{11}\xi^2 + D'_{11}}{\rho\alpha_3 R^4}}$$
(9.38)

### 9.5 Plane wave propagation within transversely isotropic micromorphic media

In this section, the focus is on the analysis of propagation of displacement plane waves within anisotropic media. First thing to note is that for anisotropic media, the dispersion behavior in different directions will be different based on the material properties and the elastic symmetries

present in the material. For demonstration purposes here, propagation of displacement plane waves inside transversely isotropic media has been studied only. Analysis of spin waves might be performed in the same manner. Moreover, analysis of wave propagation within materials with higher levels of anisotropy can also be done with the same approach as what will be presented here.

The displacement equations of motion presented in Eq. 9.13a and 9.13b should be rewritten for transversely isotropic materials. In fact, the stiffness tensors should be replaced by stiffness tensors corresponding to transversely isotropic materials. As a first approximation, it is assumed that only the macroscopic stiffness tensor  $C_{ijkl}^M$  is transversely isotropic, while the other stiffness tensors remain isotropic. For this kind of material, the displacement equations of motion will be different from the one presented in Eq. 9.14 for isotropic materials. The general form of displacement equations of motion for a material whose macroscopic stiffness tensor  $C_{ijkl}^M$  is anisotropic can be given as

$$\left\{ \begin{array}{l} C_{ijkl}^M \bar{\phi}_{k,lj} + (b_1 + b_3) \bar{\phi}_{j,ji} + (b_2) \bar{\phi}_{i,jj} - b_1 \psi_{jj,i}^\phi - b_2 \psi_{ij,j}^\phi - b_3 \psi_{ji,j}^\phi = \rho \ddot{\bar{\phi}}_i \\ a_1 \left[ \delta_{ij} (2\psi_{kn,nk}^\phi + \psi_{kk,nm}^\phi) + 2(\psi_{kk,ij}^\phi + \psi_{ki,jk}^\phi + \psi_{jk,ki}^\phi + \psi_{kj,ik}^\phi) + \psi_{ji,kk}^\phi \right] + a_4 (2\psi_{ik,kj}^\phi + \psi_{ij,kk}^\phi) \\ + (b_1 \delta_{ij} (\bar{\phi}_{k,k} - \psi_{kk}^\phi) + b_2 (\bar{\phi}_{i,j} - \psi_{ij}^\phi) + b_3 (\bar{\phi}_{j,i} - \psi_{ji}^\phi)) = \rho (\alpha_1 R^2) \ddot{\psi}_{ij}^\phi \end{array} \right. \quad (9.39)$$

Now, without loss of generality, let us consider a transversely isotropic material whose axis of rotational symmetry is axis 1. For this kind of material, the stiffness tensor will be such as the one shown in Eq. 6.3. For calculating the stiffness tensor of such a material, the approach presented in Chapter 6, section 6.3 is adopted. In the approach, material's microscopic properties include stiffness coefficient in normal direction, two stiffness coefficients in the two tangential directions.

Moreover, the directional density distribution of inter-granular properties (number of contacts, contact lengths and stiffness coefficients) are governed by the two fabric parameters  $a_{20}$  and  $a_{40}$ .

In such a material, the properties in the two directions  $y$  and  $z$  are identical. While the properties in the  $x$  direction is different from these two. So the propagation of waves along two directions,  $x$  and  $y$ , have been studied here.

### 9.5.1 Propagation of displacement waves in $x$ direction

When studying propagation of plane waves along  $x$  axis, the two displacement fields (average displacement field and the total displacement gradient, should be only functions of  $x_1$  and time.

$$\bar{\phi}_i = \bar{\phi}_i(x_1, t) \quad \text{and} \quad \psi_{ij}^\phi = \psi_{ij}^\phi(x_1, t) \quad (9.40)$$

For the second rank tensor  $\psi_{ij}^\phi$ , the same decomposition of volumetric and deviatoric components as the one presented in Eq. 9.16 and 9.17 is utilized. Harmonic wave forms identical to the ones presented in Eq. 9.18a are used as solutions to the equations of motion.

In a manner identical to the one presented in section 9.4.1, the displacement waves are decomposed into *longitudinal*, *transverse*, *in-plane shear*, and *Relative in-plane normal* waves. By a closer look at the dispersion equations pertinent to all these wave groups, given in Eq. 9.19-9.27, it is seen that only the first two groups (i.e. *longitudinal* and *transverse* waves) are affected by the macroscopic stiffness tensor components (represented in macro-scale by  $C_{ijkl}^M$ , and in micro-scale by  $K_{ij}^M$ ). In what follows, the dispersion relationships for propagation of longitudinal and transverse components of displacement waves in  $x$  direction are presented. For the two other classes (i.e. the *in-plane shear* and the *relative in-plane normal* waves) the equations for isotropic materials given in section 9.4.1 are valid.

#### I. Longitudinal waves

The system of equations pertinent to  $\bar{\phi}_1$ ,  $\psi^\phi$ , and  $\psi_{11}^{\phi D}$  will form the longitudinal dispersion relationships and it is given as follows

$$\begin{pmatrix} L_{11}\xi^2 - \rho\omega^2 & L_{12}\xi & L_{13}\xi \\ L_{12}\xi & L_{22}\xi^2 + L'_{22} - 3\rho\alpha_1 R^2 \omega^2 & L_{23}\xi^2 \\ L_{13}\xi & L_{32}\xi^2 & L_{33}\xi^2 + L'_{33} - \frac{3}{2}\rho\alpha_1 R^2 \omega^2 \end{pmatrix} \times \begin{Bmatrix} \bar{\phi}_1 \\ \psi^\phi \\ \psi_{11}^{\phi D} \end{Bmatrix} = \begin{Bmatrix} 0 \\ 0 \\ 0 \end{Bmatrix} \quad (9.41)$$

where

$$\begin{aligned} L_{11} &= l^2 N_p \left[ \left( \frac{K_n^M}{315} (63 + 36a_{20} + 8a_{40}) + \frac{K_s^M}{315} (42 + 6a_{20} - 8a_{40}) \right) + (3K_n^m + 2K_w^m) / 15 \right] \\ L_{12} &= l^2 N_p K_n^m / 3; \quad L_{13} = l^2 N_p (2K_n^m + 3K_w^m) / 15 \\ L_{22} &= l^4 N_p K_n^s / 3; \quad L'_{22} = l^2 N_p K_n^m; \quad L_{23} = 2l^4 N_p K_n^s / 15 \\ L_{33} &= l^2 N_p (22K_n^s + 27K_w^s) / 210; \quad L'_{33} = l^4 N_p (2K_n^m + 3K_w^m) / 10 \end{aligned} \quad (9.42)$$

In order to ensure that the above system of equations and unknowns will have non-trivial solutions, the determinant of the coefficients matrix should be set equal to zero. The resulting equations will be the dispersion equations for displacement plane waves propagating in x direction within a transversely isotropic material.

## II. Transverse waves

This system of equations pertinent to  $(\bar{\phi}_2, \psi_{(12)}^\phi, \text{ and } \psi_{[12]}^\phi)$  or  $(\bar{\phi}_3, \psi_{(13)}^\phi, \text{ and } \psi_{[13]}^\phi)$  components of the displacement field which are inside the plane perpendicular to the direction of propagation of the wave. The system of equations and unknowns can be written in the following matrix form

$$\begin{pmatrix} T_{11}\xi^2 - \rho\omega^2 & T_{12}\xi & T_{13}\xi \\ T_{12}\xi & T_{22}\xi^2 + T'_{22} - 2\rho\alpha_1 R^2 \omega^2 & T_{23}\xi^2 \\ T_{13}\xi & T_{23}\xi^2 & T_{33}\xi^2 + T'_{33} - 2\rho\alpha_1 R^2 \omega^2 \end{pmatrix} \times \begin{Bmatrix} \bar{\phi}_i \\ \psi_{(1i)}^\phi \\ \psi_{[1i]}^\phi \end{Bmatrix} = \begin{Bmatrix} 0 \\ 0 \\ 0 \end{Bmatrix} \quad (9.43)$$

where  $i = 2$  and  $3$  and

$$\begin{aligned}
T_{11} &= l^2 N_p \left[ \left( \frac{K_n^M}{315} (21 + 3a_{20} - 4a_{40}) + \frac{K_s^M}{315} (31.5 + 18a_{20} + 4a_{40}) + \frac{K_t^M}{30} (5 + 2a_{20}) \right) \right. \\
&\quad \left. + \frac{K_n^m + 4K_w^m}{15} \right] \\
T_{12} &= l^2 N_p (2K_n^m + 3K_w^m)/15; \quad T_{13} = l^2 N_p K_w^m/3 \\
T_{22} &= 4l^4 N_p (3K_n^s + 4K_w^s)/105; \quad T_{22}' = l^2 N_p (4K_n^m + 6K_w^m)/15; \quad T_{23} = 2l^4 N_p K_w^s/15 \\
T_{33} &= 4l^4 N_p K_w^s/15; \quad T_{33}' = 2l^2 N_p K_w^m/3
\end{aligned} \tag{9.44}$$

It is noted that due to material's transverse isotropy (axis 1 being the axis of rotational symmetry), the behavior of the material in 2 and 3 directions are identical. Dispersion relationships for these wave components will be derived by setting the determinant of the coefficients matrix in Eq. 43 equal to zero.

### 9.5.2 Propagation of displacement waves in y direction

The two displacement fields (average displacement field and the total displacement gradient) are defined in this case as a functions of  $x_2$  and time.

$$\bar{\phi}_i = \bar{\phi}_i(x_2, t) \quad \text{and} \quad \psi_{ij}^\phi = \psi_{ij}^\phi(x_2, t) \tag{9.45}$$

The volumetric-deviatoric decomposition of the second rank displacement gradient tensor in this case will be slightly different, because the longitudinal wave will be  $\psi_{22}^\phi$ . The volumetric and deviatoric components of displacement gradient tensor will be given as

$$\psi^\phi = \psi_{ii}^\phi/3 \quad \text{and} \quad \psi_{22}^{\phi D} = \psi_{22}^\phi - \psi^\phi \tag{9.46}$$

where  $\psi^\phi$  represents the volumetric component of the total gradients of displacement, while  $\psi_{22}^{\phi D}$  is the deviatoric component of the total gradients of displacement. Using this decomposition, the diagonal components of the displacement gradient tensor can be rewritten as

$$\psi_{22}^\phi = \psi^\phi + \psi_{22}^{\phi D} \quad \text{and} \quad \psi_{11}^\phi + \psi_{33}^\phi = 2\psi^\phi - \psi_{22}^{\phi D} \tag{9.47}$$



The general form of solution for harmonic waves propagating in y direction will be given as

$$\bar{\phi}_i = A_i e^{i(\xi x_2 - \omega t)}; \quad \psi_{ij}^\phi = B_{ij} e^{i(\xi x_2 - \omega t)}; \quad (9.48)$$

where  $\xi$  is the wave number with units of 1/m,  $\omega$  is the frequency with units of rad/s, and the coefficients  $A_i$ , and  $B_{ij}$  represent wave amplitudes corresponding to the average displacement and displacement gradient. Substituting the solutions given in Eq. 9.48 into the displacement equations of motion given in Eq. 9.39, 12 equations for different components of the kinematic measures of the problem are derived.

By applying the volumetric-deviatoric decomposition to the displacement gradient, it is possible to decompose the waves into distinct categories. Longitudinal, transverse, in-plane shear, and relative in-plane normal wave components will be formulated separately. However, it should be noted that, in contrast to the case of wave propagation in isotropic media or wave propagation in x direction in transversely isotropic media, the transverse components of waves in the two transverse directions will be different here. In this analysis of plane waves propagating in y direction, the two transverse directions will be directions x and z. The material does not behave in an identical manner in these two directions, since x is the axis of rotational symmetry and z lies on the plane whose normal is x.

For this reason, the waves will be categorized as follows:

- I. Longitudinal components:  $\bar{\phi}_2$ ,  $\psi^\phi$ , and  $\psi_{22}^{\phi D}$

For these components, the dispersion relationship will be given as

$$\begin{pmatrix} L_{11}\xi^2 - \rho\omega^2 & L_{12}\xi & L_{13}\xi \\ L_{12}\xi & L_{22}\xi^2 + L'_{22} - 3\rho\alpha_1 R^2 \omega^2 & L_{23}\xi^2 \\ L_{13}\xi & L_{32}\xi^2 & L_{33}\xi^2 + L'_{33} - \frac{3}{2}\rho\alpha_1 R^2 \omega^2 \end{pmatrix} \times \begin{Bmatrix} \bar{\phi}_1 \\ \psi^\phi \\ \psi_{22}^{\phi D} \end{Bmatrix} = \begin{Bmatrix} 0 \\ 0 \\ 0 \end{Bmatrix} \quad (9.49)$$

where

$$L_{11} = l^2 N_p \left[ \left( \frac{K_n^M}{315} (21 - 6a_{20} + a_{40}) + \frac{K_s^M}{420} (21 + 3a_{20} - 2a_{40}) + \frac{K_t^M}{60} (5 - a_{20}) \right) + \frac{3K_n^m + 2K_w^m}{15} \right]$$

$$L_{12} = l^2 N_p K_n^m / 3; \quad L_{13} = l^2 N_p (2K_n^m + 3K_w^m) / 15 \quad (9.50)$$

$$L_{22} = l^4 N_p K_n^g / 3; \quad L'_{22} = l^2 N_p K_n^m; \quad L_{23} = 2l^4 N_p K_n^g / 15$$

$$L_{33} = l^2 N_p (22K_n^g + 27K_w^g) / 210; \quad L'_{33} = l^4 N_p (2K_n^m + 3K_w^m) / 10$$

In order to guarantee having non-trivial solution for Eq. 9.49, the determinant of the coefficients matrix is set equal to zero, resulting in the dispersion relationships pertinent to longitudinal wave components.

II. Transverse components in xy plane:  $\bar{\phi}_1$ ,  $\psi_{(12)}^\phi$ , and  $\psi_{[12]}^\phi$

The dispersion relationships for these wave components are given in matrix form as

$$\begin{pmatrix} T_{11}\xi^2 - \rho\omega^2 & T_{12}\xi & T_{13}\xi \\ T_{12}\xi & T_{22}\xi^2 + T'_{22} - 2\rho\alpha_1 R^2 \omega^2 & T_{23}\xi^2 \\ T_{13}\xi & T_{23}\xi^2 & T_{33}\xi^2 + T'_{33} - 2\rho\alpha_1 R^2 \omega^2 \end{pmatrix} \times \begin{Bmatrix} \bar{\phi}_1 \\ \psi_{(12)}^\phi \\ \psi_{[12]}^\phi \end{Bmatrix} = \begin{Bmatrix} 0 \\ 0 \\ 0 \end{Bmatrix} \quad (9.51)$$

where

$$T_{11} = l^2 N_p \left( \frac{K_n^M}{315} (21 + 3a_{20} - 4a_{40}) + \frac{K_s^M}{315} (84 - 24a_{20} + 4a_{40}) + \frac{K_n^m + 4K_w^m}{15} \right)$$

$$T_{12} = l^2 N_p (2K_n^m + 3K_w^m) / 15; \quad T_{13} = l^2 N_p K_w^m / 3 \quad (9.52)$$

$$T_{22} = 4l^4 N_p (3K_n^g + 4K_w^g) / 105; \quad T'_{22} = l^2 N_p (4K_n^m + 6K_w^m) / 15; \quad T_{23} = 2l^4 N_p K_w^g / 15$$

$$T_{33} = 4l^4 N_p K_w^g / 15; \quad T'_{33} = 2l^2 N_p K_w^m / 3$$

Dispersion relationships for wave components  $\bar{\phi}_1$ ,  $\psi_{(12)}^\phi$ , and  $\psi_{[12]}^\phi$  are derived by setting the determinant of the coefficients matrix in Eq. 9.51 equal to zero. However, as it was stated before,

for propagation of plane waves in y direction within transversely isotropic materials, the other set of transverse wave components will have a different behavior.

### III. Transverse components in xz plane: $\bar{\phi}_3$ , $\psi_{(23)}^\phi$ , and $\psi_{[23]}^\phi$

For these components, the pertinent equations of motion can be written in matrix form as

$$\begin{pmatrix} T_{11}\xi^2 - \rho\omega^2 & T_{12}\xi & T_{13}\xi \\ T_{12}\xi & T_{22}\xi^2 + T_{22}' - 2\rho\alpha_1 R^2 \omega^2 & T_{23}\xi^2 \\ T_{13}\xi & T_{23}\xi^2 & T_{33}\xi^2 + T_{33}' - 2\rho\alpha_1 R^2 \omega^2 \end{pmatrix} \times \begin{Bmatrix} \bar{\phi}_3 \\ \psi_{(23)}^\phi \\ \psi_{[23]}^\phi \end{Bmatrix} = \begin{Bmatrix} 0 \\ 0 \\ 0 \end{Bmatrix} \quad (9.53)$$

where

$$\begin{aligned} T_{11} &= l^2 N_p \left( \frac{K_n^M}{315} (21 - 6a_{20} + a_{40}) + \frac{K_s^M}{1260} (21 + 3a_{20} - 4a_{40}) + \frac{K_t^M}{20} (5 - a_{20}) \right. \\ &\quad \left. + \frac{K_n^m + 4K_w^m}{15} \right) \\ T_{12} &= l^2 N_p (2K_n^m + 3K_w^m) / 15; \quad T_{13} = -l^2 N_p K_w^m / 3 \\ T_{22} &= 4l^4 N_p (3K_n^s + 4K_w^s) / 105; \quad T_{22}' = l^2 N_p (4K_n^m + 6K_w^m) / 15; \quad T_{23} = -2l^4 N_p K_w^s / 15 \\ T_{33} &= 4l^4 N_p K_w^s / 15; \quad T_{33}' = 2l^2 N_p K_w^m / 3 \end{aligned} \quad (9.54)$$

Setting the determinant of the coefficients matrix in Eq. 9.53 equal to zero results in the dispersion relationships for  $\bar{\phi}_3$ ,  $\psi_{(23)}^\phi$ , and  $\psi_{[23]}^\phi$  components of displacement waves propagating in y direction.

### IV. In-plane shear waves: $2\psi_{(13)}^\phi$ and $2\psi_{[13]}^\phi$

The equations of motion pertinent to the in-plane shear components of displacement waves can be written in matrix form as

$$\begin{pmatrix} S_{11}\xi^2 + S_{11}' - \rho\alpha_1 R^2 \omega^2 & 0 \\ 0 & S_{22}\xi^2 + S_{22}' - \rho\alpha_1 R^2 \omega^2 \end{pmatrix} \times \begin{Bmatrix} 2\psi_{(13)}^\phi \\ 2\psi_{[13]}^\phi \end{Bmatrix} = \begin{Bmatrix} 0 \\ 0 \end{Bmatrix} \quad (9.55)$$

where

$$\begin{aligned}
S_{11} &= l^4 N_p (2K_n^g + 5K_w^g) / 105; & S'_{11} &= l^2 N_p (2K_n^m + 3K_w^m) / 15; \\
S_{22} &= l^4 N_p K_w^g / 105; & S'_{22} &= l^2 N_p K_w^m / 3;
\end{aligned}
\tag{9.56}$$

It can be seen that the system of equations given in Eq. 55 is fully decoupled. So the equations can be solved independently. The dispersion relationships giving the frequency of these wave components as a function of their wave number can be given in close-form as

$$\begin{aligned}
\omega &= \sqrt{\frac{S_{11}\xi^2 + S'_{11}}{\rho\alpha_1 R^2}} \\
\omega &= \sqrt{\frac{S_{22}\xi^2 + S'_{22}}{\rho\alpha_1 R^2}}
\end{aligned}
\tag{9.57}$$

V. Relative in-plane normal waves:  $\psi_{11}^\phi - \psi_{33}^\phi$

Finally, the dispersion relationship for  $\psi_{11}^\phi - \psi_{33}^\phi$  component of the displacement wave propagating in y direction is given as

$$(D_{11}\xi^2 + D'_{11} - \rho\alpha_1 R^2 \omega^2) \times (\psi_{22}^\phi - \psi_{33}^\phi) = 0
\tag{9.58}$$

where

$$D_{11} = l^4 N_p (2K_n^g + 5K_w^g) / 105; \quad D'_{11} = l^2 N_p (2K_n^m + 3K_w^m) / 15
\tag{9.59}$$

The trivial solution for Eq. 9.58 is obviously  $\psi_{11}^\phi - \psi_{33}^\phi = 0$ . This, however, implies that this component of wave is always absent, since its amplitude will be always zero. Thus, for the equation to have non-trivial solution, the frequency should be

$$\omega = \sqrt{\frac{D_{11}\xi^2 + D'_{11}}{\rho\alpha_1 R^2}}
\tag{9.60}$$

The above equation gives the dispersion relationships for this component of displacement waves.

## 9.6 Results and Discussions

In this section, the dispersion behavior of both isotropic and transversely isotropic materials are studied with numerical examples.

### 9.6.1 Dispersion behavior of isotropic materials

Here, the equations of motion derived in section 9.4 are solved for an isotropic rock-like material. The microscopic material parameters used in this analysis along with the resulting macroscopic properties of the material are presented in Table 9.2. Note that, as it is clear in Table 9.2, in this study, for all kinematic measures, the stiffness in the tangential direction is assumed to be one half of the stiffness coefficient in the normal direction (For a complete analysis of the effect of ratios between normal and tangential components of inter-granular stiffness coefficients see [206]).

It is worthwhile here to note the inter-granular mechanism that is controlled by each one of the inter-granular stiffness coefficients. The stiffness coefficients  $K_n$  and  $K_w$  (normal and tangential stiffness coefficients) control the normal and tangential displacement between two grains. While the two coefficients  $G_n$  and  $G_w$  (rotational stiffness coefficients around normal and tangential axes) control torsion and bending between two neighbor grains respectively. Using this analysis, it is clear that  $K_n$  is, in a sense, representing the axial stiffness of the contact mechanism between the two grains, while  $G_n$  could be conceived to represent the torsional stiffness of the contact mechanism between two neighbor grains. This simplified analysis has been used here in order to find the stiffness coefficients presented in Table 9.1.

Table 9.2 Micro-scale parameters (left) and the corresponding macro-scale constitutive parameters (right)

Model Parameters	Values	Macroscopic Parameters	Values
$l$	$10^{-3}$ m	$\lambda$	6.67 GPa
$d$	$10^{-3}$ m	$\mu$	23.33 GPa
$N_p$	$10^9$ 1/m <sup>3</sup>	$b_1=b_3$	6.67 GPa
$\rho'$	3000 Kg/m <sup>3</sup>	$b_2$	40.00 GPa
$\rho$	1570 Kg/m <sup>3</sup>	$a_1$	$9.52 \times 10^{-6}$ MN
$\zeta$	$1/4\pi$	$a_4$	$7.62 \times 10^{-6}$ MN
$K_n^M = 2K_w^M$	200 MN/m	$\eta=v_2$	$166.67 \times 10^{-6}$ MN
$K_n^m = 2K_w^m$	200 MN/m	$v_1$	$1000.0 \times 10^{-6}$ MN
$K_n^g = 2K_w^g$	2 MN/m	$d_1=d_3$	$166.67 \times 10^{-6}$ MN
$G_n^M = 2G_w^M$	5000 N.mm	$d_2$	$1000.0 \times 10^{-6}$ MN
$G_n^m = 2G_w^m$	5000 N.mm	$e_1$	$5.95 \times 10^{-11}$ N.mm <sup>2</sup>
$G_n^g = 2G_w^g$	$1.25 \times 10^{-8}$ N.mm	$e_4$	$4.76 \times 10^{-10}$ N.mm <sup>2</sup>

In Figures 9.1 and 9.2 the dispersion curves for different components of the displacement and spin waves have been presented. In both figures, the components corresponding to longitudinal, transverse, in-plane shear, and relative in-plane normal wave components have been presented in separate sections. The kinematic component corresponding to each one of the curves is also specified on the figures.

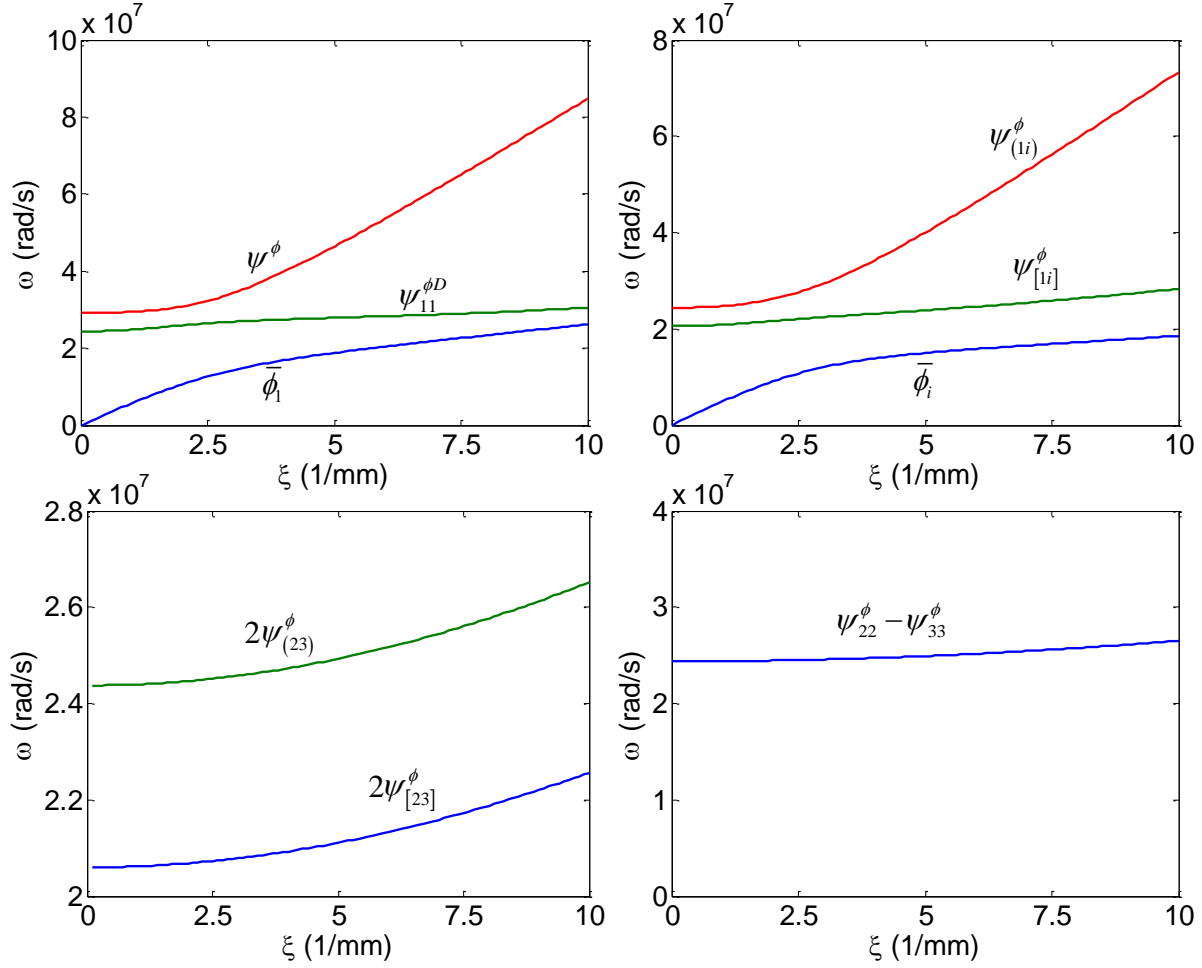


Figure 9.1 Dispersion graphs for different components of displacement waves

Here, it is interesting to point the contrast between the results of this kind of micromorphic theory to that of a usual first gradient continuum model. In the classical analysis, only two components of wave (compressive, or P, wave and shear, or S, wave) propagate through. These waves always have a constant velocity,  $C_p$  and  $C_s$  respectively. Waves with constant velocity are named *non-dispersive* waves and their frequency has a linear relationship with wave number as

$$\omega_p = C_p \xi = \left( \sqrt{\frac{\lambda + 2\mu}{\rho}} \right) \xi; \quad \omega_s = C_s \xi = \left( \sqrt{\frac{\mu}{\rho}} \right) \xi \quad (9.61)$$

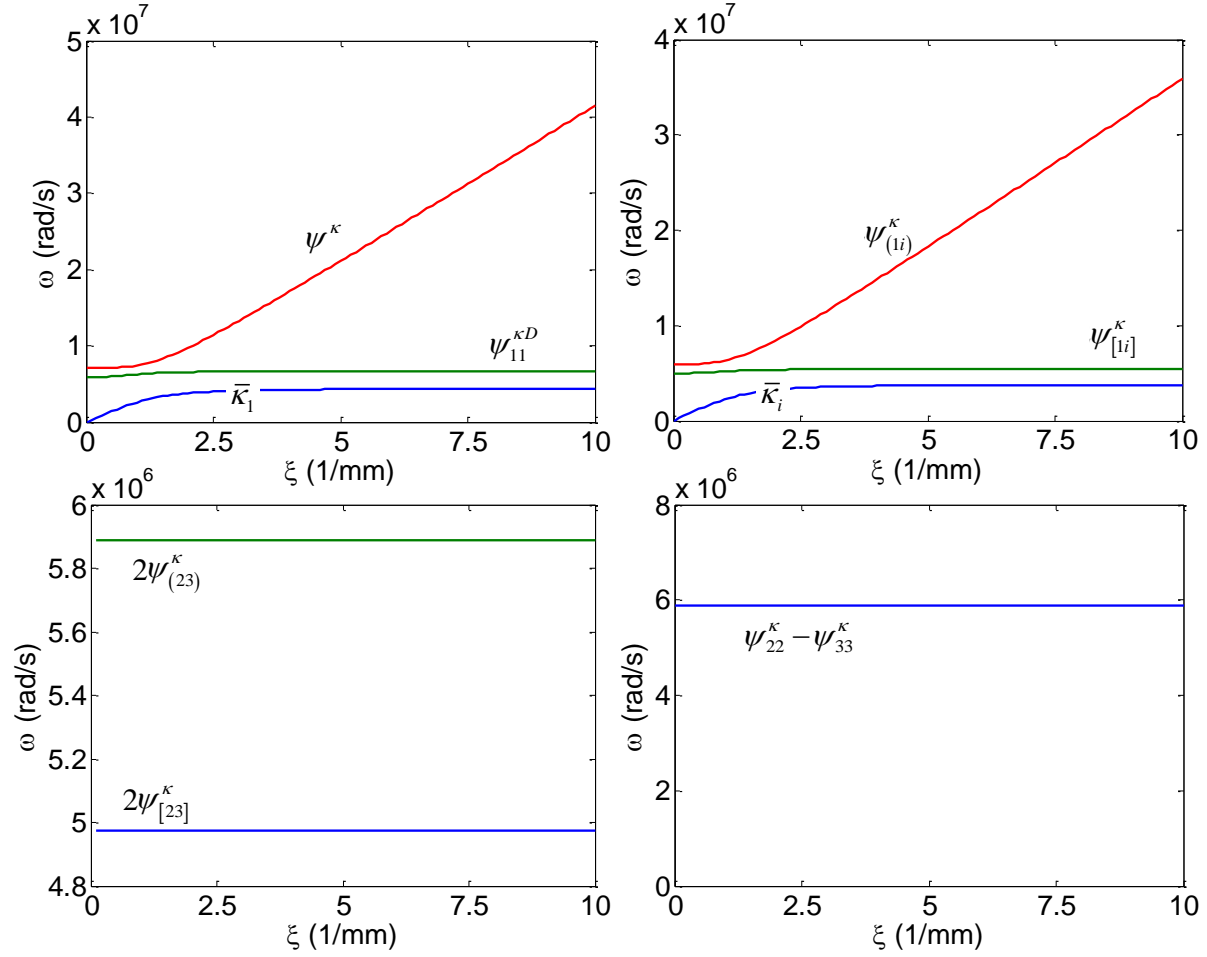


Figure 9.2 Dispersion graphs for different components of spin waves

However, as it is seen in Figure 9.1 and 9.2, almost all components of waves in the micromorphic media are dispersive, since their dispersion graphs are not straight lines.

In studying the propagation of waves two types of velocity are studied, namely phase velocity and group velocity [207]. Phase velocity,  $v_p$ , is the velocity of propagation of each wave front and is calculated as the secant slope of the dispersion graph. Whereas group velocity,  $v_g$ , is the velocity of propagation of an envelope of a wave packet and can be calculated as the tangential slope of the dispersion graph [208]. The two velocity measures are formulated as



$$v_p = \frac{\omega}{\xi} \tag{9.62}$$

$$v_g = \frac{\partial \omega}{\partial \xi}$$

It is obvious from Eq. 9.62 that if the waves are not dispersive, meaning that dispersion graphs are lines and not curves ( $\omega = v \times \xi$ ), these two velocities would be identical ( $\omega/\xi = \partial \omega / \partial \xi = v$ ).

However for the micromorphic materials modeled here, the two velocities are in fact different.

Figures 9.3 and 9.4 show the evolution of phase velocity and group velocity, respectively, for displacement waves.

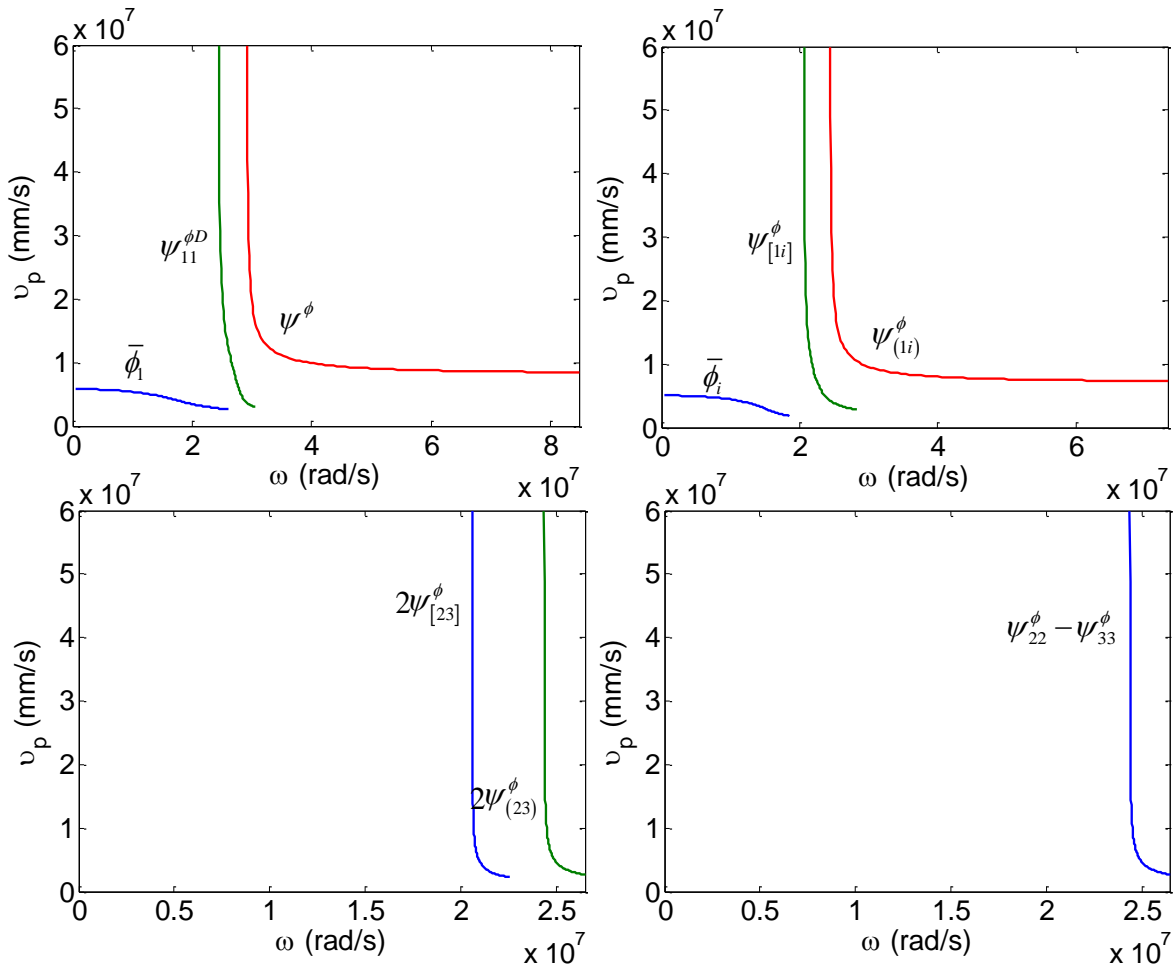


Figure 9.3 Phase velocity of different components of displacement waves vs their frequency

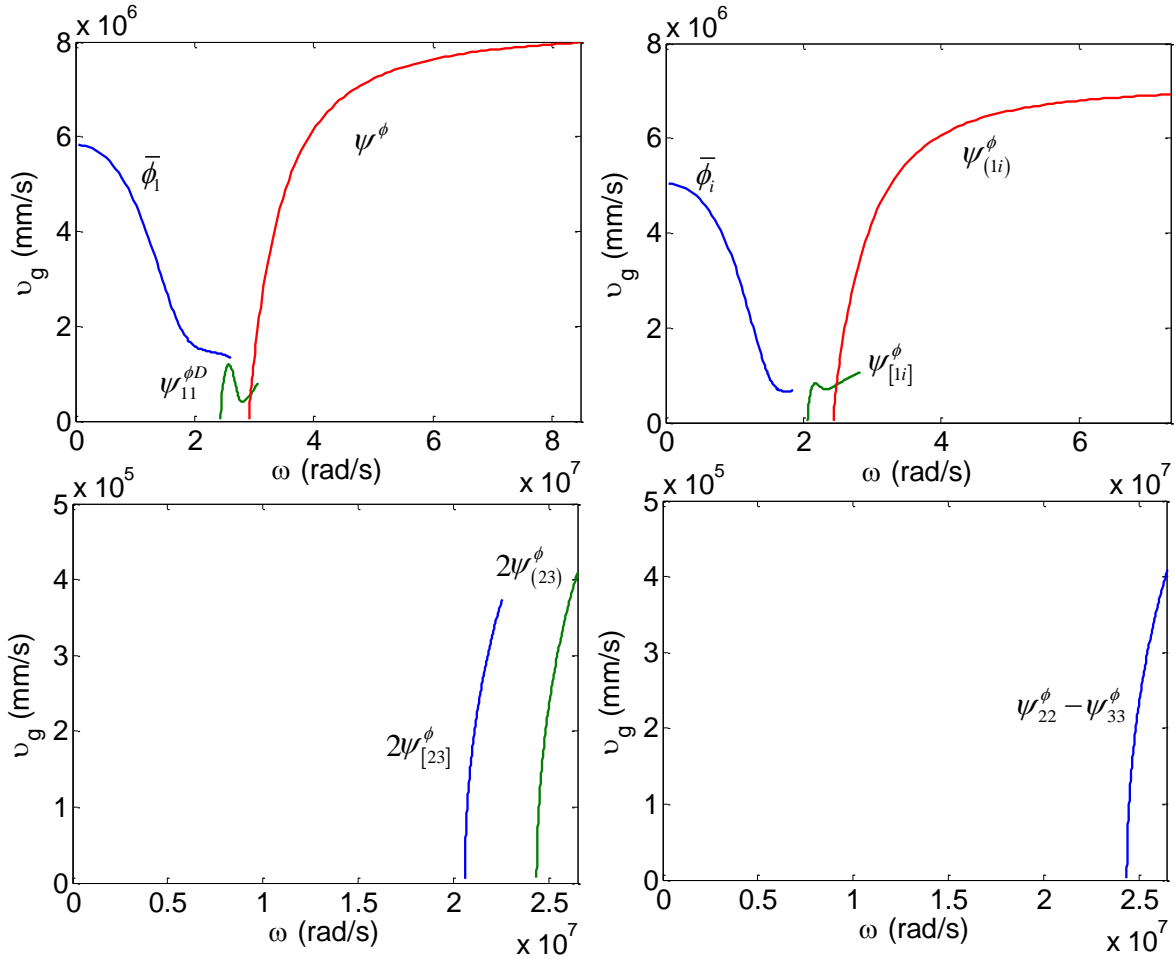


Figure 9.4 Group velocity of different components of displacement waves vs their frequency

Note that in these two figures,  $i=2$  and  $3$ . It is interesting to note that the phase velocity for all components of displacement waves are monotonically decreasing. It is also interesting to note the small frequency band that some components of displacement waves, including  $\psi_{11}^{\phi D}$ ,  $\psi_{[i]}^{\phi}$ ,  $\psi_{(23)}^{\phi}$ ,  $\psi_{[23]}^{\phi D}$ , and  $\psi_{22}^{\phi} - \psi_{33}^{\phi}$  components. The group velocity curves (representing the derivative of the dispersion curves) show a more complicated behavior. They represent a combination of decreasing and increasing behavior.

Also Figures 9.5 and 9.6 show the evolution of phase velocity and group velocity, respectively, for spin waves.

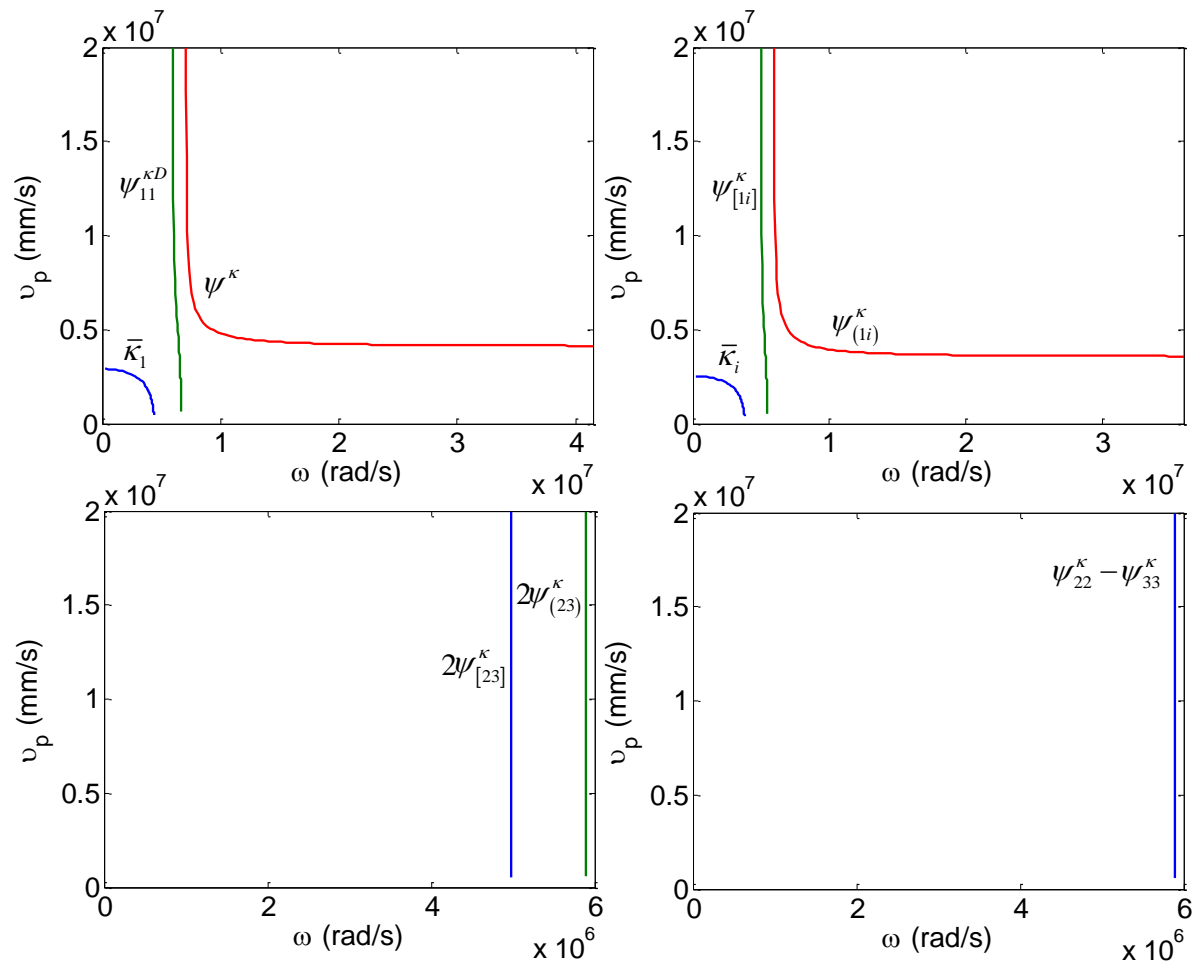


Figure 9.5 Phase velocity of different components of spin waves vs their frequency

As it was expected from the equations of motion governing the displacement and spin waves, it is seen that the behavior of phase and group velocities of the two waves are qualitatively similar. Again, phase velocities are decreasing monotonically, while group velocities show a combination of decreasing and increasing behavior. In addition, it is observed that the multiple components of waves propagate in a very narrow frequency domain.

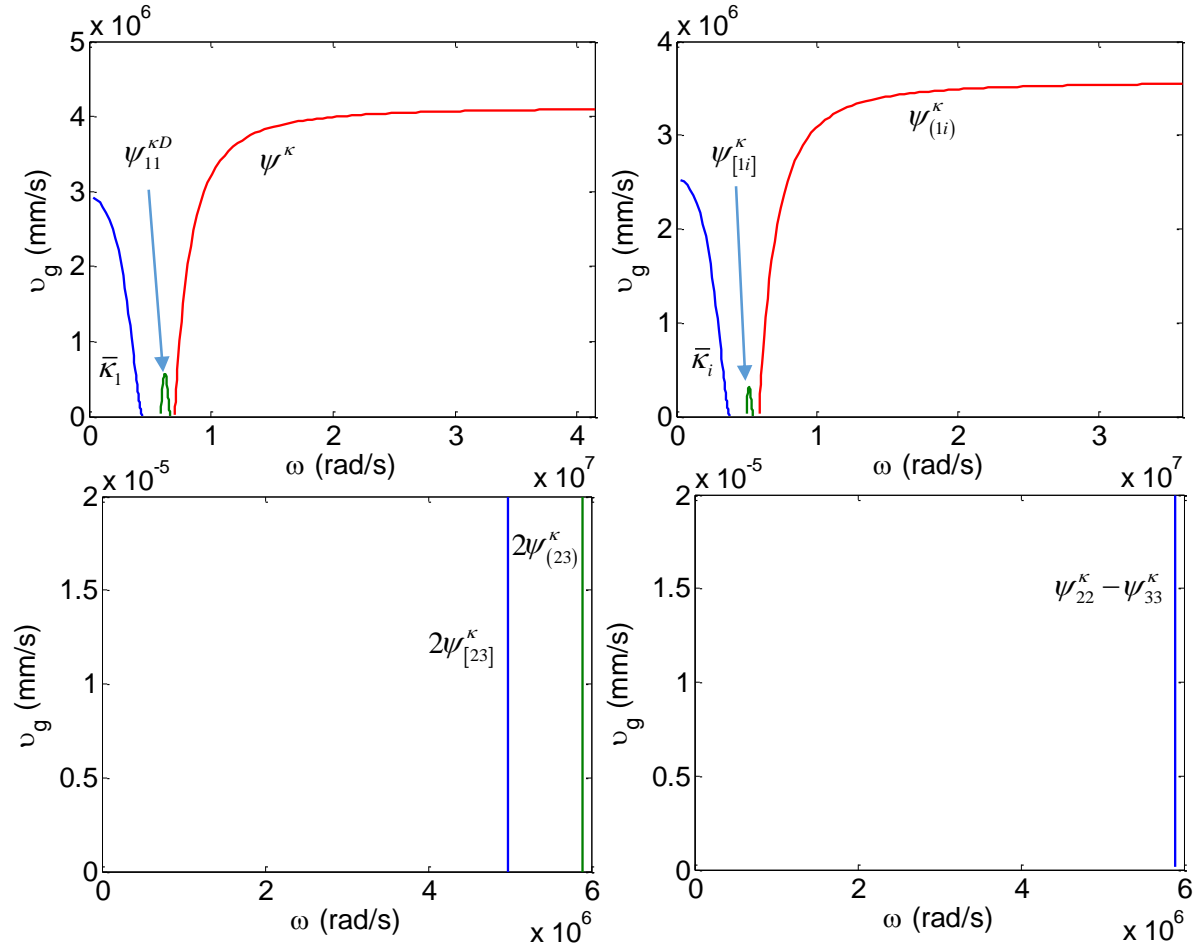


Figure 9.6 Group velocity of different components of spin waves vs their frequency

### 9.6.2 Dispersion behavior of transversely isotropic materials

As it was stated before, in transversely isotropic materials, wave propagation behavior will be a function of the direction of propagation. This section contains dispersion analysis for a transversely isotropic material where  $a_{20} = a_{40} = 2.0$ . Afterwards, a parametric study will be performed to show the effect of microstructural parameters on the dispersion behavior.

For waves propagating in x direction (along the axis of rotational symmetry), the two transverse components of waves will be identical, since they will lie on the symmetry plane. Figure 9.7

presents the dispersion curves, as well as phase velocity and group velocity of different components of the displacement wave propagating in x direction. The figure contains the dispersion graphs and also the velocities for longitudinal, transverse, in-plane shear, and the relative in-plane normal waves.

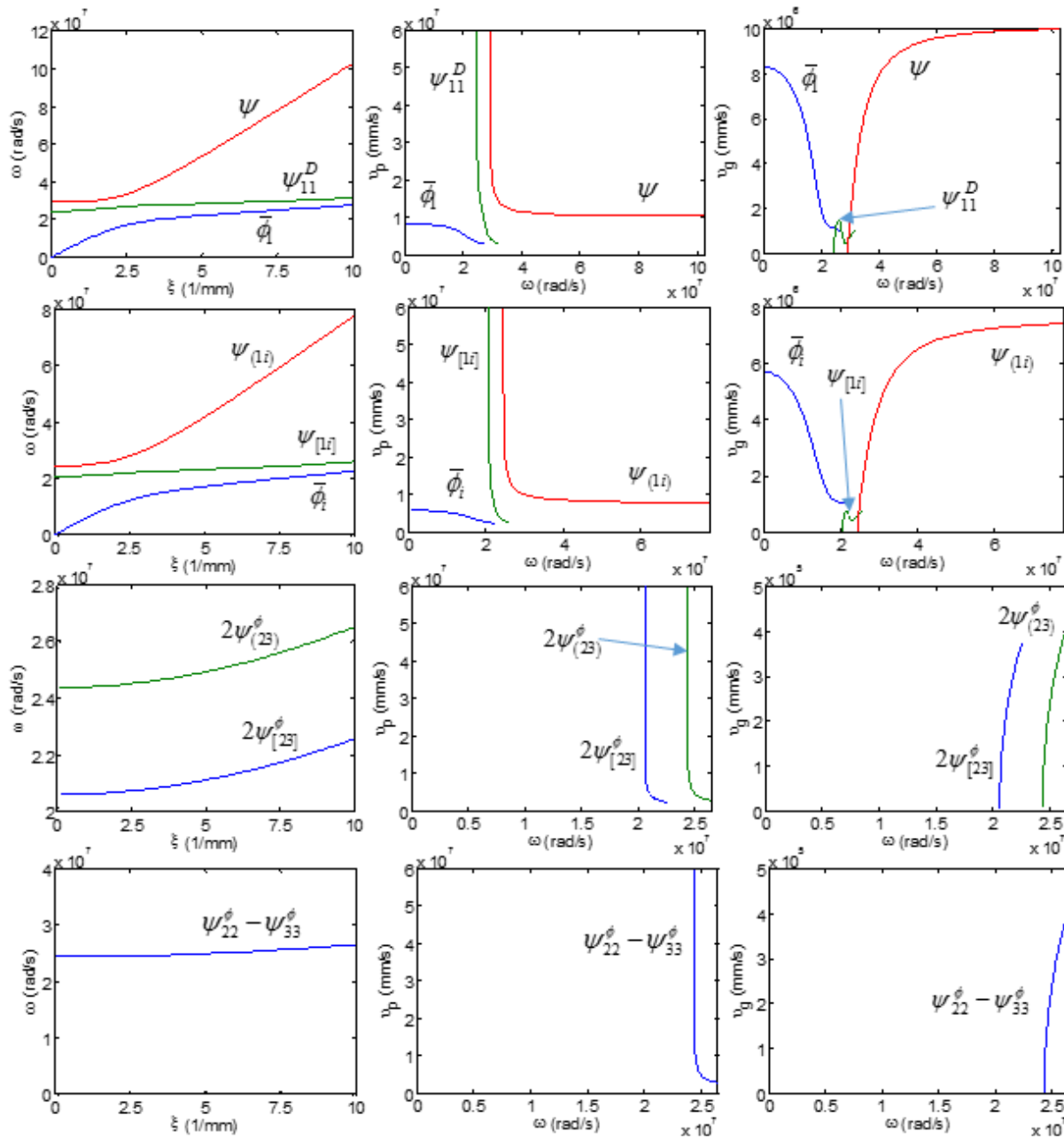


Figure 9.7 Dispersion, phase velocity vs. frequency, and group velocity vs. frequency for displacement waves propagating in x direction in transversely isotropic materials

Note that in Figure 9.7, and in transverse wave components,  $i = 2$  and  $3$ . This is because the material is transversely isotropic and axis 1 is chosen as the axis of rotational symmetry. Thus the behavior of waves in the two directions 2 and 3 will be identical. This is in contrast with propagation of waves in the  $y$  direction, where the two transverse directions, 1 and 3, will be different.

For waves propagating in  $y$  direction in a transversely isotropic material, the two transverse directions will not behave identically. Thus the wave will be decomposed into one set of longitudinal components, two sets of transverse components, one in-plane shear set, and one relative in-plane normal wave component. Figure 9.8 presents the dispersion curves, as well as phase velocity and group velocity of the aforementioned components.

Comparing the results presented in Figure 9.7 and Figure 9.8, it is seen that the dispersion behavior for the in-plane components of waves propagating in the two directions,  $x$  and  $y$ , are identical. Since, as it was stated in section 9.5, the dispersion relationships belonging to these components are not functions of the macro stiffness tensor,  $C_{ijkl}^M$ , which is the tensor that is assumed to be transversely isotropic here. For longitudinal and transverse components, however, the behavior is clearly affected by changing the macro stiffness tensor,  $C_{ijkl}^M$  (See Eq. 9.20 and 9.22 for the parameters affecting dispersion relationships in longitudinal and transverse waves and compare with Eq. 9.24 and 9.27 for the parameters affecting the dispersion relationships belonging to in-plane shear and relative in-plane normal components).

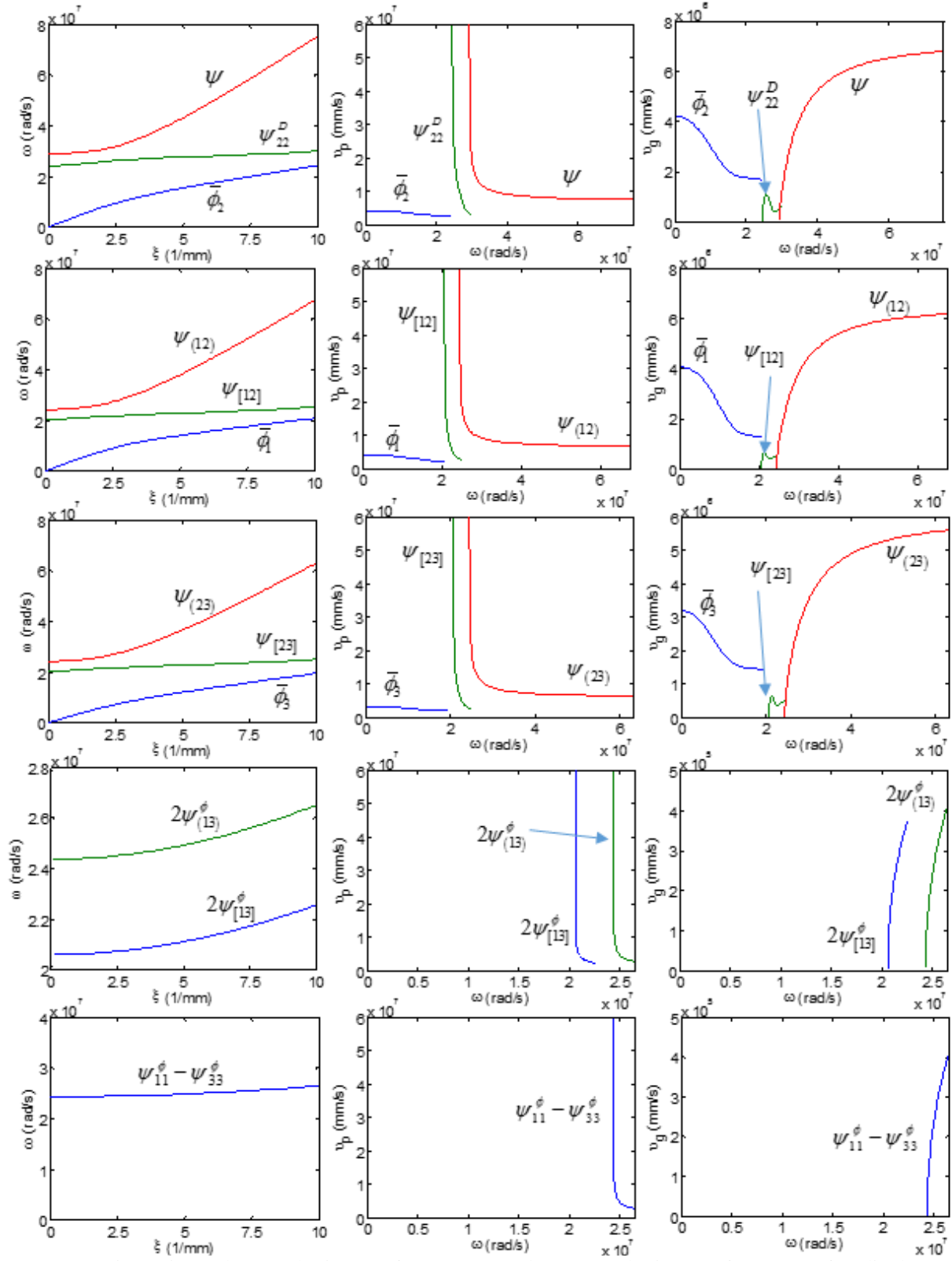


Figure 9.8 Dispersion, phase velocity vs. frequency, and group velocity vs. frequency for displacement waves propagating in y direction in transversely isotropic materials

To study the effect of model parameters on the dispersion behavior of the material in different directions, ratio of phase velocities of longitudinal and transverse components of waves propagating in x and y directions have been calculated by changing  $a_{20}$ . Change of ratios of the phase velocities of the waves propagating in x and y directions for small and large values of wave number has been presented in Figure 9.9.

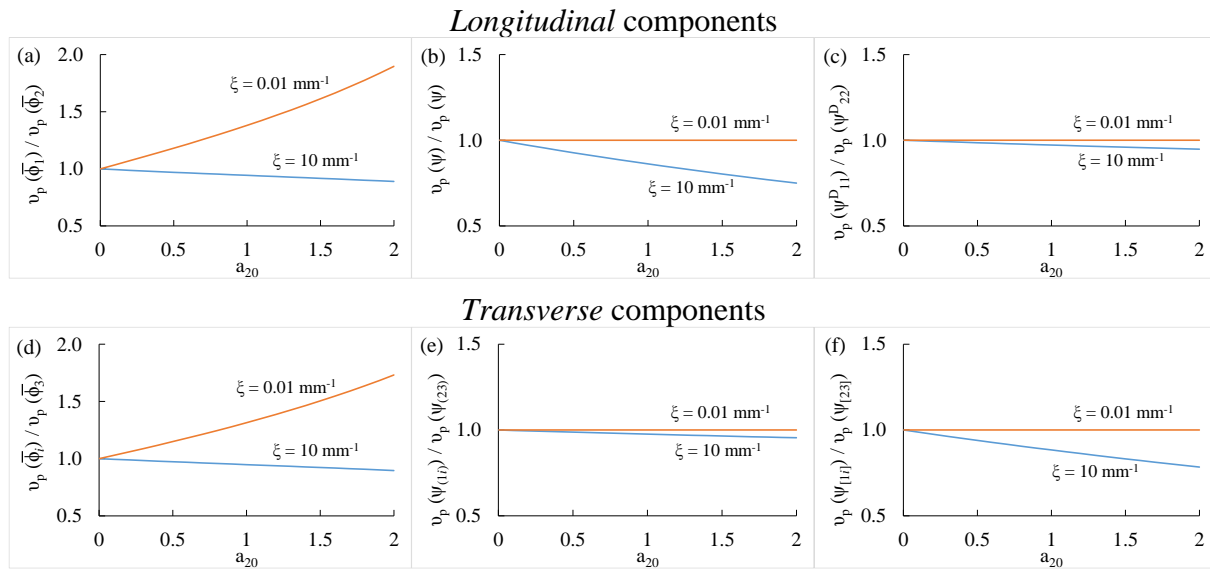


Figure 9.9 Evolution of ratios of phase velocities of different components of longitudinal and transverse components of displacement waves propagating in x and y directions by changing  $a_{20}$

As it was mentioned in Chapter 6, section 6.3.2, for modeling transversely isotropic materials, the model needs the following five independent parameters:  $k_n$ ,  $k_s$ ,  $k_t$ ,  $a_{20}$ , and  $a_{40}$ . In other words, the introduction of two different stiffness coefficients in the two tangential directions, as well as  $a_{20}$  and  $a_{40}$  impose transverse isotropy on the material. In this analysis, however, the focus is on studying the effect of  $a_{20}$  on the dispersion behavior. For this purpose, the two stiffness coefficients in the tangential direction are assumed to be equal and also  $a_{40}$  is assumed to be equal to zero. In this way, the only parameter imposing anisotropy on the material is  $a_{20}$  and its effect is thus studied.



When  $a_{20}$  is zero, the material is in fact still isotropic and the dispersion behavior for waves propagating in the two directions,  $x$  and  $y$ , are identical. On the other hand, by increasing  $a_{20}$ , the material becomes more and more anisotropic and the difference between the dispersion behaviors of the waves propagating in the two directions become increasingly accentuated. However, as it can be seen in Figure 9.9, the effect of increasing  $a_{20}$  is not the same for different components of wave. Figure 9.9a shows the ratio of the two longitudinal components of  $\bar{\phi}_i$ , while Figure 9.9d presents the transverse component belonging to  $\bar{\phi}_i$ . In both these cases, it is seen that in small wave numbers (large wave lengths), change of velocity is much more significant compared to the case when wave lengths are small. This result is expected since large wave lengths correspond to macro behavior of the material.

Further, the wave components corresponding to the total gradient of displacement are also seen to be affected by changing the parameter  $a_{20}$  and hence introducing anisotropy in the material behavior. Figure 9.9b shows the ratio between phase velocities of the volumetric components of waves propagating in  $x$  and  $y$  directions, while Figure 9.9c shows the same ratio for the deviatoric components. Figure 9.9e and 9.9f show the ratio between the symmetric and anti-symmetric parts of the transverse waves propagating in  $x$  and  $y$  directions. It is seen in these figures that these components are affected by changing  $a_{20}$  and imposing anisotropy only when the wave number is very large (small wave lengths). When the wave lengths are large, these components of waves will have a similar behavior in the two directions. Even with  $a_{20} = 2$ , which implies severe anisotropy, the dispersion behavior of these components of waves propagating in the two directions,  $x$  and  $y$ , are very similar.

## 9.7 Summary and conclusions

In this chapter the balance equations for the complete micromorphic continuum theory, presented in Chapter 7, were formulated. These balance equations, including equilibrium equations and the relevant boundary conditions, are the equations that should be used in any type of analysis for micromorphic media. In this chapter, the equations of motion were solved for studying propagation of elastic waves through the material.

Study of wave propagation through materials using usual first gradient elasticity results in the two well-known longitudinal and shear components of wave (P waves and S waves). Studying the material as a micromorphic media shows that other components of wave will also propagate in the material. In the analysis using micromorphic theory, two general groups of waves were studied: displacement waves and spin waves. Each one of these groups are then decomposed into different sets of waves: longitudinal waves, transverse waves, in-plane shear waves, and relative in-plane normal waves.

Dispersion behavior of all the above components have been studied and it is seen that all the components of waves in such media are dispersive (as opposed to the usual P and S waves, in which the relationship between frequency and wave number is linear, resulting in identical phase and group velocities). Phase velocities and group velocities of all these components are also calculated.

For isotropic materials, wave propagation is independent of direction of propagation, while for anisotropic materials, the behavior will depend on the direction of propagation. As an example of an anisotropic material, propagation of waves in transversely isotropic materials is studied. As a first approximation, it is assumed that only the macro stiffness tensor,  $C_{ijkl}^M$ , is transversely isotropic. For such a material, the stiffness tensor is derived in the manner presented in Chapter

6. Equations of motions have been modified for the existence of anisotropy in the material and wave propagation in the two principal directions,  $x$  and  $y$ , have been studied separately.

The results show that the dispersion behavior in the two directions are significantly different. Interestingly, for waves with large wave lengths, the anisotropy seems to affect the behavior of macro displacement components (terms corresponding to average displacement field). While in higher wave numbers (small wave lengths) dispersion behavior of the wave components corresponding to displacement gradient seem to be most affected by the anisotropy. In addition, the effect of changing the microstructural model parameters that impose directional dependence on material properties on the dispersion behavior of the material is studied using a parametric study.

In conclusion, the micromorphic theory presented in Chapter 7, and completed in this Chapter by presenting the pertinent equilibrium equations and boundary conditions, is shown to be able to predict non-classical phenomena which the usual elasticity theories fail to predict. Namely, the dispersion phenomena is captured by using a simple linear set of constitutive equations. Moreover, it is shown before [154] that the method is capable of predicting frequency band-gaps. That is regions in the frequency domain for which no waves with any real wave number can propagate through the material. The ability of the presented micromorphic theory to predict these non-classical phenomena point to the necessity of including terms such as fluctuations in grain movements, second gradients terms, and grain spins in the analysis of continuum media.

## 10 CONCLUDING REMARKS AND FUTURE WORKS

### 10.1 Concluding remarks

The method of granular micromechanics for deriving the constitutive model for granular materials is presented in this dissertation. In this approach, the material point is envisioned as a collection of grains, mutually interacting with their neighbors. Material's continuum response is derived, in this model, as the average of the behavior of all grain-pair interactions. The approach presented here is general and can be used for different types of materials and grain assemblies.

The method's advantages that have been utilized, worked upon, and developed in this study are briefly summarized below.

1. In this method, the macroscopic behavior of the material (typically represented by the two second rank *tensors* of stress and strain, as well as the fourth rank stiffness *tensor*) are calculated using the *scalar* values of normal and tangential components of force, displacement, or stiffness. This, simplifies modeling non-linear plastic behavior of the materials significantly. In particular, the difficulty associated with defining yield surfaces, flow rules, hardening rules, etc. in the three tensorial framework is avoided when working with scalar values and scalar functions that couple them together. The behavior of the material is formulated as scalar functions in a simpler manner.
2. The physical phenomena that can best be described in terms of interactions between grains (e.g. slip, friction, effects of confinement, etc.) can now be addressed in a straightforward

manner and there is no need to find tensorial parameters that might approximately address such issues. By defining the force-displacement relationships in a manner consistent with the physical behavior of grain interactions, as well as the macroscopic behavior of the material, all these physical phenomena will be modeled automatically.

3. During a loading process on a non-linear material, grain-pair interactions in different directions will undergo different loading histories. Many different scenarios and loading combinations can take place in different directions. Grain-pair interactions in different directions can undergo loading, unloading, reloading, hardening, softening, etc. Thus the overall behavior of the material will be completely load-path dependent. During loading, even simple monotonic loadings, the properties of grain-pair interactions in different directions will change and the induced anisotropy effect, due to the change of properties in different directions will be modeled automatically. As a result, the material behavior will be highly load-path dependent and material's response will be, at any point during the loading, a function of the loading history. This best manifests itself when studying the failure behavior of the material. As it is shown here, defining failure as a function of the current stress state will not be able to sufficiently failure of the material. Studying the behavior in different directions enables the model to incorporate the loading history in all different directions separately and to define failure as a function of the loading history.
4. Since the macroscopic response of the material is derived by averaging the grain-pair interactions in all different directions, the model is naturally strong for modeling inherently anisotropic materials. For this purpose, a directional density distribution function is introduced in the formulation that defines the directional distribution of number, length, and stiffness of grain-pair interactions in different directions. The density distribution

function is defined in a manner that is consistent with the elastic symmetries that lead to the different levels of isotropy in the material. As a result, materials with all different levels of inherent anisotropy can be modeled.

5. In this model, the macroscopic kinematic measures are interpreted in the sense of relative movements of grains. This allows for a better interpretation of additional kinematic measures that are needed for deriving enhanced continuum theories, such as micromorphic continuum theory. Additional kinematic measures such as relative deformation, second gradient of displacement, and rotation gradient tensors can be linked to the displacements and spins of grains in a meaningful manner. Utilizing this link between the kinematics of grains and the macro-scale kinematic measures, paves the way for establishing a practical approach for calibrating the micromorphic material parameters.

In summary, a robust, yet computationally efficient approach has been presented for modeling granular materials. This approach incorporates material's microstructure and its corresponding micromechanical properties into its macroscopic behavior in a statistical manner. Using this method, we bridge between traditional continuum mechanics-in which the effect of microstructure and its evolution during loading on continuum behavior is either neglected or taken into account using approximations- and atomistic calculations-in which the exact microstructure of the material might be used to derive material's exact behavior but with a huge amount of computational demand, making it inapplicable to macro scale problems.

## **10.2 Future works**

Following recommendations are made for future works on this topic.

- *Implementation of the damage-plasticity model into Finite Element Method schemes:* The non-linear constitutive approach for modeling cementitious materials presented here is fully calibrated and verified for the behavior of a material point. The next step in the verification and application of the material model would be its implementation into FE software. This will allow the model to be used for modeling different boundary value problems in structural level.
- *Implementation of rate-dependent terms for modeling viscos materials:* The model can be significantly enhanced by incorporation of viscos terms in the constitutive model from grain-scale viewpoint. This enables the method to model rate-dependent materials such as asphalt mixtures. In addition, this will help the method significantly in stabilizing the model results especially in post-peak softening region.
- *Modeling large-deformation problems:* The present work utilizes the infinitesimal strain theory for calculation of kinematic measures and consequently the conjugate stress measures. However, in order to generalize the model, the kinematic analysis of grain movements (displacements and rotations) can be enhanced to include finite deformations.
- *Modeling multi-phase (composite) materials:* The method can also be developed for modeling composite materials. For this purpose, a unified approach, which is based on the micromechanics of the behavior of materials is needed. In this approach, different phases of these materials and their interface should be modeled separately. These should then be integrated together to yield the behavior of the resulting composite material.

## Appendix A

Transversely isotropic materials have a single axis of rotational symmetry and moreover, every plane containing this axis is a plane of reflection symmetry [156]. The plane whose normal axis is the axis of rotational symmetry can be called the plane of rotational symmetry and the properties of the material in all directions in that plane are identical. If an initially isotropic non-linear material is under uniaxial loading (or conventional triaxial loading) in the  $I$  direction, it develops an axisymmetric behavior resembling that of a transversely isotropic material. In this situation, axis  $I$  will be the axis of rotational symmetry and the 23 plane (the plane in which the two lateral strains are applied) is the plane of rotational symmetry. The constitutive equation for such material can be written as follows [43].

$$\begin{pmatrix} \sigma_{11} \\ \sigma_{22} \\ \sigma_{33} \\ \sigma_{23} \\ \sigma_{13} \\ \sigma_{12} \end{pmatrix} = \begin{pmatrix} c_{11} & c_{12} & c_{12} & 0 & 0 & 0 \\ & c_{22} & c_{23} & 0 & 0 & 0 \\ & & c_{22} & 0 & 0 & 0 \\ & & & \frac{c_{22} - c_{23}}{2} & 0 & 0 \\ & \text{Symm.} & & & c_{55} & 0 \\ & & & & & c_{55} \end{pmatrix} \begin{pmatrix} \varepsilon_{11} \\ \varepsilon_{22} \\ \varepsilon_{33} \\ \gamma_{23} \\ \gamma_{13} \\ \gamma_{12} \end{pmatrix} \quad (\text{A.1})$$

As it is seen in Eq. A.1, the stiffness tensor of a transversely isotropic tensor is composed of 5 independent components. In order to study the failure mode of the material, it is worthwhile to calculate the eigenvalues and eigenvectors of the stiffness tensor. The stiffness tensor is written here as a 6×6 matrix and thus has 6 eigenvalues. However, for the case of transversely isotropic materials, only 4 independent eigenvalues exist. The closed-form solution of these eigenvalues are as follows



$$\begin{aligned}
\lambda_1 &= \frac{1}{2} \left( c_{11} + c_{22} + c_{23} + \sqrt{c_{11}^2 - 2c_{11}c_{22} - 2c_{11}c_{23} + c_{22}^2 + 2c_{22}c_{23} + c_{23}^2 + 8c_{12}^2} \right) \\
\lambda_2 &= \frac{1}{2} \left( c_{11} + c_{22} + c_{23} - \sqrt{c_{11}^2 - 2c_{11}c_{22} - 2c_{11}c_{23} + c_{22}^2 + 2c_{22}c_{23} + c_{23}^2 + 8c_{12}^2} \right) \\
\lambda_3 &= c_{22} - c_{23} \\
\lambda_4 &= c_{55}
\end{aligned} \tag{A.2}$$

As stated before, the two remaining eigenvalues are not independent from the ones that are presented here. The fifth eigenvalue is equal to  $\lambda_4$  and the sixth one is equal to  $\lambda_3/2$ . Study of the eigenvectors corresponding to these eigenvalues demonstrate the deformation mode associated with each one of them. The eigenvectors corresponding to each one of the above eigenvalues are given below

$$v_{(\lambda_1)} = \begin{pmatrix} \frac{2c_{12}}{\lambda_1 - c_{11}} \\ \lambda_1 - c_{11} \\ 1 \\ 1 \\ 0 \\ 0 \\ 0 \end{pmatrix}, \quad v_{(\lambda_2)} = \begin{pmatrix} \frac{2c_{12}}{\lambda_2 - c_{11}} \\ \lambda_2 - c_{11} \\ 1 \\ 1 \\ 0 \\ 0 \\ 0 \end{pmatrix}, \quad v_{(\lambda_3)} = \begin{pmatrix} 0 \\ -1 \\ 1 \\ 0 \\ 0 \\ 0 \end{pmatrix}, \quad v_{(\lambda_4)} = \begin{pmatrix} 0 \\ 0 \\ 0 \\ 0 \\ 1 \\ 0 \end{pmatrix} \text{ and } \begin{pmatrix} 0 \\ 0 \\ 0 \\ 0 \\ 0 \\ 1 \end{pmatrix} \tag{A.3}$$

Note that the above eigenvectors are not necessarily normalized. The deformation mode is inferred directly from the eigenvector corresponding to the eigenvalue. For  $\lambda_1$  and  $\lambda_2$ , the eigenvector clearly belongs to the normal directions, and thus the deformation mode is clearly dilatational. For  $\lambda_3$ , the eigenvector shows a deviatoric component between the 2 and 3 directions, and thus corresponds to the deviatoric mode. As it was stated before, two of the eigenvalues of the stiffness matrix are equal to  $\lambda_4$  and the eigenvectors corresponding to both of them belong to the (isochoric) shear mode of deformation. The eigenvalue corresponding to the last eigenvalue (which is equal to  $\lambda_3/2$ ) is equal to  $\langle 0, 0, 0, 1, 0, 0 \rangle$  and thus belongs to the isochoric (shear) mode of deformation.

## LIST OF REFERENCES

1. Cosserat, E. and F. Cosserat, *Theory of Deformable Bodies*, ed. T.b.D.H. Delphenich. 1909, Paris: SCIENTIFIC LIBRARY A. HERMANN AND SONS.
2. Mindlin, R.D., *Micro-Structure in Linear Elasticity*. Archive for Rational Mechanics and Analysis, 1964. **16**(1): p. 51-78.
3. Toupin, R.A., *Theories of Elasticity with Couple-Stress*. Archive for Rational Mechanics and Analysis, 1964. **17**(2): p. 85-112.
4. Eringen, A.C., *Microcontinuum field theories: foundations and solids*. Vol. 487. 1999: Springer New York.
5. Green, A.E. and R.S. Rivlin, *Multipolar Continuum Mechanics*. Archive for Rational Mechanics and Analysis, 1964. **17**(2): p. 113-147.
6. Germain, P., *Method of Virtual Power in Continuum Mechanics .2. Microstructure*. Siam Journal on Applied Mathematics, 1973. **25**(3): p. 556-575.
7. Navier, C.L., *Sur les lois de l'équilibre et du mouvement des corps solides élastiques*. Memoire de l'Academie Royale de Sciences, 1827. **7**: p. 375-393.
8. Cauchy, A.-L., *Sur l'équilibre et le mouvement d'un système de points matériels sollicités par des forces d'attraction ou de répulsion mutuelle*. Exercices de Mathématiques, 1826-1830. **3**: p. 188-212.
9. dell'Isola, F., U. Andreaus, and L. Placidi, *At the origins and in the vanguard of peridynamics, non-local and higher gradient continuum mechanics. An underestimated and still topical contribution of Gabrio Piola*. Mechanics and Mathematics of Solids 2013.
10. Auffray, N., et al., *Analytical continuum mechanics a la Hamilton-Piola least action principle for second gradient continua and capillary fluids*. Mathematics and Mechanics of Solids, 2013. **20**(4): p. 375-417.
11. Dharmawardhana, C., A. Misra, and W.-Y. Ching, *Quantum Mechanical Metric for Internal Cohesion in Cement Crystals*. Scientific reports, 2014. **4**: p. 7332.
12. Misra, A. and W.Y. Ching, *Theoretical nonlinear response of complex single crystal under multi-axial tensile loading*. Sci. Rep., 2013. **3**.
13. Qomi, M.A., et al., *Combinatorial molecular optimization of cement hydrates*. Nature communications, 2014. **5**.
14. Hentz, S., L. Daudeville, and F.V. Donzé, *Identification and validation of a discrete element model for concrete*. Journal of engineering mechanics, 2004. **130**(6): p. 709-719.
15. HEUZÉ, F.E., O.R. WALTON, and D.M. MADDIX, *Analysis of Explosions in Hard Rocks: The Power of Discrete Element*. Analysis and Design Methods: Comprehensive Rock Engineering: Principles, Practice and Projects, 2014: p. 387.
16. Tavaréz, F.A. and M.E. Plesha, *Discrete element method for modelling solid and particulate materials*. International Journal for Numerical Methods in Engineering, 2007. **70**(4): p. 379-404.
17. Walton, O.R., *Explicit particle-dynamics model for granular materials*, 1982, Lawrence Livermore National Lab., CA (USA).
18. Chang, C.S. and A. Misra, *Packing Structure and Mechanical-Properties of Granulates*. Journal of Engineering Mechanics-Asce, 1990. **116**(5): p. 1077-1093.
19. Misra, A. and C.S. Chang, *Effective elastic moduli of heterogeneous granular solids*. International Journal of Solids and Structures 1993. **30**(18): p. 2547-2566.

20. Misra, A. and Y. Yang, *Micromechanical model for cohesive materials based upon pseudo-granular structure*. International Journal of Solids and Structures, 2010. **47**(21): p. 2970-2981.
21. Misra, A. and V. Singh, *Nonlinear granular micromechanics model for multi-axial rate-dependent behavior*. International Journal of Solids and Structures, 2014. **51**(13): p. 2272-2282.
22. Misra, A. and V. Singh, *Thermomechanics based nonlinear rate-dependent coupled damage-plasticity granular micromechanics model* Continuum Mechanics and Thermodynamics, 2014.
23. Chang, C.S. and A. Misra, *Theoretical and Experimental-Study of Regular Packings of Granules*. Journal of Engineering Mechanics-Asce, 1989. **115**(4): p. 704-720.
24. Digby, P.J., *The Effective Elastic Moduli of Porous Granular Rocks*. Journal Applied Mechanics, 1981. **48**: p. 803-808.
25. Walton, K., *The Effective Elastic Moduli of a Random Packing of Spheres*. J. Mech.Phys.Solids, 1987. **35**: p. 213-226.
26. Deresiewicz, H., *Stress-Strain Relations for a Simple Model of a Granular Medium*. Journal of Applied Mechanics, 1958. **25**: p. 402-406.
27. Duffy, J. and R.D. Mindlin, *Stress-Strain Relations of a Granular Medium*. Journal of Applied Mechanics, 1957. **24**(4): p. 585-593.
28. Chang, C.S. and P.Y. Hicher, *An elasto-plastic model for granular materials with microstructural consideration*. International Journal of Solids and Structures, 2005. **42**(14): p. 4258-4277.
29. Misra, A. and P. Poorsolhjoui, *Micro-macro scale instability in 2D regular granular assemblies*. Continuum Mechanics and Thermodynamics, 2013. **27**(1-2): p. 63-82.
30. Chang, C.S., Z.Y. Yin, and P.Y. Hicher, *Micromechanical Analysis for Interparticle and Assembly Instability of Sand*. Journal of Engineering Mechanics-Asce, 2011. **137**(3): p. 155-168.
31. Chang, C.S. and J. Gao, *2nd-Gradient Constitutive Theory for Granular Material with Random Packing Structure*. International Journal of Solids and Structures, 1995. **32**(16): p. 2279-2293.
32. Suiker, A.S.J., R. de Borst, and C.S. Chang, *Micro-mechanical modelling of granular material. Part I: Derivation of a second-gradient micro-polar constitutive theory*. Acta Mechanica, 2001. **149**(1-4): p. 161-180.
33. Yang, Y. and A. Misra, *Micromechanics based second gradient continuum theory for shear band modeling in cohesive granular materials following damage elasticity*. International Journal of Solids and Structures, 2012. **49**(18): p. 2500-2514.
34. Arzt, E., *Size effects in materials due to microstructural and dimensional constraints: a comparative review*. Acta materialia, 1998. **46**(16): p. 5611-5626.
35. Turquato, S., *Random Heterogeneous Materials: Microstructure and Microscopic Properties*. 2002, New York: Springer-Verlag.
36. Greene, M.S., et al., *The archetype-genome exemplar in molecular dynamics and continuum mechanics*. Computational Mechanics, 2013. **53**(4): p. 687-737.
37. Solar, M., et al., *Mechanical behavior of linear amorphous polymers: Comparison between molecular dynamics and finite-element simulations*. Physical Review E, 2012. **85**(2): p. 1-14.

38. Silling, S.A., et al., *Peridynamic states and constitutive modeling*. Journal of Elasticity, 2007. **88**(2): p. 151-184.
39. Tadmor, E.B. and R.E. Miller, *Modeling materials: continuum, atomistic and multiscale techniques*. 2011: Cambridge University Press.
40. Bazant, Z.P. and P.C. Prat, *Microplane Model for Brittle-Plastic Material .1. Theory*. Journal of Engineering Mechanics-Asce, 1988. **114**(10): p. 1672-1687.
41. Gao, H.J. and P. Klein, *Numerical simulation of crack growth in an isotropic solid with randomized internal cohesive bonds*. Journal of the Mechanics and Physics of Solids, 1998. **46**(2): p. 187-218.
42. Misra, A. and V. Singh, *Micromechanical model for viscoelastic materials undergoing damage*. Continuum Mechanics and Thermodynamics, 2013. **25**(2-4): p. 343-358.
43. Misra, A. and P. Poorsolhjouy, *Granular micromechanics model of anisotropic elasticity derived from Gibbs potential*. Acta Mechanica, 2016. **227**(5): p. 1393-1413.
44. Weiner, J.H., *Statistical mechanics of elasticity*. 2012: Courier Corporation.
45. Chang, C.S. and C.L. Liao, *Estimates of Elastic Modulus for Media of Randomly Packed Granules* Applied Mechanics Review, 1994. **47**(1): p. 197-206.
46. Kanatani, K.I., *Distribution of Directional-Data and Fabric Tensors*. International Journal of Engineering Science, 1984. **22**(2): p. 149-164.
47. Misra, A. and H. Jiang, *Measured kinematic fields in the biaxial shear of granular materials*. Computers and Geotechnics, 1997. **20**(3-4): p. 267-285.
48. Johnson, K.L., *Contact mechanics*. 1985, Cambridge, U.K.: Cambridge University Press. 452 p.
49. Mindlin, R.D. and H. Deresiewicz, *Elastic Spheres in Contact under Varying Oblique Forces*. Journal of Applied Mechanics-Transactions of the Asme, 1953. **20**(3): p. 327-344.
50. Feenstra, P.H. and R. De Borst, *A composite plasticity model for concrete*. International Journal of Solids and Structures, 1996. **33**(5): p. 707-730.
51. Vermeer, P.A. and R. De Borst, *Non-associated plasticity for soils, concrete and rock*. HERON, 29 (3), 1984, 1984.
52. Ziegler, H., *An Introduction to thermomechanics* Second ed. 1983: North-Holland, Amsterdam.
53. Maugin, G.A., *The thermomechanics of plasticity and fracture*. Vol. 7. 1992: Cambridge University Press.
54. Bazant, Z.P., et al., *Microplane model for concrete .2. Data delocalization and verification*. Journal of Engineering Mechanics-Asce, 1996. **122**(3): p. 255-262.
55. Van Mier, J.G., *Fracture processes of concrete*. Vol. 12. 1996: CRC press.
56. Misra, A. and P. Poorsolhjouy, *Granular micromechanics model for damage and plasticity of cementitious materials based upon thermomechanics*. Mathematics and Mechanics of Solids, 2015: p. 1081286515576821.
57. Puzrin, A.M. and C. Rabaiotti, *A thermomechanical framework for non-linear hyperviscoelastic materials*. Journal of Rheology, 2010. **54**(3): p. 619-642.
58. dell'Isola, F., P. Seppecher, and A. Madeo, *How contact interactions may depend on the shape of Cauchy cuts in Nth gradient continua: approach "à la D'Alembert"*. Zeitschrift für angewandte Mathematik und Physik, 2012. **63**(6): p. 1119-1141.
59. Seppecher, P., *Second-gradient theory: application to Cahn-Hilliard fluids*, in *Continuum Thermomechanics*. 2002, Springer. p. 379-388.

60. Placidi, L., *A variational approach for a nonlinear 1-dimensional second gradient continuum damage model*. Continuum Mechanics and Thermodynamics, 2014: p. 1-16.
61. Houlsby, G.T. and A.M. Puzrin, *Principles of hyperplasticity: an approach to plasticity theory based on thermodynamic principles*. 2006: Springer.
62. Abu Al-Rub, R.K. and G.Z. Voyiadjis, *On the coupling of anisotropic damage and plasticity models for ductile materials*. International Journal of Solids and Structures, 2003. **40**(11): p. 2611-2643.
63. Einav, I., G.T. Houlsby, and G.D. Nguyen, *Coupled damage and plasticity models derived from energy and dissipation potentials*. International Journal of Solids and Structures, 2007. **44**(7-8): p. 2487-2508.
64. Marotti de Sciarra, F., *Hardening plasticity with nonlocal strain damage*. International Journal of Plasticity, 2012. **34**: p. 114-138.
65. Voyiadjis, G.Z., R.K. Abu Al-Rub, and A.N. Palazotto, *Thermodynamic framework for coupling of non-local viscoplasticity and non-local anisotropic viscodamage for dynamic localization problems using gradient theory*. International Journal of Plasticity, 2004. **20**(6): p. 981-1038.
66. Carcaterra, A., *Ensemble energy average and energy flow relationships for nonstationary vibrating systems*. Journal of Sound and Vibration, 2005. **288**(3): p. 751-790.
67. Carcaterra, A. and A. Akay, *Theoretical foundations of apparent-damping phenomena and nearly irreversible energy exchange in linear conservative systems*. Journal of the Acoustical Society of America, 2007. **121**(4): p. 1971-1982.
68. Culla, A., A. Sestieri, and A. Carcaterra, *Energy flow uncertainties in vibrating systems: Definition of a statistical confidence factor*. Mechanical Systems and Signal Processing, 2003. **17**(3): p. 635-663.
69. Rinaldi, A., et al., *Lattice models of polycrystalline micro structures: A quantitative approach*. Mechanics of Materials, 2008. **40**(1-2): p. 17-36.
70. Rinaldi, A. and Y.C. Lai, *Statistical damage theory of 2D lattices: Energetics and physical foundations of damage parameter*. International Journal of Plasticity, 2007. **23**(10-11): p. 1796-1825.
71. Rinaldi, A., *Bottom-up modeling of damage in heterogeneous quasi-brittle solids*. Continuum Mechanics and Thermodynamics, 2013. **25**(2-4): p. 359-373.
72. Chang, C.S., A. Misra, and K. Acheampong, *Elastoplastic Deformation for Particulates with Frictional Contacts*. Journal of Engineering Mechanics-Asce, 1992. **118**(8): p. 1692-1707.
73. Magoaric, H., A. Danescu, and B. Cambou, *Nonlocal Orientational Distribution of Contact Forces in Granular Samples Containing Elongated Particles*. Acta Geotechnica, 2008. **3**: p. 49-60.
74. Clausius, R., *XVI. On a mechanical theorem applicable to heat*. The London, Edinburgh, and Dublin Philosophical Magazine and Journal of Science, 1870. **40**(265): p. 122-127.
75. Swenson, R.J., *Comments on Virial Theorems for Bounded Systems*. American Journal of Physics, 1983. **51**(10): p. 940-942.
76. Irving, J.H. and J.G. Kirkwood, *The Statistical Mechanical Theory of Transport Processes .4. The Equations of Hydrodynamics*. Journal of Chemical Physics, 1950. **18**(6): p. 817-829.
77. Tsai, D.H., *Virial Theorem and Stress Calculation in Molecular-Dynamics*. Journal of Chemical Physics, 1979. **70**(3): p. 1375-1382.

78. Subramaniyan, A.K. and C.T. Sun, *Continuum interpretation of virial stress in molecular simulations*. International Journal of Solids and Structures, 2008. **45**(14-15): p. 4340-4346.
79. Zhou, M., *A new look at the atomic level virial stress: on continuum-molecular system equivalence*. Proceedings of the Royal Society a-Mathematical Physical and Engineering Sciences, 2003. **459**(2037): p. 2347-2392.
80. Contrafatto, L. and A. Cuomo, *A globally convergent numerical algorithm for damaging elasto-plasticity based on the multiplier method*. International Journal for Numerical Methods in Engineering, 2005. **63**(8): p. 1089-1125.
81. Bažant, Z.P. and L. Cedolin, *Stability of structures: elastic, inelastic, fracture and damage theories*. 2010: World Scientific.
82. Hill, R., *A general theory of uniqueness and stability in elastic-plastic solids*. Journal of the Mechanics and Physics of Solids, 1958. **6**(3): p. 236-249.
83. Rudnicki, J.W. and J. Rice, *Conditions for the localization of deformation in pressure-sensitive dilatant materials*. Journal of the Mechanics and Physics of Solids, 1975. **23**(6): p. 371-394.
84. Sulem, J. and I. Vardoulakis, *Bifurcation analysis in geomechanics*. 1995: Taylor & Francis.
85. Mehrabadi, M.M. and S.C. Cowin, *Eigensensors of Linear Anisotropic Elastic-Materials*. Quarterly Journal of Mechanics and Applied Mathematics, 1990. **43**: p. 15-41.
86. Lu, X., *Uniaxial and triaxial behavior of high strength concrete with and without steel fibers*, 2005, New Jersey Institute of Technology, Department of Civil and Environmental Engineering.
87. Biarez, J. and P.Y. Hicher, *Mechanisms of soil deformation*, in *Constitutive modeling of soils and rocks*, P.-Y. Hicher and J.-F. Shao, Editors. 2008, Wiley: Hoboken, NJ. p. 31-76.
88. Han, J., *Experimental study on the mechanical behavior of a stiff clay subjected to monotonic and cyclic loading*, 2014, Ecole Centrale de Nantes.
89. Chaboche, J.L., *A review of some plasticity and viscoplasticity constitutive theories*. International Journal of Plasticity, 2008. **24**(10): p. 1642-1693.
90. Horstemeyer, M.F. and D.J. Bammann, *Historical review of internal state variable theory for inelasticity*. International Journal of Plasticity, 2010. **26**(9): p. 1310-1334.
91. Contrafatto, L. and M. Cuomo, *A new thermodynamically consistent continuum model for hardening plasticity coupled with damage*. International Journal of Solids and Structures, 2002. **39**(25): p. 6241-6271.
92. Contrafatto, L. and M. Cuomo, *A framework of elastic-plastic damaging model for concrete under multiaxial stress states*. International Journal of Plasticity, 2006. **22**(12): p. 2272-2300.
93. Challamel, N., C. Lanos, and C. Casandjian, *Creep damage modelling for quasi-brittle materials*. European Journal of Mechanics a-Solids, 2005. **24**(4): p. 593-613.
94. Challamel, N., C. Lanos, and C. Casandjian, *Strain-based anisotropic damage modelling and unilateral effects*. International Journal of Mechanical Sciences, 2005. **47**(3): p. 459-473.
95. Altenbach, H. and V. Eremeyev, *Strain rate tensors and constitutive equations of inelastic micropolar materials*. International Journal of Plasticity, 2014. **63**: p. 3-17.
96. Poursolhjouy, P. and A. Misra, *Effect of Intermediate Principal Stress and Loading-Path on Failure of Cementitious Materials Using Granular Micromechanics*. International Journal of Solids and Structures, Under Review.

97. Wong, T.-f. and P. Baud, *The brittle-ductile transition in porous rock: A review*. Journal of Structural Geology, 2012. **44**: p. 25-53.
98. Yu, M.H., *Advances in Strength Theories for Materials Under Complex Stress State in The 20th Century*. Appl. Mech. Rev 2002. **55**(3): p. 169-218.
99. Nova, R., *Controllability of the incremental response of soil specimens subjected to arbitrary loading programmes*. Journal of the Mechanical behavior of Materials, 1994. **5**(2): p. 193-202.
100. Nova, R., *The failure concept in soil mechanics revisited*. Bifurcations and instabilities in geomechanics, 2003: p. 3-16.
101. Gosse, J.H. and S. Christensen, *Strain invariant failure criteria for polymers in composite materials*. AIAA, 2001. **1184**: p. 11.
102. Mariotto, E., *Traite du mouvement des eaux,(posthumously), de la Hire M ed*. English transl by Desvaguliers JT, London (1718). **249**.
103. de Saint-Venant, B. *Mémoire sur l'établissement des équations différent des mouvements intérieurs opérés dans les corps solides ductiles au delà des limites où l'élasticité pourrait les ramener à leur premier état*. C. in *Comptes rendus hebdomadaires des Séances de l'Académie des Sciences*,.
104. Willam, K., *Constitutive models for engineering materials*. Encyclopedia of physical science and technology, 2000. **3**: p. 603-633.
105. Baldi, G., D.W. Hight, and G.E. Thomas, *State-of-the-art paper: a reevaluation of conventional triaxial test methods*, in *Advanced triaxial testing of soil and rock*. 1988, ASTM International.
106. Jardine, R., M. Symes, and J. Burland, *Measurement of soil stiffness in the triaxial apparatus*. Géotechnique, 1984. **34**(3): p. 323-340.
107. Mogi, K., *Effect of the intermediate principal stress on rock failure*. Journal of Geophysical Research, 1967. **72**(20): p. 5117-5131.
108. Mogi, K., *Fracture and flow of rocks under high triaxial compression*. Journal of Geophysical Research, 1971. **76**(5): p. 1255-1269.
109. Mogi, K., *Experimental rock mechanics*. Vol. 3. 2007: CRC Press.
110. Kwasniewski, M., X. Li, and M. Takahashi, *True triaxial testing of rocks*. Vol. 4. 2012: CRC Press.
111. Haimson, B. and C. Chang, *A new true triaxial cell for testing mechanical properties of rock, and its use to determine rock strength and deformability of Westerly granite*. International Journal of Rock Mechanics and Mining Sciences, 2000. **37**(1): p. 285-296.
112. Haimson, B. and J.W. Rudnicki, *The effect of the intermediate principal stress on fault formation and fault angle in siltstone*. Journal of Structural Geology, 2010. **32**(11): p. 1701-1711.
113. Haimson, B.C. and C. Chang, *True triaxial strength of the KTB amphibolite under borehole wall conditions and its use to estimate the maximum horizontal in situ stress*. Journal of Geophysical Research: Solid Earth, 2002. **107**(B10).
114. Calvetti, F., G. Combe, and J. Lanier, *Experimental micromechanical analysis of a 2D granular material: relation between structure evolution and loading path*. Mechanics of Cohesive-frictional Materials, 1997. **2**(2): p. 121-163.
115. Korkolis, Y.P. and S. Kyriakides, *Path-dependent failure of inflated aluminum tubes*. International Journal of Plasticity, 2009. **25**(11): p. 2059-2080.

116. Xu, M., E. Song, and J. Chen, *A large triaxial investigation of the stress-path-dependent behavior of compacted rockfill*. *Acta Geotechnica*, 2012. **7**(3): p. 167-175.
117. Lode, W., *Versuche über den Einfluß der mittleren Hauptspannung auf das Fließen der Metalle Eisen, Kupfer und Nickel*. *Zeitschrift für Physik*, 1926. **36**(11-12): p. 913-939.
118. Bishop, A.W., *The strength of soils as engineering materials*. *Geotechnique*, 1966(16): p. 91-130.
119. Chen, W.-F., *Plasticity in reinforced concrete*. 2007: J. Ross Publishing.
120. Lade, P.V. and J.M. Duncan, *Cubical triaxial tests on cohesionless soil*. *Journal of Geotechnical and Geoenvironmental Engineering*, 1975. **101**(ASCE# 11269 Proceeding).
121. Yamada, Y. and K. Ishihara, *Undrained deformation characteristics of sand in multi-directional shear*. *Soils and Foundations*, 1983. **23**(1): p. 61-79.
122. Perić, D. and M.A. Ayari, *On the analytical solutions for the three-invariant Cam clay model*. *International Journal of Plasticity*, 2002. **18**(8): p. 1061-1082.
123. Yang, Z. and A. Elgamal, *Multi-surface cyclic plasticity sand model with Lode angle effect*. *Geotechnical and Geological Engineering*, 2008. **26**(3): p. 335-348.
124. Matsuoka, H., T. Hoshikawa, and K. Ueno, *A general failure criterion and stress-strain relation for granular materials to metals*. *Soils and Foundations*, 1990. **30**(2): p. 119-127.
125. Arramon, Y.P., et al., *A multidimensional anisotropic strength criterion based on Kelvin modes*. *International Journal of Solids and Structures*, 2000. **37**(21): p. 2915-2935.
126. Desmorat, R. and R. Marull, *Non-quadratic Kelvin modes based plasticity criteria for anisotropic materials*. *International Journal of Plasticity*, 2011. **27**(3): p. 328-351.
127. Nasser, M., K. Rao, and T. Ramamurthy, *Failure mechanism in schistose rocks*. *International Journal of Rock Mechanics and Mining Sciences*, 1997. **34**(3): p. 219. e1-219. e15.
128. Wong, T.-f., H. Szeto, and J. Zhang, *Effect of loading path and porosity on the failure mode of porous rocks*. *Applied Mechanics Reviews*, 1992. **45**(8): p. 281-293.
129. Evans, B., J.T. Fredrich, and T. Wong, *The brittle-ductile transition in rocks: Recent experimental and theoretical progress*. *The Brittle-Ductile Transition in Rocks*, *Geophys. Monogr. Ser.*, 1990. **56**: p. 1-20.
130. Rutter, E., *On the nomenclature of mode of failure transitions in rocks*. *Tectonophysics*, 1986. **122**(3): p. 381-387.
131. Hashin, Z., *Failure criteria for unidirectional fiber composites*. *Journal of applied mechanics*, 1980. **47**(2): p. 329-334.
132. Fredrich, J.T., B. Evans, and T.F. Wong, *Effect of grain size on brittle and semibrittle strength: Implications for micromechanical modelling of failure in compression*. *Journal of Geophysical Research: Solid Earth*, 1990. **95**(B7): p. 10907-10920.
133. Bazant, Z.P., *Size effect in blunt fracture: concrete, rock, metal*. *Journal of Engineering Mechanics*, 1984. **110**(4): p. 518-535.
134. Bažant, Z.P., *Size effect on structural strength: a review*. *Archive of applied Mechanics*, 1999. **69**(9-10): p. 703-725.
135. Bažant, Z.P., *Size effect*. *International Journal of Solids and Structures*, 2000. **37**(1): p. 69-80.
136. Bazant, Z.P. and J. Planas, *Fracture and size effect in concrete and other quasibrittle materials*. Vol. 16. 1997: CRC press.
137. Jaeger, J. *Failure of rocks under tensile conditions*. in *International Journal of Rock Mechanics and Mining Sciences & Geomechanics Abstracts*. 1967. Elsevier.



138. Marsal, R., *Mechanical properties of rockfill. Embankment Dam Engineering. Casagrande Volume. Hirschfeld, RC & Poulos, SJ, eds*, 1973, John Wiley & Sons.
139. Yin, Z.-Y., et al., *Modeling Mechanical Behavior of Very Coarse Granular Materials*. Journal of Engineering Mechanics, 2016: p. C4016006.
140. Bayuk, I.O., M. Ammerman, and E.M. Chesnokov, *Elastic moduli of anisotropic clay*. Geophysics, 2007. **72**(5): p. D107-D117.
141. Graham, J. and G. Houlsby, *Anisotropic elasticity of a natural clay*. Géotechnique, 1983. **33**(2): p. 165-180.
142. Li, X.S. and Y.F. Dafalias, *Constitutive modeling of inherently anisotropic sand behavior*. Journal of Geotechnical and Geoenvironmental Engineering, 2002. **128**(10): p. 868-880.
143. Ochiai, H. and P.V. Lade, *Three-dimensional behavior of sand with anisotropic fabric*. Journal of Geotechnical Engineering, 1983. **109**(10): p. 1313-1328.
144. Sayers, C. and M. Kachanov, *Microcrack-induced elastic wave anisotropy of brittle rocks*. JOURNAL OF GEOPHYSICAL RESEARCH-ALL SERIES-, 1995. **100**: p. 4149-4149.
145. Thomsen, L., *Elastic anisotropy due to aligned cracks in porous rock*. Geophysical Prospecting, 1995. **43**(6): p. 805-829.
146. Arthur, J., K. Chua, and T. Dunstan, *Induced anisotropy in a sand*. Geotechnique, 1977. **27**(1): p. 13-30.
147. Dewhurst, D.N. and A.F. Siggins, *Impact of fabric, microcracks and stress field on shale anisotropy*. Geophysical Journal International, 2006. **165**(1): p. 135-148.
148. Horii, H. and S. Nemat-Nasser, *Overall moduli of solids with microcracks: load-induced anisotropy*. Journal of the Mechanics and Physics of Solids, 1983. **31**(2): p. 155-171.
149. Johnson, D., et al., *Linear and nonlinear elasticity of granular media: Stress-induced anisotropy of a random sphere pack*. Journal of applied mechanics, 1998. **65**(2): p. 380-388.
150. Wong, R. and J. Arthur, *Induced and inherent anisotropy in sand*. Geotechnique, 1985. **35**(4): p. 471-481.
151. Brocca, M., Z.P. Bažant, and I.M. Daniel, *Microplane model for stiff foams and finite element analysis of sandwich failure by core indentation*. International Journal of Solids and Structures, 2001. **38**(44): p. 8111-8132.
152. Prat, P. and A. Gens, *Microplane formulation for quasibrittle materials with anisotropy and damage*. Fracture and Damage in Quasibrittle Structures: Experiment, modeling and computation, 2004: p. 67.
153. Cusatis, G., A. Beghini, and Z.P. Bažant, *Spectral Stiffness Microplane Model for Quasibrittle Composite Laminates—Part I: Theory*. Journal of Applied Mechanics, 2008. **75**(2): p. 021009.
154. Misra, A. and P. Poorsolhjoui, *Granular micromechanics based micromorphic model predicts frequency band gaps*. Continuum Mechanics and Thermodynamics, 2015: p. 1-20.
155. Gassmann, F., *Elastic waves through a packing of spheres*. Geophysics, 1951. **16**(4): p. 673-685.
156. Malvern, L.E., *Introduction to the Mechanics of a Continuous Medium*. 1969.
157. Nye, F., *Physical properties of crystals*. 1964: Clarendon Press Oxford.
158. Chang, C.S., J.S. Chao, and Y. Chang, *Estimates of Elastic Moduli for Granular Material With Anisotropic Random Packing Structure*. International Journal of Solids and Structures, 1995. **32**(14): p. 1989-2008.

159. Love, A.E.H., *A treatise on the mathematical theory of elasticity*. 1944: Dover.
160. Misra, A. and P. Poorsolhjouy, *Identification of higher-order elastic constants for grain assemblies based upon granular micromechanics*. Mathematics and Mechanics of Complex Systems, 2015. **3**(3): p. 285-308.
161. Misra, A. and P. Poorsolhjouy, *Elastic Behavior of 2D Grain Packing Modeled as Micromorphic Media Based on Granular Micromechanics*. Journal of Engineering Mechanics, 2016: p. C4016005.
162. Haddag, B., F. Abed-Meraim, and T. Balan, *Strain localization analysis using a large deformation anisotropic elastic-plastic model coupled with damage*. International Journal of Plasticity, 2009. **25**(10): p. 1970-1996.
163. Voigt, W., *Lehrbuch der kristallphysik (mit ausschluss der kristalloptik)*. 2014: Springer-Verlag.
164. Hardin, B.O. and F. Richart Jr, *Elastic wave velocities in granular soils*. Journal of Soil Mechanics & Foundations Div, 1963. **89**(Proc. Paper 3407).
165. Wyllie, M., A. Gregory, and G. Gardner, *An experimental investigation of factors affecting elastic wave velocities in porous media*. Geophysics, 1958. **23**(3): p. 459-493.
166. Wyllie, M.R.J., A.R. Gregory, and L.W. Gardner, *Elastic wave velocities in heterogeneous and porous media*. Geophysics, 1956. **21**(1): p. 41-70.
167. Leibig, M., *Model for the propagation of sound in granular materials*. Physical Review E, 1994. **49**(2): p. 1647.
168. Melin, S., *Wave propagation in granular assemblies*. Physical Review E, 1994. **49**(3): p. 2353.
169. Somfai, E., et al., *Elastic wave propagation in confined granular systems*. Physical Review E, 2005. **72**(2): p. 021301.
170. Datta, S. and A. Shah, *Elastic Waves in Composite Media and Structures*. 2009: CRC Press.
171. Vavrycuk, V., *Calculation of the slowness vector from the ray vector in anisotropic media*. Proceedings of the Royal Society a-Mathematical Physical and Engineering Sciences, 2006. **462**(2067): p. 883-896.
172. Misra, A., *Particle kinematics in Sheared Rod Assemblies*, in *Physics of Dry Granular Media*. 1998, Springer. p. 261-266.
173. Richefeu, V., G. Combe, and G. Viggiani, *An experimental assessment of displacement fluctuations in a 2D granular material subjected to shear*. Geotechnique Letters, 2012. **2**: p. 113-118.
174. Merkel, A., V. Tournat, and V. Gusev, *Experimental Evidence of Rotational Elastic Waves in Granular Phononic Crystals*. Physical Review Letters, 2011. **107**(22).
175. Jenkins, J., et al., *Fluctuations and the effective moduli of an isotropic, random aggregate of identical, frictionless spheres*. Journal of the Mechanics and Physics of Solids, 2005. **53**(1): p. 197-225.
176. Alibert, J.J., P. Seppecher, and F. Dell'Isola, *Truss modular beams with deformation energy depending on higher displacement gradients*. Mathematics and Mechanics of Solids, 2003. **8**(1): p. 51-73.
177. Seppecher, P., J.-J. Alibert, and F. dell'Isola, *Linear elastic trusses leading to continua with exotic mechanical interactions* Journal of Physics: Conference Series, 2011. **319**(1): p. 012018.
178. Mardia, K.V. and P.E. Jupp, *Directional statistics*. Vol. 494. 2009: John Wiley & Sons.

179. Agnolin, I., J.T. Jenkins, and L. La Ragione, *A continuum theory for a random array of identical, elastic, frictional disks*. *Mechanics of Materials*, 2006. **38**(8-10): p. 687-701.
180. dell'Isola, F., G. Sciarra, and S. Vidoli, *Generalized Hooke's law for isotropic second gradient materials*. *Proceedings of the Royal Society a-Mathematical Physical and Engineering Sciences*, 2009. **465**(2107): p. 2177-2196.
181. Germain, P., *Virtual Power Method in Mechanics of Elastic-Materials .1. Second Gradient Theory*. *Journal De Mecanique*, 1973. **12**(2): p. 235-274.
182. Andreaus, U., B. Chiaia, and L. Placidi, *Soft-impact dynamics of deformable bodies*. *Continuum Mechanics and Thermodynamics*, 2013. **25**(2-4): p. 375-398.
183. Andreaus, U., L. Placidi, and G. Rega, *Microcantilever dynamics in tapping mode atomic force microscopy via higher eigenmodes analysis*. *Journal of Applied Physics*, 2013. **113**(22).
184. Chen, Y. and J.D. Lee, *Connecting molecular dynamics to micromorphic theory.(I). Instantaneous and averaged mechanical variables*. *Physica A: Statistical Mechanics and its Applications*, 2003. **322**: p. 359-376.
185. Ganghoffer, J.-F., *On the generalized virial theorem and Eshelby tensors*. *International Journal of Solids and Structures*, 2010. **47**(9): p. 1209-1220.
186. Chang, C.S. and A. Misra, *Computer simulation and modelling of mechanical properties of particulates*. *Computers and Geotechnics*, 1989. **7**(4): p. 269-287.
187. Hill, R., *The elastic behaviour of a crystalline aggregate*. *Proceedings of the Physical Society. Section A*, 1952. **65**(5): p. 349.
188. Andreaus, U., M. Colloca, and D. Iacoviello, *An optimal control procedure for bone adaptation under mechanical stimulus*. *Control Engineering Practice*, 2012. **20**(6): p. 575-583.
189. Andreaus, U., M. Colloca, and D. Iacoviello, *Optimal bone density distributions: numerical analysis of the osteocyte spatial influence in bone remodeling*. *Computer methods and programs in biomedicine*, 2014. **113**(1): p. 80-91.
190. Ferretti, M., et al., *Modeling the onset of shear boundary layers in fibrous composite reinforcements by second-gradient theory*. *Zeitschrift für angewandte Mathematik und Physik*, 2014. **65**(3): p. 587-612.
191. dell'Isola, F., A. Madeo, and L. Placidi, *Linear plane wave propagation and normal transmission and reflection at discontinuity surfaces in second gradient 3D continua*. *Zamm-Zeitschrift Fur Angewandte Mathematik Und Mechanik*, 2012. **92**(1): p. 52-71.
192. Madeo, A., et al., *Wave propagation in relaxed micromorphic continua: modeling metamaterials with frequency band-gaps*. *Continuum Mechanics and Thermodynamics*, 2013: p. 1-20.
193. Placidi, L., et al., *Reflection and transmission of plane waves at surfaces carrying material properties and embedded in second-gradient materials*. *Mathematics and Mechanics of Solids*, 2014. **19**(5): p. 555-578.
194. dell'Isola, F. and S. Vidoli, *Continuum modelling of piezoelectromechanical truss beams: an application to vibration damping*. *Archive of Applied Mechanics*, 1998. **68**(1): p. 1-19.
195. Greco, L., N. Impollonia, and M. Cuomo, *A procedure for the static analysis of cable structures following elastic catenary theory*. *International Journal of Solids and Structures*, 2014. **51**(7-8): p. 1521-1533.

196. Madeo, A., L. Placidi, and G. Rosi, *Towards the Design of Metamaterials with Enhanced Damage Sensitivity: Second Gradient Porous Materials*. Research in Nondestructive Evaluation, 2014. **25**(2): p. 99-124.
197. Maurini, C., F. dell'Isola, and J. Pouget, *On models of layered piezoelectric beams for passive vibration control*. Journal De Physique Iv, 2004. **115**: p. 307-316.
198. Maurini, C., J. Pouget, and F. dell'Isola, *Extension of the Euler-Bernoulli model of piezoelectric laminates to include 3D effects via a mixed approach*. Computers & Structures, 2006. **84**(22-23): p. 1438-1458.
199. Porfiri, M., F. dell'Isola, and E. Santini, *Modeling and design of passive electric networks interconnecting piezoelectric transducers for distributed vibration control*. International Journal of Applied Electromagnetics and Mechanics, 2005. **21**(2): p. 69-87.
200. Vidoli, S. and F. dell'Isola, *Vibration control in plates by uniformly distributed PZT actuators interconnected via electric networks*. European Journal of Mechanics a-Solids, 2001. **20**(3): p. 435-456.
201. Andreaus, U. and P. Baragatti, *Cracked beam identification by numerically analysing the nonlinear behaviour of the harmonically forced response*. Journal of Sound and Vibration, 2011. **330**(4): p. 721-742.
202. Andreaus, U. and P. Baragatti, *Experimental damage detection of cracked beams by using nonlinear characteristics of forced response*. Mechanical Systems and Signal Processing, 2012. **31**: p. 382-404.
203. Andreaus, U., I. Giorgio, and A. Madeo, *Modeling of the interaction between bone tissue and resorbable biomaterial as linear elastic materials with voids*. Zeitschrift für angewandte Mathematik und Physik, 2014: p. 1-29.
204. Altenbach, H., et al., *Acceleration waves and ellipticity in thermoelastic micropolar media*. Archive of Applied Mechanics, 2010. **80**(3): p. 217-227.
205. Yang, Y., W.-Y. Ching, and A. Misra, *Higher-order continuum theory applied to fracture simulation of nano-scale intergranular glassy film*. Journal of Nanomechanics and Micromechanics, 2011. **1**(2): p. 60-71.
206. Misra, A. and P. Poorsolhjoui, *Granular micromechanics based micromorphic model predicts frequency band gaps*. Continuum Mechanics and Thermodynamics, 2016. **28**(1-2): p. 215-234.
207. Brillouin, L., *Wave propagation and group velocity*. Vol. 8. 2013: Academic Press.
208. Sachse, W. and Y.H. Pao, *On the determination of phase and group velocities of dispersive waves in solids*. Journal of Applied Physics, 1978. **49**(8): p. 4320-4327.